HYDRODYNAMIC CAVITATION PHENOMENON IN MULTI-PHASE FLOWS

by

Hongbo Shi

A thesis submitted in partial fulfillment of the requirements for the degree of

Doctor of Philosophy

in

Chemical Engineering

Department of Chemical and Materials Engineering
University of Alberta

Abstract

The main objective of the present study is to experimentally and numerical studies of hydrodynamic cavitation phenomenon in the Venturi tubes, in order to validate and further develop numerical multiphase flow models with the obtained data. To achieve this, a visible experimental set-up was designed. Besides, both two-dimensional and three-dimensional numerical simulations were conducted to analyze the characteristics of cavitation that cannot be experimentally evaluated, such as the volume of each phase, the turbulence distribution, and the location of cavitation and mixing zones. The cavitation behavior has been described by means of non-dimensional parameters such as cavitation number, Reynolds number, pressure loss coefficient and vapor/gas volume fraction.

The commercial computational fluid dynamics (CFD) software, ANSYS FLUENT 16.2 is utilized. For experimental data acquisition, five cavitating Venturi tubes with different geometrical parameters were manufactured and tested at different inlet flow conditions in order to measure their inflow parameters and to obtain their characteristic curves. On the numerical part, based on the two-phase (water-vapor) mixture model and four-phase (water-solid-vapor-air) Eulerian-Eulerian model, a set of global computation model was developed and applied to multi-phase modeling of cavitation process in different cavitating Venturi tubes. Predictions of the pressure drop obtained from the CFD model are generally in good conformance with experimental measurements.

In the study of two-phase cavitaitng flows, the effect of the convergent angle and divergent angle on the cavitation performance was investigated experimentally and numerically. Both the numerical and experimental studies reveal that the change in the convergent angle and divergent angle has significant effects on flow characteristics and the generation of cavitation. It was shown that a 85° convergent angle and a 2.5° divergent angle are of benefit to cavitation. A scaled-up study of the Venturi geometry has been conducted using CFD-based numerical simulations. Finally, a empirical model enabling the prediction of

cavitation in Venturi tubes has been developed and validated.

In the study of four-phase cavitaitng flows, a new four-phase global model was developed based on a simpler engineering approach and validated against experimental data. Both the numerical and experimental studies reveal that the addition of solid particles (W_s=5$\sim$30 wt%) in the cavitating Venturi tube has significant effects on the generation of cavitation. The outcomes show that the higher solid mass concentration is of benefit to cavitation intensity. The proposed CFD model has proved to be an efficient and reliable tool in predicting the cavitation activities and performance characteristics of the cavitating Venturi tube.

In the micro-scale study, the particle-flow interaction and characteristics of cavitation are investigated numerically using a CFD-based mixture model. The particle size is varied between 10 microns and 100 microns. CFD-based simulations are conducted over a wide range of particle Reynolds numbers Re from 1 to 1800 for different particle sizes. The effects of the particle shape, the surface roughness, the number of particles, and the particle surface temperature on flow characteristics and occurrence of cavitation were investigated. The results show that particle roughness significantly increases the occurrence of cavitation. Moreover, cavitation development increases as the particle surface temperature increases from 40°C to 99.9°C. Finally, an empirical relation enabling the prediction of cavitation in the particular flows has been developed based on CFD results.

In the end, a computational investigation of the cavitation and mixing characteristics of two miscible (Schmidt number $Sc = 10^3$) turbulent water flows with different viscosity ratios is conducted in a Venturi tube. The 2D axis$-$symmetric RANS and 3D LES turbulence models are used for the prediction of flow characteristics. The numerical results reveal that the RANS solutions underpredict the rate of vapor production and overestimate the mixing rate of two miscible fluids in comparison to LES simulations for the inlet Reynolds number of 19738 (Case$-$1) and 19286 (Case$-$2). In particular, there is a larger cavitation zone in the Venturi tube with LES in comparison to RANS calculations.

Preface

This thesis is presented in the paper format, and is based on four papers. To the date, one papers is published and available online, and three papers are submitted and under peer revision. The following is a statement of contributions made to collaborative work contained in this thesis:

Chapter 1: Introduction is an original work by Hongbo Shi.

Chapter 2 of this thesis is an extended version of: Hongbo Shi, Mingda Li, Petr Nikrityuk, and Qingxia Liu. Experimental and numerical study of cavitation flows in venturi tubes: from cfd to an empirical model. *Chemical Engineering Science*, Vol. 207 pp.672–687, 2019. The simulations in this study were performed in the computers provided by Dr. Petr Nikrityuk. The experiments were conducted in Dr. Qingxia Liu's labs at the University of Alberta. They were also the supervisory authors and were involved with concept formation and manuscript composition. I was responsible for writing, editing, software validations and calculations, experiments (50%) and visualization. Mingda Li contributed to the experimental design and experiments (50%).

Chapter 3 of this thesis has been published as: Hongbo Shi, Mingda Li, Qingxia Liu and Petr Nikrityuk. Experimental and numerical study of cavitating particulate flows in a venturi tube. *Chemical Engineering Science*, Vol.219, pp115598, 2020 (21 pages). The simulations in this study were performed in the computers provided by Dr. Petr Nikrityuk. The experiments were conducted in Dr. Qingxia Liu's labs at the University of Alberta. They were also the supervisory authors and were involved with concept formation and manuscript composition. I was responsible for writing, editing, software validations and calculations, experiments (50%) and visualization. Mingda Li contributed to the experimental design and experiments (50%).

Chapter 4 of this thesis has been accepted as: Hongbo Shi, Qingxia Liu and Petr Nikrityuk. Modeling of cavitating flows past a micro-sized particle. *International Journal of Multiphase Flow*, 2020. This Chapter has been presented at the 69th Canadian Chemical Engineering Conference in Halifax, Canada and the Faculty of Engineering Graduate Research Symposium 2019 in Edmonton, Canada. The simulations in this study were performed in the computers provided by Dr. Petr Nikrityuk. Dr. Petr Nikrityuk and Dr. Qingxia Liu were the supervisory authors and were involved with concept formation and manuscript composition. I was responsible for writing, editing, software validations and calculations and visualization.

Chapter 5 of this thesis has been submitted as: Hongbo Shi, Qingxia Liu and Petr Nikrityuk. Numerical study of mixing of cavitating flows in a Venturi tube. *The Canadian Journal of Chemical Engineering*. The simulations in this study were performed in the computers provided by Dr. Petr Nikrityuk. Dr. Petr Nikrityuk and Dr. Qingxia Liu were the supervisory authors and were involved with concept formation and manuscript composition. I was responsible for writing, editing, software validations and calculations and visualization.

Chapter 6: Conclusions and future work are original works by Hongbo Shi.

Acknowledgements

I would like to take this opportunity to express my gratitude to all the people who gave great help for my PhD studies in Department of Chemical and Materials at University of Alberta.

Firstly, I would like to give my most sincere gratitude and appreciation to my two co-supervisors, **Dr. Petr A. Nikrityuk** and **Dr. Qingxia Liu** who gave me numerous kind and patient help not only on the academic and research areas, but also on my personal life and career development. Without their unconditional support and great guidance during the study and research period, I could not complete my PhD degree. I will not forget the knowledge they taught me, the skills they helped me to develop the professional ethics and the enthusiasm of scientific researches they delivered. All of these will give me great help for my life and career as a chemical science engineer. My deep appreciation also goes to my exam committee members, Dr. Robert E. Hayes and Dr. Tony Yeung for participating in my exam committee and for the time to scrutinize my thesis. Their comments are highly appreciated.

I would also like to acknowledge my former supervisor, Dr. Alexandra Komrakova, from Mechanical Department, University of Alberta, for providing me opportunity at the early stage of research and your faith in my abilities.

I would like to show my appreciation to Mingda Li for giving me valuable suggestions and assistance on the experimental design and data analysis. I am grateful to Ivan Cornejo for your great suggestions on the CFD modeling. Without your effort on answering my questions, my work could not be smoothly processed. I would like to extend a special thanks to Dr. Nguyen Thuy Vu Truong for sharing your experience on the fundamental knowledge of multiphase flows and the advice you provided to fill out some of my knowledge gaps.

To close this on an emotional note, I must acknowledge all those professors, staffs and students, to numerous to list, at University of Alberta who have educated and helped me over the years.

It is love, however, that truly motivates. I would like to express my deepest gratitude and appreciation to my parents, Fuqiang Shi and Jinying Yuan for their constant love, support and encouragement over the years. The final word of thanks is dedicated to my girlfriend, Anna, your continuing support and optimism kept me motivated to work hard and enjoy this journey.

I have been very lucky for being surrounded by such wonderful people in my life.

Table of Contents

List of Tables

List of Figures

List of Symbols

C_D	drag coefficient	
C_p	heat capacity	J/kg-K
d	diameter of throat section	mm
D	diameter of inlet pipe	mm
D_{50}	volume median diameter	μm
$D_{i,m}$	mass diffusivity	m^2/s
D_p	diameter of particle	μm
e_{ss}	coefficient of restitution	
E	energy	
g	gravitational acceleration	m/s^2
$g_{0,ss}$	radial distribution function	
H	height of the domain	μm
K	pressure loss coefficient	
K_c	critical pressure loss coefficient	
K_{pq}	interphase momentum exchange coefficient	
$k-\varepsilon$	K-Epsilon turbulence model	
$k-\omega$	K-Omega turbulence model	
L	length of the Venturi tube or pipe	mm
$\dot{m}$	mass flow rate	kg/s
n	bubble number density	$1/m^3$
P	pressure	Pa
P_d	dynamic pressure	Pa
$P_{d,c}$	critical dynamic pressure	Pa
P_{in}	upstream pressure	Pa
P_∞	downstream pressure	Pa

ΔP	static pressure drop	Pa
Q	slurry flow rate	m^3/s
R_b	radius of bubble	μm
$\vec{Re}_{pq}$	interaction force between phases	
R	mass transfer between phases	kg/s
R_e	mass transfer source term connected to the growth of the bubbles	
R_c	mass transfer source term connected to the collapse of the bubbles	
Re_{in}	inlet Reynolds number	
Re_c	critical inlet Reynolds number	
Re_s	Reynolds number for solid particle	
S_E	sensible enthalpy	kj/kg
S_{ij}	mean rate-of-strain tensor	
Sc	Schmidt number	
Sc_t	turbulent Schmidt number	
t	time	s
T_f	temperature of fluid flow	°C
T_{in}	inlet temperature	°C
T_p	temperature of particle surface	°C
<U>	volume-averaged flow velocity	m/s
U_{in}	upstream flow velocity	m/s
U_{th}	throat flow velocity	m/s
$\vec{u}$	velocity vector in LES model	
$\vec{v}$	velocity vector in RANS model	
V	volume	m^3
$\overline{v}$	volume-averaged velocity	
W_s	solid mass concentration	
Y	component	

Greek letters

α	convergent angle
β	divergent angle
γ	surface tension
γ_{θ_s}	collisional energy dissipation

λ_s	bulk viscosity of solid phase
μ	viscosity
μ_t	turbulent viscosity
μ_o	laminar viscosity
$\mu_{s,col}$	solid collisional viscosity
$\mu_{s,kin}$	solid kinetic viscosity
$\mu_{s,fr}$	frictional viscosity
ω	specific dissipation rate
ε	dissipation of turbulence energy rate
ϕ	volume fraction
$\phi_{l,s}$	local volume fraction of solid phase
ρ	density
σ	cavitation number
σ_{est}	standard deviation of the estimate
λ	thermal conductivity
λ_{eff}	effective thermal conductivity
$\overline{\overline{\tau}}_q$	q^{th} phase stress-strain tensor
Θ_q	granular temperature

Subscripts

a	air phase
l	liquid phase
m	mixture phase
p	phase p
q	phase q
s	solid phase
v	vapor phase

Chapter 1

Introduction

1.1 Existing technologies in hydrodynamic cavitation

Numerous chemical, petroleum, environmental, and mineral engineering processes involve the cavitation phenomenon. Cavitation, by definition, is a process which occurs by the effect of a rapid change in the local static pressure at a constant ambient temperature [1, 2]. It involves the formation and growth of vapor bubbles as a consequence of varied pressure applied in a liquid flow system. Cavitation process can be classified into four principle types: hydrodynamic cavitation, acoustic cavitation, optic cavitation and particle cavitation. Among various types of cavitation, hydrodynamic cavitation has been widely concerned by researchers because of its competitive advantages such as high energy efficiency, lower capacity and operation costs, ease in process control and quantification, and feasibility of scaling up at industrial applications [3, 4, 5, 6]. In the case of hydrodynamic cavitation, vapor bubbles are generated when the local static pressure falls below the vapor pressure as the fluid flows through geometric constrictions. The governing principle of hydrodynamic cavitation is based on the Bernoulli's Principle [7]:

$$P_1 + \frac{1}{2}\rho_l V_1^2 = P_2 + \frac{1}{2}\rho_l V_2^2 = C(constant) \tag{1.1}$$

Where ρ_l is the density of the liquid, V and P are the liquid flow velocity and pressure at a point of the flowing liquid, respectively. The change of geometric constrictions results in an increase in the kinetic energy and the decrease of the local pressure in the restricted area. If the local pressure falls below the vapor pressure of the medium, tiny vapor bubbles are generated in this area.

Various designs have been developed to generate hydrodynamic cavitation. The first modern reactor based on the hydrodynamic cavitation is liquid whistle reactor (see Fig.1.1) (e.g Benchtop Sonolator^{TM} 2000). The main purpose of this reactor is for emulsification,

homogenization and dispersion. Cavitation is generated with the vibrations as liquid passes through the steel plate at a high velocity. The dominant features of liquid whistle reactor is the high efficient mixing and the reversed power transfer process [8]. However, This reactor suffers some considerable challenges, such as low vibrational power, high pumping cost, and erosion of the vibrating blade with some particulate particles [8]. Moreover, the operating geometry of this reactor is fixed which means that the hydrodynamic cavitation intensity can not be easily controlled.

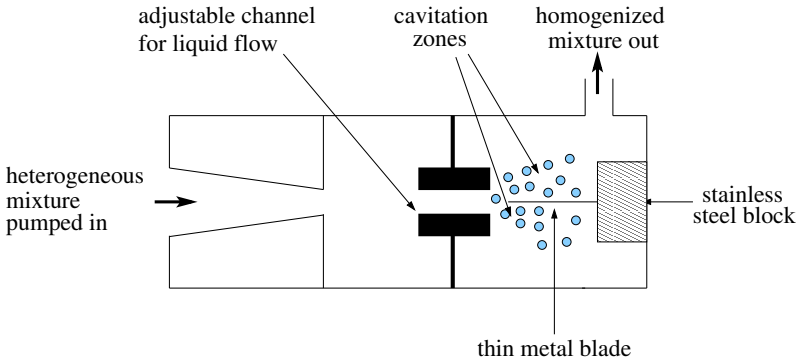

Figure 1.1: Schematic diagram of the liquid whistle reactor, adapted from[9].

High-pressure homogenizer (see Fig.1.2) (e.g GEA Ariete Homogenizer 5400) is the most widely used device for creating homogeneous dispersions. The main idea behind of this technique is to generate a homogeneous size particles suspension from the non-homogenized liquid under the effect of hydrodynamic cavitation [10]. As the feed enters the closed clearance between the homogenization valve and valve seat under a high pressure in the range of 20 to 70 MPa, the local velocity increases and the pressure decreases [11]. The hydrodynamic cavitation starts at a certain critical local pressure. High-pressure homogenizer is very suited for the emulsification processes in the food, pharmaceutical and bioprocess industrial applications [8]. The demerits of this technique are the lack of control on the population of cavitation events and the magnitude of the pressure pulses that produced at the end of cavitation [8].

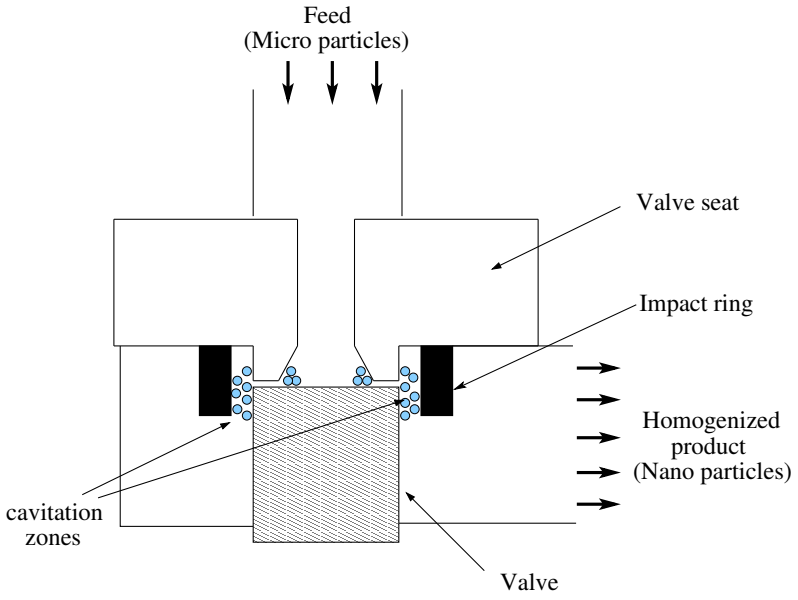

Figure 1.2: Schematic diagram of the high-pressure homogenizer, adapted from[12].

In spite of pressure based equipments, hydrodynamic cavitation can also be generated from the rotating equipments. High-speed homogenizer (e.g Kos-140) is a typical hydrodynamic cavitation rotating reactor. This technique consists of a stator-rotor and a plate with holes attached to the stator. The local pressure close to the periphery of the impeller significantly decreases due to the high speed of the impeller [13]. Subsequently, the cavitation bubbles are generated. By varying the voltage, the rotational speed for this reactor can be changed in the range between 4000 rpm to 20000 rpm [8]. The disadvantages of high-speed homogenizer are the high energy consumption at such high speed rotation and low flexibility on the design parameters in comparison with low-pressure cavitation reactors (e.g. Venturi tubes or orifice).

Low-pressure hydrodynamic cavitation reactor (e.g CavTube) is the most efficient cavitating devices in creating cavitational intensity conditions [14]. The applications of low-pressure hydrodynamic cavitation reactor can be observed in many industrial fields, such as wastewater treatment [15], biotechnology [16], chemical synthesis [3], and mineral processing [17]. To date, intense studies have focused on low-pressure hydrodynamic cavitation reactors since they can provide high flexibility on operating (regulation of temperature, inlet pressure and flow rate) and geometric conditions (setting of holes on the orifice). The maximum cavitational intensity can be achieved with minimum energy consumption in this type reactor for varied requirements and applications [13].

The low-pressure hydrodynamic cavitation reactor has different constructions, such as single- or multiple-holes orifice (see Fig.1.3) or Venturi tubes (see Fig. 1.4). The cavitation

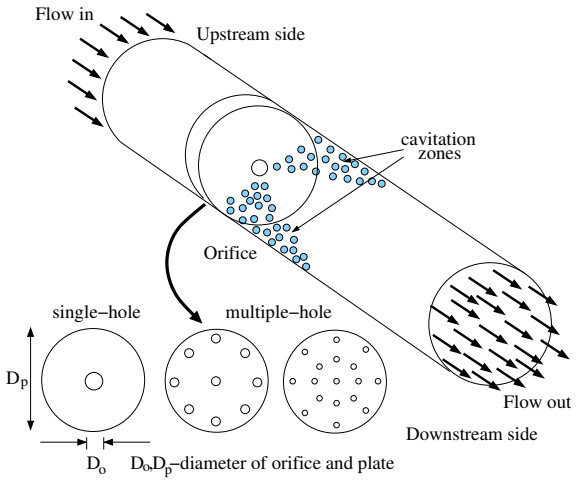

Figure 1.3: Schematic diagram of the single and multuple-hole orifices. adapted from[14].

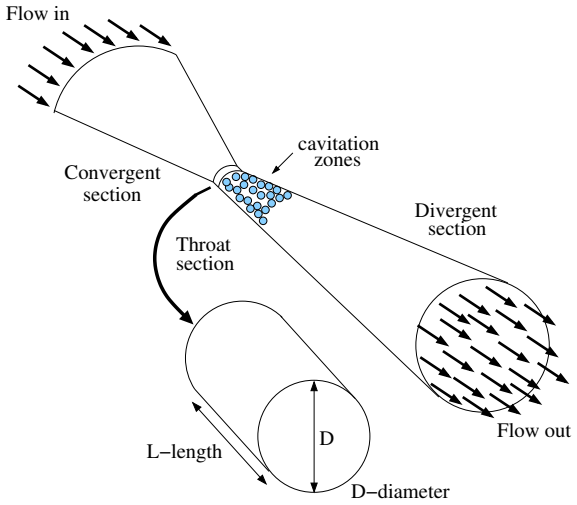

Figure 1.4: Schematic diagram of the cavitating venturi tube, adapted from [14].

in a Venturi tube is generally stable due to geometrical configurations while that in a orifice (single/multiple) is transient in nature [14]. The three main compositions of a venturi are convergent section, throat section, and divergent section as shown in Fig.1.4. When the liquid pressure in the throat of the venturi is lower than the vapor pressure, a quick phase transition from liquid to vapor occurs. Some important geometrical parameters such as the throat area, throat height/diameter to length ratio, convergent and divergent angles play a significant role in the design of a venturi-based reactor since these parameters greatly affect the cavitational activities (e.g. cavitational population, magnitude of the collapse pressure, and residence time of the cavity in low pressure field) [14]. In comparison with other low-pressure hydrodynamic cavitation reactors (e.g. single-hole or multiple-holes orifice), the

cavitation bubble can reach a maximum size before their collapse in the Venturi tube since the smooth divergent section restricts the dramatic pressure recovery and affords more time for a bubble to stay in a low pressure field [18]. The stable and large number of cavitation bubbles generated in the Venturi tube is advantageous for the applications that needs longer cavitational exposure time, such as mineral extraction and wastewater treatment. Therefore, Venturi-based hydrodynamic cavitation reactor is the main cavitating device investigated in this study.

1.2 State of the art in modeling

Analysis of different types of hydrodynamic cavitation technologies in industry shows that even though great advances of cavitation application have been achieved in each field, the performance is still far from the optimum. Parallel to the continuing effort to obtain better experimental result, there is an increasing demand for CFD models to reduce experimental blind testing and accurately describe and predict the hydrodynamic cavitation phenomena in the cavitation reactors. An ideal cavitation model consisting of various physical models requires special modeling strategies. These modeling strategies are usually built based on empirical hypothesis for multiphase environment. It is very challenging to build such ideal model since cavitating flows are highly dynamic with a complex interaction with two-phase or four-phase structures. In addition, large density changes associated with phase change. For example, the ratio of liquid water density to vapor water density ($\frac{\rho_l}{\rho_v}$) is over 40000 at room temperate [19]. Moreover, the existence of the turbulence with a complex interaction with multiphase structures significantly affect cavitation flows in different designed Venturi tubes. Nevertheless, considerable numerical studies have been devoted to understanding and developing hydrodynamic cavitation over the decades.

In the study of two-phase cavitating flows, many scholars−such as Barre et al. [20], Goncalves et al. [21], Charriere et al. [22], Zhang et al. [23], and Zhao et al. [24]−have made significant contributions, completing numerical studies in Venturi tubes by varying the geometrical parameters (e.g. throat diameter, throat length, and convergent angle), model parameters (e.g. multiphase model, turbulence model, and cavitation model), and operation conditions (e.g. upstream flow rate, temperature, pressure drop). Although different aspects of two-phase cavitating flows have been studied, the effect of convergent angle and the difference between lab-scale and large-scale Venturi tubes have not been investigated in details. Bashir et al. [25] conducted CFD analyses of different Venturi tubes such as circular, slit, and elliptical Venturis, at different ratios of throat diameter to throat length (1:0.5, 1:1, 1:2, and 1:3) and divergent angle (5.5°, 6.5°, 7.5°, and 8.5°). $k-\varepsilon$ was applied to model fluid turbulence in both 2D and 3D domains. The optimum

divergent angle and ratio of throat diameter to throat length were found to be 5.5° and 1:1 for all the Venturi tubes considered. Simpson et al. [26] used a 2D k-ω SST turbulence model to investigate the influences of geometrical parameters, such as the ratio of the throat section length to diameter and divergent angle, and operating conditions, such as flow rate and pressure drop on the inception and extent of cavitation in Venturi tubes. The numerical results indicate that the optimum configuration exits with a low divergent angle (7.5°) and the ratio of the throat section length to diameter of 1:1. Kumar and Moholka [27] proposed a conceptual design for a novel hydrodynamic cavitation reactor that uses a converging-diverging nozzle with a gas sparger to generate cavitational bubbles. Based on the simulation results, they found that increasing the upstream pressure (from 1 to 1.5 atm) and the nozzle length (from 3 to 6 inches) and decreasing the initial bubble size (from 200 to 100 μm) is a means of intensifying the sonochemical effects (bubble size, temperature and pressure peaks reached in the bubble at the first compression). They also found that an argon bubble can produce greater sonochemical effects in comparison with an air bubble. Jin et al. [28] performed a 2D CFD simulations using a $k-\varepsilon$ turbulence model to study the effect of heat transfer in a Venturi tube. The simulation and experimental results were relatively close by considering the thermal phase change model. They concluded that the release of latent heat from the cavitation phenomenon lead to a temperature drop in the vapor phase. Margot et al. [29] used seven different 3D turbulence models ($k-\varepsilon$/ low Re/ hybrid, $k-\varepsilon$/ high Re/ standard, $k-\varepsilon$ Re-Normalisation Group (RNG)/ standard, $k-\omega$ shear stress transport (SST) and standard/ high and low Re/hybrid and standard) to study the cavitation flow within a throttle channel at different operation conditions. The results show that the vapor volume fraction decreases as the liquid viscosity increases. The $k-\varepsilon$/ low Re/ hybrid model provides a better agreement against experiment data as compared to other models.

In the study of four-phase cavitating flows, the addition of solid particles into Venturi tubes have been the subject of a number of recent experimental studies. Gu et al. [30], Medrano et al. [31], Dunn et al. [32], and Li [33] each presents a clear description of positive outcome of solid particles on the cavitation inception and growth in different hydrodynamic cavitation reactors. However, only the experimental studies of four-phase cavitating flows have been carried out, the numerical simulation of cavitating particulate flows with different particle shapes, size, and concentrations has not been conducted in Venturi tubes. Gregorc et al. [34] performed experimental and three-dimensional (3D) CFD simulations using an Eulerian-Eulerian model to investigate how solid particles affect the turbulent cavitation flow over a hydrofoil. The author showed that the magnitude of torque increases with the presence of solid particles in the fluid. As the solid mass fraction rises from 0.001 to 0.0032, the vapor volume fraction increases significantly on the

surface of the hydrofoil. Kabeel and Abdelgaied [35] studied the influences of the alumina nano-particles (AL_2O_3) on cavitation behaviors in the orifice using a two-dimensional (2D) mixture model. The vapor volume fraction rises to a maximum value of 0.17 as the solid volume fraction increases from 0 to 0.1. Chen et al. [36] used a 3D mixture model to analyze how nanoparticles influence the turbulent cavitation flow in the pipe. The results show that higher nanoparticle concentrations and a larger nanoparticle size increase the cavitation zone with a lower inlet pressure (0.4 MPa), while the effects of the nanoparticle concentration and diameter are limited for the higher inlet pressures (0.6 and 1.0 MPa). The vapor volume fraction increases significantly as the particle size increases from 13 nm to 80 nm at a lower operating temperature (25 °C), while the effect of particle size on cavitation is limited under a higher operating temperature (40 °C). Li et al. [37] used molecular dynamic simulations to investigate the inception of cavitation in water with solid nanoparticles. They observed that the presence of the nanoparticles reduces the number and energy of the hydrogen bond network in the water. The results show that polyethylene particles can generate more vapor bubbles in the water as compared to SiO_2 particles. Pendar et al. [38] used a 3D Large Eddy Simulation (LES) to investigate the wall-bounded flow characteristics of sphere cavitation over a wide range of cavitation numbers (0.36 to 1). The numerical results indicated that the vortical region behind the sphere grows as the cavitation number rises from 0.4 to 1 because of the presence of the vortical flow inside the cavity. It was found that the formation of a re-entrant jet appears at a cavitation number of 0.9, and the thickness of the re-entrant jet decreases as the cavity length increases.

1.3 Review of current cavitation models in ANSYS Fluent

Treatment of hydrodynamic cavitation is the crucial component of numerical prediction of cavitation in Venturi tubes. In the last few decades, several computational fluid dynamics (CFD) methods for analyzing cavitation phenomenon have been developed and implemented in commercial CFD software, e.g. ANSYS FLUENT [39, 40, 41], STAR-CCM+ [42, 43, 44] and open-source CFD software, e.g. OPEN Foam [45, 38, 46]. One of the methods used in the current commercial CFD software is the homogeneous fluid approach based on the vapor transport equation model. In the homogeneous fluid approach, the continuity and momentum equations for the mixture and an additional transport equation for the vapor volume fraction are solved. It is commonly assumed in the vapor transport model that the flow is isothermal and liquid and vapor phases is incompressible [47]. The mass transfer model is required a source term to evaluate the phase change between liquid

and vapor (evaporation and condensation) as indicated in the right hand side of Eq. 1.2:

$$\frac{\partial}{\partial t}(\alpha_v \rho_v) + \nabla \cdot (\alpha_v \rho_v \vec{v}_v) = R_e - R_c \tag{1.2}$$

where α_v, ρ_v, and $\vec{v}_v$ are the volume fraction, density, and velocity of the vapor phase, respectively. The mass source terms, R_e and R_c, are derived from a reduced form of Rayleigh-Plesset equation describing the growth of a single vapor bubble in a liquid.

Under the condition of zero velocity slip between the liquid and vapor phases, the generalized Rayleigh-Plesset equation is expressed as [2]:

$$\frac{P_B - P_\infty}{\rho_l} = R_B \frac{d^2 R_B}{dt^2} + \frac{3}{2}(\frac{dR_B}{dt})^2 + \frac{4\nu_l}{R_B}\frac{dR_B}{dt} + \frac{2S}{\rho_l R_B} \tag{1.3}$$

where P_B and P_∞ are bubble pressure and local far-field pressure, respectively. R_B is the bubble radius, ν_l is the liquid dynamic viscosity, σ is the surface tension coefficient between the liquid phase and vapor phase.

Since in most multiphase flow cases the inertial forces plays a dominant role in comparison with the viscous effect and the surface tension force, the generalized Rayleigh-Plesset equation is further simplified to:

$$\frac{dR_B}{dt} = \pm\sqrt{\frac{2}{3}\frac{|P_B - P_\infty|}{\rho_l}} \tag{1.4}$$

This simplified form of the Rayleigh-Plesset equation has been used to develop the cavitation models in most of the commercial CFD softwares. In ANSYS Fluent, the three most popular cavitation models are: Singhal et al. model [19], Schnerr-Sauer et al. model [48], and Zwart et al. model [49]. These models are based on the same vapor transport equation and the same bubble dynamics considerations but differ by the expression of the mass change rate, R_e and R_c. To improve the model accuracy, some empirical calibration coefficients and other parameters such as the non-condensable gas fraction in Singhal et al. model, the vapor bubble radius in Zwart et al. model and the number of spherical bubbles per volume of liquid in Schnerr-Sauer et al. model are implemented in each model.

The Singhal et al. model is known as the full-cavitation model. In this model, many factors that affect the cavitation process such as the phase change, bubble dynamics, local turbulent pressure fluctuations and non-condensable gas are considered.

In particular, for Singhal et al. model, the vaporization and condensation mass transfer rates are expressed as:

if $P_V \geq P_\infty$,

$$R_e = F_{vap} \frac{max(1.0, \sqrt{k})(1 - f_v - f_g)}{\sigma} \rho_l \rho_v \sqrt{\frac{2(P_v - P_\infty)}{3\rho_l}} \tag{1.5}$$

and if $P_V \leq P_\infty$,

$$R_c = F_{cond} \frac{max(1.0, \sqrt{k}) f_v}{\sigma} \rho_l \rho_v \sqrt{\frac{2(P_\infty - P_v)}{3\rho_l}} \tag{1.6}$$

The symbols in the above expressions are defined as follows: F_{vap}=0.02 and F_{cond}=0.01 are two empirical calibration coefficients for evaporation and condensation, respectively. f_v and f_g are vapor mass fraction and non-condensable gas mass fraction, respectively. The value of non-condensable gas mass fraction is considered as 1.5×10^{-5}, which is the default value set in ANSYS Fluent.

The Zwart et al. model assumes that the vapor bubbles are all in the same size. In this model, the bubble density number and the mass change rate of a single bubble are used to determine the total interphase mass transfer rate. The bubble number density is defined as the number of spherical bubbles per volume of liquid.

For Zwart et al. model, the vaporization and condensation mass transfer rates are expressed as:

if $P_V \geq P_\infty$,

$$R_e = F_{vap} \frac{3\alpha_{nuc}(1 - \alpha_v)\rho_v}{R_B} \sqrt{\frac{2(P_v - P_\infty)}{3\rho_l}} \tag{1.7}$$

and if $P_V \leq P_\infty$,

$$R_c = F_{cond} \frac{3\alpha_v \rho_v}{R_B} \sqrt{\frac{2(P_\infty - P_v)}{3\rho_l}} \tag{1.8}$$

The symbols in the above expressions are defined as follows: F_{vap}=50 and F_{cond}=0.001 are two empirical calibration coefficients for evaporation and condensation, respectively; R_B=5×10^{-6} is the default bubble radius; α_{nuc}=5×10^{-4} is the default nucleation site volume fraction.

The Schnerr-Sauer et al. model follows a similar approach as the Singhal et al. model to derive the expression of interphase mass transfer rate from liquid to vapor. In this model, the bubble density number is consider to be constant.

For Schnerr-Sauer et al. model, the vaporization and condensation mass transfer rates are expressed as:

if $P_V \geq P_\infty$,

$$R_e = \frac{\rho_v \rho_l}{\rho} \alpha_v (1 - \alpha_v) \frac{3}{R_B} \sqrt{\frac{2(P_v - P_\infty)}{3\rho_l}} \tag{1.9}$$

and if $P_V \leq P_\infty$,

$$R_c = \frac{\rho_v \rho_l}{\rho} \alpha_v (1 - \alpha_v) \frac{3}{R_B} \sqrt{\frac{2(P_\infty - P_v)}{3\rho_l}} \tag{1.10}$$

where the vapor volume fraction is defined as:

$$\alpha_v = \frac{n \frac{4}{3} \pi R_B^3}{1 + n \frac{4}{3} \pi R_B^3} \tag{1.11}$$

and bubble radius is defined as:

$$R_B = \left(\frac{\alpha_v}{1 - \alpha_v} \frac{3}{4\pi n}\right)^{\frac{1}{3}} \tag{1.12}$$

The Schnerr-Saue et al. model and Zwart et al. model are more stable with faster convergence in comparison with Singhal et al. model. In addition, both cavitation models are compatible with the mixture and Eulerian multiphase model, while Singhal et al. model can only be applied in the mixture model. The main limit of the Schnerr-Saue and Zwart et al. models is that the consideration of non-condensable gas is not taken into account.

1.4 Main objectives and thesis outlines

As our review of the literature shows, although a few scholars have focused on the experimental investigations of four-phase (liquid-solid-vapor-air) flows and numerical treatments of two-phase (liquid-vapor) flows in cavitating Venturi tubes from different aspects, there are almost no studies carrying out a detailed CFD investigation of four-phase cavitating flows. Therefore, the main objective of this work is to develop an appropriate four-phase Eulerian-Eulerian−based model for multiphase cavitating flows in a Venturi tube. The second objective is to study how the geometrical parameters affect the cavitation performance and how scale-up affects cavitation phenomena in the two-phase cavitating flows. The third objective is to investigate numerically the occurrence of cavitation past micro-sized particles moving in water. Additionally, effects of the particle shape, the surface roughnesses and the surface temperature are studied numerically. The fourth objective is to study numerically the mixing characteristics of two miscible water flows with high viscosity difference in a cavitating Venturi tube. In this work, the performance of lab-

scale Venturi tube is investigated experimentally and numerically. Lab-scale experiments were carried out to validate the simulation results. The commercial CFD software ANSYS FLUENT 16.2 [50] is employed in this study.

To realize all the objectives that have been set in the previous paragraph the thesis is divided into 6 chapters to accomplish each of these objectives. Chapter 2 to Chapter 5 contain the papers that have been either published or submitted. The detailed content in each chapter is introduced below:

Chapter 1 provides a brief introduction about the existing technologies in hydrodynamic cavitation. The literature review of CFD study towards multiphase cavitating flows in Venturi tubes is described there. Then, a short description of cavitation models used in commercial CFD software ANSYS FLUENT 16.2 is present. This chapter ends with the main objectives and the structure of the thesis.

Chapter 2 presents the experimental and numerical study of two-phase cavitation flows in Venturi tubes. The influence of the convergent angle of cavitating Venturi tubes on flow characteristics and generation of cavitation is studied experimentally and numerically. The effect of scale−ratio on cavitational activities is investigated numerically. Finally, an empirical model enabling of cavitation to be predicted in Venturi tubes is established employing regression analysis based on CFD results.

Chapter 3 contains the experimental and numerical study of cavitating particulate flows in a venturi tube. A new global model of four-phase cavitating flows is developed based on this simple engineering approach, and validated against the experimental measurements. The influence of solid mass concentrations on the flow characteristics and the generation of cavitation at different inlet flow velocities is investigated experimentally and numerically.

Chapter 4 presents work done on the modeling of cavitating flows past a micro-sized particle. The influence of the particle shape, the surface roughness, the number of particles, and the surface temperature on flow characteristics and cavitation behaviors were studied. Additionally, a CFD-based empirical mathematical model for the particle size is proposed to accurately estimate the inception of cavitation for particles with various particle sizes.

Chapter 5 describes the modeling of mixing behaviors of two miscible turbulent water flows with high viscosity difference in a Venturi tube. The RANS and LES turbulence models were compared and evaluated to accurately predict the cavitation and mixing behaviors.

Chapter 6 gives a summary of the conclusions of Chapter 2 to Chapter 5. This is followed by a list of recommendations for future progress on this work.

Bibliography

[1] Robert T Knapp, James W Daily, and Frederick G Hammitt. *Cavitation*. McGraw-Hill, 1970.

[2] Christopher E Brennen. *Cavitation and bubble dynamics*. Cambridge University Press, 2013.

[3] P Senthil Kumar, M Siva Kumar, and AB Pandit. Experimental quantification of chemical effects of hydrodynamic cavitation. *Chemical Engineering Science*, 55(9): 1633–1639, 2000.

[4] Parag R Gogate and Aniruddha B Pandit. A review and assessment of hydrodynamic cavitation as a technology for the future. *Ultrasonics sonochemistry*, 12(1-2):21–27, 2005.

[5] S Arrojo and Y Benito. A theoretical study of hydrodynamic cavitation. *Ultrasonics Sonochemistry*, 15(3):203–211, 2008.

[6] Jitendra Carpenter, Suja George, and Virendra Kumar Saharan. Low pressure hydrodynamic cavitating device for producing highly stable oil in water emulsion: Effect of geometry and cavitation number. *Chemical Engineering and Processing: Process Intensification*, 116:97–104, 2017.

[7] ZA Zhou, Zhenghe Xu, JA Finch, H Hu, and SR Rao. Role of hydrodynamic cavitation in fine particle flotation. *International Journal of Mineral Processing*, 51(1-4):139–149, 1997.

[8] Parag R Gogate. Application of hydrodynamic cavitation for food and bioprocessing. In *Ultrasound Technologies for Food and Bioprocessing*, pages 141–173. Springer, 2011.

[9] Timothy J Mason and J Phillip Lorimer. Applied sonochemistry: the uses of power ultrasound in chemistry and processing. 2002.

[10] Francesca Patrignani and Rosalba Lanciotti. Applications of high and ultra high pressure homogenization for food safety. *Frontiers in microbiology*, 7, 2016.

[11] Muthupandian Ashokkumar et al. *Theoretical and experimental sonochemistry involving inorganic systems*. Springer Science & Business Media, 2010.

[12] Fabiana A Perrechil and RL Cunha. Oil-in-water emulsions stabilized by sodium caseinate: Influence of ph, high-pressure homogenization and locust bean gum addition. *Journal of Food Engineering*, 97(4):441–448, 2010.

[13] Manickam Sivakumar and Aniruddha B Pandit. Wastewater treatment: a novel energy efficient hydrodynamic cavitational technique. *Ultrasonics sonochemistry*, 9(3):123–131, 2002.

[14] Jitendra Carpenter, Mandar Badve, Sunil Rajoriya, Suja George, Virendra Kumar Saharan, and Aniruddha B Pandit. Hydrodynamic cavitation: an emerging technology for the intensification of various chemical and physical processes in a chemical process industry. *Reviews in Chemical Engineering*, 33(5):433–468, 2017.

[15] M. Gagola, A. Przyjaznyb, and G. Boczkaja. Wastewater treatment by means of advanced oxidation processes based on cavitation - A review. *Chemical Engineering Journal*, 338:599–627, 2018.

[16] Mark Duerkop, Eva Berger, Astrid Dürauer, and Alois Jungbauer. Impact of cavitation, high shear stress and air/liquid interfaces on protein aggregation. *Biotechnology journal*, 13(7):1800062, 2018.

[17] V Ross, A Singh, and K Pillay. Improved flotation of pgm tailings with a high-shear hydrodynamic cavitation device. *Minerals Engineering*, 137:133–139, 2019.

[18] Mohan M Gore, Virendra Kumar Saharan, Dipak V Pinjari, Prakash V Chavan, and Aniruddha B Pandit. Degradation of reactive orange 4 dye using hydrodynamic cavitation based hybrid techniques. *Ultrasonics sonochemistry*, 21(3):1075–1082, 2014.

[19] Ashok K Singhal, Mahesh M Athavale, Huiying Li, and Yu Jiang. Mathematical basis and validation of the full cavitation model. *Transactions-American Society of Mechanical Engineers Journal of Fluids Engineering*, 124(3):617–624, 2002.

[20] Stéphane Barre, Julien Rolland, Guillaume Boitel, E Goncalves, and R Fortes Patella. Experiments and modeling of cavitating flows in venturi: attached sheet cavitation. *European Journal of Mechanics-B/Fluids*, 28(3):444–464, 2009.

[21] Eric Goncalves and Regiane Fortes Patella. Numerical simulation of cavitating flows with homogeneous models. *Computers & Fluids*, 38(9):1682–1696, 2009.

[22] Boris Charrière, Jean Decaix, and Eric Goncalvès. A comparative study of cavitation models in a venturi flow. *European Journal of Mechanics-B/Fluids*, 49:287–297, 2015.

[23] JX Zhang. Analysis on the effect of venturi tube structural parameters on fluid flow. *AIP Advances*, 7(6):065315, 2017.

[24] Liang Zhao, Licheng Sun, Zhengyu Mo, Min Du, Jiang Huang, and Jingjing Bao. Effects of the divergent angle on bubble transportation in a rectangular venturi channel

and its performance in producing fine bubbles. *International Journal of Multiphase Flow*, 2019.

[25] Tausif A Bashir, Advait G Soni, Amit V Mahulkar, and Aniruddha B Pandit. The cfd driven optimisation of a modified venturi for cavitational activity. *The Canadian Journal of Chemical Engineering*, 89(6):1366–1375, 2011.

[26] Alister Simpson and Vivek V Ranade. Modeling hydrodynamic cavitation in venturi: influence of venturi configuration on inception and extent of cavitation. *AIChE Journal*, 65(1):421–433, 2019.

[27] K. Sampath Kumar and Vijayanand S. Moholka. Conceptual design of a novel hydrodynamic cavitation reactor. *Chemical Engineering Science*, 62:2698–2711, 2007.

[28] Mei-Shan Jin, Cong-Tu Ha, and Warn-Gyu Park. Numerical study on heat transfer effects of cavitating and flashing flows based on homogeneous mixture model. *International Journal of Heat and Mass Transfer*, 109:1068–1083, 2017.

[29] X Margot, S Hoyas, A Gil, and S Patouna. Numerical modelling of cavitation: validation and parametric studies. *Engineering Applications of Computational Fluid Mechanics*, 6(1):15–24, 2012.

[30] Youwei Gu, Buxuan Li, and Min Chen. An experimental study on the cavitation of water with effects of sio2 nanoparticles. *Experimental Thermal and Fluid Science*, 79: 195–201, 2016.

[31] M Medrano, PJ Zermatten, Christian Pellone, Jean-Pierre Franc, and Frédéric Ayela. Hydrodynamic cavitation in microsystems. i. experiments with deionized water and nanofluids. *Physics of Fluids*, 23(12):127103, 2011.

[32] Patrick F Dunn, Flint O Thomas, Michael P Davis, and Irina E Dorofeeva. Experimental characterization of aviation-fuel cavitation. *Physics of Fluids*, 22(11):117102, 2010.

[33] Mingda Li. Influence of venturi tube geometry and particle properties on the hydrodynamic cavitation for fine particle flotation. *Master thesis*, 2017.

[34] Bostjan Gregorc, Matjaz Hribersek, and Andrej Predin. The analysis of the impact of particles on cavitation flow development. *Journal of Fluids Engineering*, 133(11): 111304, 2011.

[35] AE Kabeel and Mohamed Abdelgaied. Study on the effect of alumina nano-fluid on sharp-edge orifice flow characteristics in both cavitations and non-cavitations turbulent flow regimes. *Alexandria Engineering Journal*, 55(2):1099–1106, 2016.

[36] Min-Rui Chen, Jin-Yuan Qian, Zan Wu, Chen Yang, Zhi-Jiang Jin, and Bengt Sunden. The hydraulic cavitation affected by nanoparticles in nanofluids. *Computation*, 6(3): 44, 2018.

[37] Buxuan Li, Youwei Gu, and Min Chen. Cavitation inception of water with solid nanoparticles: A molecular dynamics study. *Ultrasonics sonochemistry*, 51:120–128, 2019.

[38] Mohammad-Reza Pendar and Ehsan Roohi. Cavitation characteristics around a sphere: An les investigation. *International Journal of Multiphase Flow*, 98:1–23, 2018.

[39] Matevž Dular, Rudolf Bachert, Bernd Stoffel, and Brane Širok. Influence of the velocity distribution at the inlet boundary on the cfd prediction of local velocity and pressure fields around a hydrofoil. *Experimental thermal and fluid science*, 32(3): 882–891, 2008.

[40] Narotam Jangir, Prateek Diwedi, and Sumana Ghosh. Design of a hydrodynamic cavitating reactor. *Chemical Engineering & Processing: Process Intensification*, 122: 128–142, 2017.

[41] Eduardo Gomez Santos, Junmei Shi, Manolis Gavaises, Celia Soteriou, Mark Winterbourn, and Wolfgang Bauer. Investigation of cavitation and air entrainment during pilot injection in real-size multi-hole diesel nozzles. *Fuel*, 263:116746, 2020.

[42] Anne Boorsma and Stewart Whitworth. Understanding the details of cavitation. In *Second International Symposium on Marine Propulsors*, pages 319–327, 2011.

[43] Stefano Gaggero and Diego Villa. Steady cavitating propeller performance by using openfoam, starccm+ and a boundary element method. *Proceedings of the Institution of Mechanical Engineers, Part M: Journal of Engineering for the Maritime Environment*, 231(2):411–440, 2017.

[44] S Brinkhorst, E von Lavante, and G Wendt. Experimental and numerical investigation of the cavitation-induced choked flow in a herschel venturi-tube. *Flow Measurement and Instrumentation*, 54:56–67, 2017.

[45] Boxiong Chen and Michael Oevermann. An eulerian stochastic field cavitation model coupled to a pressure based solver. *Computers and Fluids*, 162:1–10, 2018.

[46] Abolfazl Asnaghi, Urban Svennberg, and Rickard E Bensow. Large eddy simulations of cavitating tip vortex flows. *Ocean Engineering*, 195:106703, 2020.

[47] Kazem Hejranfar, Eslam Ezzatneshan, and Kasra Fattah-Hesari. A comparative study of two cavitation modeling strategies for simulation of inviscid cavitating flows. *Ocean Engineering*, 108:257–275, 2015.

[48] Günter H Schnerr and Jürgen Sauer. Physical and numerical modeling of unsteady cavitation dynamics. In *Fourth international conference on multiphase flow, New Orleans, USA*, volume 1, 2001.

[49] Philip J Zwart, Andrew G Gerber, Thabet Belamri, et al. A two-phase flow model for predicting cavitation dynamics. In *Fifth international conference on multiphase flow, Yokohama, Japan*, volume 152, 2004.

[50] Inc Ansys. Ansys fluent theory guide. *Canonsburg, Pennsylvania*, page 794, 2011.

Chapter 2

Experimental and Numerical Study of Cavitation Flows in Venturi Tubes: From CFD to an Empirical Model[1]

2.1 Introduction

Cavitation, by definition, is the process by which vapor bubbles forming and growing in a liquid when the local static pressure falls below the vapor pressure at a constant ambient temperate [2, 3].It is one of the most effective process that having been widely adopted in various industrial applications ranging from wastewater treatment [4], chemical synthesis and food processing to mineral processing [5]. In the specific case of applications in mineral processing, a Venturi tube is of great significance for improving fine particle flotation efficiency. Flotation is a primary used mineral extraction process in which bubbles of air attach on the intended minerals for separation from the solid particles with varied surface wettabilities [6, 7]. Due to the difference of densities, the intended minerals (hydrophobic) agglomerate on the top surface and then be collected for the next purification process, while the rest of particles (hydrophilic) settle down on the bottom and then be discharged. Flotation efficiency significantly depends on the particle size. A high flotation efficiency is limited to the minerals size in the range between 10 μm to 100 μm [8]. The recovery rate decreases significantly for particles smaller than 20 μm [9]. The low possibility of particle-

[1]The content of this chapter is an extended version of: Hongbo Shi, Mingda Li, Petr Nikrityuk, and Qingxia Liu. Experimental and numerical study of cavitation flows in venturi tubes: from cfd to an empirical model. *Chemical Engineering Science*, Vol. 207 pp.672–687, 2019.

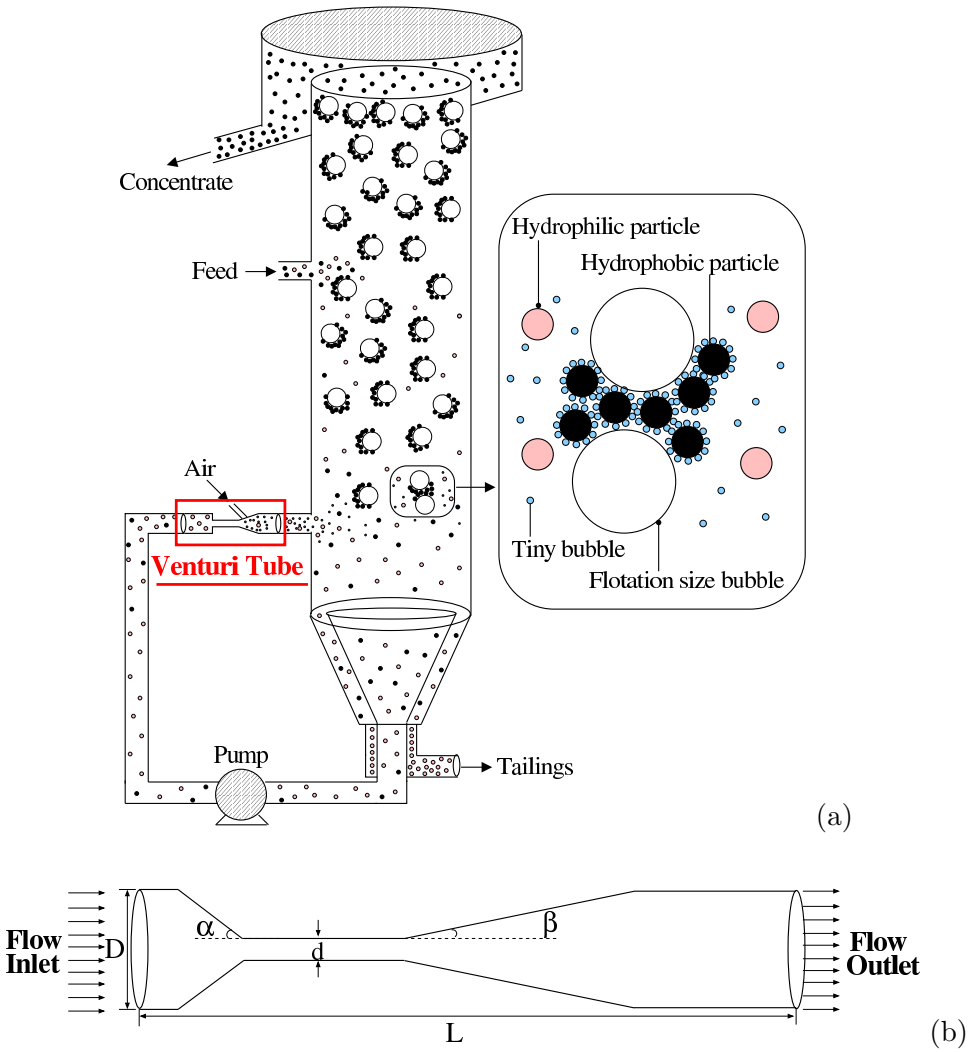

Figure 2.1: Schematic view of flotation column used in mineral processing (adapted from [1]) - (a), scheme of cavitation tube - (b).

bubble collisions contributed by the low mass and kinetic energy is responsible for the inefficient fine particles recovery [9]. For this reason, hydrodynamic cavitation provides a practical method for efficient fine particle flotation as a result of increasing particle-bubble collision and attachment probability and decreasing detachment probability. The main advantages of using cavitation in flotation technologies are both the production of micron- and nano-sized vapor bubbles [10], which are advantageous for particle aggregation, and more effective collision of solid hydrophobic particles with air and vapor bubbles generated by cavitation. Fig. 2.1a shows a schematic drawing of a flotation column and the role of cavitational bubbles generated from a Venturi tube. It can be seen that a Venturi tube is composed of a convergent section, throat section, and divergent section, see Fig. 2.1b.

When the pressure in the throat of the Venturi is lower than the vapor pressure as the fluid flows through the throat section, a quick phase transition from liquid to vapor occurs. Tiny bubbles generated by the cavitating Venturi tube coat the surface of hydrophobic particles and act as a bridge, producing an attractive force between the hydrophobic particle and the flotation size bubble [11, 12]. This attractive force enhances the fine particle aggregation, increasing their flotation efficiency [5]. Thus, improving the efficiency of a cavitating Venturi tube, thereby enhancing the flotation performance of fine particles, has long been a goal in the minerals industry [13].

The efficiency of the cavitating Venturi tube is mainly dependent on the cavitation phenomenon and its interaction with turbulent flow, which in turn depends on the geometry of the Venturi tube [14, 15, 16]. Some important geometrical parameters such as the throat length, the throat diameter or the convergent and divergent angles play a significant role in the design of a Venturi tube, since these parameters greatly affect the cavitational inception and yield in Venturi tubes.

With the continuous improvement of various cavitation models based on computational fluid dynamics (CFD) and their implementation in commercial CFD software, e.g. ANSYS Fluent [17, 18] and open-source CFD software, e.g. OPEN Foam [19], noticeable numerical works have been published focusing on the influences of Venturi tube geometric parameters and operational conditions on cavitation flows in different Venturi tubes. For example, Ashrafizadeh et al. [15] used a two-dimensional (2D) K-Epsilon (k-ε) turbulence model to investigate the influences of geometrical parameters such as the throat diameter, throat length and divergent angle on the critical pressure ratio and cavitation region. The numerical results indicate that the cavitating region and critical pressure ratio decrease as the throat diameter is reduced from 1.5 mm to 0.7 mm. The critical pressure ratio increases as the divergent angle decreases from 15 to 5°, and decreases as the throat length rises from 1 to 2.5 mm. Zhang et al. [16] carried out three-dimensional (3D) CFD simulations using a $k-\varepsilon$ standard turbulence model to analyze the effects of the divergent angle, the contraction ratio (d/D), and the ratio of the throat section length to diameter (L/d) on the fluid flow and pressure distribution in the Venturi tube. The numerical results show that the vacuum pressure (the pressure difference between minimum pressure and atmosphere) and mass flux increase by 19 KPa and 0.03 kg/s respectively as the contraction ratio increases from 0.2 to 0.8. On the other hand, as the ratio of the throat section length to diameter increases from 1 to 7, the vacuum pressure and mass flux decrease by 2 KPa and 0.0002 kg/s, respectively. In addition, both the vacuum pressure and the mass flux drop 12 KPa and 12 kg/s as the divergent angle ascends from 15° to 60°. Zhao et al. [20] performed 2D CFD simulations using a K-Omega ($k-\omega$) turbulence model to study the effect of divergent angle on bubble breakup in Venturi tubes. The author showed that

vortex region increases and bubble breakup positions are brought forward as the increase in the divergent angle from 5° to 12.5°. Bashir et al. [14] conducted CFD analyses of different Venturi tubes such as circular, slit, and elliptical Venturis, at different ratios of throat diameter to throat length (1:0.5, 1:1, 1:2, and 1:3) and divergent angle (5.5°, 6.5°, 7.5°, and 8.5°). $k-\varepsilon$ was applied to model fluid turbulence in both 2D and 3D domains. The optimum divergent angle and ratio of throat diameter to throat length were found to be 5.5° and 1:1 for all the Venturi tubes considered.

Margot et al. [21] used seven different 3D turbulence models ($k-\varepsilon$/ low Re/ hybrid, $k-\varepsilon$/ high Re/ standard, $k-\varepsilon$ Re-Normalisation Group (RNG)/ standard, $k-\omega$ shear stress transport (SST) and standard/ high and low Re/ hybrid and standard) to study the cavitation flow within a throttle channel at different operation conditions. The results show that the void volume fraction decreases as the liquid viscosity increases. The $k-\varepsilon$/ low Re/ hybrid model provides a better agreement against experiment data as compared to other models. It was shown that the total pressure distribution predicted numerically is lower than the experimental data due to the pressure loss at the entrance.

Srinivasan et al. [22] developed a novel modeling approach (Volume-of-Fluid-Cavitation-Induced-Momentum-Defect) capable of simultaneously predicting the cavitation activities of liquid-vapor phases and the break-up dynamics of liquid-gas phases within the internal and exterior regions of the nozzle, in conjunction with the RNG $k-\varepsilon$ turbulence model. The simulation results showed reasonable fit on the velocity profile against experimental data published in the literature. The cavitation cluster length is reduced as Reynolds number decreases from 70000 to 58000. In addition, the stretching or diffusion effects of the cluster in the downstream region decreased as the cavitation number increases from 0.65 to 0.94.

Kumar and Moholka [23] proposed a conceptual design for a novel hydrodynamic cavitation reactor that uses a converging-diverging nozzle with a gas sparger to generate cavitational bubbles. Based on the simulation results, they found that increasing the upstream pressure (from 1 to 1.5 atm) and the nozzle length (from 3 to 6 inches) and decreasing the initial bubble size (from 200 to 100 μm) is a means of intensifying the sonochemical effects (bubble size, temperature and pressure peaks reached in the bubble at the first compression). They also found that an argon bubble can produce greater sonochemical effects in comparison with an air bubble.

The analysis of various works on the cavitating Venturi tube shows that the existing CFD models [22, 18] and CFD studies[17, 14, 15, 16] have largely been used to investigate the effect of some critical geometric parameters, including the divergent angle, the ratio of the throat section length to diameter, and the contraction ratio, on Venturi performances. However, little attention paid to the effect of the convergent angle in the cavitating Venturi

tube. Additionally, the difference between lab-scale and large-scale Venturi tubes has not been investigated in details. Therefore, the main objective of this work is to study how the convergent angle affects the cavitation performance and to produce a numerical study of how scale-up affects cavitation phenomena. In this work the performance of lab-scale Venturi tube was investigated experimentally and numerically. Lab-scale experiments were carried out to validate the simulation results. The commercial CFD software ANSYS Fluent 16.2 [24] was employed in this study. The paper is organized as follows. Section 2.2 presents a description of the experiments. The details of the computational model are given in Section 2.3. Section 2.4 outlines the results of the present study. Finally, conclusions are drawn in Section 2.5.

2.2 Experimental setup

The experimental system is schematically illustrated in Fig. 2.2. The setup consists in a computer, an oscilloscope, a pressure transducer, a flow meter, a pump, a water tank and a cavitating Venturi tube. The whole system is a closed-loop system. The peristaltic pump (Masterflex I/P Easy-Load, Germany) can deliver the tap water flow from 0 to 10 LPM.

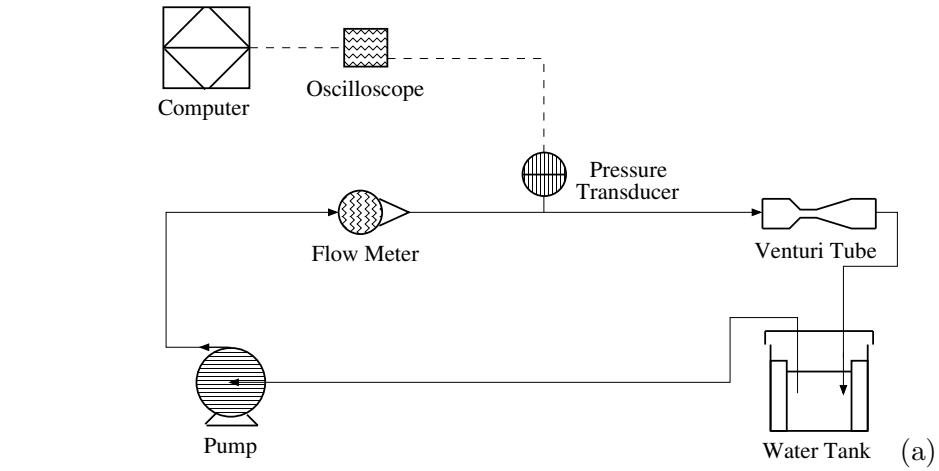

Figure 2.2: Experimental setup: (a) - schematic diagram, (b) - cavitating Venturi tube test section, (c) - cavitating Venturi tube of Design−1.

For the measurements, a pressure transducer (Transducers Direct TDH40, USA) with an accuracy of ± 0.4% FS records information on the inlet pressure, P_{in} and sends it to an oscilloscope (Rigol DS1054Z, USA) in a voltage signal via a coaxial wire connection. The straight distance between the pump and the pressure transducer is 0.9 m and the distance between the pressure transducer and the inlet of Venturi tube is 0.7 m. The outlet pressure, P_{∞} remains constant and is equal to the atmospheric pressure. The flow rate, Q is monitored using the flow meter (Omega FLR 1001, USA) with an accuracy of ± 3% FS. The flow meter consists in a turbine wheel which can rotate at different rates in response to the liquid flow. Infrared light energy is emitted to the turbine wheel, and then reflected and absorbed by the black and white spokes, evenly spread over on the surface of the turbine wheel. The light sensor generates the electrical pulses that reflect the liquid flow rate. Simultaneously, the electrical pulses are displayed on the oscilloscope through the connection.

Two Venturi tubes, Design−1 and Design−2 were designed using computer-aided design (CAD) software and manufactured by the Formlabs Form 2 Printer equipped with Stereolithography (SLA) technology. Fig. 2.2a and Fig. 2.2b respectively show a photographs of the cavitating Venturi tube test section and of the Venturi tubes used in this study. The schematic drawing of the tested Venturi tubes and their specifications are shown in Fig. 2.3 and Table 2.1, respectively.

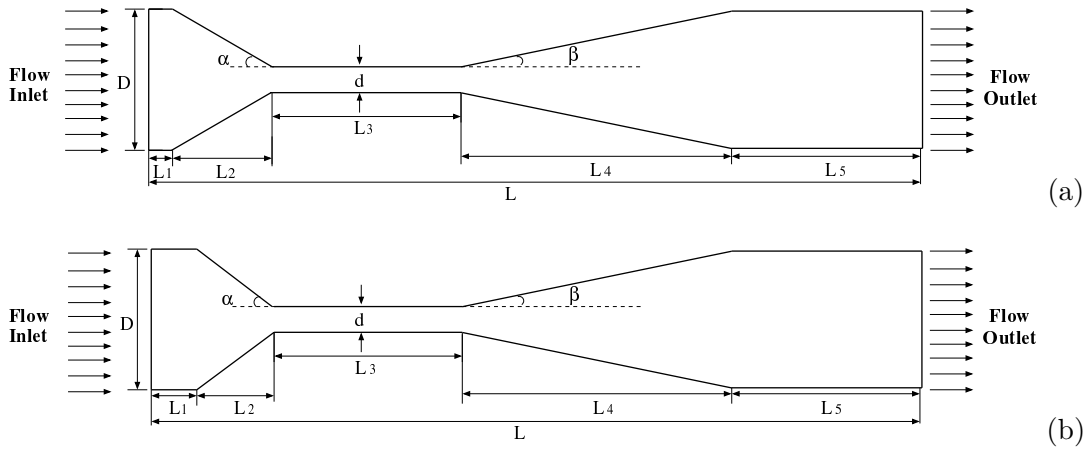

Figure 2.3: Schematic diagram of the Venturi tubes used in the experiments: (a) - Design−1 and (b) - Design−2.

Design	$D(mm)$	$d(mm)$	$L_1(mm)$	$L_2(mm)$	$L_3(mm)$	$L_4(mm)$	$L_5(mm)$	$\alpha(^\circ)$	$\beta(^\circ)$
1	12.7	3.18	6	14	20	54	6	19	5
2	12.7	3.18	15	5	20	54	6	45	5

Table 2.1: Specifications of cavitating Venturi tubes.

2.3 Computational model

For the multiphase flow solutions, the single-fluid mixture model (available in the commercial CFD software ANSYS-Fluent [24]) is employed to simulate cavitating two-phase flows (water-vapor) in this study. The mixture model is capable to predict cavitation phenomena in water flows by solving a set of transport equations governing the mixture continuity, momentum, energy and the disperse phase for the volume fraction equation [24]. The mixture model assumes that the velocities, temperature and densities of both the liquid phase and the vapor phase are the same at every position in the two-phase fluid field. The steady Reynolds-averaged Navier-Stokes (RANS) solver is used to solve the two-phase flows with turbulence effect. Both the liquid and vapor phases are modeled using the standard k-ω turbulence model with a standard wall function, which can provide more accurate solutions in the near wall boundary regions. The k-ω turbulence model is evaluated based on the Boussinesq hypothesis and involves transport equations for the turbulent kinetic energy, k, and the specific dissipation rate, ω. The Schnerr-Sauer cavitation model [25] is used to calculate the phase transition between the water-liquid phase and the vapor phase. This model derived on the assumption of isothermal, incompressible, and zero-slip velocity between the liquid phase and vapor phase [24]. Positive mass transfer from the liquid phase to the vapor phase is considered in this model. The Rayleigh-Plesset equation is applied to this model to describe the expansion of a single cavitation bubble in the liquid. The number of spherical bubbles per volume of liquid is the only parameter which needs be determined; it is assumed to be 10^{13} in this study since extensive works suggest that the value of 10^{13} is the optimal value, e.g. see works [26, 27, 28]. It should be noted that, the effect of non-condensable gas is not accounted for in the Schnerr-Sauer model. Thus, in numerical simulations, only the effect of vapor-driven cavitation was considered and the effect of dissolved gas-caused cavitation was not included in the model since we assumed that the dissolved gas has little effect on the cavitation phenomenon.

In all simulations, the saturation vapor pressure, P_V remained constant and equal to 2338 Pa (20°C). The saturation vapor pressure is calculated based on the Antoine equation [29]:

$$LogP_V = A - \frac{B}{T + C} \tag{2.1}$$

where P_V is the absolute vapor pressure of the water, T is the temperature of the water. A, B, and C are substance-specific coefficients. When $1^oC \leq T < 100^oC$, the value of A, B, and C are 8.07131, 1730.63, and 233.426, respectively. The governing equations for the entire system are presented in Table 2.2. It should be mentioned that the dissolved gas effect is assumed to have a minor effect on vaporous cavitation. However, vapor-driven cavitation and gas-caused cavitation are different physical processes and it is difficult to split them in experiments. To take into account the dissolved gas effect on the final cavitation, we refer to the work [18].

As the inlet boundary condition, a specified total pressure in the range between 102000 to 400000 Pa is set. In particular, in this range, we observed the trend of pressure drop as a function of inlet velocity. The outlet boundary condition is the static pressure outlet, with a constant value of 101325 Pa. The boundary conditions for turbulence are specified as having a uniform value: 10% for the turbulence intensity and 10 for the turbulence viscosity ratio. The no-slip boundary condition is applied at walls.

The simulation was performed using the commercial CFD software ANSYS FLUENT 16.2. The 2D axisymmetric computational geometry is discretized with block-structured (hexahedral) meshes using a finite-volume method with 310000 (Design−1) and 316000 (Design−2) computational cells (see Fig. 2.4).

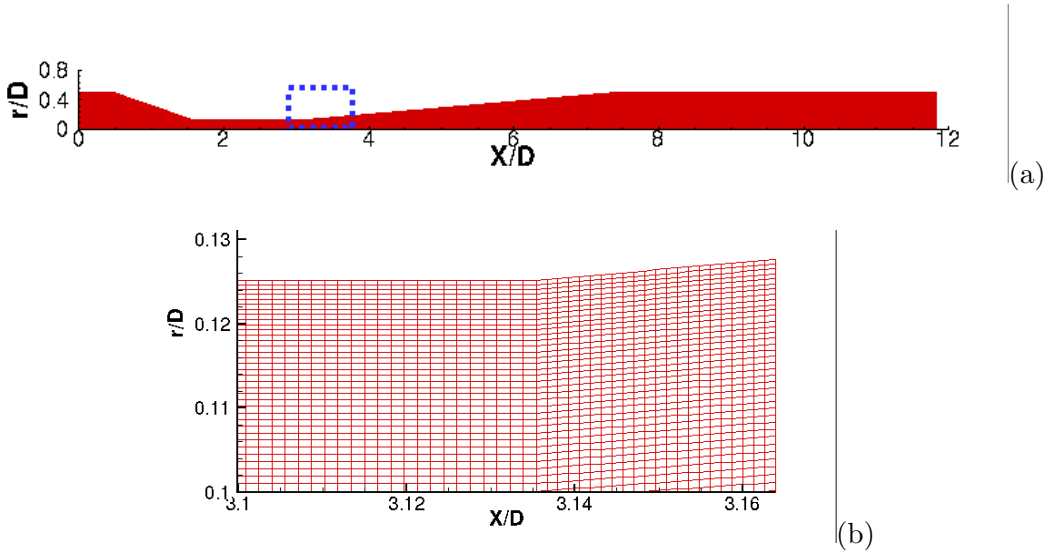

Figure 2.4: The computational structured mesh (Grid−2) for Design−1: (a) - full view (b) - zoom view.

The pressure-velocity-based coupled scheme [24] was used to solve the mass and momentum conservation equations corresponding to the behavior of the cavitating flow in the mixture model. To fulfil the coupling algorithms, implicit discretizations of both the pres-

sure gradient terms and the face mass flux were included in the equation. The Quadratic Upwind Interpolation for Convection Kinematics (QUICK) scheme [24] was used to discretize convective terms in the transport equation for the volume fraction of vapor. Due to the change of geometry, the flow field is expected to have a steep pressure gradient at the cell face. The pressure from the cell to face values was therefore calculated using the PREssure STaggering Option (PRESTO) scheme. The second−order upwind scheme is utilized to discretize the convection terms in the momentum equations and in the RANS model. All CFD simulations are performed based on steady-state conditions. Table 2.3 contains a summary of the simulation cases. The details of the models and schemes used in the numerical simulation of cavitating Venturi tubes are given in Table 2.4.

Name	*Model/ Scheme Name*
Multiphase Flow	Mixture [24]
Viscous Model	RANS-k-ω model [24]
Cavitation Model	Schnerr-Sauer [25]
Pressure-Velocity Coupling	Coupled Scheme [24]
Spatial Discretization-Gradient	Least Squares Cell Based [24]
Spatial Discretization-Pressure	PRESTO! [24]
Spatial Discretization-Momentum	2nd−Order Upwind [24]
Spatial Discretization-Volume Fraction	QUICK [30]
Spatial Discretization-Turbulence	k-ω 2nd−Order Upwind [24]

Table 2.4: List of different models and schemes used in mixture model for modeling two-phase cavitating flows.

Continuity equation	$\frac{\partial}{\partial t}(\rho_m) + \nabla \cdot (\rho_m \vec{v}_m) = 0$
	$\vec{v}_m = \frac{\sum_{q=1}^{n} \alpha_q \rho_q \vec{v}_q}{\rho_m}$
	$\rho_m = \sum_{q=1}^{n} \alpha_q \rho_q$
Momentum equation	$\frac{\partial}{\partial t}(\rho_m \vec{v}_m) + \nabla \cdot (\rho_m \vec{v}_m \vec{v}_m) =$
	$-\nabla P + \nabla \cdot [\mu_m (\nabla \vec{v}_m + \nabla \vec{v}_m^T)] + \rho_m \vec{g} + \vec{F} + \nabla \cdot (\sum_{q=1}^{n} \alpha_q \rho_q \vec{v}_{dr,q} \vec{v}_{dr,q})$
	$\mu_m = \sum_{q=1}^{n} \alpha_q \mu_q$
Volume fraction equation for the vapor phase	$\frac{\partial}{\partial t}(\alpha_v \rho_v) + \nabla \cdot (\alpha_v \rho_v \vec{v_m}) = R_e - R_c$
Schnerr and Sauer cavitation equations	When $P_V \geq P_\infty$, $R_e = \frac{\rho_v \rho_l}{\rho_m} \alpha_v (1 - \alpha_v) \frac{3}{R_B} (\frac{2}{3} \frac{P_V - P_\infty}{\rho_l})^{0.5}$
	When $P_V \leq P_\infty$, $R_c = \frac{\rho_v \rho_l}{\rho_m} \alpha_v (1 - \alpha_v) \frac{3}{R_B} (\frac{2}{3} \frac{P_\infty - P_V}{\rho_l})^{0.5}$
	$\alpha_v = \frac{n_b \frac{4}{3} \pi R_B^3}{1 + n_b \frac{4}{3} \pi R_B^3}$, $R_B = (\frac{\alpha_v}{1 - \alpha_v} \frac{3}{4 \pi n})^{\frac{1}{3}}$, $n = 10^{13}$
Standard k-ω turbulence model	$\frac{\partial k}{\partial t} + u_j \frac{\partial k}{\partial x_j} = \tau_{ij} \frac{\partial u_i}{\partial x_j} - \beta_w^* k \omega + \frac{\partial}{\partial x_j} [(v + \sigma_w^* v_t) \frac{\partial k}{\partial x_j}]$
	$\frac{\partial \omega}{\partial t} + u_j \frac{\partial \omega}{\partial x_j} = \alpha_w \frac{\omega}{k} \tau_{ij} \frac{\partial u_i}{\partial x_j} - \beta_w \omega^2 + \frac{\partial}{\partial x_j} [(v + \sigma_w v_t) \frac{\partial \omega}{\partial x_j}]$
	$\alpha_w = \frac{5}{9}$, $\beta_w = \frac{3}{40}$, $\beta_w^* = \frac{9}{100}$, $\sigma_w = \sigma_w^* = \frac{1}{2}$
	$\tau_{ij} = 2 v_t S_{ij}$, $S_{ij} = \frac{1}{2}(u_{i,j} + u_{j,i})$

Table 2.2: Mixture model equations available by ANSYS FLUENT 16.2 which were used to model the two-phase cavitating flows from[24].

No.	*Design*	*No. of cells*	*D(mm)*	*d(mm)*	L_1*(mm)*	L_2*(mm)*	L_3*(mm)*	L_4*(mm)*	L_5*(mm)*	α *(°)*	β *(°)*
1	1	77500	12.7	3.18	6	14	20	54	56	19	5
2	1	310000	12.7	3.18	6	14	20	54	56	19	5
3	1	1240000	12.7	3.18	6	14	20	54	56	19	5
4	2	316000	12.7	3.18	15	5	20	54	56	45	5
5	1	310000	79.9	20	37.7	88	125	340	352	19	5
6	1	310000	159.8	40	75.4	176	250	680	704	19	5
7	3	358000	12.7	3.18	19.44	0.56	20	54	56	85	5
8	4	434000	12.7	3.18	0	20	20	100	50	90	2.5
9	5	664000	12.7	3.18	0	20	20	110	0	90	2.5
10	6	508000	12.7	3.18	0	20	20	31	79	90	90&5
11	7	476000	12.7	3.18	6	14	20	31	79	19	90&5

Table 2.3: Parameters and mesh resolutions of simulation cases performed in this study. Geometrical parameters - D: diameter of tube; d: diameter of throat section; L_{1-5}: length of inlet section, convergent section, throat section, divergent section, and outlet section; α: convergent angle; β: divergent angle.

2.4 Results

To analyse the results, we use the cavitation number, σ, which is one of the special dimensionless parameters in the Venturi tube used to evaluate the potential for the cavitation. It is defined as the ratio of the pressure drop between the throat and downstream section of the cavitating device to the kinetic head at the throat. The formula of the cavitation number is given as [3]:

$$\sigma = \frac{P_\infty - P_V(T_\infty)}{\frac{1}{2}\rho_l U_{th}^2} \tag{2.2}$$

where P_∞ is the fully recovered downstream pressure, P_V is the vapor pressure of the liquid at the reference temperature (T_∞), ρ_l is the density of the liquid, and U_{th} is the flow velocity at the throat of the Venturi tube. As the cavitation number reduces, the throat velocity increases, and the cavity generated in the throat section becomes large.

The velocity was measured upstream leading to the definition of pressure loss coefficient, K:

$$K = \frac{(\Delta P)_{static}}{\frac{1}{2}\rho_l U_{in}^2} \tag{2.3}$$

where ΔP is the static pressure drop between the upstream and downstream pressures and U_{in} is the inlet velocity. The pressure loss coefficient is used to determine the energy consumption. A higher value of pressure loss coefficient leads to a higher energy consumption.

The inlet velocity can be expressed as:

$$U_{in} = \frac{D_{in}^2}{d^2} U_{th} = 16 U_{th} = \frac{64 Q_{in}}{\pi d^2} \tag{2.4}$$

where Q_{in} is the inlet flow rate, D_{in} is the inlet pipe diameter, and d is the throat diameter.

The inlet Reynolds number, Re_{in} measures viscous effects in all Navies-Stokes solutions. The formula of the inlet Reynolds number is given as [3]:

$$Re_{in} = \frac{\rho_l U_{in} D_{in}}{\mu_l} \tag{2.5}$$

where μ_l is the dynamic viscosity of the liquid. The density ρ_l and inlet velocity U_{in} are defined in the same way as in Equations 2.2 and 2.3. A higher value of inlet Reynolds number indicates that the inertial force is more dominant than the viscous force in the upstream of the Venturi tube.

Overall, six different simulations were performed in the simulation conditions outlined in Table 2.3. To gain a general understanding of the accuracy of numerical predictions of

cavitation yield, the standard deviations of the simulations were estimated based on the follow equation [31]:

$$\sigma_{est}\% = \sqrt{\frac{\sum(Y_{simulation} - Y_{experiment})^2}{N}} \cdot 100 \tag{2.6}$$

where σ_{est} is the standard deviation of the estimate and $Y_{experiment}$ and $Y_{simulation}$ are the experimental and predicted points of the inlet velocity, respectively. The predicted inlet velocity is calculated based on the mass-weighted average velocity at the inlet surface. The standard deviation provides a reliable means of measuring deviation as compared to other functions (e.g. weight standard deviation) since this method comes from Linear Least Squares Regression, as used in curve fitting [32].

2.4.1 Grid independence study

Before studying the effect of geometric parameters on the cavitating flow, in this section the influence of the grid resolution was studied to define an appropriate grid size for the simulations. The investigation was performed in Design−1 using three sets of grids with 77500 cells (Grid−1), 310000 cells (Grid−2), and 1240000 cells (Grid−3). Simulations with the same settings were conducted for all three grids. The maximum value of the non-dimensional wall distance y^+ near the walls is about 17.5 (Grid−1), 10.6 (Grid−2) and 4.4 (Grid−3).

To analyze which grid resolution was sufficient to obtain a stable solution, the output results from the three different meshes were compared to experimental measurements. Fig. 2.5a presents the profile of the pressure drop as a function of inlet velocity. From this profile one can conclude that all cases will predict similar upwards trend to the inlet velocity. Though Grid−2 shows good agreement with experimental data, with a deviation of 2.23%, Grid−1 and Grid−3 overpredict and underpredict the inlet flow velocity in most pressure-drop conditions, with deviations of 2.48% and 2.44%, respectively.

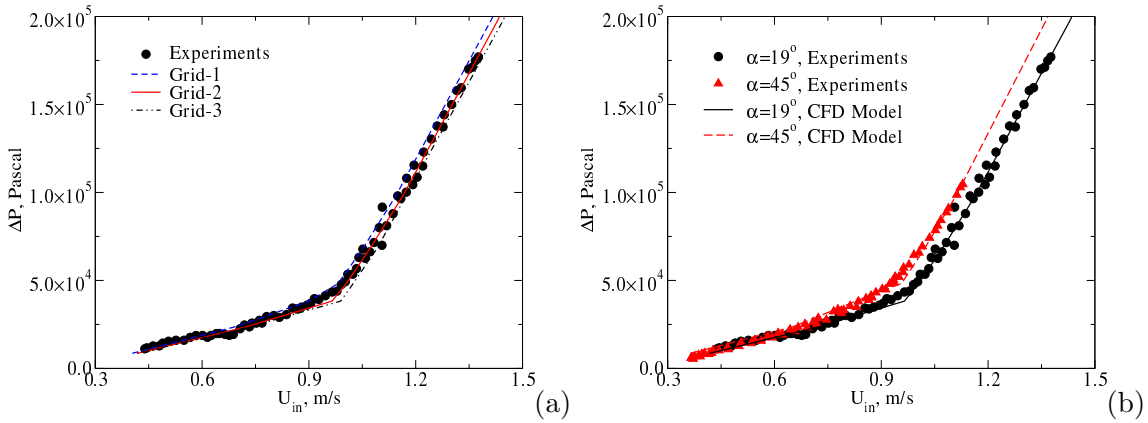

Figure 2.5: Validation: (a) - Experimental and simulated static pressure drop as a function of inlet velocity for Design-1. Mesh resolution: Grid−1: 77500 cells; Grid−2: 310000 cells ; Grid−3: 1240000 cells; (b) - Experimental and simulated static pressure drop as a function of inlet velocity for Design−1 (α=19°) and Design−2 (α=45°).

Fig. 2.6 shows the volume fraction of the vapor phase predicted by Grid−1, Grid−2, and Grid−3 mesh resolutions. As can be seen, the Grid-1 and Grid−2 meshes, with 77500 cells and 310000 cells, underestimate the amount of vapor in the throat section, while the Grid−3 mesh, with 1240000 cells, can fully capture the cavitation behavior in the system, especially in the throat section near the wall. In general, the continuous increase in mesh resolution may provide better numerical results. However, the computational cost (e.g. CPUs and memory resources) is a significant limitation when utilizing a finer mesh.

Based on the results obtained from the simulations, it was decided that the number of total cells varies from 310000 to 316000 due to different geometrical structures which will be used for the rest of the simulations. This provides good agreement with experimental data and reasonable computational cost is required.

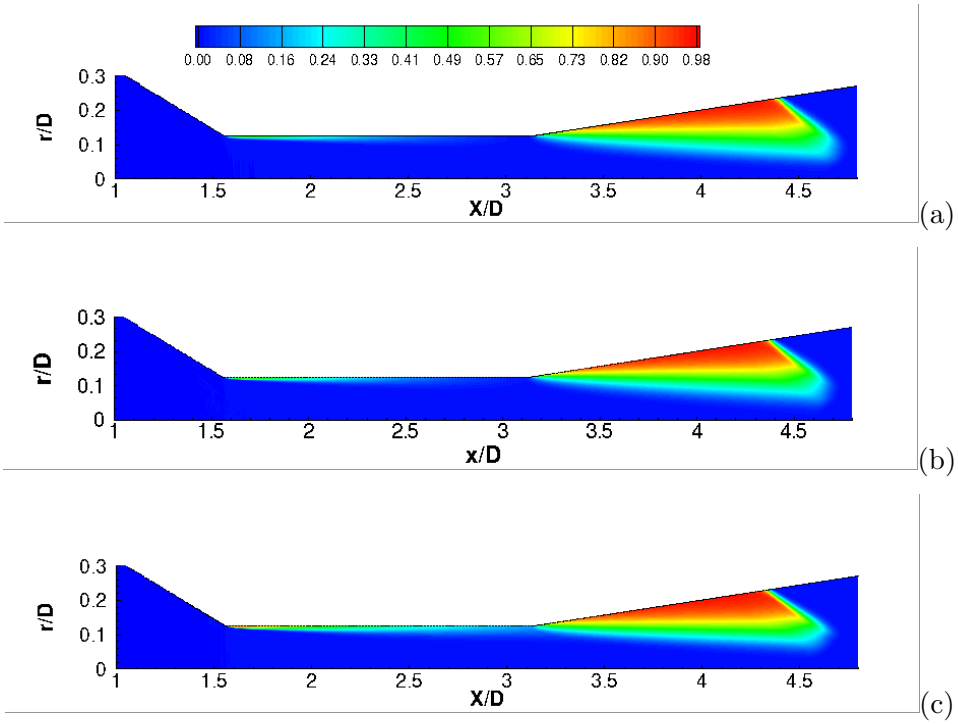

Figure 2.6: Vapor volume fraction for Design−1 at total inlet pressure of 400000 Pa: (a) - Grid−1: 77500 cells; (b) - Grid−2: 310000 cells; (c) - Grid−3: 1240000 cells.

2.4.2 Validation

To validate the numerical results obtained in the framework of the mixture model, simulations were carried out of the cavitating Venturi tube with Design−1 and Design−2, which shown in Fig. 2.5b. As can be seen, both the numerical and the experimental results present gradually increasing trend in the inlet velocity with an ascending pressure drop for all designs. The inlet velocity decreases as the convergent angle increases from 19 to 45° because of the presence of a large amount of vapor in the throat section. Moreover, the predicted results closely follow the experimental data for Design−1 and Design−2. The deviations from the experimental data are 2.23% and 5.41% for Designs 1 and 2, respectively.

2.4.3 Effect of convergent angle

Fig. 2.7a shows the vapor volume fraction, ϕ_v as a function of the cavitation number, σ profile for various angles of the convergent section. From the profile, the cavitation inception can be observed at σ=1.3 to 1.4 for all designs. With the continuous decline in σ from 1.4 to 0.3, all numerical cases present a significant increase in the cavitation

yield. The cavitating Venturi tube with α=45° has the highest level of cavitation, and that with α=19° has the minimum degree of cavitation. Therefore, it can be concluded that a cavitating Venturi tube with a higher convergent angle is easier to cavitate in comparison to one with a smaller convergent angle.

Fig. 2.7b presents the relationship between the volume-averaged volume fraction of vapor, ϕ_v and the pressure loss coefficient, K at two convergent angles. As the pressure loss coefficient decreases, the vapor volume fraction starts to decline step by step until a dramatic reduction occurs at $K<K_c$. This confirms the theory that the cavitation inception appears at a critical pressure loss coefficient K_c. After the cavitation phenomenon appears, the pressure loss coefficient K of the case with a higher convergent angle is larger than that with a lower convergent angle, under the same level of vapor volume fraction. In fact, a higher value of K corresponds to a relatively large pressure drop and thus a higher power consumption in the case with a higher value of α.

The numerical results for the relationship between the pressure loss coefficient, K and the inlet Reynolds number, Re_{in} for different convergent angles under cavitational and non-cavitational conditions are presented in Fig. 2.7c. Inflection points can be observed in all cavitation cases. The inflection point is the critical pressure loss coefficient, K_c, and corresponds to the critical inlet Reynolds number, Re_c. Two significant stages of the characteristic curve can be found in this profile. In the first stage ($Re_{in}<Re_c$), the characteristic curves for cavitation cases and non-cavitation cases overlap and present a decreasing trend. In the second stage ($Re_{in}>Re_c$), all curves continue to fall together for non-cavitation cases, while a dramatically increasing trend on K can be obtained for cavitation cases. This can be explained by the appearance of cavitation in the cavitating Venturi tube, which reduces the inlet velocity and therefore decreases the value of the inlet Reynolds number. From this profile one can observe that the cavitating Venturi tube with α=45° shows a early cavitation inception in comparison to one with α=19°. At a fixed value of Re_{in}, the cavitating Venturi tube with α=45° gives a higher value of K while that with α=19° shows a minimum value of K. This suggests that the cavitating Venturi tube with a higher convergent angle can generate a relatively larger pressure drop as compared with the tube with a lower convergent angle. Such a large pressure drop can be attributed to the existence of a higher level of cavitation in the cavitating Venturi tube with larger α. Based on the analysis of the results, we can conclude that there is a strong correlation between Re_{in}, K, and ϕ_v in a cavitating Venturi tube. These relations are seen to depend strongly on the geometric structure of the cavitating Venturi tube. Further investigations were conducted to develop an empirical model based on this relation.

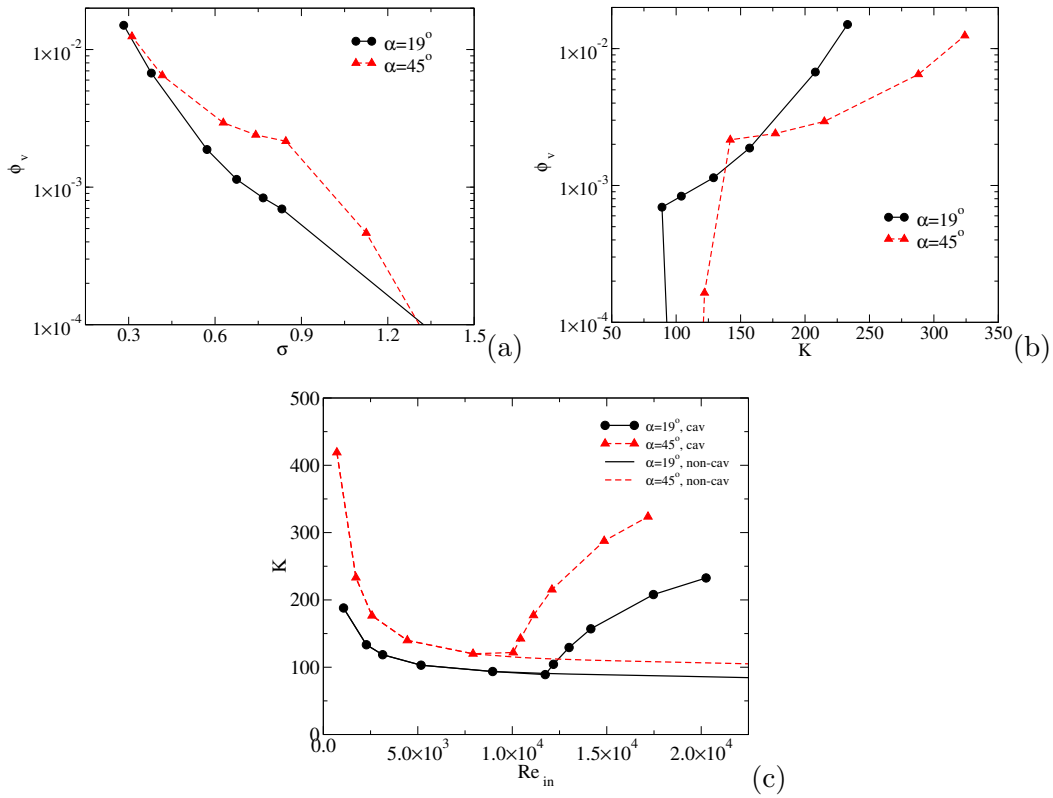

Figure 2.7: Integral characteristics predicted numerically for Design−1 (α=19°) and Design−2 (α=45°): (a) - volume-averaged vapor volume fraction as a function of cavitation number; (b) - volume-averaged vapor volume fraction as a function of pressure loss coefficient; (c) - pressure loss coefficient as a function of inlet Reynolds number.

Investigating the reason for the increase in the vapor volume fraction during the rise in the convergent angle, Fig. 2.8 and Fig. 2.9 depict the vapor volume fraction and turbulent viscosity ratio contours at a specific inlet pressure of 400000 Pa for various convergent angles from 19 to 45°. As can be seen from Fig. 2.8, a higher vapor volume fraction (0.73-0.98) is distributed in the beginning of the divergent section for all cases. With the increase in the convergent angle from 19 to 45°, the length of the vapor bubble in the divergent section decreases 20%, from 1.5 to 1.2. On the other hand, it can be observed that the cavitation yield increases in the throat section as the value of the convergent angle rises. The turbulent viscosity ratio − defined as the ratio between the turbulent μ_t and molecular μ_o dynamic viscosities − is necessary to estimate the level of turbulence within the simulation domain, as shown in Fig. 2.9. It is found that the turbulence viscosity ratio decreases from 1720 to 1540 as the convergent angle increases from 19 to 45°. A higher turbulent viscosity, which is mainly concentrated in the divergent section for all cases, leads to more cavitation bubble collapse and therefore reduces the cavitation yield.

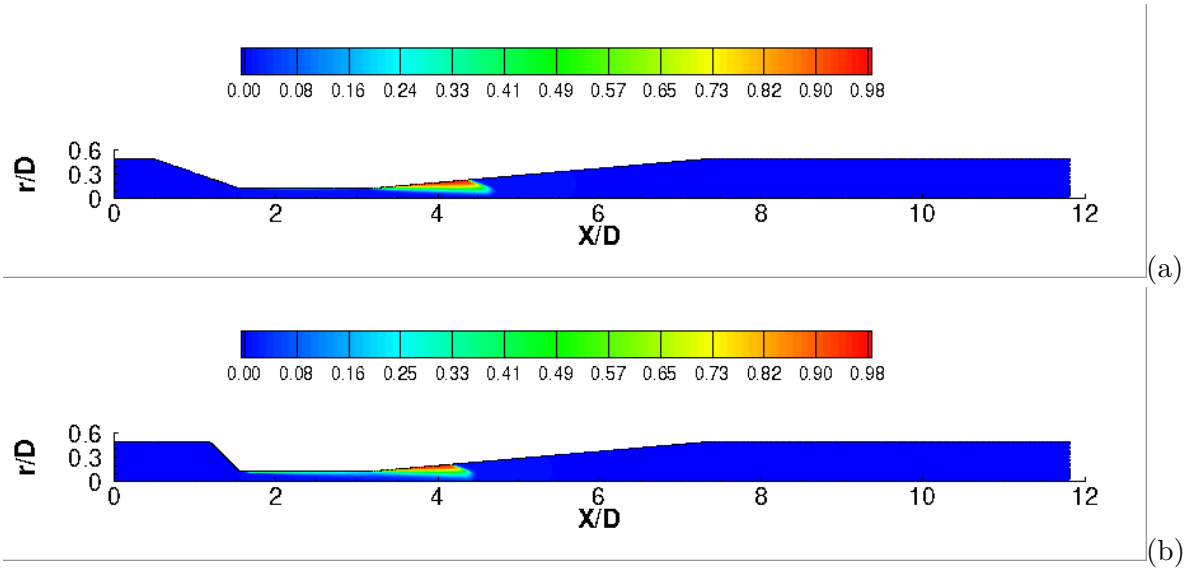

Figure 2.8: Vapor volume fraction at total inlet pressure of 400000 Pa: (a) - α=19°; (b) - α=45°.

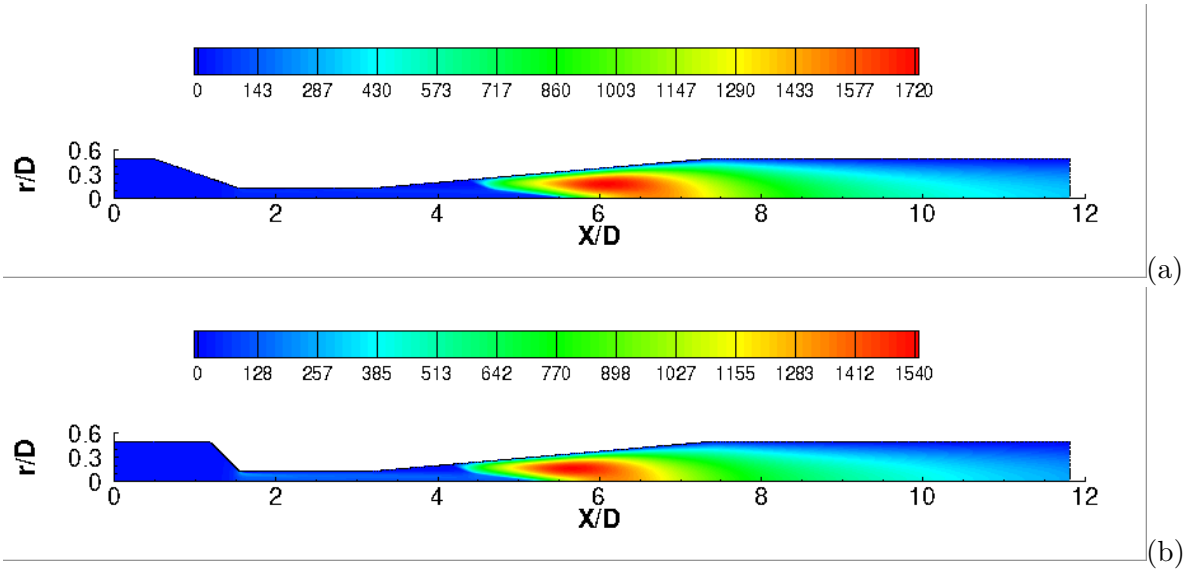

Figure 2.9: Turbulent viscosity ratio at total inlet pressure of 400000 Pa: (a) - α=19°; (b) - α=45°.

Recalling the discussion about the inlet flow velocity in the previous section, Fig. 2.10 depicts the contour plot for the velocity magnitude across cavitating Venturi tubes. A similar distribution of the velocity pattern can be observed in all cases. A higher velocity magnitude (26-28 m/s) is present in the throat section and the beginning of the diver-

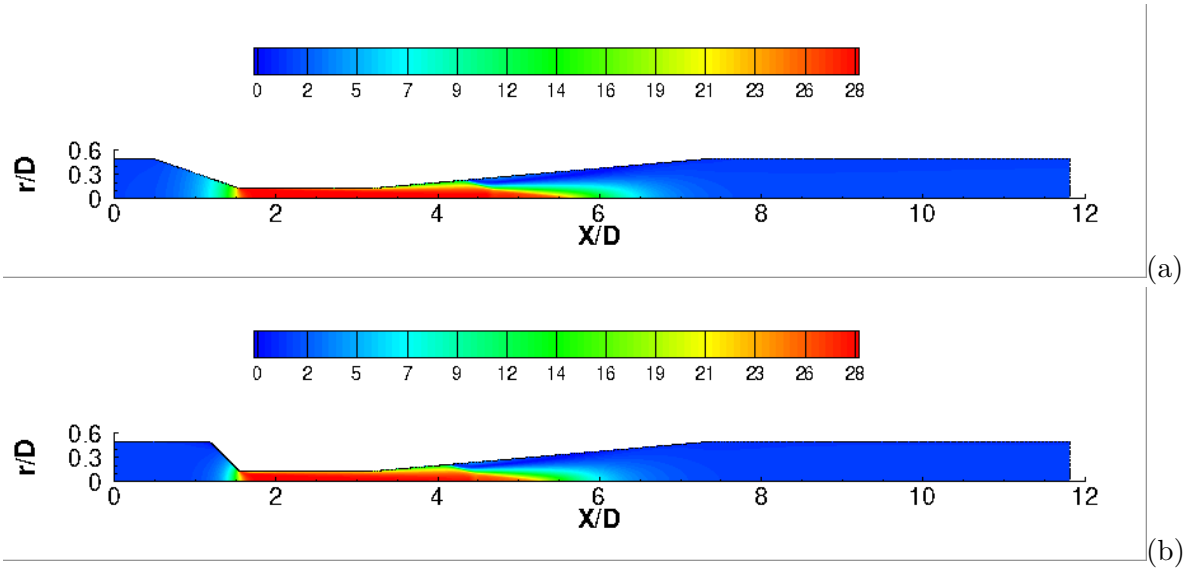

Figure 2.10: Velocity magnitude at total inlet pressure of 400000 Pa: (a) - α=19°; (b) - α=45°.

gent section, while a lower velocity magnitude (0-10 m/s) is distributed in other sections. It becomes apparent that the averaged throat velocity decreases from 27 to 25 m/s as the convergent angle increases from 19 to 45°, which indicates that the convergent angle significantly affects the velocity profile within the hydrodynamic entrance region (throat section); hence, the turbulent viscosity ratio is also varied intensively. Therefore, it can be concluded that the convergent angle is a significant structural parameter that can affect the cavitational activities inside the Venturi tube and hence should be optimized to obtain the maximum cavitation yield in industrial operations.

2.4.4 Effect of scale−ratio

Fig. 2.11 shows the characteristic curves of the Design−1 cavitating Venturi tube with scale ratios of 1, 6, and 12. As can be seen, as the static pressure difference increases from 9000 Pa to 300000 Pa, the inlet velocity exhibits an ascending trend from 0.45 m/s to 1.65 m/s for all cases. In the no-cavitating flow regime (ΔP<39000 Pa), the inlet velocity increases as the scale ratio rises from 1 to 12. A maximum 19% increment in the inlet velocity can be observed for the scaled-up case with a ratio of 12 at ΔP=24000 Pa. This suggests that the dominant effect of the scale ratio on inlet velocity before the appearance and development of cavitation bubbles. Once the cavitation inception is reached, the presence of cavitation bubbles in the throat section causes a blockage effect, reducing the inlet velocity intensively. In the cavitating flow regime (ΔP>39000 Pa), the increase in the inlet velocity of scaled-up

cases is slightly small compared to the original case, with averaged values of 2.45% and 3.24% for scale ratios of 6 and 12, respectively. This indicates that the effect of the scale ratio on inlet velocity is relatively small under the cavitational conditions.

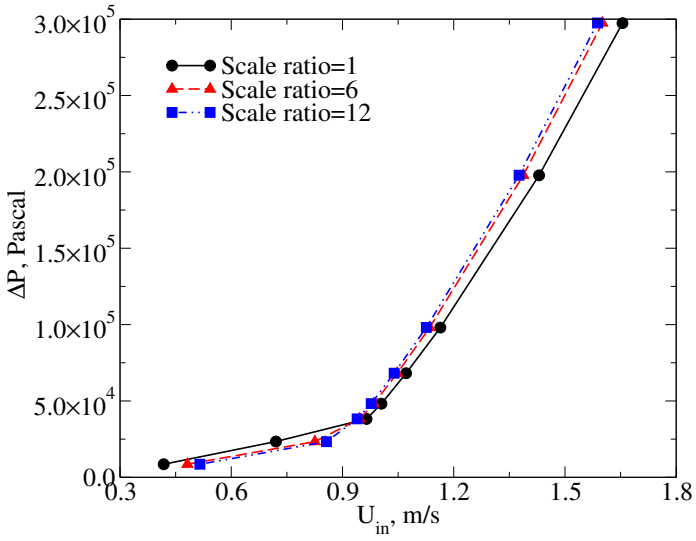

Figure 2.11: Simulated static pressure drop as a function of inlet velocity for scale ratios of 1, 6, and 12.

Fig. 2.12a shows the relationship between K and Re_{in} at different scale ratios under cavitational and non-cavitational conditions. Under non-cavitation conditions, a sharp decrease in the pressure loss coefficient happened in the range of Re_{in} between 1×10^3 to 1×10^4 and a gradually declining trend can be observed over the range between 1×10^4 to 3×10^5. On the other hand, a dramatic increase in K occurs at the critical inlet Reynolds number under cavitational conditions. In addition, we found that the critical inlet Reynolds number in the scaled-up Venturi tube is higher than that for the original Venturi tube. This can be explained by the diameter of the inlet tube. As the scale ratio increases from 1 to 12, the diameter of the inlet tube increases notably, which affects the critical inlet Reynolds number significantly.

To further explore the relationship between K and the scale−ratio, the evolution of K in terms of $Re_{in}/scale\ ratio$ was compared at different scale ratios with and without cavitation in Fig. 2.12b. It is observed that K decreases when $Re_{in}/scale\ ratio$ increases from 0 to 1.15×10^4, and starts to rise as $Re_{in}/scale\ ratio$ further increases once the cavitation inception is reached for all cases. For different sizes of Venturi tube, the change of K is largely different under the non-cavitational conditions, while the differences of K is reduced under the cavitational conditions. This confirms that the effect of scale ratio on K is significant before the cavitation inception, while that impact is weakened after the

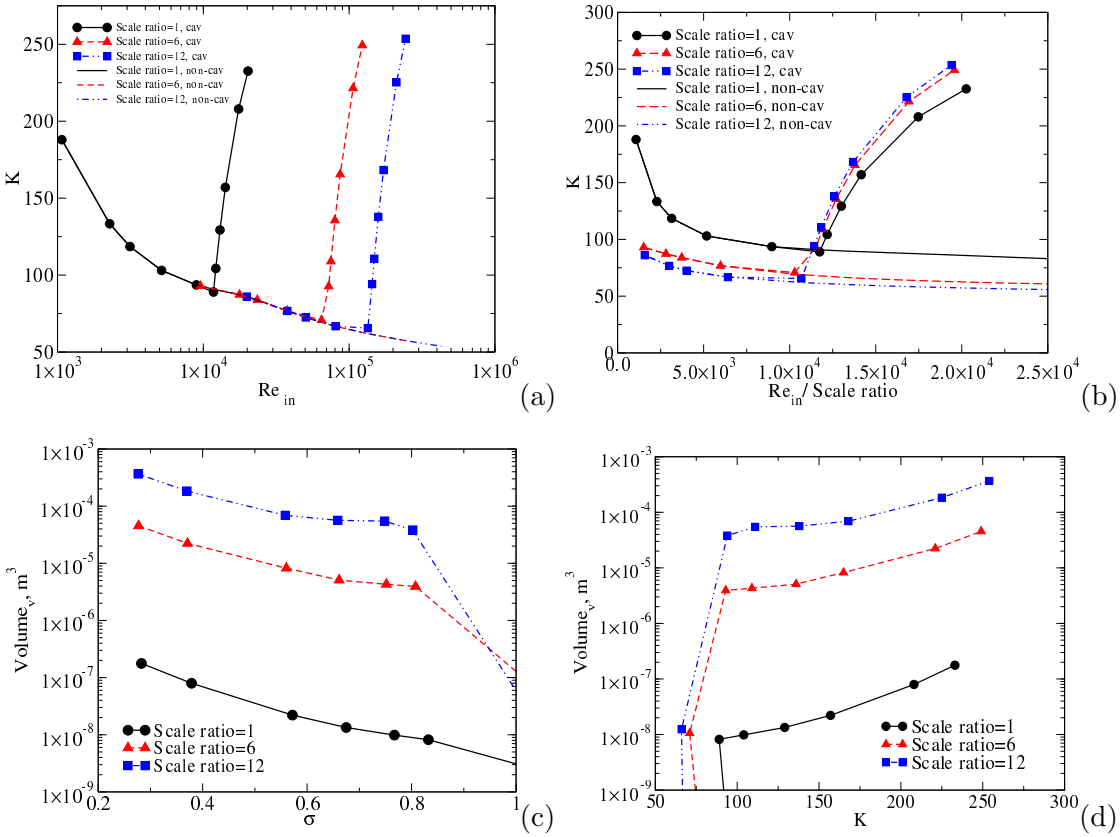

Figure 2.12: Integral parameters predicted numerically for different scale ratios of 1, 6, and 12: (a) - pressure loss coefficient as a function of inlet Reynolds number; (b) - pressure loss coefficient as a function of the ratio of inlet Reynolds number to scale ratio; (c) - volume of vapor as a function of cavitation number; (d) - volume of vapor as a function of pressure loss coefficient.

appearance and development of cavitation bubbles.

Referring to the comparison between different sizes of Venturi tube on the cavitation yield, Fig. 2.12c presents the volume of vapor as a function of σ in Design$-$1 with different scale ratios. It can be observed that the volume of vapor increases when σ decreases from 1 to 0.3, and a rapidly increase in the volume of vapor is evident at $\sigma \leq 0.8$ for all cases. As compared to the cavitating Venturi tube, with a scale ratio of 1, the increase in the vapor volume predicted in scaled-up Venturi tubes with ratios of 6 and 12 is significant.

Fig. 2.12d presents the relationship between volume of vapor and K. It can be observed that the volume of vapor shows the same trend over a wide range of K. A rapid increase of the vapor volume happens at $K < K_c$ and a steady rise in the volume of vapor occurs over $K > K_c$. It is obvious that the cavitating Venturi tubes with different scale ratios exhibit different cavitation performance over the full range of K. This can be further confirmed

by the contour plots, which will be discussed later.

Studying the overall behavior of the cavitating flow in the cavitating Venturi tube with scale ratios of 1 and 12, the vapor volume fraction and turbulent viscosity ratio plots at a specific inlet pressure of 400000 Pa are depicted in Fig. 2.13. As can be seen from Figs. 2.13a and b, similar stable cavitating flow behaviors are displayed in both the original and scaled-up cavitating Venturi tubes. Mass transfer from water to vapor starts along the wall of the throat section and then extends into the divergent section. A higher value of vapor volume fraction (around 73% to 98%) is clearly observed at the beginning of the divergent section along the wall for the cavitating Venturi tube with scale ratios of 1 and 12. However, it becomes apparent that the volume fraction of vapor in the throat section for the scaled-up case is much higher than that for the original case. This confirms that there is a slightly change in the nature of the variation of the cavitation performance when the scale ratio is varied from 1 to 12.

The snapshots of the turbulent viscosity ratio for the same simulation cases are depicted in Fig. 2.13c and d. Similarly to the results in the previous section, higher turbulence exists in the divergent section for all simulation cases. It is interesting that the maximum turbulent viscosity ratio of the cavitating Venturi tube with the scale ratio of 12 ($\mu_t/\mu_o =$ 21800) is about 13 orders of magnitude larger than that of the scale ratio of 1 ($\mu_t/\mu_o =$ 1720). This suggests that the maximum turbulent viscosity ratio is linearly proportional to the scale ratio. The resistance to the flow increases with the increase in the scale ratio, inducing an increase in the turbulent viscosity. Based on the study of the effect of the scale−ratio, we can conclude that the scale−ratio has a small impact on the cavitation inception but a large effect on the cavitation intensity.

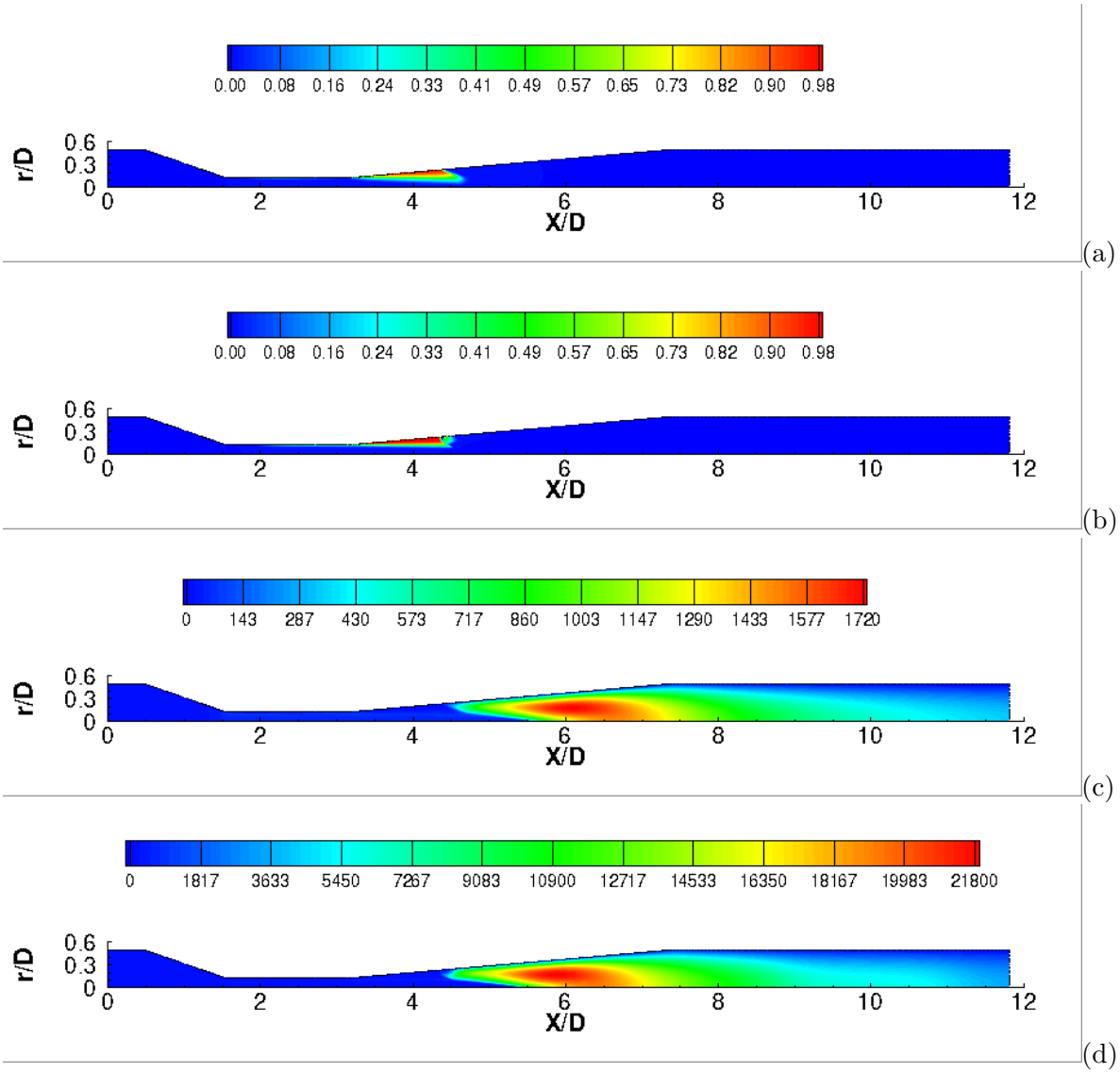

Figure 2.13: Vapor volume fraction at total inlet pressure of 400000 Pa for (a) - scale−ratio=1; (b) - scale−ratio=12. Turbulent viscosity ratio $\frac{\mu_t}{\mu_0}$ at total inlet pressure of 400000 Pa for (c) - scale−ratio=1; (d) - scale−ratio=12.

2.4.5 Empirical Model

This section outlines the development of empirical models for different cavitating Venturi tubes, employing dimensionless equations based on the inlet Reynolds number, the pressure loss coefficient, the cavitation number and the vapor volume fraction. In order to develop empirical models, linear and nonlinear regression methods are proposed using the statistical toolbox of MATLAB [33]. Regression analysis is a powerful statistical technique for

establishing the relationship between a dependent variable and one or more independent variables, helping us to understand how much the dependent variable changes with the variation of any one of the independent variables [34]. The parameters in the regression equation are calculated based on the least square method. Tables 2.5 and 2.6 summarize the functional structure of the empirical models under various conditions and application ranges.

To ensure that empirical model developed is reliable and accurate, it is critical to validate it against the CFD results. Fig. 2.14 illustrates how the approximations obtained from the empirical model fit all the CFD predictions based on the relationship between the inlet Reynolds number Re_{in}, the pressure loss coefficient K, the cavitation number σ, and the vapor volume fraction ϕ_v. In Design-1, cubic regression is employed to establish the relationship between ϕ_v-σ (a1), and ϕ_v-K (a2), while quadratic regression is applied for the relationship between K-Re_{in} (a3). In Design-2, the relationships between ϕ_v-σ (b1), ϕ_v-K (b2), and K-Re_{in} (b3) are obtained with exponential, cubic and quadratic regressions, respectively. As can be seen from the figure, the general trends of approximations are similar in different designs. The empirical models developed predict the CFD values very well and can be used to design and estimate the performance of Venturi tubes.

Fig. 2.15 depicts the comparison results between the approximation and the CFD model for scale ratios in the range between 1 and 12. In order to predict K and Re_{in} based on any given value of scale ratio, we first need to establish the relationship between the critical inlet Reynolds number $Re_{in,cr}$, the critical pressure loss coefficient K_{cr}, and the parameters a_1 and a_2. As can be seen from Fig 2.15 a-d, linear regression is aplied to the relationship between $Re_{in,cr}$-$Scale\ ratio$ (a). Logarithmic regression is used to predict the relationship between K_{cr}-$Re_{in,cr}$ (b). The relationship between parameter a_1-$Re_{in,cr}$ (c), and parameter a_2-$Re_{in,cr}$ (d) are obtained using power and quadratic regressions, respectively. Figs. 2.15 e and f respectively show the linear relationship between K-Re_{in} based on logarithmic scale and linear scale. The regression lines are seen to be in reasonable agreement with CFD results for scale ratios of 1 and 6, but there is a slight deviation in the model test results from scale ratios of 12. In conclusion, the approximation results obtained from empirical models work reasonably well in these validation cases.

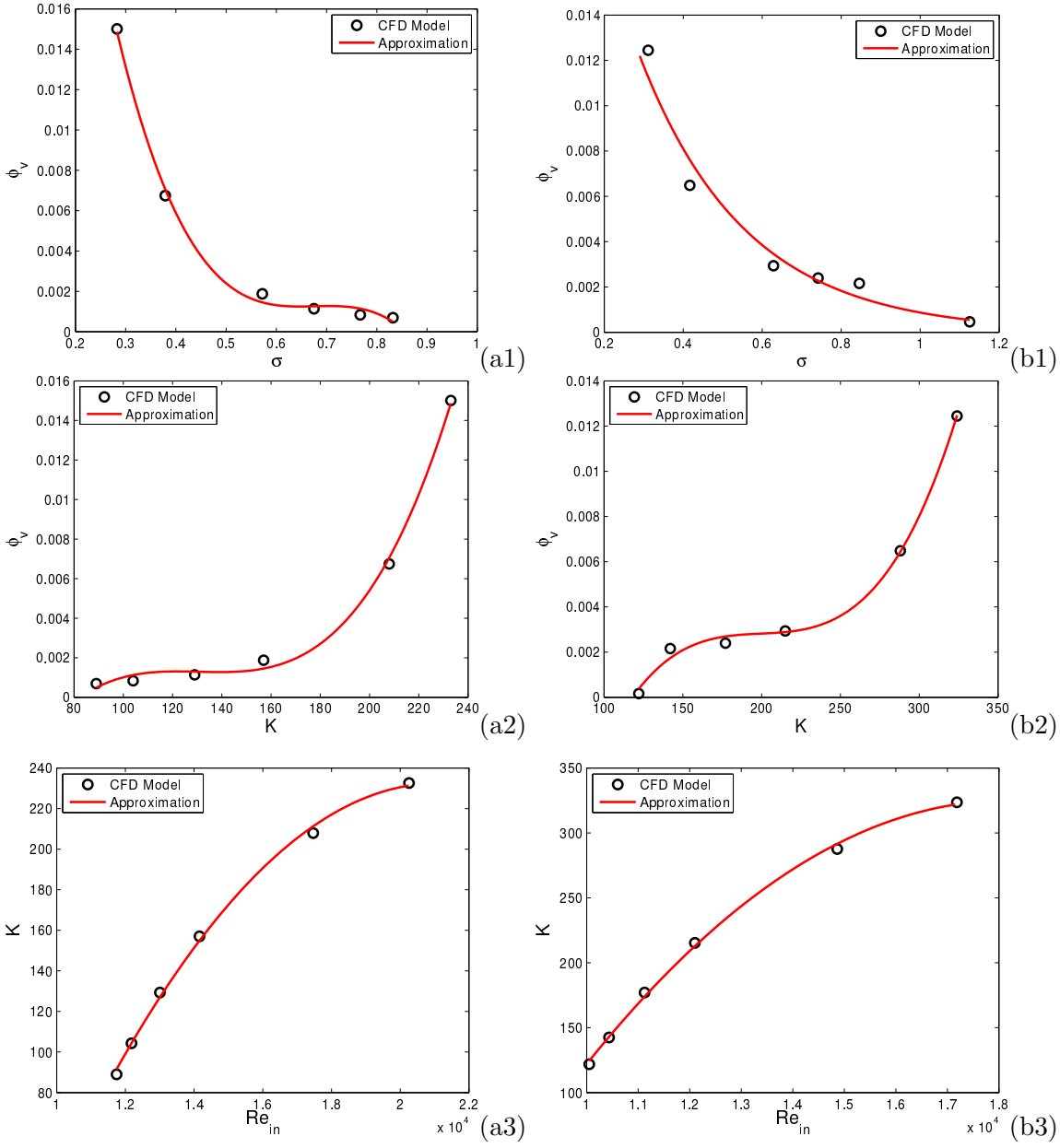

Figure 2.14: Global fit between the approximation and CFD results for (a) - Design−1 (α=19°) and (b) - Design−2 (α=45°): 1) - volume-averaged vapor volume fraction as a function of cavitation number; 2) - volume-averaged vapor volume fraction as a function of pressure loss coefficient; 3) - pressure loss coefficient as a function of inlet Reynolds number.

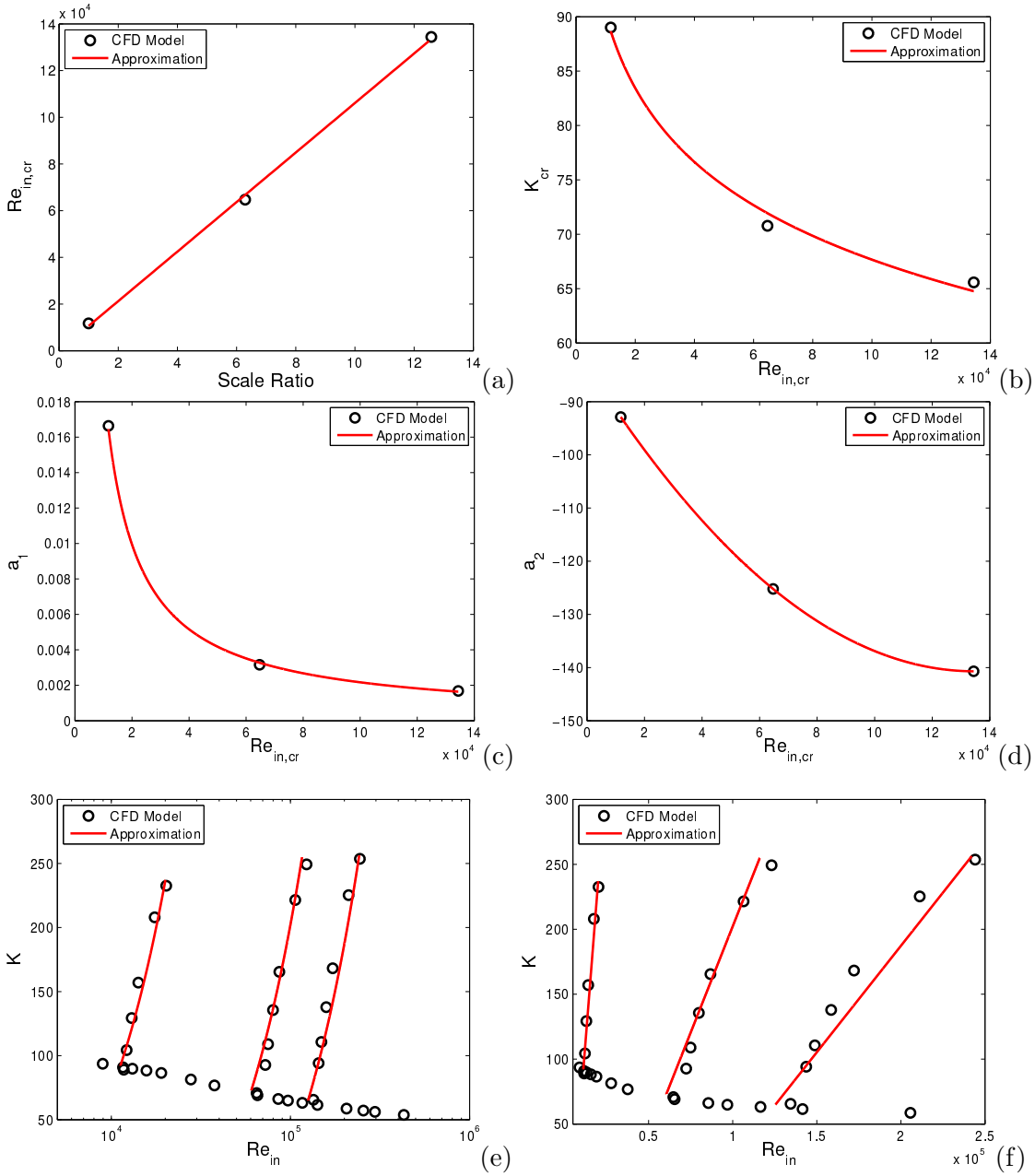

Figure 2.15: Global fit between the approximation and CFD results: (a) - critical inlet Reynolds number as a function of scale ratio; (b) - critical pressure loss coefficient as a function of critical inlet Reynolds number; (c) - parameter a_1 as a function of critical inlet Reynolds number; (d) - parameter a_2 as a function of critical inlet Reynolds number; (e) - pressure loss coefficient as a function of inlet Reynolds number (logarithmic plot); (f) - pressure loss coefficient as a function of inlet Reynolds number (linear plot).

Design	*Input*	*Output*	*Empirical Model*	*Application Range*
1 (α=19°)	σ	ϕ_v	ϕ_v = 0.071164 - 0.31132 * σ + 0.46127 * σ^2 - 0.22738 * σ^3	0.28< σ <0.83
	K	ϕ_v	ϕ_v = -0.027086 + 0.00065775 * K - 5.0591e-06 * K^2 + 1.2914e-08 * K^3	89< K <233
	Re_{in}	K	K = -485.24 + 0.068059 * Re_{in} - 1.6135e-06 * Re_{in}^2	11743< Re_{in} <20257
2 (α=45°)	σ	ϕ_v	ϕ_v = 0.035853 * exp(-3.7186 * σ)	0.31< σ <1.12
	K	ϕ_v	ϕ_v = -0.035544 + 0.00057111 * K - 2.8501e-06 * K^2 + 4.7682e-09 * K^3	122< K <324
	Re_{in}	K	K = -677.88 + 0.11032 * Re_{in} - 3.0337e-06 * Re_{in}^2	10051< Re_{in} <17184

Table 2.5: Summary of multiple empirical model for Design 1 and Design 2.

Input	*Output*	*Empirical Model*	*Application Range*
ScaleRatio	$Re_{in,cr}$	$Re_{in,cr}$= 30.162 + 10608 * Scale Ratio	1<Scale Ratio<12
$Re_{in,cr}$	K_{cr}	K_{cr}= 180.55 - 9.805 * ln($Re_{in,cr}$)	11743<$Re_{in,cr}$<134403
$Re_{in,cr}$	a_1	a_1= 116.51 * $Re_{in,cr}^{-0.94601}$	11743<$Re_{in,cr}$<134403
$Re_{in,cr}$	a_2	a_2= -83.301 - 0.00085235 * $Re_{in,cr}$ + 3.1643e-09 * $Re_{in,cr}^2$	11743<$Re_{in,cr}$<134403
Re_{in}	K	K= a_1 * Re_{in} + a_2	$Re_{in,cr}$<Re_{in}<244096

Table 2.6: Summary of multiple empirical model for different Venturi tube scale ratios.

2.4.6 Geometry study

For optimization of Venturi geometry, different designed Venturi tubes are studied experimentally and numerically. The configurations and dimensions of Design−1 to Design−7 are presented in Fig. 2.16 and Table 2.3. Fig. 2.17 compares the predicted throat velocity as a function of inlet pressure against the experiment data. As can be seen, both the numerical and the experimental results present gradually increasing trend in the throat velocity with an ascending inlet pressure for all designs. The predicted results well follow the experimental data for Design 1, 2, 5 and 7 with an averaged deviation of 5.3%. Meanwhile, the comparison of the numerical and experimental data shows that Design−6 tends to overpredict experimental results with a deviation of 15.32%.

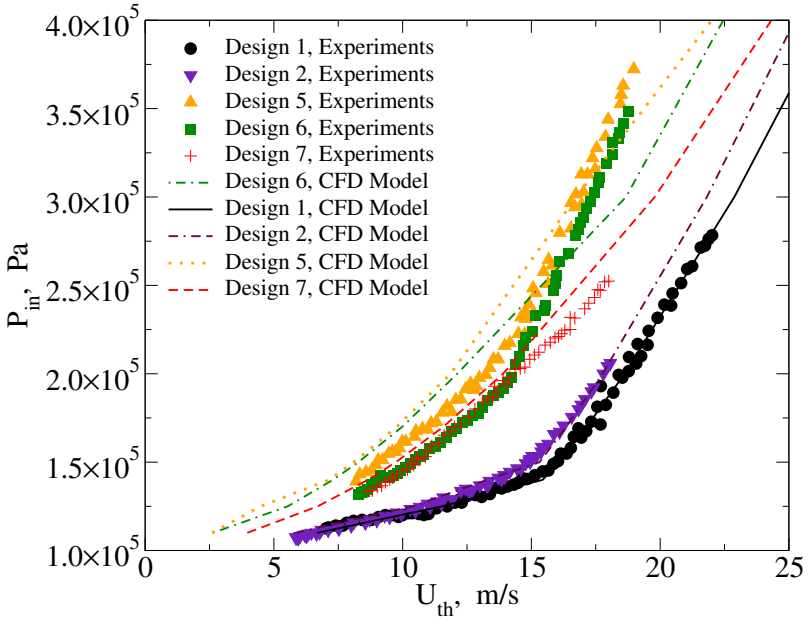

Figure 2.17: Experimental and simulated inlet pressure as a function of throat velocity for Design 1-6.

Fig. 2.18a shows the relationship between K and Re_{in} for Design 1-6 under cavitational and non-cavitational conditions. In the first stage (Re_{in}<Re_c), the characteristic curves for cavitation cases and non-cavitation cases overlap and have decline briefly. In the second stage (Re_{in}>Re_c), all curves fall together further for non-cavitation cases, while the value of K sees a sharp ascent for the cavitation cases. From the profile one can observe that the value of Re_c decreases from 11743 to 8402 as the convergent angle increases from α=19° (Design−1) to α=85° (Design−3). The value of Re_c increases slightly from 8314 to 8717 as the divergent angle increases from β=2.5° (Design−4) to β=90° (Design−5). This indicates that the cavitating Venturi tube with higher convergent angle shows a early inception in

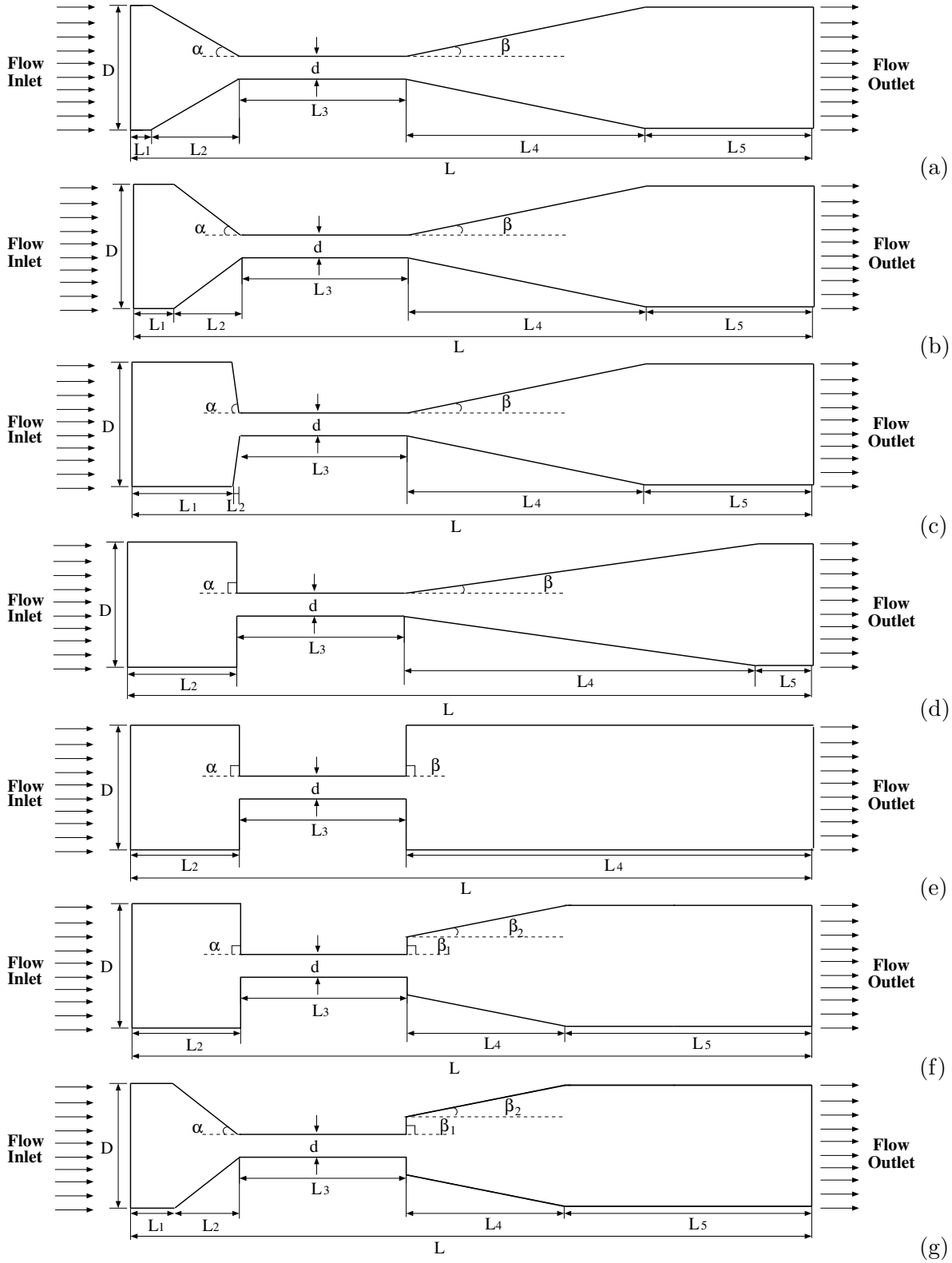

Figure 2.16: Schematic diagram of the Venturi tube for Design 1-7 - (a-g).

comparison to one with lower convergent angle. However, the changing of divergent angle has negligible effect on the inception of cavitation.

Fig. 2.18b presents the relationship between ϕ_v and σ for Design 1-6. It can be seen that different designs share the same increasing tendency in terms of the vapor volume fraction as σ declines from 1.5 to 0.3. At a fixed value of σ, Design$-$4 gives a higher value of ϕ_v in comparison to other designs. It indicates that the lower divergent angle can produce more cavitation bubbles in comparison with the one with higher divergent angle. The pressure recovery is the main reason contributing the variation of cavitation intensity. The Venturi tube with lower divergent angle can contribute smooth pressure recovery and therefore cavitation bubbles can expand to its maximum size. The Venturi tube with higher divergent angle causes rapid pressure recovery resulting into early bubble collapse.

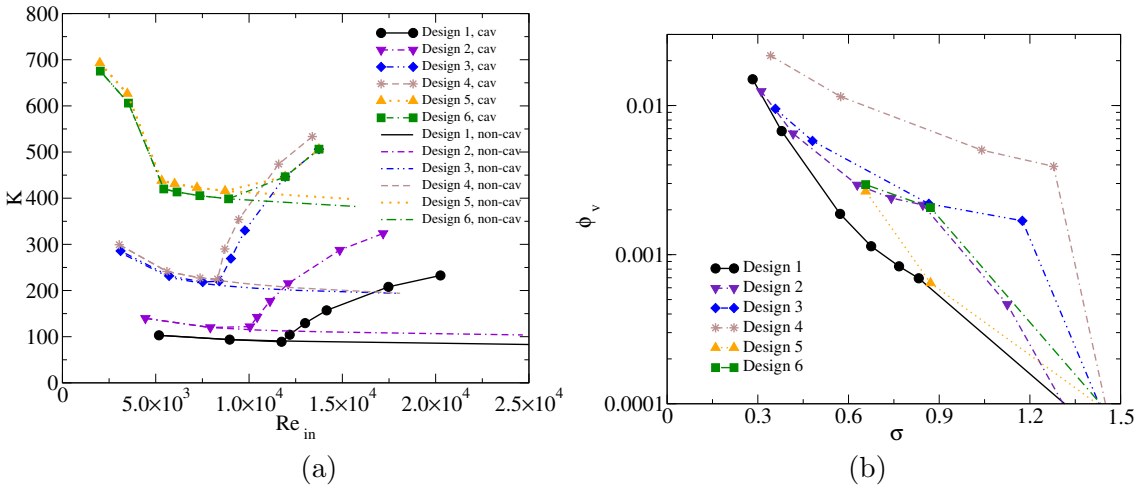

Figure 2.18: Integral characteristics predicted numerically for Design$-$1 to Design$-$6: (a) - pressure loss coefficient as a function of inlet Reynolds number; (b) - volume-averaged vapor volume fraction as a function of cavitation number.

Fig. 2.19 depicts the vapor volume fraction contours at a specific inlet pressure of 400000 Pa for Design 1-7. As can be seen from the figure, Design$-$4 shows the largest cavitation zone in the throat and divergent sections in comparison with other designs. The length of the vapor bubble in the divergent section decreases as the convergent angle increases from α=19° (Design$-$1) to α=85° (Design$-$3). The cavitation intensity increases in the throat section as the value of the convergent angle rises. In addition, the Venturi tube with divergent angle of β=90° (Design$-$5, 6 and 7) leads to more cavitation bubble collapse and therefore reduces the cavitation intensity in the divergent section.

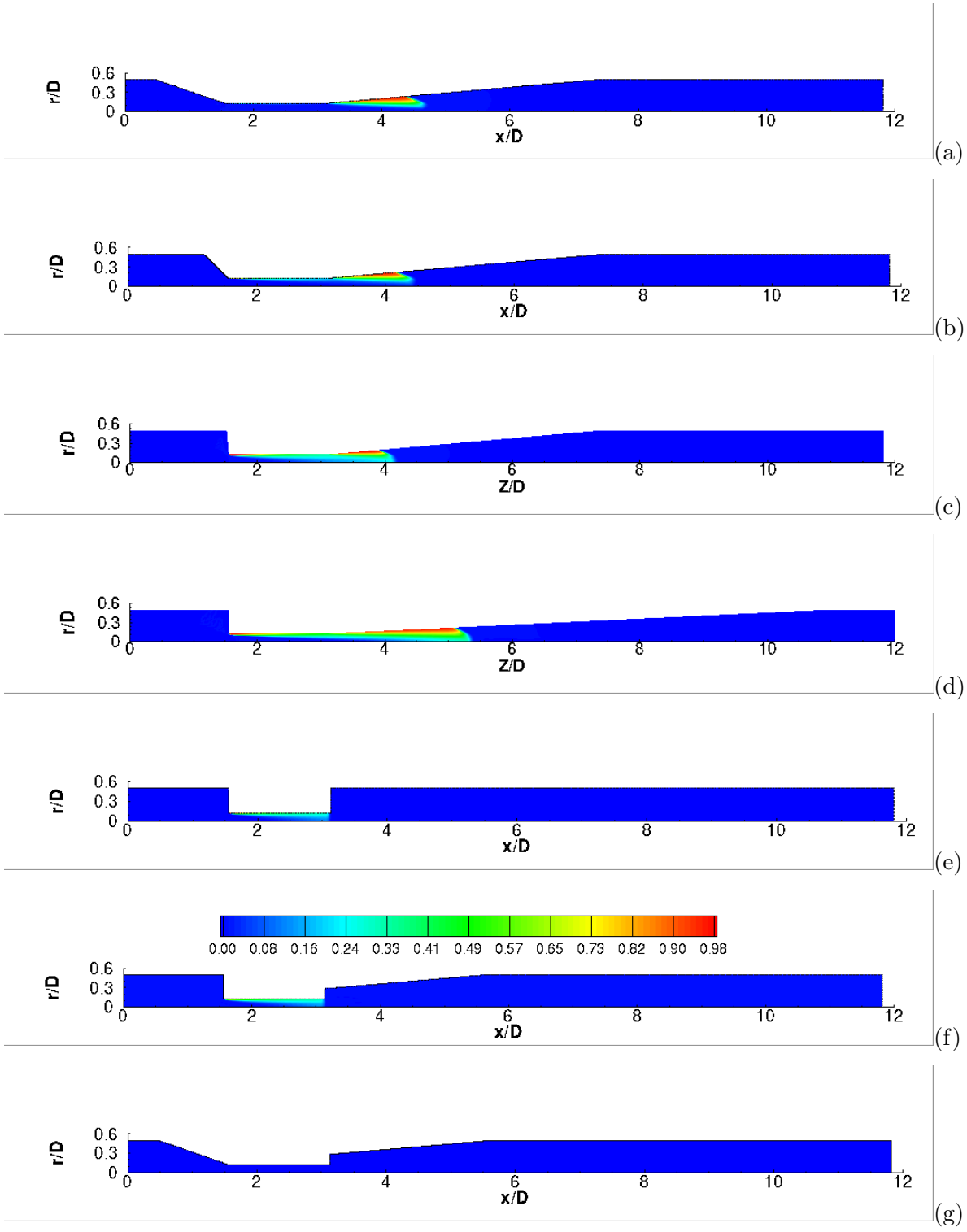

Figure 2.19: Vapor volume fraction at inlet pressure of 400000 Pa: (a)-Design 1; (b)-Design 2; (c)-Design 3; (d)-Design 4; (e)-Design 5; (f)-Design 6; (g)-Design 7.

2.5 Conclusions

In the present study, numerical simulations of cavitating Venturi tubes were performed using an axisymmetric 2D CFD-based model available in the commercial CFD software ANSYS FLUENT 16.2. A mixture model based on a water-vapor-phase mixture is used to reproduce the experiments. Comparison between the experimental measurements and numerical simulations showed good agreement. The influence of the convergent angle of cavitating Venturi tubes on flow characteristics and generation of cavitation was studied experimentally and numerically. In particular, the results of the CFD study clearly illustrate that the higher convergent angle is of benefit to cavitation yield but requires higher power consumption. In this view, a required cavitational intensity can be controlled by the convergent angle of the cavitating Venturi tube taking into account the effect of energy consumption. The higher divergent angle leads to a reduction of cavitation extent in the divergent section. Additionally, it was shown numerically that turbulence alters the structure of the flow and restricts the development of cavitation in the downstream section of the cavitating Venturi tube.

The effect of scale−ratio on cavitational activities was investigated numerically. It was shown that the scaled-up Venturi tubes produce more vapor as lab-scale Venturi tubes, which is favorable to achieve commercialization capacity and greatly benefit industrial operations in mineral processing.

Finally, an empirical model enabling of cavitation to be predicted in Venturi tubes was established employing regression analysis based on CFD results. In particular, based on the best-fitting results for the validation cases, the empirical models developed are capable of giving reliable predictions for different Venturi tubes. The developed empirical model serves as a valuable tool for industrial engineers to accurately estimate the significant dimensionless parameters (the inlet Reynolds number Re_{in}, the pressure loss coefficient K, the cavitation number σ, and the vapor volume fraction ϕ_v) and involves in the design of cavitating Venturi tubes with different geometrical parameters and scales.

2.6 Acknowledgments

Financial support from the Natural Science and Engineering Research Council of Canada (NSERC), the Canadian Centre for Clean Coal/Carbon and the Mineral Processing Technologies (C5MPT) and Canadian Mining Industry Research Organization (CAMIRO) is greatly appreciated.

Bibliography

[1] Seyed Shaham Aldin Hosseininejad. *CFD Modeling of Cavitation for Fine Particle Flotation*. PhD thesis, University of Alberta, 2016.

[2] Robert T Knapp, James W Daily, and Frederick G Hammitt. *Cavitation*. McGraw-Hill, 1970.

[3] Christopher E Brennen. *Cavitation and bubble dynamics*. Cambridge University Press, 2013.

[4] M. Gagola, A. Przyjaznyb, and G. Boczkaja. Wastewater treatment by means of advanced oxidation processes based on cavitation - A review. *Chemical Engineering Journal*, 338:599–627, 2018.

[5] Z. Zhou, Z. Xu, J.A. Finch, H. Hu, and S.R. Rao. Role of hydrodynamic cavitation in fine particle flotation. *Int. J. Miner. Process.*, 51:139–149, 1997.

[6] RH Yoon and GH Luttrell. The effect of bubble size on fine coal flotation. *Coal Preparation*, 2(3):179–192, 1986.

[7] Roe-Hoan Yoon, Darrin H Flinn, and Yakov I Rabinovich. Hydrophobic interactions between dissimilar surfaces. *Journal of colloid and interface science*, 185(2):363–370, 1997.

[8] Daniel Tao. Role of bubble size in flotation of coarse and fine particles—a review. *Separation Science and Technology*, 39(4):741–760, 2005.

[9] ZA Zhou, Zhenghe Xu, JA Finch, H Hu, and SR Rao. Role of hydrodynamic cavitation in fine particle flotation. *International Journal of Mineral Processing*, 51(1-4):139–149, 1997.

[10] H. Oliveira, A. Azevedo, and J. Rubio. Nanobubbles generation in a high-rate hydrodynamic cavitation tube. *Minerals Engineering*, 116:32–34, 2018.

[11] Rahman Ahmadi, Darban Ahmad Khodadadi, Mahmoud Abdollahy, and Maoming Fan. Nano-microbubble flotation of fine and ultrafine chalcopyrite particles. *International Journal of Mining Science and Technology*, 24(4):559–566, 2014.

[12] Haipeng Li. Role of hydrodynamic cavitation in fine particle flotation. Master's thesis, University of Alberta, 2014.

[13] W. Zhou, H. Chen, L. Ou, and Q. Shi. Aggregation of ultra-fine scheelite particles induced by hydrodynamic cavitation. *International Journal of Mineral Processing*, 157:236–240, 2016.

[14] Tausif A Bashir, Advait G Soni, Amit V Mahulkar, and Aniruddha B Pandit. The cfd driven optimisation of a modified venturi for cavitational activity. *The Canadian Journal of Chemical Engineering*, 89(6):1366–1375, 2011.

[15] Seyed Mehdi Ashrafizadeh and Hojat Ghassemi. Experimental and numerical investigation on the performance of small-sized cavitating venturis. *Flow measurement and Instrumentation*, 42:6–15, 2015.

[16] JX Zhang. Analysis on the effect of venturi tube structural parameters on fluid flow. *AIP Advances*, 7(6):065315, 2017.

[17] Narotam Jangir, Prateek Diwedi, and Sumana Ghosh. Design of a hydrodynamic cavitating reactor. *Chemical Engineering & Processing: Process Intensification*, 122: 128–142, 2017.

[18] Donghua Li, Shenghua Liu, Yanju Wei, Tongtong Ren, and Yonghong Tang. A turbulent two-phase model for predicting cavitating flow based on homogenous nucleation theory. *International Communications in Heat and Mass Transfer*, 97:17–19, 2018.

[19] Boxiong Chen and Michael Oevermann. An eulerian stochastic field cavitation model coupled to a pressure based solver. *Computers and Fluids*, 162:1–10, 2018.

[20] Liang Zhao, Licheng Sun, Zhengyu Mo, Min Du, Jiang Huang, and Jingjing Bao. Effects of the divergent angle on bubble transportation in a rectangular venturi channel and its performance in producing fine bubbles. *International Journal of Multiphase Flow*, 2019.

[21] X Margot, S Hoyas, A Gil, and S Patouna. Numerical modelling of cavitation: validation and parametric studies. *Engineering Applications of Computational Fluid Mechanics*, 6(1):15–24, 2012.

[22] Vedanth Srinivasan, Abraham J. Salazar, and Kozo Saito. Modeling the disintegration of cavitating turbulent liquid jets using a novel vof-cimd approach. *Chemical Engineering Science*, 65:2782–2796, 2010.

[23] K. Sampath Kumar and Vijayanand S. Moholka. Conceptual design of a novel hydrodynamic cavitation reactor. *Chemical Engineering Science*, 62:2698–2711, 2007.

[24] Inc Ansys. Ansys fluent theory guide. *Canonsburg, Pennsylvania*, page 794, 2011.

[25] Günter H Schnerr and Jürgen Sauer. Physical and numerical modeling of unsteady cavitation dynamics. In *Fourth international conference on multiphase flow, New Orleans, USA*, volume 1, 2001.

[26] D Li, Mikael Grekula, and Per Lindell. A modified sst k-ω turbulence model to predict the steady and unsteady sheet cavitation on 2d and 3d hydrofoils. *7th International Symposium on Cavitation*, 2009.

[27] Hou-lin Liu, Dong-xi Liu, Yong Wang, Xian-fang Wu, and Jian Wang. Application of modified κ-ω model to predicting cavitating flow in centrifugal pump. *Water Science and Engineering*, 6(3):331–339, 2013.

[28] Huiying Li, Frank J Kelecy, Aleksandra Egelja-Maruszewski, and Sergio A Vasquez. Advanced computational modeling of steady and unsteady cavitating flows. In *ASME 2008 International Mechanical Engineering Congress and Exposition*, pages 413–423. American Society of Mechanical Engineers, 2008.

[29] George Wm Thomson. The antoine equation for vapor-pressure data. *Chemical reviews*, 38(1):1–39, 1946.

[30] Brian P Leonard. A stable and accurate convective modelling procedure based on quadratic upstream interpolation. *Computer methods in applied mechanics and engineering*, 19(1):59–98, 1979.

[31] Henry Scheffe. The relation of control charts to analysis of variance and chi-square tests. *Journal of the American Statistical Association*, 42(239):425–431, 1947.

[32] Hongbo Shi, Alexandra Komrakova, and Petr Nikrityuk. Fluidized beds modeling: Validation of 2d and 3d simulations against experiments. *Powder Technology*, 343: 479–494, 2019.

[33] MATLAB User's Guide. The mathworks. *Inc., Natick, MA*, 5:333, 1998.

[34] William Mendenhall, Terry Sincich, and Nancy S Boudreau. *A second course in statistics: regression analysis*, volume 5. Prentice Hall Upper Saddle River, NJ, 1996.

Chapter 3

Experimental and Numerical Study of Cavitating Particulate Flows in a Venturi Tube[1].

3.1 Introduction

Hydrodynamic cavitation is defined as the formation, growth, and collapse of micro- or nano-bubbles as the static pressure drops locally below the saturated vapor pressure corresponding to the liquid temperature [1, 2]. The applications of cavitation can be observed in many industrial fields, such as wastewater treatment [3], biotechnology [4], chemical synthesis [5], and mineral processing [6]. The froth flotation of fine particles has long been the most frequently-addressed challenge in the field of mineral processing. Fig. 3.1a shows an outline of a flotation column featuring a cavitating Venturi tube. The physical principle of froth flotation is to extract valuable minerals based on differences in the selective ability of air bubbles attached to the intended minerals in a slurry flow [7, 8]. The particles with attached air bubbles (hydrophobic particles) agglomerate on the top surface and overflow into a collector for the next purification process, while the rest of the particles (hydrophilic particles) settle down and can then be removed from the bottom as tailings. The efficiency of froth flotation strongly depends on the particle size. Conventional flotation usually achieves a high recovery rate for minerals in the size range between 10 μm and 100 μm [9]. The flotation rate dramatically declines for particles smaller than 20 μm [10]. The poor flotation performance is primarily due to the low collision efficiency of particle-bubble

[1]This chapter has been published as: Hongbo Shi, Mingda Li, Qingxia Liu and Petr Nikrityuk. Experimental and numerical study of cavitating particulate flows in a venturi tube. *Chemical Engineering Science*, Vol.219, pp115598, 2020 (21 pages)

collisions, influenced by the low mass and kinetic energy [11, 10, 12].

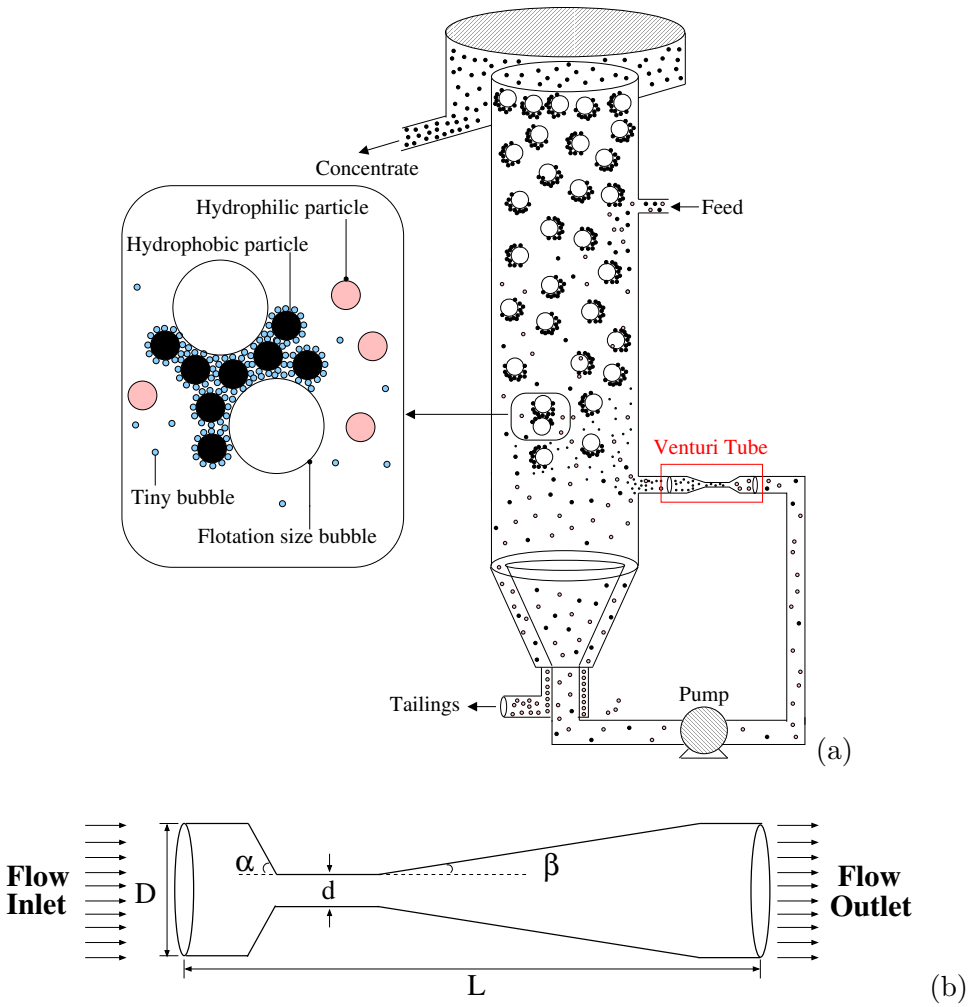

Figure 3.1: Schematic view of flotation column used in mineral processing (adapted from [13]) - (a), scheme of cavitation tube - (b).

In the past decades, many researchers have tried different methods to improve the efficiency of fine particle flotation, among which a new technology known as the cavitating Venturi tube has drawn attention. The cavitating Venturi tube is considered to be the most efficient means of creating an intense, stable cavitation condition. The major advantages of using a flotation column featuring a cavitating Venturi tube are the generation of micron- and nano-sized vapor bubbles [14], which are characterized by effective collision and aggregation, a high probability of the attachment and a low probability of the detachment of solid hydrophobic particles with air and vapor bubbles generated by cavitation. The Venturi shown in Fig. 3.1b is the most commonly used hydrodynamic cavitation de-

vice in mineral processing industry. It consists of three main parts: a convergent section, a throat section, and a divergent section. As the fluid flows through the throat of the Venturi tube, the liquid in the throat section is at a lower pressure than the saturated vapor due to the narrowing diameter, resulting in an instant phase transition from liquid to vapor. Tiny bubbles produced by the cavitating Venturi tube coat the surface of hydrophobic particles and activate flotation by promoting their attachment to the flotation size bubble [15, 16, 17], leading to the improved flotation recovery of fine particles. In fact, making the Venturi tube a highly efficient cavitation device for producing fine bubbles, and thus enhancing the flotation performance of fine particles, has been the subject of considerable research in the minerals industry [18].

There has been a great deal of work aimed at increasing the efficiency of a cavitating Venturi tube and consequently enhancing the flotation performance of fine particles, either by focusing on the design and study of the geometrical parameters [19, 20, 21] or by concentrating on the operation conditions [22, 23, 24] of a cavitating Venturi tube. However, another significant method that has been considered as an effective means of generating a high level of cavitation bubbles and improving the efficiency of fine particle recovery is the addition of solid particles to the cavitating Venturi tube. The effects of solid particles on cavitation have been widely studied experimentally (e.g. [25, 26, 27]). It is well known that the influence of solid particles mainly comes from the dissolved gases stabilized on particle surfaces [28]. The trapped, dissolved gases are usually formed inside crevices on particle surfaces and develop into larger, stabilized cavitation nuclei, diminishing the free energy barrier [28, 25, 2]. The reduced free energy barrier consequently promotes the probability of cavitation inception around the particle.

Considering the advantages of solid particles in hydrodynamic cavitation, notable experiments have been made investigating the use of four-phase flows to improve the performance of cavitating Venturi tubes. Gu et al. [29] proposed an acoustic method to experimentally study how SiO_2 nanoparticles with different volume fractions and sizes affect cavitation inception. The results show that cavitation inception is promoted as the particle concentration increases from 0.15% ml SiO_2/ml water to 1.5 % ml SiO_2/ml water, whereas increasing the particle size from 20 to 100 nm has little influence on the cavitation inception. Both the cavitation pressure and the free energy of the critical bubble are seen to decline as the operating temperature increases from 0 °C to 80 °C.

Medrano et al. [30] conducted an experimental study to examine the effects of SiO_2 nanoparticles with diameters of 2 to 3 nm on cavitation behaviors in a Venturi tube. In the research, the low solid volume fraction ($<10^{-4}$ ml SiO_2/ml water) shows negligible effects on the threshold of the cavitation flow. However, the slurry flow through the throat section of the Venturi tube cannot sustain negative pressures and consequently promotes

cavitation once the critical solid concentration is reached. They also found that the onset of cavitation is delayed in the Venturi tube, as with the deionized water.

Dunn et al. [22] performed experiments on aviation−fuel cavitation in a Venturi tube, and compared the flow characteristics between the aviation−fuel and the distilled water. The authors found that the solid micro-particles which are present in the aviation−fuel cause the cavitation to initiate on the particle surfaces. As the solid concentration increases from 0 g/L to 0.55 g/L, the cavitation zone expands from the lower wall of the throat section to the entire throat section. Additionally, they found that bubbles coalesce intensively in the case of distilled water cavitation, while they remain as individually spherical bubbles in aviation−fuel cavitation.

Li [31] studied how micro-particle properties influence hydrodynamic cavitation using a Venturi tube. It was found that the increased amount of the bare silica (with a contact angle of 8^o) concentration (from 5 g/L to 150 g/L) has no influence on the cavitation activities, but more power is consumed. However, the early cavitation inception can be achieved utilizing the hydrophobic treated silica (with a contact angle of 65^o). The glass beads and graphite particles have a limited effect on the promotion of cavitation inception. When additional nitrogen gas (0.2 LPM) is injected upstream of the Venturi tube, the throat velocity of the cavitation inception decreases significantly, from 16 m/s to 4m/s.

Parallel to the continuing effort to obtain better experimental results, there is increasing demand for a computational fluid dynamics (CFD) approach to investigate the basic fundamental understanding of cavitation phenomena in multiphase flows. One advantage of commercial CFD software (e.g. ANSYS FLUENT [32, 33]) or open-source CFD software (e.g. OPEN Foam [34, 35]) is to evaluate the multiphase cavitating flow problems under various flow conditions, which is difficult or impossible via experimental method. Ashrafizadeh et al. [36] employed the mixture multiphase approach to simulate two-phase flows in cavitating Venturi tubes and observed that the cavitation activities can be promoted by a lower divergence angle, higher throat diameter and shorter throat length. Shi et al. [13] conducted a CFD study to examine how cavitation was promoted by the convergent angle depending on the mixture model and found that a higher convergence angle is beneficial to the cavitation inception and yield. Zhang et al. [20] utilized the mixture multiphase model to analyze the effects of pressure drops in a Venturi tube, and suggested that the minimum pressure declines and the throat velocity ascends as the inlet and outlet pressure difference increases. Brinkhorst et al. [37] numerically investigated two-phase cavitating flows in two different Venturi tubes using the Volume-of-Fluid−method (VOF−method). The results show that the Herschel Venturi tube can provide a stabler and more constant mass flow than the Toroidal Venturi tube. They also found that the 3D model is superior to the 2D model, as it can capture the unsteady behavior of the cavity.

As our review of the literature shows, although a few scholars have focused on the experimental investigations of four-phase (liquid-solid-vapor-air) flows and numerical treatments of two-phase (liquid-vapor) flows in cavitating Venturi tubes, there are almost no studies carrying out a detailed CFD investigation of four-phase flows. Therefore, the aim of this work is to develop an appropriate four-phase Eulerian-Eulerian−based model for multiphase cavitating flows in a Venturi tube. It should be noted that the reason for calling four-phase flow instead of three-phase flow (liquid-solid-gas) is the steam phase and air phase are considered as two individual phases with different properties such as density, visocisty and cavitation pressure. Based on the Eulerian-Eulerian multiphase flow models, the continuity and momentum equations are solved separated for steam phase and air phase. Therefore, the number of Eulerian phases are considered as four (1-solid, 2-water, 3-steam and 4-air) in this study. Additionally, in this work, the lab-scale experimental results are used to validate the simulated results, and the flow characteristics at different solid mass concentrations are analyzed. The numerical simulations are carried out using the commercial CFD software ANSYS FLUENT 16.2 [38]. The rest of the paper is organized as follows. Section 3.2 describes the problem formulation. Section 3.3 presents a description of the model formulation. The validation of CFD models is described in Section 3.4. Results and discussions of the present study are provided in Section 3.5, and Section 3.6 outlines the conclusions.

3.2 Problem formulation

One significant issue when developing successful four-phase cavitating CFD frameworks is the choice of global formulations meaning a set of all input parameters in each submodel or closure. As a first step in developing the global model that can be applied to four-phase flows including liquid-solid-vapor-air through a Venturi tube, the two-phase (liquid-vapor) cavitating flow predictions from the Eulerian-Eulerian multiphase approach are evaluated. In this case, an experimental setup was designed and manufactured for the validation. The experimental system shown in Fig. 3.2a, is a closed−loop water circuit composed of a cavitating Venturi tube, a pressure transducer, a flow meter, an oscilloscope, a water tank, a pump and a computer. The tap water is delivered into the Venturi tube (see Fig. 3.3a) at ambient conditions. The inlet pressure measurements are carried out using the pressure transducer mounted at the inlet of the Venturi tube. The flow rate was recorded by a flow meter, which is mounted upstream of the pressure transducer.

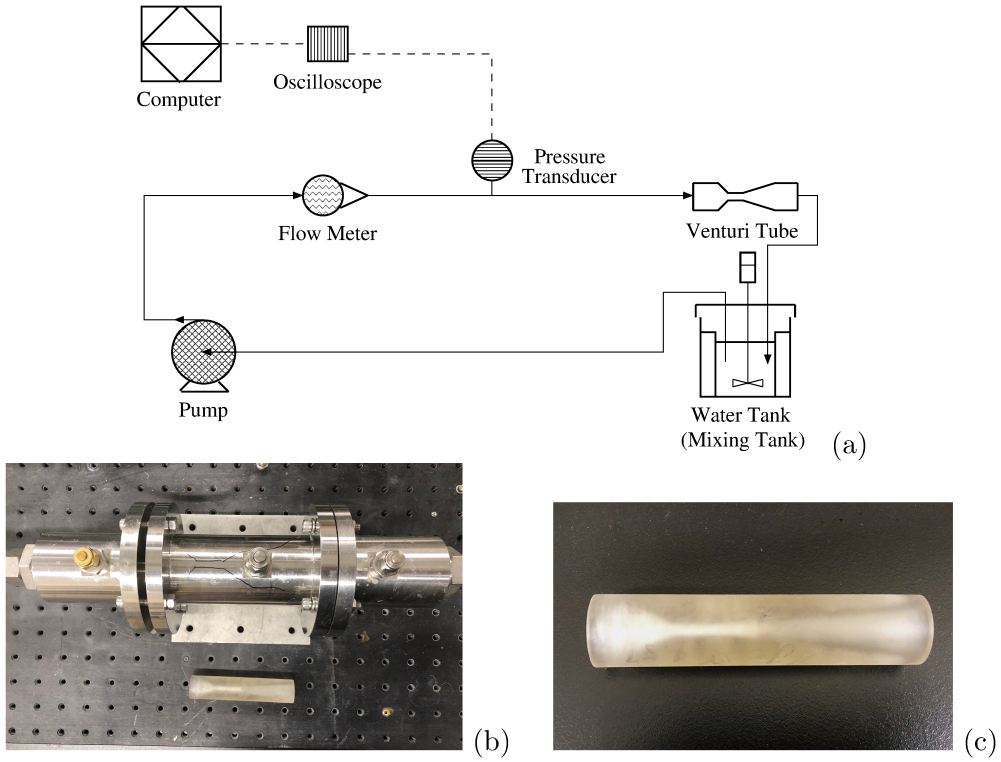

Figure 3.2: Experimental setup: (a) - schematic diagram, (b) - cavitating Venturi tube test section, (c) - cavitating Venturi tube.

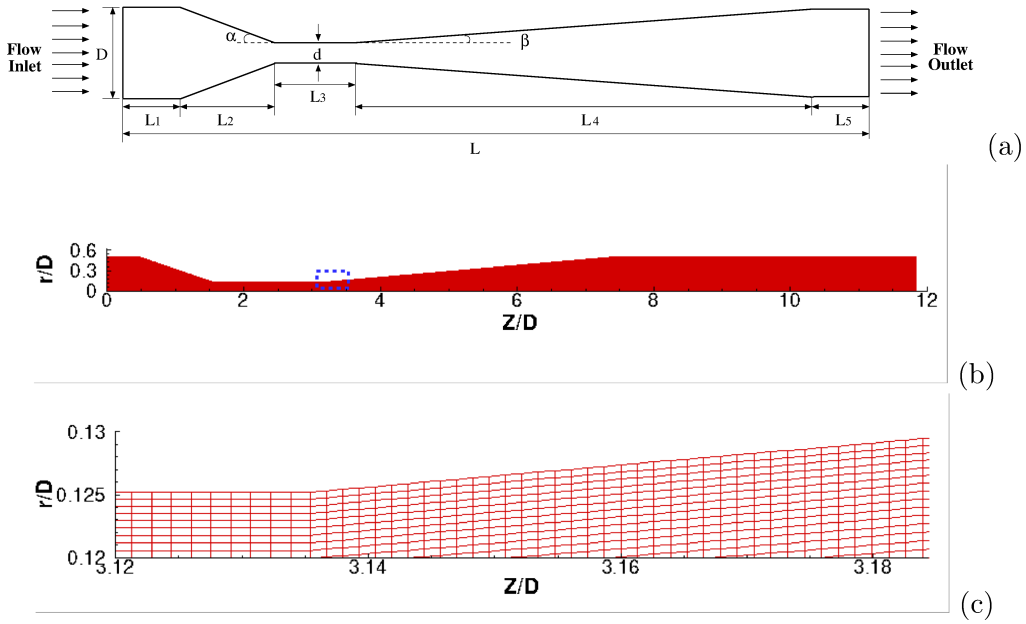

Figure 3.3: Schematic diagram of the cavitating Venturi tube - (a); full view - (b) and zoom view - (c) of the computational structured mesh (Grid−1).

$D(mm)$	$d(mm)$	$L_1(mm)$	$L_2(mm)$	$L_3(mm)$	$L_4(mm)$	$L_5(mm)$	$\alpha(^\circ)$	$\beta(^\circ)$
12.7	3.18	6	14	20	54	6	19	5

Table 3.1: Specifications of the cavitating Venturi tube.

Next, a two-phase (liquid-solid) slurry flow must be modeled numerically to validate the results and choose a suitable global model. For this purpose, the experiment by Kaushal et al. [39] is numerically replicated using a 3D model. According to the experimental setup, the horizontal pipe has a diameter of 54.9 mm and a length of 3294 mm. The multi-sized mixture of spherical glass beads with diameters of 0.125 mm and 0.44 mm with an equal mass fraction and a density of 2470 kg/m^3 are transported into the pipe with water at ambient conditions. The solid volume fraction ϕ_s is in a wide range between 0.2 and 0.4. The maximum packing limit for the solid phase is α_{max}=0.63. In the experiments, the overall pressure drop and slurry volumetric flow rate were monitored at an average slurry velocity of 2 m/s and 4 m/s. To compare the numerical results with experiments, the solid concentration measurements were conducted with a sampling probe at 3 mm above the end of the pipe, across the pipe cross−section.

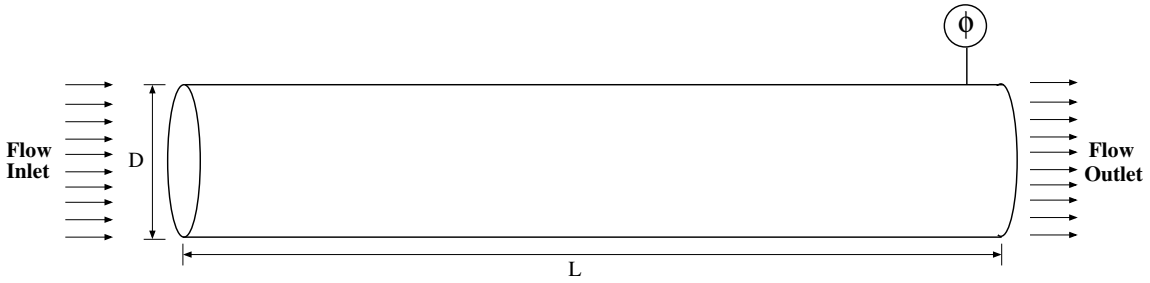

Figure 3.4: Schematic diagram of the horizontal pipe.

After we identify the appropriate Eulerian-Eulerian−based model for simulating two-phase cavitating flows in a Venturi tube and two-phase slurry flows in a pipe, this Eulerian-Eulerian model can be further implemented into the four-phase fluid flow system and validated against experimental data. In this case, an experimental setup is built (see Fig. 3.2a) to investigate the behavior of four-phase flows through the cavitating Venturi tube. In this study, the water tank was replaced by a mixing tank and filled with tap water and solid particles. The tap water was used as the medium and silica particles with a volume median diameter (D_{50}) of 23 μm were used as the solid particles. An impeller driven by an adjustable agitator (IKA RW 20 digital, USA) is used to mix the water and solid particles. The impeller speed was set at 500 rpm, 700 rpm, and 900 rpm to mix solid particles with a mass concentration of 5 wt% (V_s=1.94 %), 15 wt% (V_s=6.23 %), and 30 wt% (V_s=13.9

%), respectively. The peristaltic pump (Masterflex I/P Easy-Load, Germany), which can deliver the slurry flow from 0 to 10 LPM, is placed 1.6 m ahead of the inlet of the Venturi tube.

For the measurements, the inlet pressure, P_{in} was measured using a pressure transducer (Transducers Direct TDH40, USA) with an accuracy of ± 0.4% FS. The recorded data is sent to an oscilloscope (Rigol DS1054Z, USA) in a voltage signal via a coaxial wire connection. The outlet pressure, P_{∞} remains constant and is equal to the atmospheric pressure. The slurry flow rate, Q is measured using a flow meter (Omega FLR 1001, USA) with an accuracy of ±3% FS. The flow meter was calibrated before each run in order to obtain the most accurate Venturi tube performance in the experimental measurement.

The transparent cavitating Venturi tube was designed using the computer-aided design software (CAD) and manufactured by the Formlabs Form 2 Printer equipped with Stereolithography (SLA) technology. The Venturi tube is horizontally placed in the test section between the pressure pump and the mixing tank. Fig. 3.2b and Fig. 3.2c respectively show the photographs of the cavitating Venturi tube test section and the Venturi tube used in this study. The schematic drawing of the tested Venturi tube and its specifications are shown in Fig. 3.3a and Table 3.1, respectively.

3.3 Model formulation

To model a four-phase cavitating flow, solid, liquid, vapor and air phases were treated as interacting interpenetrating continua with an Eulerian-Euerlian model. In this model the liquid is considered to be a continuous phase, while the solid, vapor and air are dispersed phases. The mass and momentum conservation equations are solved individually for each phase. The solid phase is consided to be a granular flow and the fluctuations and collisions between the particles are modeled with the the kinetic theory of granular flows (KTGF) [38]. The vapor phase and air phase are considered to be a non-granular flow and the collision between the vapor-particle is not taken into account in the simulations. Additionally, we neglect the mass transfer between solid-liquid, solid-vapor and solid-air. However to take into account the air bubbles entrapped on the small unwetted cracks of the solid particles we assume that the individual solid particles entrap bubbles on the surfaces. Then, we consider an idealized case in which the size of entrapped bubble (R_a) is comparable to the size of the crevice mouth. The range of crevice mouth size can be identified experimentally by using the scanning electron microscope (SEM). After we obtain the size of air bubble, the pressure inside the air bubble (P_a) can be calculated through the Laplace's equation. Finally, the calculated P_a can be used on the mass transfer between liquid-air phases.

The turbulence is described by the standard k-ϵ turbulence with enhanced wall treat-

ment. The mixture turbulence model, which is applicable for stratified multiphase flows, is utilized to estimate turbulent quantities (turbulent kinetic energy, turbulent dissipation rate, and turbulent viscosity) for each phase. The turbulent dispersion between the solid-liquid, vapor-liquid and air-liquid interfaces are estimated using the theory developed by Simoning & Viollet [40]. The Schiller-Naumann drag sub-model [41] is used for liquid-vapor, liquid-air, and vapor-air interfaces, and the Syamlal-O'Brien [42] drag sub-model is applied to solid-liquid, solid-vapor and solid-air interfaces.

In ANSYS Fluent, three most popular cavitation models are: Singhal et al. model [43], Schnerr-Sauer et al model [44], and Zwart et al. model [45]. The effect of non-condensable gas are considered in Singhal et al. model but not in Schnerr-Sauer et al model and Zwart et al. model. However, the main limitation of Singhal et al. model is that this cavitation model cannot be used in Eulerian-Eulerian multiphase model [38]. Thus, the mass transfer between liquid-vapor phases and liquid-air phases is described based on the Schnerr-Sauer cavitation model [44]. The equation for the vapor or air volume fraction can be described as [44]:

$$\frac{\partial}{\partial t}\left(\alpha_{v,a}\rho_{v,a}\right) + \nabla \cdot \left(\alpha_{v,a}\rho_{v,a}\vec{v}_{v,a}\right) = R \tag{3.1}$$

where $\alpha_{v,a}$ is the volume fraction of the vapor phase or air phase, $\rho_{v,a}$ is the vapor or air density, ρ_l is the liquid density and $\vec{v}_{v,a}$ is the vapor phase or air phase velocity. The phase change due to cavitation is governed by the net mass transfer rate R (=R_e-R_c) on the right side of Eq.3.1. R_e and R_c are the mass transfer source terms connected to the growth (evaporation) and collapse (condensation) of bubbles in the cavitating flows. The phenomena such as, collision and coalescence are not taken into account in this study.

The net mass transfer rate can be written as follows [44]:

$$R = \frac{\rho\rho_l}{\rho_m}\frac{D\alpha}{Dt} \tag{3.2}$$

where ρ_m is the mixture density and t is the time.

The volume fraction of the vapor phase or air phase can be represented as [44]:

$$\alpha = \frac{V_{v,a}}{V_m} = \frac{n_b \frac{4}{3}\pi R_b^3}{1 + n_b \frac{4}{3}\pi R_b^3} \tag{3.3}$$

where $V_{v,a}$ is the volume of the vapor phase or air phase inside the volume of the mixture V_m, R_b is the radius of the vapor- or air-filled bubble, and n_b is the bubble number density. The bubble number density n_b is defined as number of cavitation nuclei per volume of liquid and it is the only parameter which needs be determined. In this study, the bubble number density is assumed to hold a constant value of $10^{13}/\mathrm{m}^3$ as previously used by researchers

[46, 47, 48].

Based on the simplified Rayleigh-Plesset equation [2], the bubble dynamics equation can be expressed as [2]:

$$\frac{DR_b}{Dt} = \sqrt{\frac{2}{3}\frac{P_{v,a} - P_l}{\rho_l}} \tag{3.4}$$

where $P_{v,a}$ is the vapor pressure or the air pressure and P_l is the liquid pressure.

After Eq. 3.3 and Eq. 3.4 are inserted into Eq. 3.2, the final form of the equation describing the process of evaporation R_e and condensation R_c can be obtained [44]:

When $P_{v,a} \geq P_l$,

$$R_e = \frac{\rho_{v,a}\rho_l}{\rho_m}\alpha_{v,a}(1-\alpha_{v,a})\frac{3}{R_b}\sqrt{\frac{2}{3}\frac{P_{v,a} - P_l}{\rho_l}} \tag{3.5}$$

When $P_{v,a} \leq P_l$,

$$R_c = \frac{\rho_{v,a}\rho_l}{\rho_m}\alpha_{v,a}(1-\alpha_{v,a})\frac{3}{R_b}\sqrt{\frac{2}{3}\frac{P_l - P_{v,a}}{\rho_l}} \tag{3.6}$$

The radius of bubbles can be computed by:

$$R_b = (\frac{\alpha_{v,a}}{1-\alpha_{v,a}}\frac{3}{4\pi n_b})^{\frac{1}{3}} \tag{3.7}$$

The saturation vapor pressure, P_v is the pressure of a vapor when it is in equilibrium with the liquid phase and remains constant with a value of 2338 Pa at 20°C. The saturated vapor pressure is calculated based on the Antoine equation [49]:

$$LogP_v = A - \frac{B}{T+C} \tag{3.8}$$

where T is the temperature of the water and A, B, and C are substance-specific constants. In the temperature range 1°C and 99°C, the values of A, B, and C are 8.07131, 1730.63, and 233.426, respectively. The governing equations for the four-phase cavitating system is presented in Table 3.2. The governing equations for the two-phase cavitating system and two-phase slurry system can be obtained in ANSYS FLUENT Theory Guide [38].

At the inlet, a uniform velocity is used for the solid and liquid with a value of 0.01 to 1.2 m/s. The specified inlet solid volume fraction is 0.0194 (5 wt%), 0.0623 (15 wt%), and 0.1390 (30 wt%). At the outlet of the Venturi, the atmospheric pressure boundary condition is used. The boundary conditions for turbulence are specified with uniform

value: 10% for turbulence intensity and 10 for the turbulence viscosity ratio. At the wall, a specularity coefficient with a value of 0.451 and a particle-particle restitution coefficient with a value of 0.9 are applied in the simulation. The wall boundary conditions are no-slip boundary conditions for the liquid, vapor and air phases. The boundary conditions for each multiphase system are shown in Table 3.3.

The phase-coupled SIMPLE algorithm is used for pressure-velocity coupling with second-order discretization applied to the momentum and turbulent quantities in each instance. The QUICK scheme [38] was used to ensure convergence in terms of discretization of the volume fraction. The details of the models and schemes used in the two-phase cavitating system, two-phase slurry system, and four-phase cavitating system are given in Tables 3.4, 3.5, and 3.6, respectively. The CFD simulations is calculated using a transient condition. To avoid instability, a small constant time step of 10^{-5} s was used for each case, and the number of inner iterations at each time step was set to 30. The maximum value of the non-dimensional wall distance y^+ near the walls is about 3.45. The physical properties for each system are specified in Table 3.7. It should be noted that each phase are considered to be incompressible flows since the value of Mach number is much less than 1.0 in this multiphase flows study.

Name	*Model/ Scheme Name*
Multiphase Flow	Eulerian-Eulerian [38]
Volume Fraction Parameters	Implicit Scheme [38]
Viscous Model	RANS-k-ω model [38]
Cavitation Model	Schnerr-Sauer model [44], [38]
Drag Model	Schiller-Naumann [41], [38]
Pressure-Velocity Coupling	Coupled Scheme [38]
Spatial Discretization-Gradient	Least Squares Cell Based [38]
Spatial Discretization-Momentum	2nd Order Upwind [38]
Spatial Discretization-Volume Fraction	QUICK [50]
Spatial Discretization-Turbulence	k-ω 2nd Order Upwind [38]
Transient Formulation	First Order Implicit

Table 3.4: List of different models and schemes used in Eulerian-Eulerian model for modeling two-phase (liquid-vapor) cavitating flows.

Volume of phase	$V_q = \int_v \alpha_q dv$
Volume fraction balance	$\sum_{q=1}^{n} \alpha_q = 1$
Effective density	$\hat{\rho_q} = \alpha_q \rho_q$
Continuity equation	$\frac{\partial}{\partial t}(\alpha_q \rho_q) + \nabla \cdot (\alpha_q \rho_q \vec{v}_q) = \sum_{q=1}^{n}(R_{pq} - R_{qp})$
Momentum balance	$\frac{\partial}{\partial t}(\alpha_q \rho_q \vec{v}_q) + \nabla \cdot (\alpha_q \rho_q \vec{v}_q \vec{v}_q) = -\alpha_q \nabla p + \nabla \cdot \overline{\overline{\tau}_q} + \alpha_q \rho_q \vec{g}$ $+ \sum_{p=1}^{n}(\vec{R}_{pq} + R_{pq}\vec{v}_{pq} - R_{qp}\vec{v}_{qp})$
Solid phase stress tensor	$\overline{\overline{\tau}_q} = \alpha_q \mu_q \left(\nabla \vec{v}_q + \nabla \vec{v}_q^T\right) + \alpha_q \left(\lambda_q - \frac{2}{3}\mu_q\right) \nabla \cdot \vec{v}_q \overline{\overline{I}}$
Interphase force	$\sum_{p=1}^{n} \vec{R}_{pq} = \sum_{p=1}^{n} K_{pq}(\vec{v}_p - \vec{v}_q)$
Schiller-Naumann drag model	$K_{pq} = \frac{\alpha_q \alpha_p \rho_p f}{\tau_p}$; $\tau_p = \frac{\rho_p d_p^2}{18\mu_q}$; $f = \frac{C_D Re}{24}$; $Re = \frac{\rho_q \lvert\vec{v}_p - \vec{v}_q\rvert D_p}{\mu_q}$
	When $Re \leq 1000, C_D = 24(1 + 0.15Re^{0.687})/Re$
	When $Re > 1000, C_D = 0.44$
Syamlal-O'Brien drag model	$K_{sl} = \frac{\alpha_s \rho_s f}{\tau_s}$; $\tau_s = \frac{\rho_s d_s^2}{18\mu_l}$
	$f = \frac{C_D Re_s \alpha_l}{24}$; $Re_s = \frac{\rho_l d_s \lvert\vec{v}_s - \vec{v}_l\rvert}{\mu_l}$; $C_D = (0.63 + \frac{4.8}{\sqrt{Re_s/v_{r,s}}})^2$
Solid pressure	$p_s = \alpha_s \rho_s \theta_s + 2\rho_s(1 + e_{ss})\alpha_s^2 g_{0,ss}\theta_s$
Radial distribution function	$g_{0,ss} = \left[1 - (\alpha_s/\alpha_{s,max})^{\frac{1}{3}}\right]^{-1}$
Collisional energy dissipation	$\gamma_{\theta_s} = \frac{12(1-e_{ss}^2)g_{0,ss}}{d_s \pi^{0.5}} \rho_s \alpha_s^2 \theta_s^{1.5}$
Kinetic energy transfer	$\phi_{ls} = -3 \cdot K_{l,s}\theta_s$
Solid shear viscosity	$\mu_s = \mu_{s,col} + \mu_{s,kin} + \mu_{s,fr}$
Collisional viscosity	$\mu_{s,col} = \frac{4}{5}\alpha_s \rho_s d_s g_{0,ss}(1 + e_{ss})\left(\frac{\theta_s}{\pi}\right)^{1/2}$
Kinetic viscosity	$\mu_{s,kin} = \frac{10\rho_s d_s \sqrt{\theta_s \pi}}{96\alpha_s(1+e_{ss})g_{0,ss}}\left[1 + \frac{5}{4}g_{0,ss}\alpha_s(1 + e_{ss})\right]^2$
Frictional viscosity	$\mu_{s,fr} = \frac{p_s sin\phi}{2\sqrt{I_{2D}}}$
Bulk viscosity	$\lambda_s = \frac{4}{3}\alpha_s \rho_s d_s g_{0,ss}(1 + e_{ss})\left(\frac{\theta_s}{\pi}\right)^{1/2}$
Granular temperature	$\Theta_q = \frac{1}{3}(\vec{v_q}'^2)$
Standard k-ε mixture model	$\frac{\partial}{\partial t}(\rho_m k) + \nabla(\rho_m \vec{v}_m k) = \nabla \cdot (\frac{\mu_{t,m}}{\sigma_k}\nabla k) + G_{k,m} - \rho_m \varepsilon$
	$\frac{\partial}{\partial t}(\rho_m \varepsilon) + \nabla(\rho_m \vec{v}_m \varepsilon) = \nabla \cdot (\frac{\mu_{t,m}}{\sigma_\varepsilon}\nabla \varepsilon) + \frac{\varepsilon}{k}(C_{1\varepsilon}G_{k,m} - C_{2\varepsilon}\rho_m \varepsilon)$
	$\rho_m = \sum_{q=1}^{n} \alpha_q \rho_q$, $\vec{v}_m = (\sum_{q=1}^{n} \alpha_q \rho_q \vec{v}_q)/(\sum_{i=q}^{n} \alpha_q \rho_q)$
	$\mu_{t,m} = \rho_m C_\mu \frac{k^2}{\omega}$, $G_{k,m} = \mu_{t,m}(\nabla \vec{v}_m + (\nabla \vec{v}_m)^T) : \nabla \vec{v}_m$
	$C_{1\varepsilon} = 1.44, C_{2\varepsilon} = 1.92, C_\mu = 0.09, \sigma_k = 1.0, \sigma_\varepsilon = 1.3$

Table 3.2: Eulerian-Eulerian model equations available in ANSYS FLUENT 16.2 which were used to model the four-phase (liquid-solid-vapor-air) cavitating flows from [38].

Flow	Surface	Boundary condition	Input
Two-phase cavitating flows	Inlet	Pressure inlet	P_{in}=110000 $\sim$ 400000 Pa Turbulent intensity=10% Turbulent viscosity ratio=10
	Outlet	Pressure outlet	P_{out}=101325 Pa Turbulent intensity=10% Turbulent viscosity ratio=10
	Walls	No slip	–
Two-phase slurry flows	Inlet	Velocity inlet and phase fraction	$U_{in,w}$=0.2, 0.4 m/s; $U_{in,s}$=0.2, 0.4 m/s ϕ_w=0.8, 0.6; $\phi_{s,1}$=0.1, 0.2; $\phi_{s,2}$=0.1, 0.2 Turbulent intensity=10% Turbulent viscosity ratio=10
	Outlet	Pressure outlet	P_{out}=101325 Pa Turbulent intensity=10% Turbulent viscosity ratio=10
	Walls	Slip	Specularity coefficient=0.451 Restitution coefficient=0.9
Four-phase cavitating flows	Inlet	Velocity inlet and phase fraction	$U_{in,w}$=0.01$\sim$1.2 m/s; $U_{in,s}$=0.01$\sim$1.2 m/s ϕ_s=0.0194, 0.0623, 0.139 Turbulent intensity=10% Turbulent viscosity ratio=10
	Outlet	Pressure outlet	P_{out}=101325 Pa Turbulent intensity=10% Turbulent viscosity ratio=10
	Walls	Slip	Specularity coefficient=0.451 Restitution coefficient=0.9

Table 3.3: Boundary conditions used for CFD computations in multiphase flows study.

Name	*Model/ Scheme Name*
Multiphase Flow	Eulerian-Eulerian [38]
Volume Fraction Parameters	Implicit Scheme [38]
Viscous Model	RANS-k-ε model [38]
Drag Model	Syamlal-O'Brien[42], [38]
Granular Temperature	Algebraic [38]
Granular Viscosity	Syamlal-O'Brien [42], [38]
Granular Bulk Viscosity	Lun et al. [51], [38]
Frictional Viscosity	Johnson-et-al [52], [38]
Frictional Pressure (Pa)	Based-KTGF [53], [38]
Solid Pressure	Lun et al. [51], [38]
Radial Distribution	Syamlal-O'Brien [42], [38]
Pressure-Velocity Coupling	Phase-coupled SIMPLE Scheme [38]
Spatial Discretization-Gradient	Least Squares Cell Based [38]
Spatial Discretization-Momentum	2nd Order Upwind [38]
Spatial Discretization-Volume Fraction	QUICK [50]
Spatial Discretization-Turbulence	k-ε 2nd order Upwind [38]

Table 3.5: List of different models and schemes used in Eulerian-Eulerian model for modeling two-phase (liquid-solid) slurry flows.

Name	*Model/ Scheme Name*
Multiphase Flow	Eulerian-Eulerian [38]
Volume Fraction Parameters	Implicit Scheme [38]
Viscous Model	RANS-k-ε model [38]
Cavitation Model	Schnerr-Sauer model [44], [38]
Drag Model	Schiller-Naumann & Syamlal-O'Brien [41],[42], [38]
Granular Temperature	Algebraic [38]
Granular Viscosity	Syamlal-O'Brien [42], [38]
Granular Bulk Viscosity	Lun et al. [51], [38]
Frictional Viscosity	Johnson-et-al [52], [38]
Frictional Pressure (Pa)	Based-KTGF [53], [38]
Solid Pressure	Lun et al. [51], [38]
Radial Distribution	Syamlal-O'Brien [42], [38]
Pressure-Velocity Coupling	Phase-coupled SIMPLE Scheme [38]
Spatial Discretization-Gradient	Least Squares Cell Based [38]
Spatial Discretization-Momentum	2nd Order Upwind [38]
Spatial Discretization-Volume Fraction	QUICK [50]
Spatial Discretization-Turbulence	k-ε 2nd order Upwind [38]
Transient Formulation	First Order Implicit

Table 3.6: List of different models and schemes used in Eulerian-Eulerian model for modeling four-phase (liquid-solid-vapor-air) cavitating flows.

Flow	Material	ρ (kg/m^3)	μ $(kg/m-s)$	D (μm)
Two-phase cavitating flows	water	998.16	1.001×10^{-3}	–
	vapor	0.0173	9.727×10^{-6}	10
Two-phase slurry flows	solid-1	2470	1.789×10^{-5}	125
	solid-2	2470	1.789×10^{-5}	440
	water	998.16	1.001×10^{-3}	–
Four-phase cavitating flows	solid	2650	1.789×10^{-5}	23
	water	998.16	1.001×10^{-3}	–
	vapor	0.0173	9.727×10^{-6}	10
	air	1.2047	1.825×10^{-5}	3, 6, 10

Table 3.7: Physical properties used for CFD computations in multiphase flows study.

3.4 Validation

In order to quantify the error and uncertainty in the CFD simulations, the population standard deviations (Eq. 3.9 from [54]) were calculated to compare the experimental and numerical inlet velocities.

$$\sigma_{est}\% = \sqrt{\frac{\sum(Y_{simulation} - Y_{experiment})^2}{N}} \cdot 100 \tag{3.9}$$

where σ_{est} is the standard deviation of the estimate and $Y_{experiment}$ and $Y_{simulation}$ are the inlet velocity data for the experimental and predicted results, respectively. N is the total number of data taken into account to calculate the standard deviation. The predicted inlet velocity is calculated based on the mass-weighted average velocity at the inlet surface. The population standard deviation is a reliable approach for measuring deviation as compared to other approaches (e.g. the weight standard deviation) since this approach comes from Linear Least Squares Regression, as used in curve fitting [55].

Fig. 3.5 shows the static pressure drop as a function of the inlet velocity for Grid−1 (310000 cells) and Grid−2 (1240000 cells). To describe the cavitation activities in the two-phase cavitating flows, the Schnerr-Sauer cavitation model was applied and evaluated in this study. It can be seen from the figure that the numerical results for the pressure drop in line with the experimental data, with a clear indication of cavitation inception at an inlet velocity of 0.96 m/s. The deviations from the experimental data are 2.07% and 4.36% for Grid−1 and Grid−2, respectively, which indicates that Grid−1 is sufficient to provide accurate results at a lower computational cost. Therefore, we can confirm that the Eulerian-Eulerian approach coupled with the Schnerr-Sauer cavitation model is capable of capturing the physics of two-phase flows including liquid-vapor in cavitating Venturi tubes.

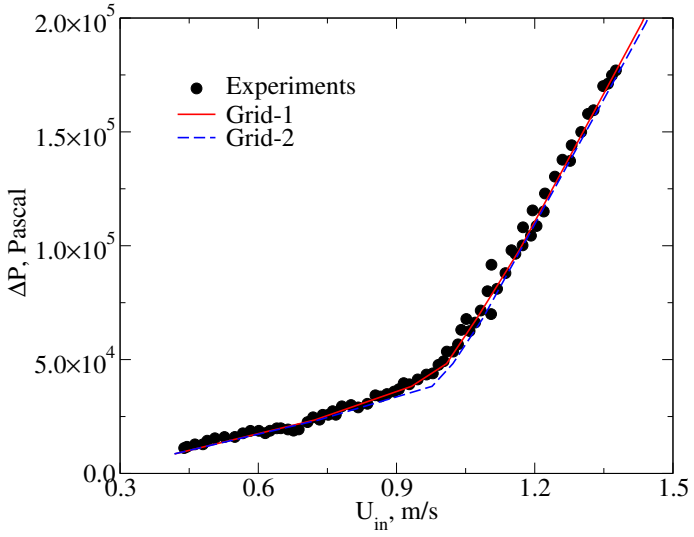

Figure 3.5: Validation of two-phase cavitating flows: experimental and simulated static pressure drop as a function of inlet velocity. Experimental measurement accuracy= ±1.7%.

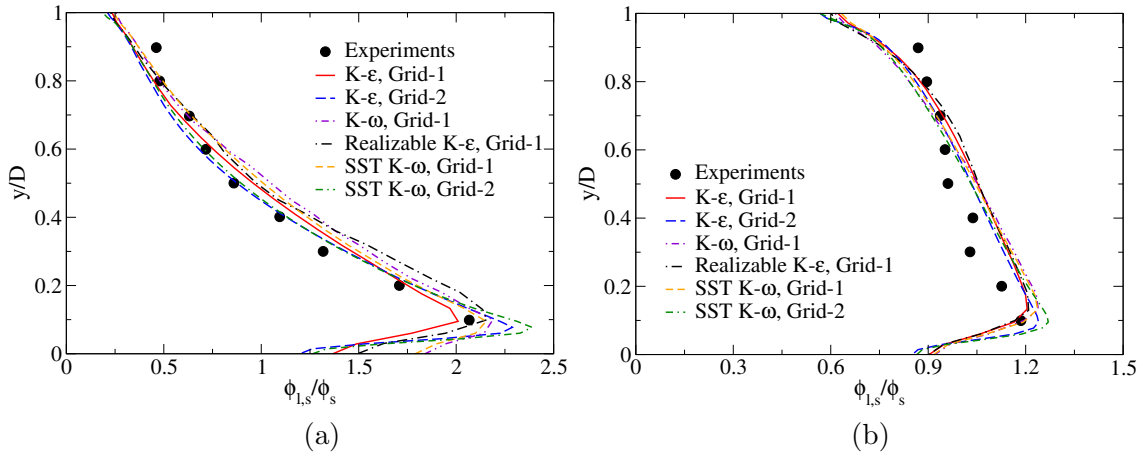

Figure 3.6: Validation of two-phase slurry flows: experimental and simulated solid concentration distribution in multi-sized slurry (D_p=125 μm and 440 μm) at (a) - U_{in}=2 m/s, Re_{in}=109598, ϕ_s=0.2; (b) - U_{in}=4 m/s, Re_{in}=219196, ϕ_s=0.4.

Figs. 3.6a and b depict experimental and simulation results concerning the distribution of mixture solid concentration along the y-coordinate at z/D=55, corresponding to inlet velocities of U_{in}=2 m/s, ϕ_s=0.2 and U_{in}=4 m/s, ϕ_s=0.4. It can be seen that the higher solid concentration is distributed along the region near the bottom wall due to the effect of gravity. A distinct change in the shape of the solid concentration profiles along the vertical plane can be observed as the inlet velocity increases from 2 to 4 m/s and the solid volume

fraction from 0.2 to 0.4. This study evaluated four different turbulence models (standard $k-\varepsilon$, $k-\omega$, Realizable $k-\varepsilon$, and SST $k-\omega$). As can be seen from Figs. 3.6a and b, all four turbulence models exhibit the same trend against the experimental data. Though the standard $k-\varepsilon$ turbulence model with enhanced wall treatment shows good agreement with the experimental data, with an averaged deviation of 8.7%, the ST $k-\omega$, $k-\omega$, and Realizable $k-\varepsilon$ turbulence models overpredict the solid concentrations in y/D=0 to 0.4, with averaged deviations of 9.53%, 10.69% and 10.78%, respectively. The results suggests that the standard $k-\varepsilon$ turbulence model with enhanced wall treatment is more accurate at predicting slurry flows than the other turbulence models. Two sets of grids from the standard $k-\varepsilon$ turbulence model and SST $k-\omega$ turbulence model are used to study how the mesh resolution influences the numerical results. As can been seen from Figs. 3.6a and b, both grids show a consistent trend against the experimental data in the upper part of the pipe (y/D=0.2 to 1). If the grid is refined from 456000 cells to 3648000 cells, the numerical results deviate considerably from the experimental measurements in the bottom near-wall region (y/D=0 to 0.2). Thus, Grid−1 produces a good agreement with experimentally measured solid concentration profiles.

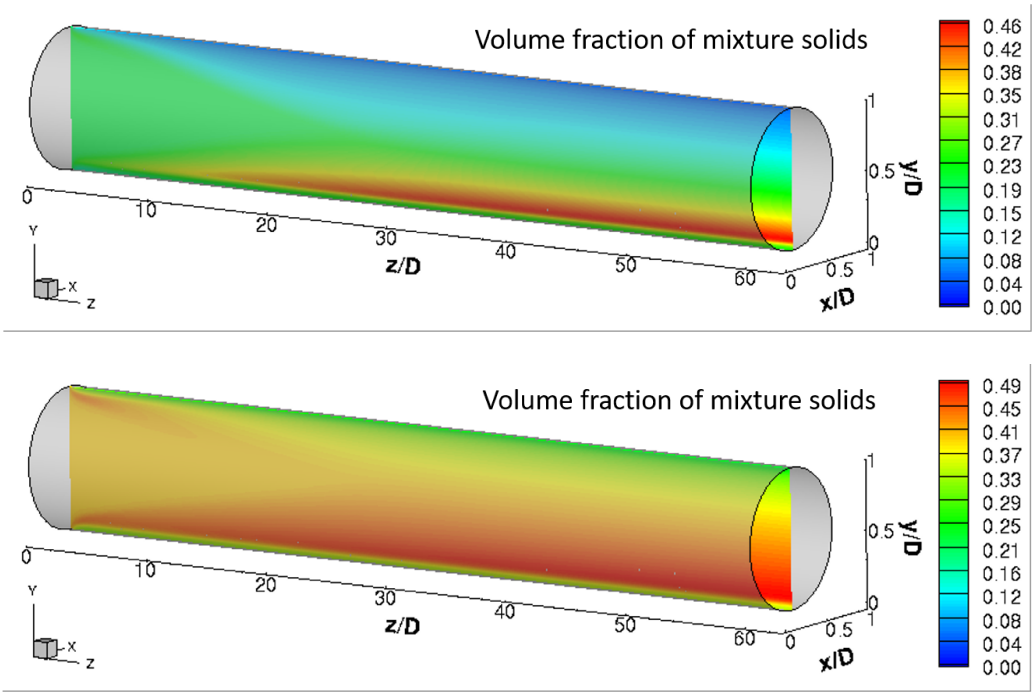

Figure 3.7: Solid volume fraction distribution along z/D-coordinate at x/D=0.5 for (a) - U_{in}=2 m/s, Re_{in}=109598, ϕ_s=0.2, and (b) - U_{in}=4 m/s, Re_{in}=219196, ϕ_s=0.4.

Fig. 3.7 shows the snapshots of a slice of the 3D contour plot of the solid volume

fraction along the z/D-coordinate at x/D=0.5. The higher solid concentration is mainly distributed along the region of the bottom wall, with a maximum value of 0.46 and 0.49, after the onset of a fully developed flow at z/D=30. Fig. 3.8 shows the contours of the local solid volume fraction, velocity and turbulent viscosity ratio in the vertical plane at z/D=55. When the results from U_{in}=2 m/s, ϕ_s=0.2 and U_{in}=4 m/s, ϕ_s=0.4 were compared, it was noted that the increase of inlet flow rate and solid concentration causes the increase of solid concentration, flow velocity and turbulence viscosity ratio. The solid concentration and turbulent viscosity ratio in the lower-half section (y/D=0 to 0.5) are higher than those in other sections of the pipe, which suggests that the higher solid concentration has a positive effect on turbulence phenomena.

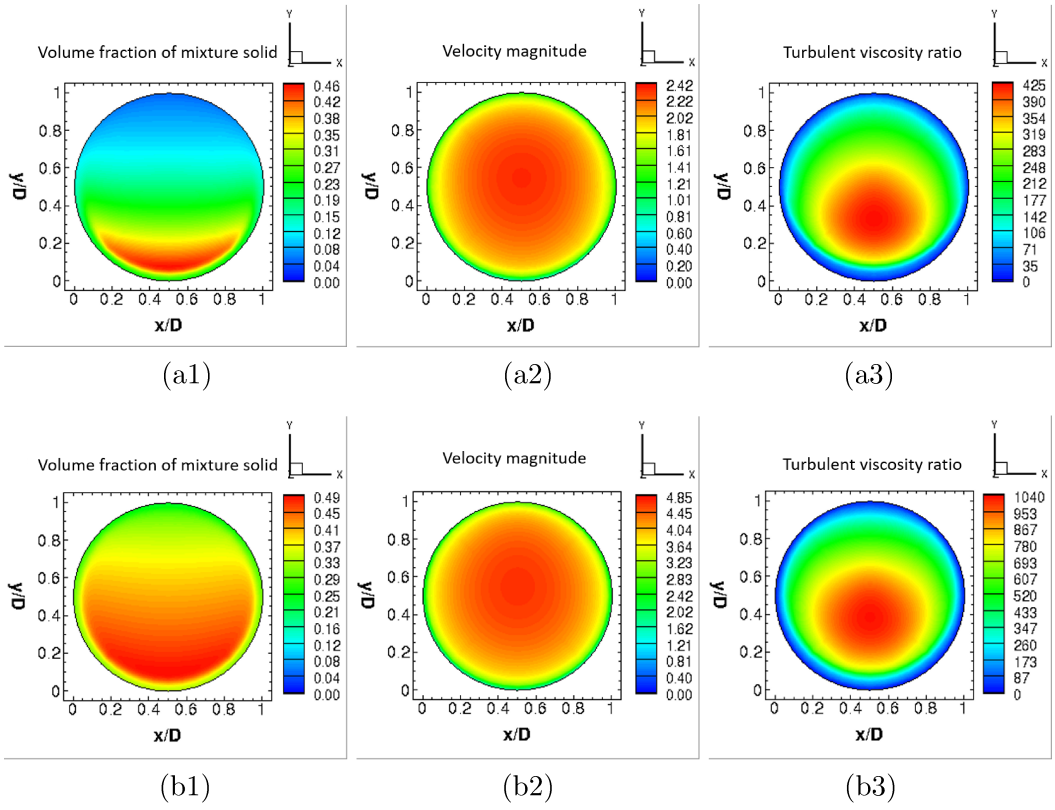

Figure 3.8: Contour plots for (a) - U_{in}=2 m/s, Re_{in}=109598, ϕ_s=0.2 and (b) - U_{in}=4 m/s, Re_{in}=219196, ϕ_s=0.4 at z/D=55: (1) - solid volume fraction, (2) - velocity and (3) - turbulent viscosity ratio $\frac{\mu_t}{\mu_0}$.

3.5 Results and discussions

To analyse the results, we use the cavitation number, σ, which is the most fundamental non-dimensional parameter in the Venturi tube used to predict the occurrence of cavitation. It is defined as the ratio of the pressure difference between the throat and downstream sections of the cavitating Venturi tube to the kinetic head at the throat. The inlet Reynolds number, Re_{in}, is the non-dimensional ratio of the inertial force to the viscous force. It measures viscous stresses in the fluid field. The pressure change is usually characterized by the pressure loss coefficient, K. The formulations of the cavitation number (σ), pressure loss coefficient (K), and inlet Reynolds number (Re_{in}) are expressed as follows [2].

$$\sigma = \frac{P_\infty - P_v(T_\infty)}{\frac{1}{2}\rho_l U_{th}^2} \tag{3.10}$$

$$K = \frac{(P_{in} - P_\infty)_{static}}{\frac{1}{2}\rho_l U_{in}^2} \tag{3.11}$$

$$Re_{in} = \frac{\rho_l U_{in} D}{\mu_l} \tag{3.12}$$

where P_∞ is the fully recovered static downstream pressure, P_{in} is the static upstream pressure and P_v is the vapor pressure of the liquid at the reference temperature (T_∞). ρ_l is the density of the liquid, and U_{in} and U_{th} are the flow velocity upstream of and at the throat of the Venturi tube, respectively. D is the inlet pipe diameter, and μ_l is the dynamic viscosity of the liquid.

Based on the study of two-phase cavitating flows and two-phase slurry flows, we can confirm that the Eulerian-Eulerian multiphase model is capable of satisfactorily predicting the flow physics of multiphase flows. In this view, the Eulerian-Eulerian multiphase model is applied to numerically solve the four-phase fluid flow system. One major challenge in the prediction of four-phase flows using the CFD approach is simulating the stabilized air bubbles on the small unwetted cracks and crevices on the surface of solid particles. To take this effect into account in the CFD model, we assume that individual solid particles entrap stablized air bubbles on their surface. As can be seen from Fig. 3.9, the solid particles are added into the water tank, and a pre-existing air bubble is found inside a pit on the particle surface after mixing. The size of the air bubble is related to the pressure balance in an equilibrium situation (Laplace's law). Since the air bubbles are usually stable, the water surface is convex towards the air and the curvature of the air bubble interface is negative [25].

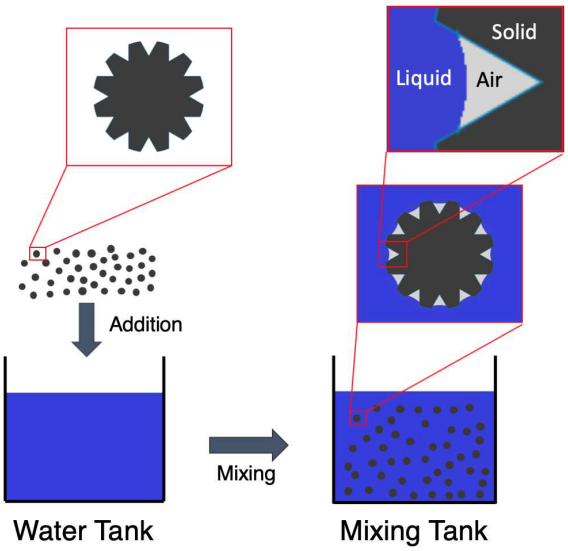

Figure 3.9: Principle sketch of the entrapped air bubbles in the crevices on the surface of particle.

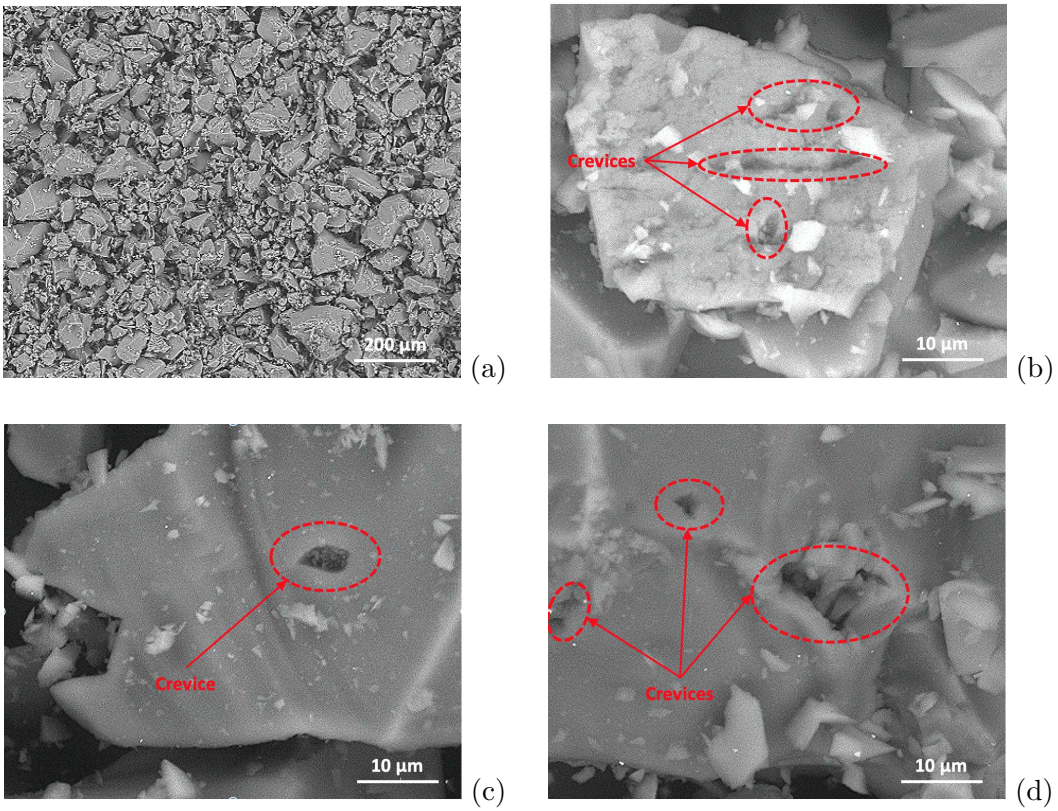

Figure 3.10: SEM images of silica microparticles: (a) - low magnification (×50); (b-d) - high magnification (×1000).

To determine the size of the air bubbles trapped in the crevices on the surface of particles, we considered an idealized case in which the size of the entrapped bubble is comparable to the size of the crevice mouth, for simplicity. In this case, it is critical to evaluate the surface patterns of the particles first. A scanning electron microscope (SEM, Zeiss EVO LS15, Germany) with an acceleration voltage of 25 kV is used to observe the microstructures of the silica particles. As can be seen from Fig. 3.10, SEM images of silica particles have been taken at two different magnifications ($\times$50 and $\times$2000). Low-magnification SEM images (Fig. 3.10a) shows that the silica particle has various shapes with defined corners and edges. The particle diameter of the sample is analyzed using the Mastersizer 3000 laser diffraction particle size analyzer (Malvern Panalytical, Canada). The results indicate that the volume median diameter of D_{50} is about 23 μm. Figs. 3.10b, c, and d present detailed features of the microstructures on the silica particles. Noticeable micro-scale crevices can be observed on the surface of the silica particles. The size of the crevices varies from 2 to 10 μm. Accordingly, the size of the entrapped air bubbles is considered in a range between 2 and 10 μm in diameter. In order to estimate the specific air bubble size under different solid mass concentrations, we proposed a new correction to the air bubble size based on the solid mass concentration. As we know, the solid particle collision rate rose with increasing slurry concentration in the cavitating Venturi tube, causing an improvement in bubble coalescence efficiency on the crevices and the concave surfaces of the solid particles. Actually, as the fluid flows through the throat section, the reduction in the local pressure leads to the rapid growth of entrapped bubbles. Meanwhile, multi-particle collision is more frequently encountered in the throat section, playing a significant role in intensifying the bubble coalescence. The highly localized, large-amplitude shock waves associated with the cavitation bubble collapse is another possible reason of the increase of the average air bubble size. The micro-jets can break the particle into small size and increase its surface area due to the powerful forces created by each bubble in a cavitation zone. As a result, the average size of the entrapped air bubble increases as the size of the crevices increases. Thus, this simple engineering approach that associates the variations of the air bubble size with the changes in the solid mass concentration allows us to solve the four-phase cavitating flow problem using the commercial CFD software ANSYS FLUENT. Based on the size range of the crevices on the surface of the particles, the air bubbles are assumed to be R_b=1.5 μm, 3 μm and 5 μm in size for solid mass concentrations of 5 wt% (V_s=1.94 %), 15 wt% (V_s=6.23 %), and 30 wt% (V_s=13.9 %), respectively. The pressure inside the air bubble can be calculated for a specific bubble radius based on Laplace's equation [25]:

$$P_a + P_v = P_l - \frac{2\gamma}{R_b} \tag{3.13}$$

where P_v is the saturated vapor pressure (=2338 Pa at 20°C), P_l is the liquid pressure outside a bubble (=1 atm), γ is the liquid/vapor surface tension coefficient (=0.07275 N/m at 20°C), and R_b is the radius of the air bubble. For air bubble sizes of R_b=1.5 μm, 3 μm and 5 μm, the pressure inside the air bubbles, P_a is calculated to be 1987, 50487 and 69887 Pa, respectively. As a result, these specified values of P_a were implemented in the Schnerr-Sauer cavitation model to describe the mass transfer process between the liquid phase and the air phase.

W_s (wt %)	5	15	30
V_s (%)	1.94	6.23	13.9
R_b (μm)	1.5	3	5
P_a (Pa)	1987	50487	69887

Table 3.8: Air bubble pressure produced for various air bubble sizes.

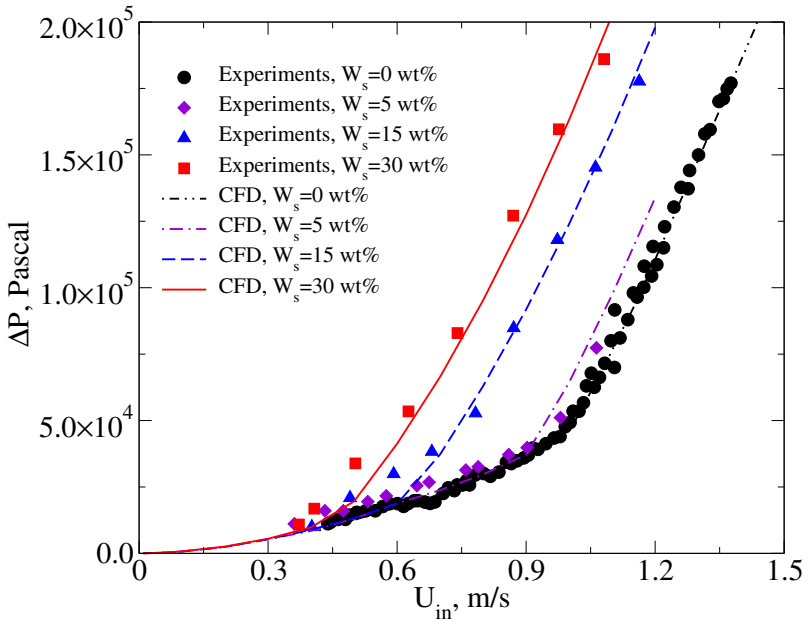

Figure 3.11: Validation of four-phase cavitating flows: experimental and simulated static pressure drop as a function of inlet velocity for different solid mass concentrations. Experimental measurement accuracy= ±1.7%.

To validate the numerical results obtained in the framework of the Eulerian-Eulerian model, the simulations were carried out of an axisymmetric Venturi tube, as shown in Fig. 3.3a. The Venturi tube considered has the following geometric parameters: D/d=4, L/d=6.29, α=19°, and β=5°. Fig. 3.11 shows the relationship between the pressure drop and the inlet velocity for both the two-phase and four-phase cavitating flows. Three solid

mass concentrations are considered in the current work to illustrate the effect of the solid mass concentrations on the flow characteristics and the generation of cavitation. As can be seen from the figure, both the numerical and the experimental results exhibit a gradually increasing trend in the inlet velocity, with an ascending pressure drop before the onset of cavitation in all cases. After the cavitation phenomenon appears, the presence of cavitation bubbles in the throat section produces an effect: the blocking of the flow, which results in a significant decrease in the inlet velocity. The simulation results fit closely with the experimental data in all cases. The deviations from the experimental data are 2.07%, 4.49%, 5.51% and 8.07% for solid mass concentrations of 0 wt% , 5 wt%, 10 wt% and 30 wt%, respectively. From the profile, the cavitation inception can be observed at U_{in}=0.9 m/s, U_{in}=0.6 m/s, and U_{in}=0.4 m/s for the Venturi tube with W_s=5 wt% (V_s=1.94 %), W_s=15 wt% (V_s=6.23 %), W_s=30 wt% (V_s=13.9 %), respectively. At a fixed pressure drop value, the value of the inlet velocity displays a slightly decrease in the 5 wt% slurry flow as compared to the 0 wt% slurry flow (liquid-vapor flow). As the solid mass concentrations increases from 5 to 30 wt%, an obvious decline in the inlet velocity can be observed. The high concentration of solids results in intensive particle-particle and particle-wall friction in the throat region, so the velocity in this region is lower than those in the same region with a low solid mass concentration.

Fig. 3.12 presents numerical analysis results with respect to the solid mass concentration, employing different dimensionless parameters (the inlet Reynolds number Re_{in}, the pressure loss coefficient K, the cavitation number σ, the vapor volume fraction ϕ_v, and the air volume fraction ϕ_a). Fig. 3.12a shows the pressure loss coefficient, K, as a function of the inlet Reynolds number, Re_{in}, for different solid mass concentrations under cavitational and non-cavitational conditions. The characteristic curve in this profile is found to have two distinct stages, separated by an inflection point. This inflection point is labelled the critical inlet Reynolds number Re_c, which indicates the inception of cavitation. In the first stage ($Re_{in}<Re_c$), the characteristic curves for cavitation cases and non-cavitation cases overlap and have decline briefly. In the second stage ($Re_{in}>Re_c$), all curves fall together further for non-cavitation cases, while the value of K sees a sharp ascent for the cavitation cases. This phenomenon is expected, since the appearance of cavitation bubbles in the Venturi tube reduces the inlet velocity and further leads to a decrease in the inlet Reynolds number. In addition, the value of Re_c decreases from 11391 to 5063 as the solid mass concentration increases from 5 wt% (V_s=1.94 %) to 30 wt% (V_s=13.9 %). This suggests that the higher solid mass concentration causes an early cavitation inception in a Venturi tube.

Figs. 3.12b and c present the relationship between the volume-averaged volume fraction of the vapor, ϕ_v, the volume-averaged volume fraction of the air, ϕ_a, and the cavitation number, σ, for various solid mass concentrations. From the profiles, the cavitation inception

appears early, from σ=0.98 to σ=3.35 for vapor-induced cavitation and from σ=0.98 to σ=4.35 for gas-induced cavitation, with an increase in the solid mass concentration from 5 wt% (V_s=1.94 %) to 30 wt% (V_s=13.9 %). This further confirms that the cavitation inception appears at various times under the influence of the solid mass concentration. As the cavitation number decreases from 4.5 to 0.1, both the vapor volume fraction and air volume fraction exhibit an almost linearly increasing trend from 1×10^{-5} to 2×10^{-1}.

Figs. 3.12d and e plot the numerical results of the volume-averaged volume fraction of the vapor, ϕ_v, and the volume-averaged volume fraction of the air, ϕ_a, as a function of the pressure loss coefficient, K, respectively. As indicated in Figs. 3.12d and e, the vapor volume fraction and air volume fraction decreases step by step until a notable reduction occurs at the critical pressure loss coefficient, K_c, indicating that the cavitation inception appears at K_c with a value of 92 (W_s=5 wt% or V_s=1.94 %), 152 (W_s=15 wt% or V_s=6.23 %), and 157 (W_s=30 wt% or V_s=13.9 %). In addition, we found that the solid mass concentration plays a significant role in the power consumption. After the onset of cavitation (K>K_c), the pressure loss coefficient K of the case with a higher solid mass concentration is larger than that with a lower solid mass concentration, with the same-level vapor or air volume fraction. This phenomenon is expected, since particle-particle and particle-wall friction increases together with the increased particle concentration at the same velocity. A higher friction corresponds to a relatively large pressure drop; thus, a significant power consumption is required for the fluid flow with a higher solid mass concentration.

A further comparison is presented in Figs. 3.12f and g with respect to the volume-averaged volume fraction of vapor and air as the function of the inlet Reynolds number, Re_{in} for three solid mass concentrations. From the profiles, the solid mass concentration is clearly seen to have a significant influence on the production of vapor and air bubbles. It can be seen that different solid mass concentrations share the same increasing tendency in terms of the vapor and air volume fraction as Re_{in} increases from 5000 to 16000. At a fixed value of Re_{in}, the cavitating Venturi tube with W_s=30 wt% (V_s=13.9 %) gives a higher value of ϕ_v and ϕ_a while that with W_s=5 wt% (V_s=1.94 %) shows a lower value of ϕ_v and ϕ_a. Raising the solid mass concentration from 5 wt% (V_s=1.94 %) to 30 wt% (V_s=13.9 %) generally increases the number of entrapped air bubbles on the cracks or crevices of particles' surface. As a consequence, the higher solid mass concentration is a means of intensifying the cavitation yield.

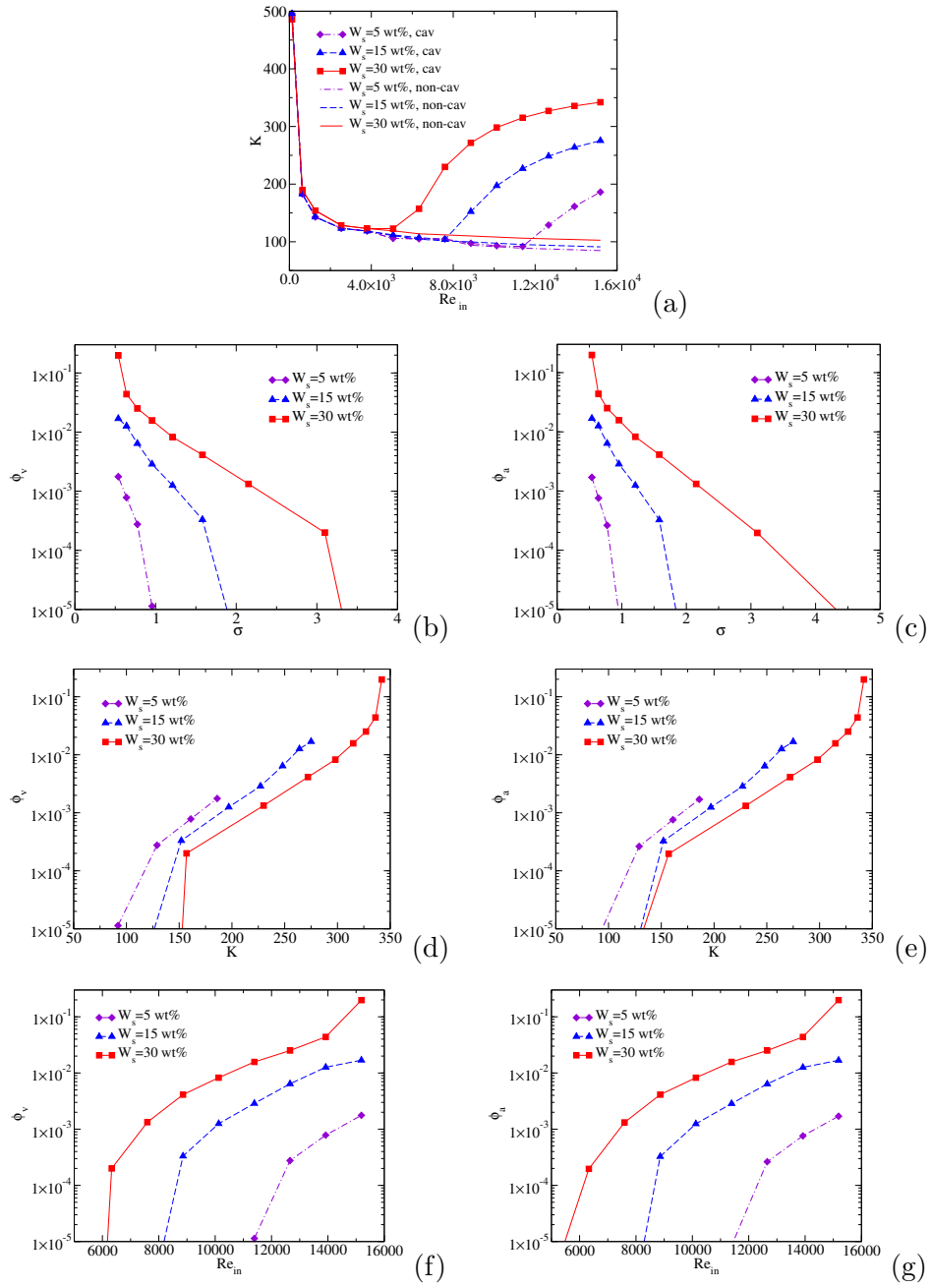

Figure 3.12: Integral characteristics predicted numerically for W_s=5%, 15% and 30% (V_s=1.94 %, 6.23 %, and 13.9 %): (a) - pressure loss coefficient as a function of inlet Reynolds number; (b) - volume-averaged vapor volume fraction as a function of cavitation number; (c) - volume-averaged air volume fraction as a function of cavitation number; (d) - volume-averaged vapor volume fraction as a function of pressure loss coefficient; (e) - volume-averaged air volume fraction as a function of pressure loss coefficient; (f) - volume-averaged vapor volume fraction as a function of inlet Reynolds number; (g) - volume-averaged air volume fraction as a function of inlet Reynolds number.

Fig. 3.13 presents axial profiles of fluid characteristics along r/D near the outlet of the throat section (z/D=3) for the four-phase cavitating flows at an inlet velocity of U_{in}=1 m/s and Re=12656. The profiles are plotted at several solid mass concentrations (W_s=5 wt% (V_s=1.94 %), 15 wt% (V_s=6.23 %), and 30 wt% (V_s=13.9 %)). As shown in Fig. 3.13a, all the solid mass concentrations predict the same flow velocity distribution along r/D. There is a higher flow velocity in the core region (r/D=0 to 0.09) and a lower flow velocity near the upper wall region (r/D=0.09 to 0.125) for all solid mass concentrations. This can be explained by the blockage effect produced by the significant number of cavitation bubbles near the wall region.

Figs. 3.13b and c depict the vapor volume fraction and air volume fraction profiles along the r/D axis. The slurry flow with 5 wt% solid mass concentration (V_s=1.94 %) predicts the same amount of vapor volume fraction (ϕ_v=0.01) and air volume fraction (ϕ_a=0.06) along the r/D axis. Meanwhile, the slurry flow with 15 wt% (V_s=6.23 %) and 30 wt% (V_s=13.9 %) solid mass concentrations shows an increasing trend across the r/D axis. Higher vapor volume fractions and air volume fractions can be observed near the wall region (r/D=0.09 to 0.125), which further confirms that there is an intensive decrease in the flow velocity due to the presence of cavitation bubbles.

Fig. 3.13d shows the distribution of the solid volume fraction along the r/D axis. As r/D increases from 0 to 0.1252, the solid volume fraction predicted in all cases exhibits a downwards trend. The trend changes more intensively as the solid mass concentration increases from 5 wt% (V_s=1.94 %) to 30 wt% (V_s=13.9 %). Fig. 3.13e reveals that the turbulence viscosity ratio is affected by the variation in the solid mass concentrations in the range between 5 wt% and 30 wt%. In particular, the turbulence viscosity ratio predicted at a higher solid mass concentration (W_s=30%) is slightly higher than those calculated at a lower solid mass concentration (W_s=5%). As r/D continues to increase from 0.09 to 0.1252, this trend becomes less obvious. This indicates that the presence of a higher solid volume fraction generates strong turbulence in the center region (r/D=0 to 0.09), while weak turbulence appears close to the wall region where the cavitation activities are significant.

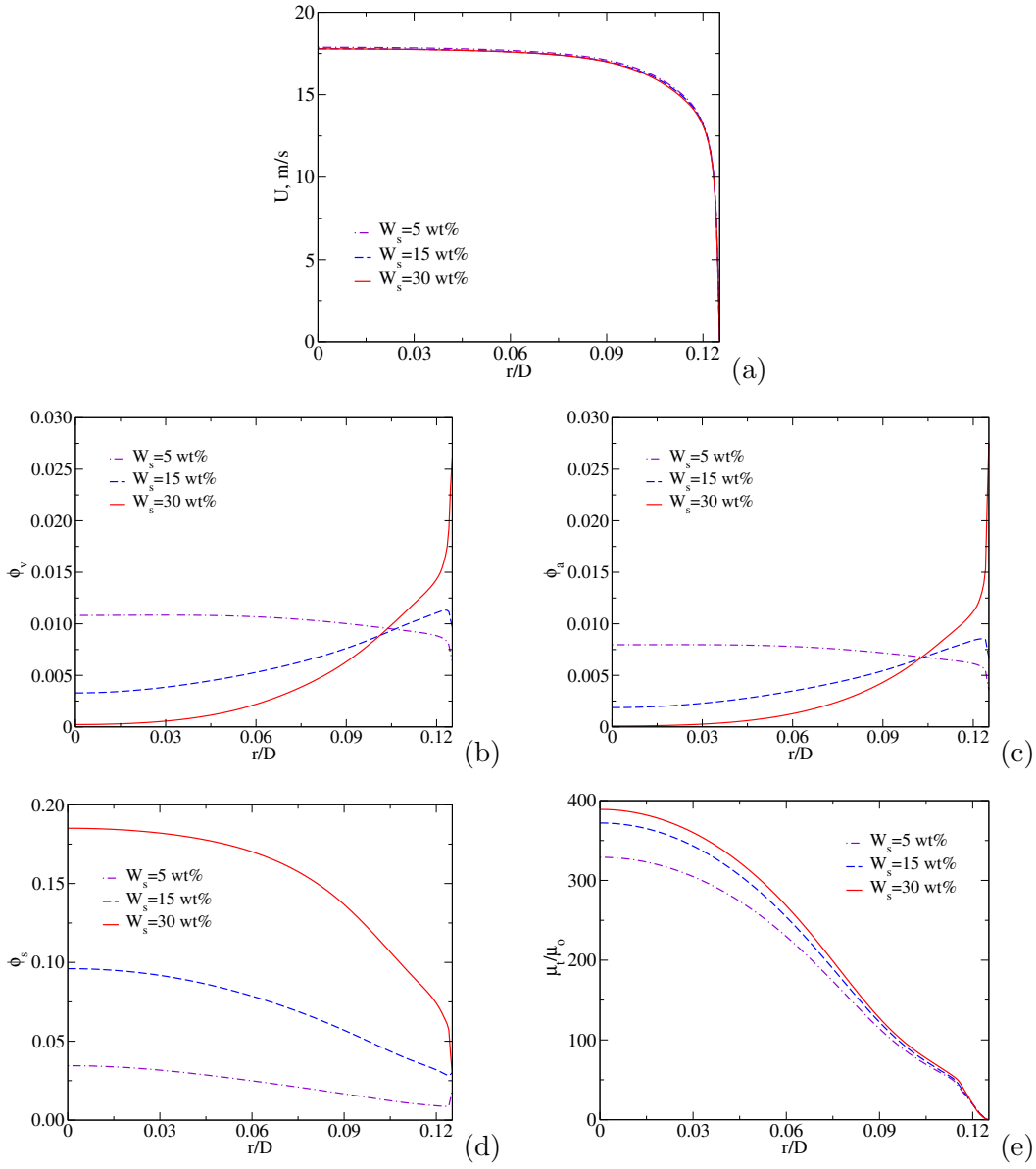

Figure 3.13: The distribution of velocity magnitude - (a), volume-averaged vapor volume fraction - (b), volume-averaged air volume fraction - (c), volume-averaged solid volume fraction - (d), and turbulent viscosity ratio - (e) along r/D near the outlet of the throat section Z/D=3, U_{in}=1 m/s, Re_{in}=12656.

Studying the overall behavior of the cavitating flow in the cavitating Venturi tube with solid mass concentrations of 5 wt% (V_s=1.94 %) to 30 wt% (V_s=13.9 %), the vapor volume fraction and air volume fraction plots at a specific inlet velocity of 1 m/s are presented in Fig. 3.14 and Fig. 3.15, respectively. As can be seen from both figures, similar stable cavitation behaviors can be obtained from both the vapor-induced cavitation and

gas-induced cavitation. The cavitation starts at the entrance of the throat section and develops further along the wall of the Venturi tube. Higher vapor and air volume fractions can be observed at the beginning of the divergent section in all cases. As the solid mass concentration increases from 5 wt% (V_s=1.94 %) to 30 wt% (V_s=13.9 %), the vaporous and gaseous cavitation zones expand and eventually fill the divergent section of the Venturi tube. Additionally, the maximum value of the vapor volume fraction increases from 0.48 to 0.5 and that of the air volume fraction increases from 0.42 to 0.49 with increased particle concentration.

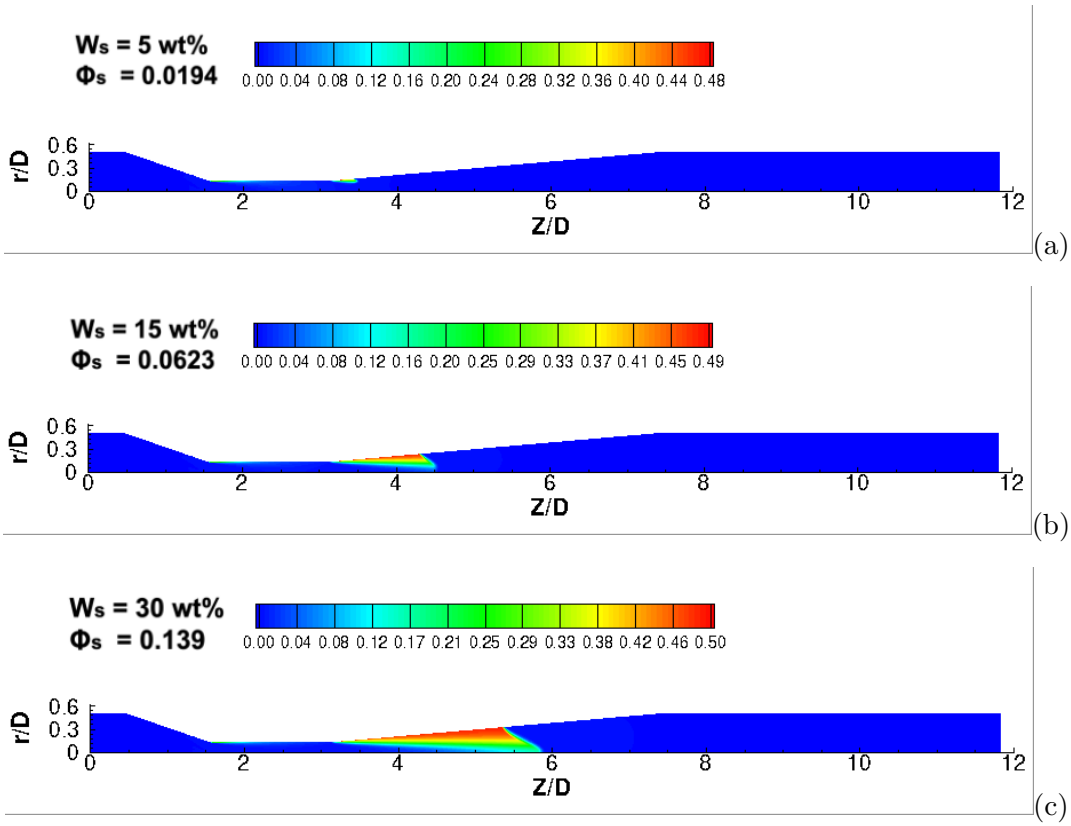

Figure 3.14: Vapor volume fraction at inlet velocity of U_{in}=1 m/s, Re_{in}=12656: (a) - W_s=5 wt% (V_s=1.94 %); (b) - W_s=15 wt% (V_s=6.23 %); (c) - W_s=30 wt% (V_s=13.9 %).

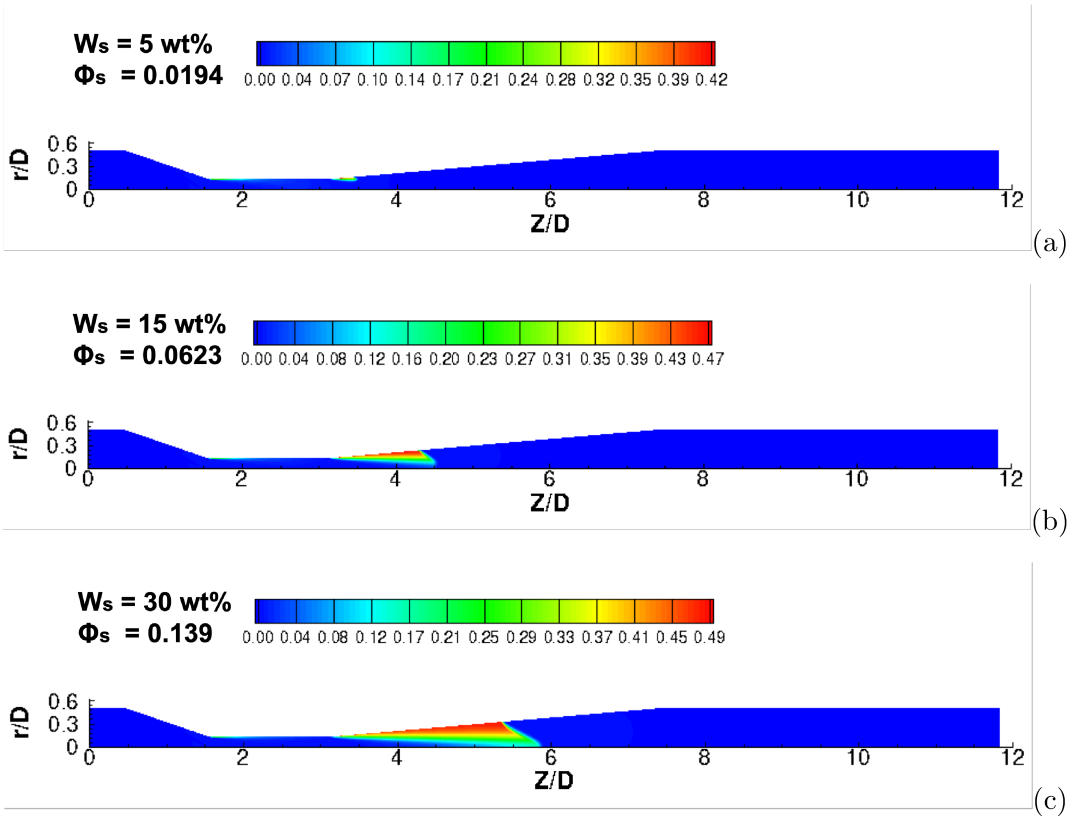

Figure 3.15: Air volume fraction at inlet velocity of U_{in}=1 m/s, Re_{in}=12656: (a) - W_s=5 wt% (V_s=1.94 %); (b) - W_s=15 wt% (V_s=6.23 %); (c) - W_s=30 wt% (V_s=13.9 %).

Fig. 3.16 shows the distribution of the solid phase across the Venturi tube. From this figure, the particle flow is seen to choke at the throat section and the divergent cone center. This is expected, because of the cavitation bubbles occupy more space in the throat section and divergent section, improving the particle-particle and particle-wall collision probability. As a consequence, solid particles agglomerate within the throat section and then accumulate along the divergent cone center. It is observed that for the higher solid mass concentrations (W_s=15 wt% and 30 wt%), more solid particles accumulate at the closure of the cavitation zone in the divergent section. This can be explained by the formation of a re-entrant jet, induced by the internal recirculation of the particle flows. This strong re-entrant jet transports more solid particles back into the closure region behind the cavity with the increased solid mass concentration from 5 wt% (V_s=1.94 %) to 30 wt% (V_s=13.9 %). As the flow reaches the end of the divergent section, the distribution of the solid particles becomes more uniform.

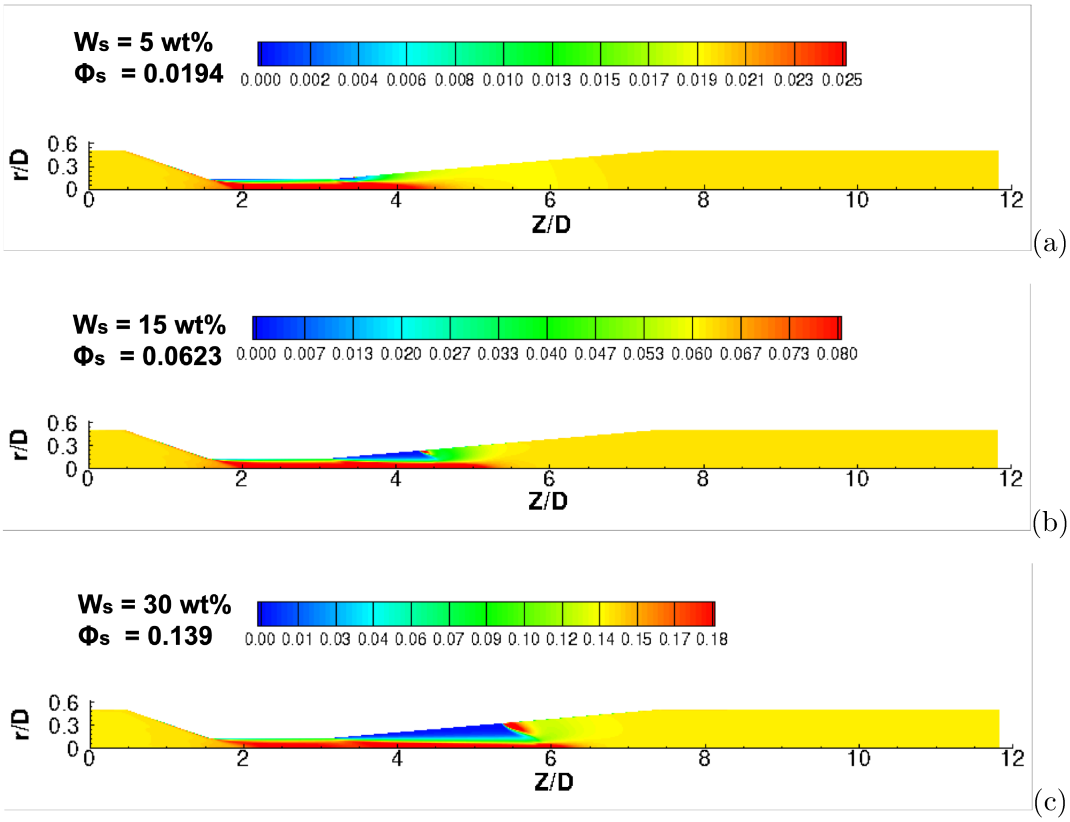

Figure 3.16: Solid volume fraction at inlet velocity of U_{in}=1 m/s, Re_{in}=12656 for different inlet values of solid phase concentrations: (a) - W_s=5 wt% (V_s=1.94 %); (b) - W_s=15 wt% (V_s=6.23 %); (c) - W_s=30 wt% (V_s=13.9 %).

Fig. 3.17 depicts snapshots of the turbulent viscosity ratio for the same simulation cases. The turbulent viscosity ratio, which is defined as the ratio between the turbulent μ_t and molecular μ_o dynamic viscosities, is used to estimate the magnitude of turbulence within the simulation. It can be observed that higher turbulence is mainly distributed in the divergent section of the Venturi tube for all simulation cases. As the solid mass concentration increases from 5 wt% (V_s=1.94 %) to 30 wt% (V_s=13.9 %), the magnitude of the turbulence viscosity ratio increases from 620 to 1560. The turbulent viscosity is clearly seen to have a significant influence on the cavitation behaviors. The higher turbulent viscosity induces the collapse of the bubble cluster and therefore leads to the formation of the cavity closure. In the cavity closure region, the local pressure recovers to almost the ambient pressure and the re-entrain jet occurs.

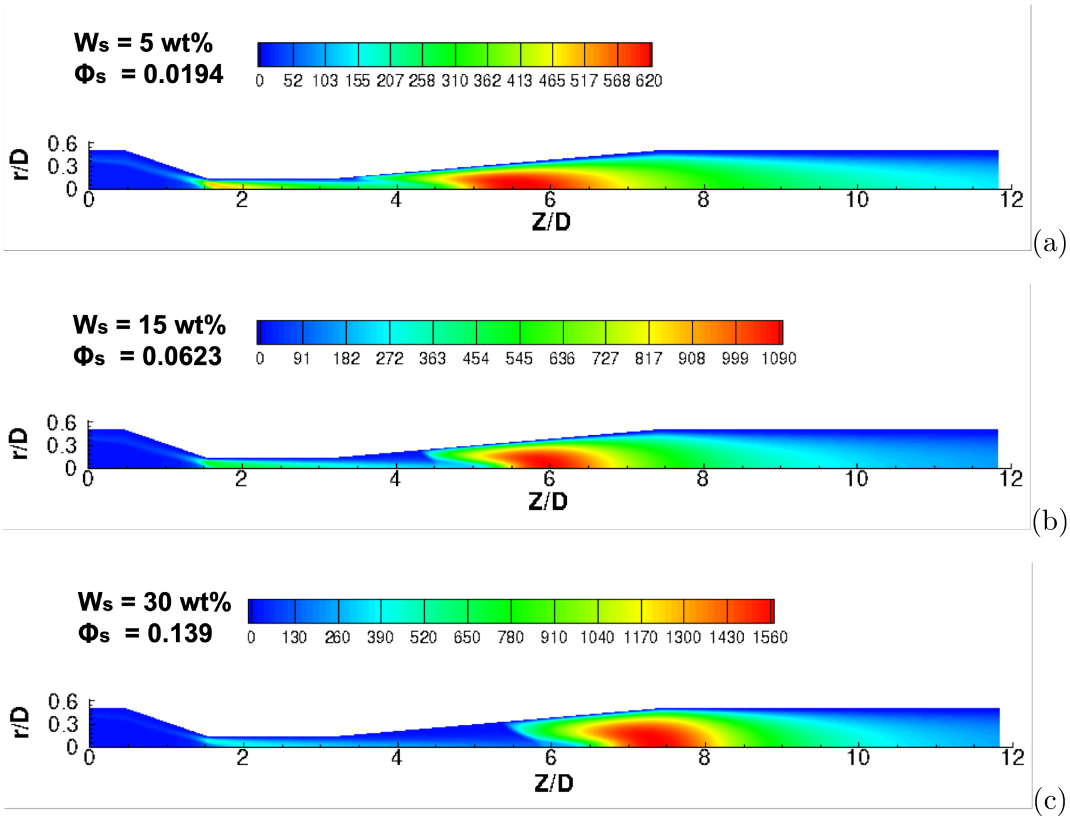

Figure 3.17: Turbulent viscosity ratio $\frac{\mu_t}{\mu_0}$ at inlet velocity of U_{in}=1 m/s, Re_{in}=12656: (a) - W_s=5 wt% (V_s=1.94 %); (b) - W_s=15 wt% (V_s=6.23 %); (c) - W_s=30 wt% (V_s=13.9 %).

3.6 Conclusions

In this paper, the numerical simulation of four-phase flows through the Venturi tube was studied using an axisymmetric 2D CFD-based model available in the commercial CFD software ANSYS FLUENT 16.2. A new global model of four-phase (liquid-solid-vapor-air) cavitating flows was developed based on this simple engineering approach, and validated against the experimental measurements. The experimental data obtained provided good agreement with numerical results, with a deviation in the pressure drop within [4.49−8.07]%. The influence of solid mass concentrations (W_s=5∼30 wt%) on the flow characteristics and the generation of cavitation at different inlet flow velocities was investigated experimentally and numerically.

To the best of our knowledge, this appears to be first time that a four-phase cavitating flows through a Venturi tube has been successfully simulated using the CFD model. In particular, the results of the experimental and CFD studies clearly illustrate that the

presence of solid particles has a significant influence on the cavitation behaviors. In general, the higher the solid mass concentration, the earlier the cavitation inception and the greater the vapor and air production, but accompanied by a higher energy consumption. Accordingly, the required cavitation yield can be controlled by adding solid particles to the cavitating Venturi tube, taking into account the effect of the energy consumption. In addition to this, it was shown numerically that the distribution of the solid volume fraction in the four-phase flows is increased significantly in the throat section and the divergent cone center of the cavitating Venturi tube. The numerical analysis also indicates that the flow structure is altered and the growth of cavitation clusters is restricted by the presence of turbulence in the downstream section of the cavitating Venturi tube.

3.7 Acknowledgments

Financial support from the Natural Science and Engineering Research Council of Canada (NSERC), the Canadian Centre for Clean Coal/Carbon and Mineral Processing Technologies (C5MPT) and the Canadian Mining Industry Research Organization (CAMIRO) is greatly appreciated.

Bibliography

[1] Robert T Knapp, James W Daily, and Frederick G Hammitt. *Cavitation*. McGraw-Hill, 1970.

[2] Christopher E Brennen. *Cavitation and bubble dynamics*. Cambridge University Press, 2014.

[3] Matevž Dular, Tjaša Griessler-Bulc, Ion Gutierrez-Aguirre, Ester Heath, Tina Kosjek, Aleksandra Krivograd Klemenčič, Martina Oder, Martin Petkovšek, Nejc Rački, Maja Ravnikar, et al. Use of hydrodynamic cavitation in (waste) water treatment. *Ultrasonics sonochemistry*, 29:577–588, 2016.

[4] Mark Duerkop, Eva Berger, Astrid Dürauer, and Alois Jungbauer. Impact of cavitation, high shear stress and air/liquid interfaces on protein aggregation. *Biotechnology journal*, 13(7):1800062, 2018.

[5] P Senthil Kumar, M Siva Kumar, and AB Pandit. Experimental quantification of chemical effects of hydrodynamic cavitation. *Chemical Engineering Science*, 55(9): 1633–1639, 2000.

[6] V Ross, A Singh, and K Pillay. Improved flotation of pgm tailings with a high-shear hydrodynamic cavitation device. *Minerals Engineering*, 137:133–139, 2019.

[7] SK Kawatra and TC Eisele. Froth flotation-fundamental principles. *Research, Michigan Technical University*, pages 1–30, 2002.

[8] Roe-Hoan Yoon, Darrin H Flinn, and Yakov I Rabinovich. Hydrophobic interactions between dissimilar surfaces. *Journal of colloid and interface science*, 185(2):363–370, 1997.

[9] Daniel Tao. Role of bubble size in flotation of coarse and fine particles—a review. *Separation Science and Technology*, 39(4):741–760, 2005.

[10] ZA Zhou, Zhenghe Xu, JA Finch, H Hu, and SR Rao. Role of hydrodynamic cavitation in fine particle flotation. *International Journal of Mineral Processing*, 51(1-4):139–149, 1997.

[11] HJ Schulze, B Radoev, Th Geidel, H Stechemesser, and E Töpfer. Investigations of the collision process between particles and gas bubbles in flotation—a theoretical analysis. *International Journal of Mineral Processing*, 27(3-4):263–278, 1989.

[12] Daniel Chipfunhu, M Zanin, and S Grano. Flotation behaviour of fine particles with respect to contact angle. *Chemical engineering research and design*, 90(1):26–32, 2012.

[13] Hongbo Shi, Mingda Li, Petr Nikrityuk, and Qingxia Liu. Experimental and numerical study of cavitation flows in venturi tubes: from cfd to an empirical model. *Chemical Engineering Science*, 207:672–687, 2019.

[14] H. Oliveira, A. Azevedo, and J. Rubio. Nanobubbles generation in a high-rate hydrodynamic cavitation tube. *Minerals Engineering*, 116:32–34, 2018.

[15] FAN Maoming, TAO Daniel, Rick HONAKER, and LUO Zhenfu. Nanobubble generation and its application in froth flotation (part i): nanobubble generation and its effects on properties of microbubble and millimeter scale bubble solutions. *Mining Science and Technology (China)*, 20(1):1–19, 2010.

[16] Rahman Ahmadi, Darban Ahmad Khodadadi, Mahmoud Abdollahy, and Maoming Fan. Nano-microbubble flotation of fine and ultrafine chalcopyrite particles. *International Journal of Mining Science and Technology*, 24(4):559–566, 2014.

[17] Haipeng Li. Role of hydrodynamic cavitation in fine particle flotation. Master's thesis, University of Alberta, 2014.

[18] W. Zhou, H. Chen, L. Ou, and Q. Shi. Aggregation of ultra-fine scheelite particles induced by hydrodynamic cavitation. *International Journal of Mineral Processing*, 157:236–240, 2016.

[19] Tausif A Bashir, Advait G Soni, Amit V Mahulkar, and Aniruddha B Pandit. The cfd driven optimisation of a modified venturi for cavitational activity. *The Canadian Journal of Chemical Engineering*, 89(6):1366–1375, 2011.

[20] JX Zhang. Analysis on the effect of venturi tube structural parameters on fluid flow. *AIP Advances*, 7(6):065315, 2017.

[21] Mingda Li, Adrien Bussonnière, Matthew Bronson, Zhenghe Xu, and Qingxia Liu. Study of venturi tube geometry on the hydrodynamic cavitation for the generation of microbubbles. *Minerals Engineering*, 132:268–274, 2019.

[22] Patrick F Dunn, Flint O Thomas, Michael P Davis, and Irina E Dorofeeva. Experimental characterization of aviation-fuel cavitation. *Physics of Fluids*, 22(11):117102, 2010.

[23] Jiakai Zhu, Huangjun Xie, Kesong Feng, Xiaobin Zhang, and Minqiang Si. Unsteady cavitation characteristics of liquid nitrogen flows through venturi tube. *International Journal of Heat and Mass Transfer*, 112:544–552, 2017.

[24] Jiong Wang, Luyan Wang, Shuangjie Xu, Bin Ji, and Xinping Long. Experimental investigation on the cavitation performance in a venturi reactor with special emphasis on the choking flow. *Experimental Thermal and Fluid Science*, 2019.

[25] Anthony A Atchley and Andrea Prosperetti. The crevice model of bubble nucleation. *The Journal of the Acoustical Society of America*, 86(3):1065–1084, 1989.

[26] HB Marschall, Knud Aage Mørch, AP Keller, and M Kjeldsen. Cavitation inception by almost spherical solid particles in water. *Physics of fluids*, 15(2):545–553, 2003.

[27] JJ Kwan, S Graham, R Myers, R Carlisle, E Stride, and CC Coussios. Ultrasound-induced inertial cavitation from gas-stabilizing nanoparticles. *Physical Review E*, 92 (2):023019, 2015.

[28] Robert E Apfel. The role of impurities in cavitation-threshold determination. *The Journal of the Acoustical Society of America*, 48(5B):1179–1186, 1970.

[29] Youwei Gu, Buxuan Li, and Min Chen. An experimental study on the cavitation of water with effects of sio2 nanoparticles. *Experimental Thermal and Fluid Science*, 79: 195–201, 2016.

[30] M Medrano, PJ Zermatten, Christian Pellone, Jean-Pierre Franc, and Frédéric Ayela. Hydrodynamic cavitation in microsystems. i. experiments with deionized water and nanofluids. *Physics of Fluids*, 23(12):127103, 2011.

[31] Mingda Li. Influence of venturi tube geometry and particle properties on the hydrodynamic cavitation for fine particle flotation. *Master thesis*, 2017.

[32] XiaoBin Zhang, JiaKai Zhu, LiMin Qiu, and XueJun Zhang. Calculation and verification of dynamical cavitation model for quasi-steady cavitating flow. *International Journal of Heat and Mass Transfer*, 86:294–301, 2015.

[33] Guo-Dong Li, Song-Sheng Deng, Jin-Fa Guan, and Su Yao. Numerical analysis on cavitation effects in submerged water jet added with turbulent drag-reducing additives of ctac. *Chemical Engineering Science*, 196:391–401, 2019.

[34] Mohammad-Reza Pendar and Ehsan Roohi. Cavitation characteristics around a sphere: An les investigation. *International Journal of Multiphase Flow*, 98:1–23, 2018.

[35] Houcun Zhou, Min Xiang, Shiwei Zhao, and Weihua Zhang. Development of a multiphase cavitation solver and its application for ventilated cavitating flows with natural cavitation. *International Journal of Multiphase Flow*, 115:62–74, 2019.

[36] Seyed Mehdi Ashrafizadeh and Hojat Ghassemi. Experimental and numerical investigation on the performance of small-sized cavitating venturis. *Flow measurement and Instrumentation*, 42:6–15, 2015.

[37] S Brinkhorst, E von Lavante, and G Wendt. Numerical investigation of cavitating herschel venturi-tubes applied to liquid flow metering. *Flow Measurement and Instrumentation*, 43:23–33, 2015.

[38] Inc Ansys. Ansys fluent theory guide. *Canonsburg, Pennsylvania*, page 794, 2011.

[39] DR Kaushal, Kimihiko Sato, Takeshi Toyota, Katsuya Funatsu, and Yuji Tomita. Effect of particle size distribution on pressure drop and concentration profile in pipeline flow of highly concentrated slurry. *International Journal of Multiphase Flow*, 31(7): 809–823, 2005.

[40] C Simonin and PL Viollet. Predictions of an oxygen droplet pulverization in a compressible subsonic coflowing hydrogen flow. *Numerical Methods for Multiphase Flows, FED91*, pages 65–82, 1990.

[41] Z Naumann and L Schiller. A drag coefficient correlation. *Z. Ver Deutsch. Ing*, 77: 318–323, 1935.

[42] Madhava Syamlal and Thomas J O'Brien. Computer simulation of bubbles in a fluidized bed. In *AIChE Symp. Ser*, volume 85, pages 22–31, 1989.

[43] Ashok K Singhal, Mahesh M Athavale, Huiying Li, and Yu Jiang. Mathematical basis and validation of the full cavitation model. *Transactions-American Society of Mechanical Engineers Journal of Fluids Engineering*, 124(3):617–624, 2002.

[44] Günter H Schnerr and Jürgen Sauer. Physical and numerical modeling of unsteady cavitation dynamics. In *Fourth international conference on multiphase flow, New Orleans, USA*, volume 1, 2001.

[45] Philip J Zwart, Andrew G Gerber, Thabet Belamri, et al. A two-phase flow model for predicting cavitation dynamics. In *Fifth international conference on multiphase flow, Yokohama, Japan*, volume 152, 2004.

[46] Huiying Li, Frank J. Kelecy, Aleksandra Egelja-Maruszewski, and Sergio A. Vasquez. Advanced computational modeling of steady and unsteady cavitating flows. In *ASME*

2008 International Mechanical Engineering Congress and Exposition, pages 413–423. American Society of Mechanical Engineers, 2008.

[47] D Li, Mikael Grekula, and Per Lindell. A modified sst k-ω turbulence model to predict the steady and unsteady sheet cavitation on 2d and 3d hydrofoils. *7th International Symposium on Cavitation*, 2009.

[48] Hou-lin Liu, Dong-xi Liu, Yong Wang, Xian-fang Wu, and Jian Wang. Application of modified κ-ω model to predicting cavitating flow in centrifugal pump. *Water Science and Engineering*, 6(3):331–339, 2013.

[49] George Wm Thomson. The antoine equation for vapor-pressure data. *Chemical reviews*, 38(1):1–39, 1946.

[50] Brian P Leonard. A stable and accurate convective modelling procedure based on quadratic upstream interpolation. *Computer methods in applied mechanics and engineering*, 19(1):59–98, 1979.

[51] CKK Lun, S Br Savage, DJ Jeffrey, and N Chepurniy. Kinetic theories for granular flow: inelastic particles in couette flow and slightly inelastic particles in a general flowfield. *Journal of fluid mechanics*, 140:223–256, 1984.

[52] Paul C Johnson and Roy Jackson. Frictional–collisional constitutive relations for granular materials, with application to plane shearing. *Journal of fluid Mechanics*, 176:67–93, 1987.

[53] Jianmin Ding and Dimitri Gidaspow. A bubbling fluidization model using kinetic theory of granular flow. *AIChE journal*, 36(4):523–538, 1990.

[54] Henry Scheffe. The relation of control charts to analysis of variance and chi-square tests. *Journal of the American Statistical Association*, 42(239):425–431, 1947.

[55] Hongbo Shi, Alexandra Komrakova, and Petr Nikrityuk. Fluidized beds modeling: Validation of 2d and 3d simulations against experiments. *Powder Technology*, 343: 479–494, 2019.

Chapter 4

Modeling of Cavitating Flows Past a Micro-sized Particle[1]

4.1 Introduction

Cavitation is a multi-phase phenomenon that occurs between a bulk liquid and liquid solid objects such as particles moving in it, or no-slip walls constricting that liquid, e.g. Venturi tubes [1, 2]. The main features of cavitation are vapor bubbles forming and growing in a liquid medium when the static pressure drops locally below the saturated vapor pressure at a constant temperature [3, 4]. Cavitation has been widely researched as a useful phenomenon which has been applied to many industrial fields such as mineral processing [5], food processing [6], chemical reactions [7], water purification [8], etc. In the mineral extraction process, a Venturi tube is used to improve the efficiency of fine particle separation using flotation technology. The Venturi tubes are used in industry as a source of cavitation. Venturi tubes mainly comprise a convergent section, throat section and divergent section. When large pressure differentials are generated within the liquid medium as the fluid passes through the throat section of the Venturi tube, an intense phase change from liquid to vapor appears. Venturi tubes are used to generate micro- and nano-size vapor and air bubbles. Injecting such bubbles from Venturi tubes into flotation columns can significantly improve the performance of flotation processes by increasing the collision probability between solid particles and cavitation bubbles. In this respect, hydrodynamic cavitation plays a crucial role in the operation of fine particle flotation [5, 9].

The intensity of cavitation in a hydrodynamic cavitating Venturi tube mainly depends on geometrical parameters such as the throat diameter, the convergent and divergent an-

[1]This chapter has been accepted as: Hongbo Shi, Qingxia Liu and Petr Nikrityuk. Modeling of cavitating flows past a micro-sized particle. *International Journal of Multiphase Flow*, 2020.

gles, and operating conditions such as the flow rate, the fluid temperature, the upstream and downstream pressures, but more importantly it depends on the addition of solid particles to the Venturi tube. In general, the effect of solid particles mainly comes from the air bubbles trapped in the cracks or crevices on the surface of the solid particles [10]. The growth of air bubbles into larger bubbles has been identified as the source of cavitation inception, leading to the promotion of cavitation generation. A considerable deal of experimental work has been carried out to gain an insight into multiphase cavitating flows and the influence of solid particles on the cavitation characteristics [11, 12]. Unfortunately, most of the experimental works cannot distinguish between the individual contribution of trapped air bubbles on the particle surface and the solid particle itself. In fact, the characteristics of the cavitation behavior of the solid particles utilised, in the absence of dissolved gases, are still not well understood. Therefore, studying the impact of solid particles in the development of the cavitation flow is most frequently addressed.

As more computational fluid dynamics (CFD) methods for predicting cavitation have been developed and implemented in commercial CFD software, e.g. ANSYS FLUENT [13, 14, 15] and open-source CFD software, e.g. OPEN Foam [16, 17, 18], notable numerical works have provided valuable insight into the relationship between the solid particles and cavitation. Gregorc et al. [19] performed experimental and three-dimensional (3D) CFD simulations using an Eulerian-Eulerian model to investigate how solid particles affect the turbulent cavitation flow over a hydrofoil. The author showed that the magnitude of torque increases with the presence of solid particles in the fluid. As the solid mass fraction rises from 0.001 to 0.0032, the vapor volume fraction increases significantly on the surface of the hydrofoil. Li et al. [20] used molecular dynamic simulations to investigate the inception of cavitation in water with solid nanoparticles. They observed that the presence of the nanoparticles reduces the number and energy of the hydrogen bond network in the water. The free energy of the critical bubble decreases and the nucleation energy increases as the particle size rises from half to ten times the critical bubble size. On the other hand, the effect of particle size on cavitation is limited if the particle size exceeds this range. In addition, the results show that polyethylene particles can generate more vapor bubbles in the water as compared to SiO_2 particles. Kabeel and Abdelgaied [21] studied the influences of the alumina nano-particles (AL_2O_3) on cavitation behaviors in the orifice using a two-dimensional (2D) mixture model. The turbulent kinetic energy is seen to drop 21% in the downstream and the turbulent intensity decreases 11% in the whole domain as the solid concentration increases from 0 to 10%. In addition, the vapor volume fraction rises to a maximum value of 0.17 as the solid volume fraction increases from 0 to 0.1.

Chen et al. [22] used a 3D mixture model to analyze how nanoparticles influence the turbulent cavitation flow in the pipe. The results show that higher nanoparticle concentra-

tions and a larger nanoparticle size increase the cavitation zone with a lower inlet pressure (0.4 MPa), while the effects of the nanoparticle concentration and diameter are limited for the higher inlet pressures (0.6 and 1.0 MPa). The vapor volume fraction increases significantly as the particle size increases from 13 nm to 80 nm at a lower operating temperature (25 °C), while the effect of particle size on cavitation is limited under a higher operating temperature (40 °C).

Pendar et al. [18] used a 3D Large Eddy Simulation (LES) to investigate the wall-bounded flow characteristics of sphere cavitation over a wide range of cavitation numbers (0.36 to 1). The numerical results indicated that the vortical region behind the sphere grows as the cavitation number rises from 0.4 to 1 because of the presence of the vortical flow inside the cavity. The laminar flow condition can be observed inside the cavity, while intense turbulent kinetic energy is distributed above the cavity leading edge. It was found that the formation of a re-entrant jet appears at a cavitation number of 0.9, and the thickness of the re-entrant jet decreases as the cavity length increases.

Cheng et al. [23] carried out 3D CFD simulations using a mixture model to study unsteady turbulent cavitation flow over a spherical particle in a wall-bounded domain. The numerical results are in line with the experimental data obtained from the literature. Based on the simulation results, they found that the cavity length increases and the location of the cavity inception point moves downstream over the particle surface as the cavitation number declines from 0.95 to 0.36. The analysis indicated that the effect of cavitation shedding on the lift force is significant when the cavitation number is lower than 0.8.

Gnanaskandan and Mahesh [24] performed 3D CFD simulations using a LES turbulence model to investigate the unsteady features of the cavitating flow past a circular cylinder in a free-stream domain. The author showed that the mean cavity length obtained in the case of a laminar flow (Re=200) is much lower than that in the case of a turbulent flow (Re=3900) at the same cavitation number. The shedding frequency cavity detachment is found at a cavitation number of σ=1, while low-frequency and shedding frequency cavity detachment are obtained at a cavitation number of σ=0.5 to 0.7. The cavity separation location in the cavitating flow moves downstream as compared to the separation location in the non-cavitating flow. In addition, the variation in the initial void fraction (α_o=0.005 to 0.01) does not affect the inception of cavitation over the cylinder surface.

Alongside the numerical studies focused on the physics of three-phase (solid-liquid-vapor) cavitating flows, there are almost no CFD studies considering a detailed numerical consideration of a cavitating flow past fine particles with different particle shapes and surface roughnesses. Also, the effect of the number of particles arranged in a line and the heat transfer between the particle surface and cavitating flow has not yet been numerically investigated. In fact, understanding and predicting the cavitation behavior of the utilized

solid particles with various shapes, roughnesses, quantities, and temperature can be considered in the Venturi tube to improve its performance. Therefore, the main objective of this work is to investigate numerically the occurrence of cavitation past micro-sized particles moving in water. Additionally, effects of the particle shape, the surface roughnesses and the surface temperature have been studied numerically. Mainly laminar flow conditions have been utilized except in some cases for particles with a diameter larger than $50 \cdot 10^{-6}$ m. The commercial CFD software ANSYS FLUENT 16.2 [25] was employed in this study. The paper is organized as follows. Section 4.2 gives an overview of the problem of research into the particle cavitation simulation. Section 4.3 presents a description of the computational model. The validation results are given in Section 4.4. Section 4.5 outlines the results and discussions of the present study. Conclusions from this work are then summarized in Section 4.6.

4.2 Problem description

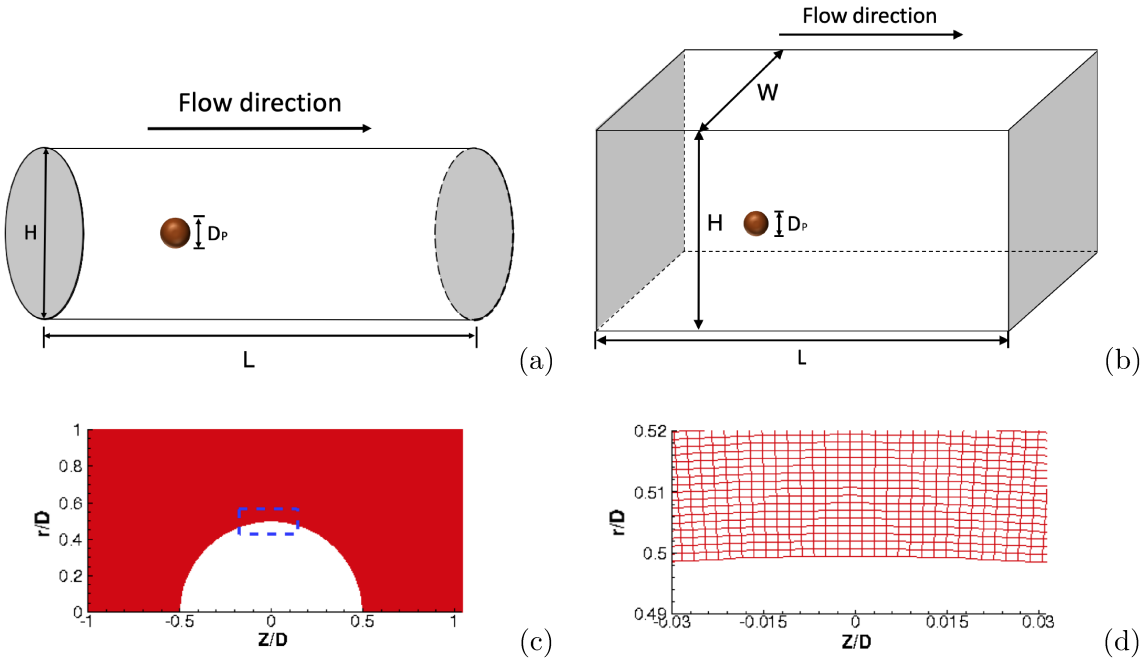

Figure 4.1: Schematic diagram of the 2D and 3D computational domains - (a) and (b); the 2D computational structured mesh (Grid−3) for Particle−1 - (c) and (d).

In order to evaluate the cavitation characteristics induced by a solid particle moving in water, the numerical simulations of water-vapor-phase flows around a solid particle were carried out mainly under laminar flow conditions at Re <1800. A 2D axis−symmetric domain was used for $Re \leq 250$ and a 3D domain was applied where the asymmetric flow

exists as $Re > 300$. Figs. 4.1a and 4.1b show schematics of the 2D and 3D domain, respectively. The 2D free-stream domain is $130D_p$ in length (the length in front of the particle is $30D_p$ and the distance behind the particle is $100D_p$) and $40D_p$ in height. The 3D domain is $66D_p$ in length (the length in front of the particle is $18D_p$ and the distance behind the particle is $48D_p$) and $35D_p$ in height and width. A spherical solid particle, with a diameter in the range between D_p=10 μm and 100 μm, is placed at the center of the domain. Liquid water enters the inlet of the domain with a uniform velocity in the range between 0.1 and 25 m/s at a temperature of 293.15 K. Four different particles were examined in this study:

- Particle-1 is a smooth spherical particle, Fig. 4.2a.
- Particle-2 is a smooth cylindrical particle, Fig. 4.2b.
- Particle-3 is a rough spherical particle with a roughness coefficient of K_R=0.08, Fig. 4.2c.
- Particle-4 is a rough spherical particle with a roughness coefficient of K_R=0.18, Fig. 4.2d.

The formulation of the roughness coefficient is expressed as [26, 27]:

$$K_R = \frac{K_s}{D_p} \tag{4.1}$$

where K_s is the height of the irregular surface and D_p is the diameter of the particle. The schematic diagram of a 2D axis$-$symmetric computational domain for Particle-1 to Particle-4 is shown in Fig. 4.2a to 4.2d.

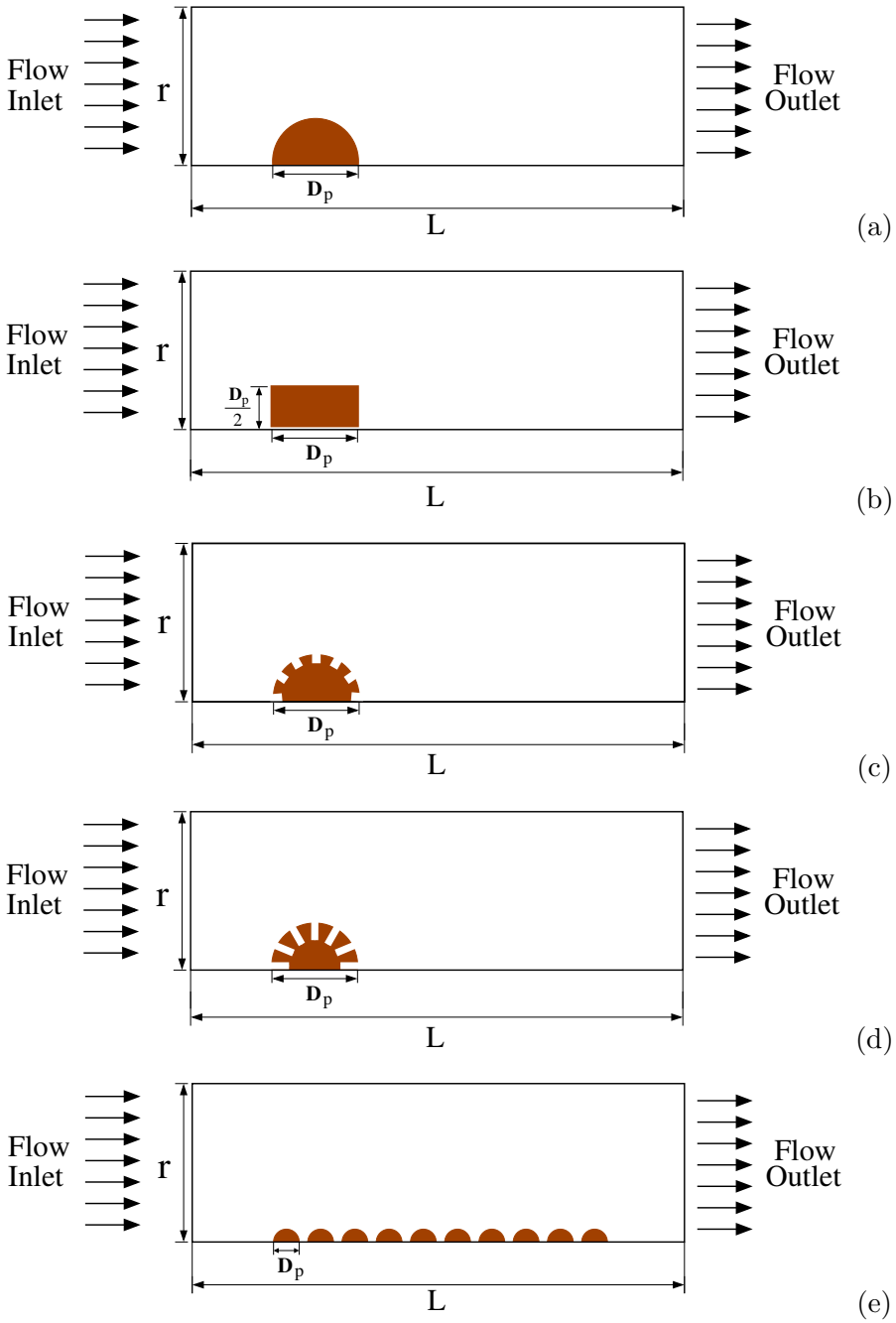

Figure 4.2: Schematic diagram of a 2D axis−symmetric computational domain for single Particle−1 to Particle−4 - (a) - (d) and multiple Particle−1 - (e).

4.3 Computational model

In this study, the single-fluid mixture model is employed to simulate two-phase flows (water-vapor) over a solid particle. The mixture model can model the liquid phase or vapor phase by solving a set of governing equations of fluid flow including continuity, momentum, energy and the transport of the volume fraction between two phases. In the mixture model, the liquid phase and vapor phase of the cavitating flow are assumed to be in mechanical equilibrium and the velocities and densities of both phases are identical at every position in the multiphase fluid field [25]. The steady and unsteady Navier-Stokes solvers are used to solve the two-phase laminar flow using 2D axis−symmetric ($Re \leq 250$) and 3D domains ($300 < Re < 1800$), respectively. The standard $k-\varepsilon$ turbulence model with enhanced wall treatment is used in a 3D domain to simulate the unsteady turbulent flow phenomenon around the particle by $Re \geq 1800$. k and ε represent the turbulent kinetic energy and the dissipation rate of kinetic energy in the flow, respectively. It should be noted that the two phases are treated as incompressible and the slip velocity between the water phase and vapor phase is assumed to be low and neglected in the mixture model. Additionally, this study does not take into account the effects of surface tension and gravity. The fluid flow is considered to be isothermal and non-isothermal, respectively.

The Schnerr-Sauer cavitation model [28] serves as the mass transfer model to calculate the net mass transition from the water phase to the vapor phase. It considers vapor phase as the dispersed phase in the continuum liquid phase in the homogeneous mixture flow field [25]. The Rayleigh-Plesset equation is applied to this model to describe the condensation and evaporation of a spherical cavitation bubble in the liquid. The number of spherical bubbles per volume of liquid is assumed to be constant during the simulation procedure. Additionally, the presence and expansion of non-condensable gas in the liquid is not accounted for in the Schnerr-Sauer model. For the isothermal simulations, the saturation vapor pressure, P_V is kept constant and equal to 2338 Pa (20°C). For the non-isothermal simulations, the change of fluid flow temperature is utilized to compute the variation of saturation vapor pressure based on the Antoine equation [29]:

$$Log P_V = A - \frac{B}{T + C} \tag{4.2}$$

In Equation 4.2, the absolute vapor pressure of the water, P_V is in mmHg and the saturation temperature of the water, T is in °C. A, B, and C are substance-specific coefficients with a value of 8.07131, 1730.63, and 233.426, respectively. The formulations of the governing equations for the water-vapor system are presented in Table 4.1. In order to distinguish between the individual contribution to cavitation activities made by dissolved gases on the particle surface and the solid particle itself, this study did not take the effect

of dissolved gas into account in the fluid field.

The flow boundary conditions are defined in terms of inlet velocity and outlet pressure. The inlet velocity is specified in the range of $0.1 \sim 25$ m/s, while a static pressure outlet with a constant value of zero is adopted. The boundary conditions for a turbulent flow are specified as 10% for the turbulence intensity and 10 for the turbulent viscosity ratio. The no-slip condition is imposed on the particle surface and free-stream conditions are set on all far-field boundaries. In the isothermal process, no particle-to-fluid heat transfer occurs in the system and the temperature of the fluid flow is constant at T_f=20°C. In the non-isothermal process, the inlet flow is maintained at a constant temperature of T_{in}=20°C and the temperatures on the particle surface are set as T_p=40°C, 60°C, 80°C, and 99.9°C.

The mixture multiphase model is established and computed based on the commercial CFD software ANSYS FLUENT 16.2. The 2D axisymmetric computational geometry is discretized with four structured hexahedral meshes using a finite-volume method with 1328640 (Particle−1), 3522560 (Particle−2), 1391872 (Particle−3) and 1443520 (Particle−4) computational cells, and the 3D computational geometry is discretized with 4817181 (Particle−1) computational cells. A representative 2D mesh is shown in Fig. 4.1c and d.

The pressure-velocity-based coupled scheme [25] was utilized to solve the momentum equations and the continuity equations together, corresponding to the two-phase cavitating flow in the present simulations. The second−order upwind scheme was used to discretize the momentum equations, turbulent kinetic energy and turbulent dissipation rate. The Quadratic Upwind Interpolation for Convection Kinematics (QUICK) scheme [25] was employed for the vapor volume fraction transport equation. The PREssure STaggering Option (PRESTO) scheme was adopted for the pressure interpolation. The transient simulations with a fixed time step of 1×10^{-4} sec are required to obtain a stable converged solution. Table 4.2 lists the details of the models and schemes used in the numerical simulation of cavitating flow around a solid particle. The physical properties for isothermal and thermal systems are specified in Table 4.3.

Continuity equation	$\frac{\partial}{\partial t}(\rho_m) + \nabla \cdot (\rho_m \vec{v}_m) = 0$
	$\vec{v}_m = \frac{\sum_{q=1}^{n} \alpha_q \rho_q \vec{v}_q}{\rho_m}$
	$\rho_m = \sum_{q=1}^{n} \alpha_q \rho_q$
Momentum equation	$\frac{\partial}{\partial t}(\rho_m \vec{v}_m) + \nabla \cdot (\rho_m \vec{v}_m \vec{v}_m) =$
	$-\nabla P + \nabla \cdot [\mu_m (\nabla \vec{v}_m + \nabla \vec{v}_m^T)] + \rho_m \vec{g} + \vec{F} + \nabla \cdot (\sum_{q=1}^{n} \alpha_q \rho_q \vec{v}_{dr,q} \vec{v}_{dr,q})$
	$\mu_m = \sum_{q=1}^{n} \alpha_q \mu_q$
Energy equation	$\frac{\partial}{\partial t} \sum_{q=1}^{n} (\alpha_q \rho_q E_q) + \nabla \cdot \sum_{q=1}^{n} (\alpha_q \vec{v_q} (\rho_q E_q + p)) = \nabla \cdot (\lambda_{eff} \nabla T) + S_E$
Volume fraction equation for the vapor phase	$\frac{\partial}{\partial t}(\alpha_v \rho_v) + \nabla \cdot (\alpha_v \rho_v \vec{v_m}) = R$
	$R = R_e + R_c = \frac{\rho_v \rho_l}{\rho_m} \frac{D\alpha_v}{Dt}$
Schnerr and Sauer cavitation equations	When $P_V \geq P_\infty$, $R_e = \frac{\rho_v \rho_l}{\rho_m} \alpha_v (1 - \alpha_v) \frac{3}{R_B} (\frac{2}{3} \frac{P_V - P_\infty}{\rho_l})^{0.5}$
	When $P_V \leq P_\infty$, $R_c = \frac{\rho_v \rho_l}{\rho_m} \alpha_v (1 - \alpha_v) \frac{3}{R_B} (\frac{2}{3} \frac{P_\infty - P_V}{\rho_l})^{0.5}$
	$\alpha_v = \frac{n_b \frac{4}{3} \pi R_B^3}{1 + n_b \frac{4}{3} \pi R_B^3}$
	$R_B = (\frac{\alpha_v}{1 - \alpha_v} \frac{3}{4\pi n})^{\frac{1}{3}}$
	$n = 10^{13}$
Standard k-ε mixture model	$\frac{\partial}{\partial t}(\rho_m k) + \nabla(\rho_m \vec{v}_m k) = \nabla \cdot (\frac{\mu_{t,m}}{\sigma_k} \nabla k) + G_{k,m} - \rho_m \varepsilon$
	$\frac{\partial}{\partial t}(\rho_m \varepsilon) + \nabla(\rho_m \vec{v}_m \varepsilon) = \nabla \cdot (\frac{\mu_{t,m}}{\sigma_\varepsilon} \nabla \varepsilon) + \frac{\varepsilon}{k}(C_{1\varepsilon} G_{k,m} - C_{2\varepsilon} \rho_m \varepsilon)$
	$\rho_m = \sum_{q=1}^{n} \alpha_q \rho_q$, $\vec{v}_m = (\sum_{q=1}^{n} \alpha_q \rho_q \vec{v}_q)/(\sum_{i=q}^{n} \alpha_q \rho_q)$
	$\mu_{t,m} = \rho_m C_\mu \frac{k^2}{\omega}$, $G_{k,m} = \mu_{t,m}(\nabla \vec{v}_m + (\nabla \vec{v}_m)^T) : \nabla \vec{v}_m$
	$C_{1\varepsilon} = 1.44, C_{2\varepsilon} = 1.92, C_\mu = 0.09, \sigma_k = 1.0, \sigma_\varepsilon = 1.3$
Standard k-ω mixture model	$\frac{\partial}{\partial t}(\rho_m k) + \nabla(\rho_m \vec{v}_m k) = \nabla \cdot (\frac{\mu_{t,m}}{\sigma_k} \nabla k) + G_{k,m} - Y_{k,m}$
	$\frac{\partial}{\partial t}(\rho_m \omega) + \nabla(\rho_m \vec{v}_m \omega) = \nabla \cdot (\frac{\mu_{t,m}}{\sigma_\omega} \nabla \omega) + G_{w,m} - Y_{w,m}$
	$\rho_m = \sum_{q=1}^{n} \alpha_q \rho_q$, $\vec{v}_m = (\sum_{q=1}^{n} \alpha_q \rho_q \vec{v}_q)/(\sum_{i=q}^{n} \alpha_q \rho_q)$
	$\mu_{t,m} = \frac{\rho_m k}{\omega}$
	$\alpha_\infty^* = 1, \alpha_\infty = 0.52, \beta_\infty^* = 0.09, \beta_\infty = 0.072, \sigma_k = 2, \sigma_\omega = 2$

Table 4.1: Mixture model equations available in ANSYS FLUENT 16.2 which were used in the study from [25].

Name	*Model/ Scheme Name*
Multiphase Flow	Mixture [25]
Viscous Model	Laminar model, k-ε model and k-ω model [25]
Cavitation Model	Schnerr-Sauer [28]
Pressure-Velocity Coupling	Coupled Scheme [25]
Spatial Discretization-Gradient	Least Squares Cell Based [25]
Spatial Discretization-Momentum	2nd−Order Upwind [25]
Spatial Discretization-Pressure	PRESTO! [25]
Spatial Discretization-Volume Fraction	QUICK [30]
Spatial Discretization-Turbulence	2nd−Order Upwind [25]
Transient Formulation	1st−Order Implicit

Table 4.2: List of different models and schemes used in the study.

Properties	Isothermal system	Non-isothermal system
ρ_l (kg/m^3)	998.16	ρ_l=765.33 + 1.82 T_f - 3.5×10^{-3} T_f^2
ρ_v (kg/m^3)	0.0173	Ideal gas
μ_l $(kg/m-s)$	1.001 × 10^{-3}	μ_l=9.67×10^{-2} - 8.21×10^{-4} T_f + 2.34×10^{-6} T_f^2 - 2.24×10^{-9} T_f^3
μ_v $(kg/m-s)$	9.727 × 10^{-6}	Kinetic-theory
$C_{p,l}$ $(J/kg-K)$	−	$C_{p,l}$=31245 - 321.49 T_f + 1.43 T_f^2 - 2.85×10^{-3} T_f^3 + 2.13×10^{-6} T_f^4
$C_{p,v}$ $(J/kg-K)$	−	$C_{p,v}$=1609.8 + 0.74 T_f - 9.13×10^{-6} T_f^2 - 3.81×10^{-8} T_f^3 + 4.8×10^{-12} T_f^4
λ_l $(W/m-K)$	−	λ_l=-0.575 + 6.4×10^{-3} T_f - 8.15×10^{-6} T_f^2
λ_v $(W/m-K)$	−	Kinetic−theory

Table 4.3: Physical properties used for CFD computations in this study at fluid temperatures from T_f=273.15 K to 373.05 K, taken from [31], [25].

4.4 Validation

To evaluate the capabilities of a commercial CFD software to capture the physics around a solid particle, the experiment by Brandner et al. [32] is numerically replicated. The schematic of the experiment is shown in Fig. 4.4a. According to the experiment setup, a sphere 0.15 m in diameter was placed on the centreline of the closed recirculating water tunnel (with no-slip walls) with a dimension of 0.6 m × 0.6 m × 2.6 m. The upstream

distance is 0.75 m and the downstream distance is 1.85 m. The 3D-mixture approach in conjunction with the Schnerr-Sauer cavitation model was performed to replicate the experimental conditions. Two different RANS turbulence models were tested: the standard k-ω, and the standard k-ε with enhanced wall treatment. The grid resolution for the 3D geometry was 4518215 cells. Transient simulations are performed with a constant time step of 1×10^{-4} and the maximum iterations per time step of 30. The simulations converge if the residuals are less than 1×10^{-4}. The second$-$order upwind discretization scheme is used to solve the momentum, turbulent kinetic energy, and turbulent dissipation energy, while the PRESTO and QUICK discretization schemes are selected to solve the pressure and volume fraction equations, respectively. In the experimental study, the inlet flow rate is specified at 9 m/s and the outlet static pressure is used to adjust the cavitation number σ ranging from 0.36 to 0.8. However, the CFD model cannot reproduce the experimental results by changing the static outlet pressure. To obtain the same cavitation numbers, the numerical simulation was carried out at varied inlet velocity between 24 and 36 m/s. The cavitation number σ is defined as [4]:

$$\sigma = \frac{P_\infty - P_V(T_\infty)}{\frac{1}{2}\rho_l U_{in}^2} \tag{4.3}$$

where P_∞ is the outlet static pressure, P_v is the saturation vapor pressure at the reference temperature (T_∞), ρ_l is the density of the liquid phase, and U_{in} is the inlet velocity. To compare the numerical results with the experiment, the measurements of the position angle α on the sphere surface (see Fig. 4.4b) were conducted over a wide range of cavitation numbers from 0.36 to 0.8.

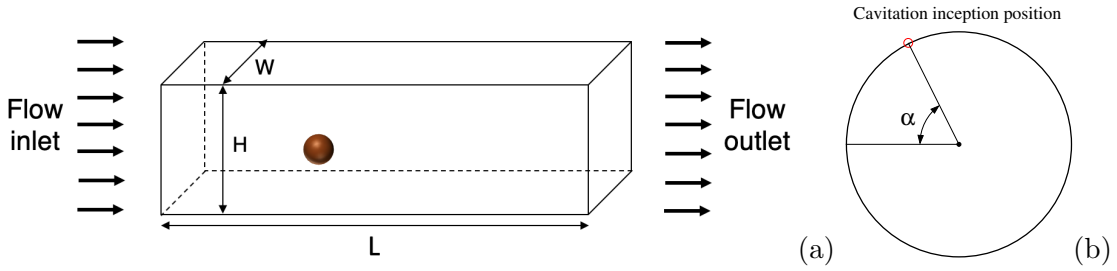

Figure 4.3: Schematic view of an experimental water tunnel - (a) and the position angle α -(b).

Fig. 4.4 compared the predicted inception position of the cavitation from two different turbulence models against the experimental data on the surface of the particle at various cavitation numbers. The experimental data is adapted from the experiment carried out by Brandner et al. [32]. As can be seen from the figure, the k-ε turbulence model can suc-

cessfully predict the position of cavitation inception at various cavitation numbers between 0.36 and 0.8, while a significant deviation is produced from the k-ω model in comparison to the experimental measurements. In this figure, the 3D views of the cavitation zones are illustrated by the time-averaged iso-surfaces of the vapor volume fraction of 0.1 at σ=0.36 and 0.8. The predicted mean angular position angle α increases linearly from 72^o to 87^o as the cavitation number rises from 0.36 to 0.8, which indicates that the onset of the cavitation is significantly affected by the cavitation number.

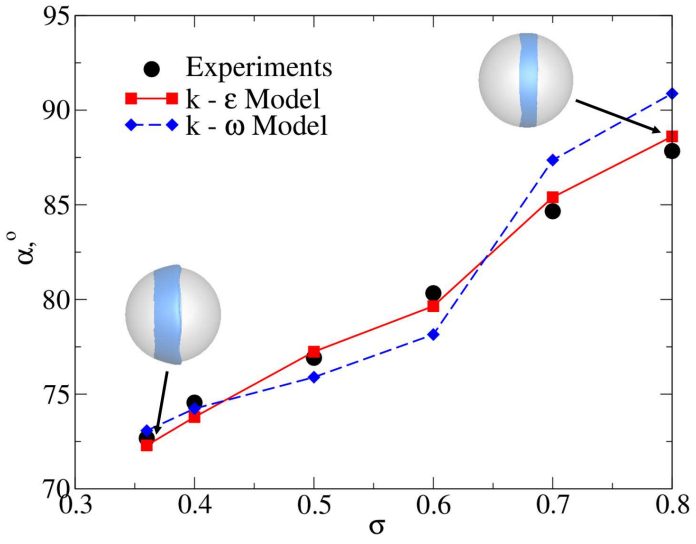

Figure 4.4: Experimental and simulated mean angular position of the cavity at a range of cavitation numbers.

4.5 Results and discussions

In order to unify the results from the simulations, we use two dimensionless parameters: the Reynolds number, Re, and the pressure loss coefficient, K, are considered in this study. The formula of each parameter is expressed as [4] [32]:

$$Re = \frac{\rho_l U_{in} D_p}{\mu_l} \tag{4.4}$$

$$K = \frac{(P_{in} - P_{min})_{static}}{\frac{1}{2}\rho_l U_{in}^2} \tag{4.5}$$

where U_{in} is the inlet velocity, D_p is the diameter of a particle, ρ_l and μ_l are the density and the viscosity of the liquid phase and P_{in} and P_{min} are the inlet and minimum static pressure.

4.5.1 Grid independence study

The resolution of the computational grid has a significant influence on the accuracy of numerical results. To define an appropriate grid size for the simulations, the smooth spherical particle (Particle−1) and smooth cylindrical particle (Particle−2) were employed at Re=240. Four different grids were tested for different particle types, containing 83040 to 220160 (Grid−1), 332160 to 880640 (Grid−2), 1328640 to 3522560 (Grid−3), and 1713963 to 4083659 (Grid−3) computational cells (see Table 4.4). A simulation with the same boundary conditions was conducted for all four grids.

Particle shape	*Grid−1, cells*	*Grid−2, cells*	*Grid−3, cells*	*Grid−4, cells*
Particle−1	83 040	332 160	1 328 640	1 713 963
Particle−2	220 160	880 640	3 522 560	4 083 659

Table 4.4: The mesh resolutions for Particle−1 and Particle−2.

To select an optimum grid resolution for the laminar cavitating flow, the concentration profiles of the vapor phase along the surface of Particle−1 and Particle−2 are illustrated in Fig. 4.5. It was found that Grid−3 and Grid−4 show less deviation in results when compared to the distribution of the vapor volume fraction with different meshes for Particle−1 and Particle−2. Fig. 4.6 presents the volume fraction of the vapor phase predicted by the Grid−2, Grid−3, and Grid−4 mesh resolutions. The red color represents the maximum value of the vapor volume fraction, while the blue color indicates the minimum value of the vapor volume fraction. It can be observed that the Grid−2 mesh, with 332160 cells and 880640 cells, underestimate the magnitude of vapor on the cavitation region (Z/D=0.05 to 0.2) from the surface of Particle−1 and at Z/D=0 to 0.5 from the surface of Particle−2. Meanwhile, the Grid−3 and Grid−4 meshes, with 1328640 cells and 1713963 cells for Particle−1 and 3522560 cells and 4083659 cells for Particle−2, provide close solutions for predicting the characteristic of the cavitation around the particle surface. In the view of the influence of calculation accuracy, we performed our further simulations varying the number of total cells from 1328640 to 3522560 (Grid−3) depending on the different particle types. This provides an optimal value to ensure the appropriate accuracy in the numerical simulations and reasonable computational cost is required.

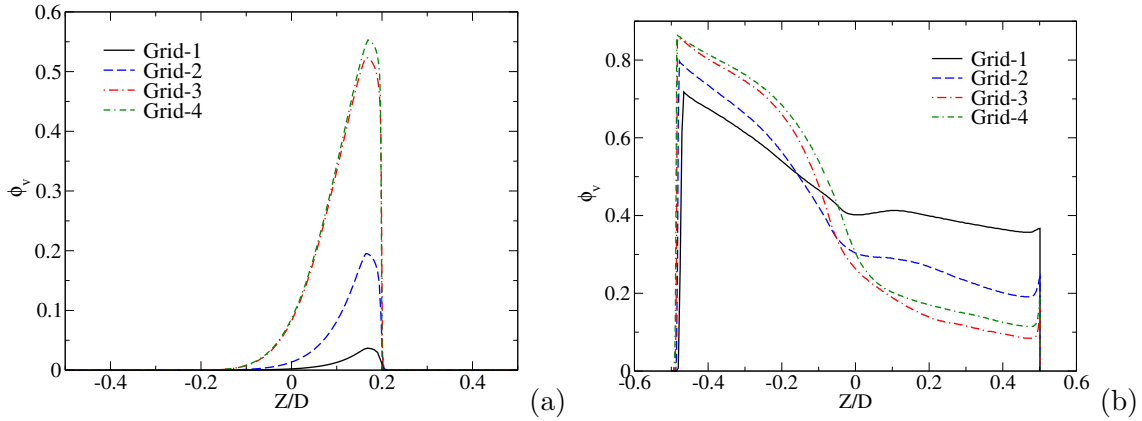

Figure 4.5: The distribution of the volume-averaged vapor volume fraction along the surface of (a) - Particle−1 and (b) - Particle−2 at Re=240. The details of the mesh resolutions for Particle−1 and Particle−2 are given in Table 4.4.

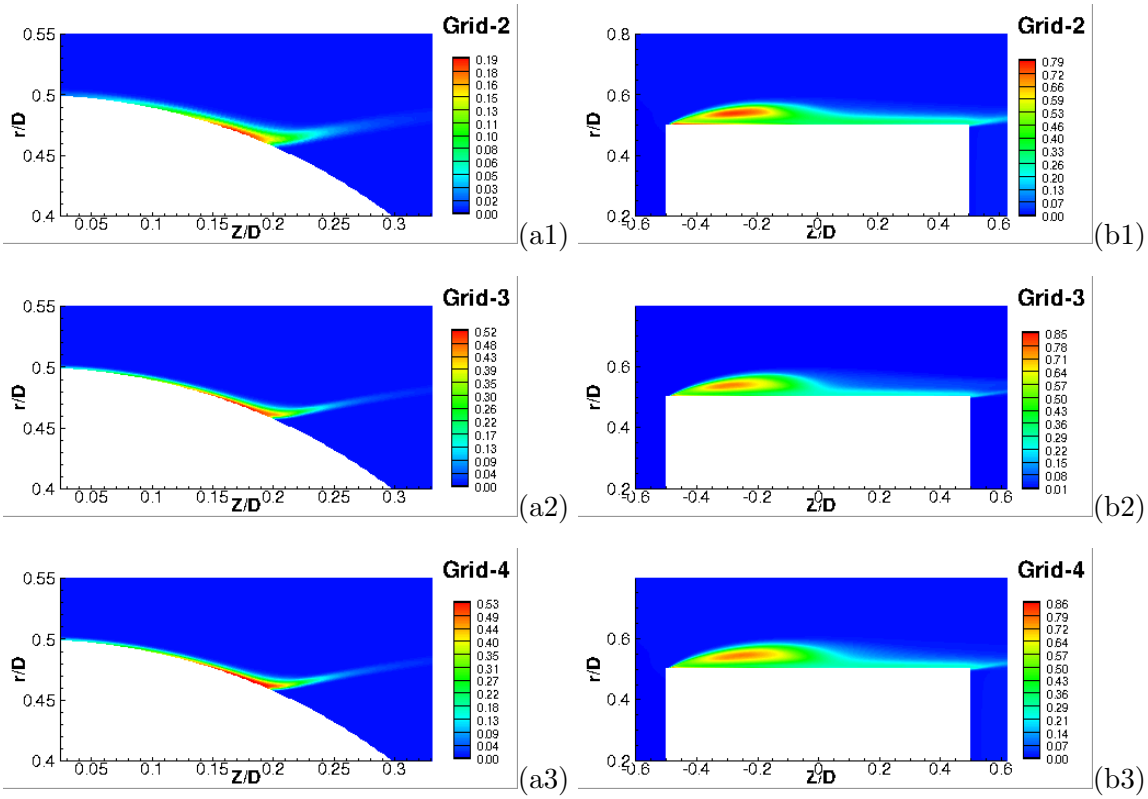

Figure 4.6: Contours of the vapor volume fraction over (a) - Particle−1 and (b) - Particle−2 with D_p=10 μm at Re=240: (1) - Grid−2: 332 160 cells for Particle−1 and 880 640 cells for Particle−2, (2) - Grid−3: 1 328 640 cells for Particle−1 and 3 522 560 cells for Particle−2, (3) - Grid−4: 1 713 963 cells for Particle−1 and 4 083 659 cells for Particle−2.

4.5.2 Effect of the particle shape and surface roughness

The influence of the particle shape and surface roughness on the cavitation is studied for different particle types (Particle−1 to 4) under the same operation conditions explored in the previous section. In particular, the simulations are performed based on a 2D steady axis−symmetric model. The particle diameter was set to 10 μm and the inlet velocity was changed in the range from 0.1 to 25 m/s ($Re \leq 250$).

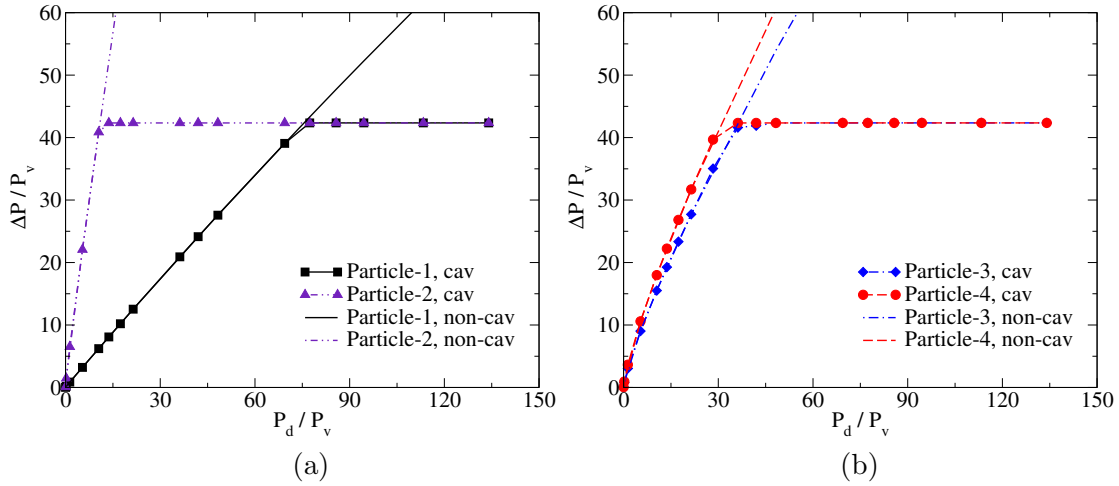

Figure 4.7: The ratio of static pressure drop to vapor pressure $\Delta P/P_V$, as a function of the ratio of dynamic head to vapor pressure, P_d/P_V for (a) - Particle−1 and Particle−2 and (b) - Particle−3 and Particle−4 with D_p=10 μm.

Fig. 4.7 shows the ratio of the static pressure drop to the vapor pressure $\Delta P/P_V$, as a function of the ratio of the dynamic head to the vapor pressure, P_d/P_V, from cavitating and non-cavitating flows for Particle−1 to Particle−4. A virtually linear relation can be observed between the static pressure drop and dynamic head from non-cavitating flows. However, the inflection point can be found concerning the cavitating flows. This inflection point corresponds to the onset of cavitation, where vapor bubbles start to form on the surface of the particle. As the dynamic head increases from the onset of cavitation, the maximum static pressure drop is reached and the static pressure drop becomes invariant with respect to further increases in the dynamic head. Under different characteristic curves illustrated in Fig. 4.7a, the critical $P_{d,c}/P_V$ for Particle−1 and Particle−2 are 77 and 10, respectively. This suggests that the cavitation starts much earlier over the surface of the particle with a cylindrical shape (flat surface) than the one with a spherical shape (curved surface). Fig. 4.7b exhibits the same static pressure drop profile for Particle−3 and Particle−4. It can be observed that Particle−3 (K_R=0.08) and Particle−4 (K_R=0.18) exhibit the same trend in the static pressure drop over the full range of P_d. The corre-

sponding $P_{d,c}/P_V$ is observed to be 36 for Particle−3 and 4, indicating that the cavitation inception is not influenced by the height of the irregular surface on the particle. However, the inception of cavitation is earlier in the spherical particle with a rough surface (Particle−3 and Particle−4) than in that with a smooth surface (Particle−1). This phenomenon is mainly because the local pressure of the fluid drops significantly over the rough particle surface compared to the smooth particle. Fig. 4.8 shows the pressure contours at different Reynolds numbers. Examination of the pressure contours reveals that the location of the minimum pressure moves upstream along the particle surface as the Reynolds number increases from 1 to 250.

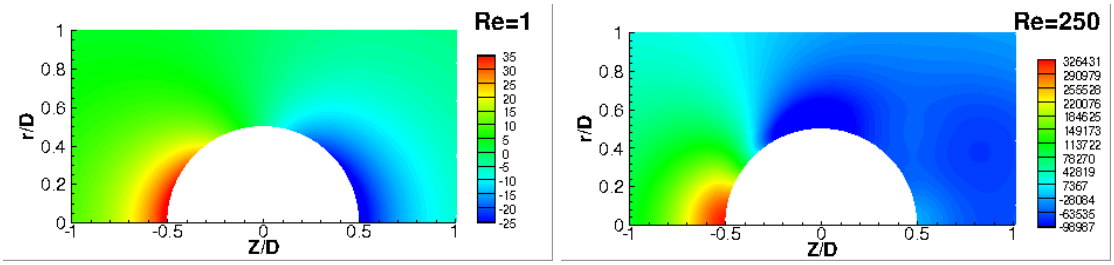

(a) (b)

Figure 4.8: Countour plots of pressure at (a) - Re=1 and (b) - Re=250.

Figs. 4.9a and b depict the calculated pressure loss coefficient K as a function of the Reynolds number Re for Particle−1 to Particle−4. As Re increases from 1 to 10, the value of K decreases dramatically for all particle types. In non-cavitating flow conditions, a slightly declining trend on K can be found over a wide range of Re (10 to 250). In cavitating flow conditions, the decreasing trend on K is more significant after the inception of cavitation. We can clearly observe the predicted critical Reynolds number Re_c, which indicates the cavitation inception for all particles from the profiles. When the particle shape changes from the sphere (Particle−1) to the cylinder (Particle−2), the value of Re_c decreases from 190 to 70. By contrast, the change in the surface roughness coefficient from 0.08 (Particle−3) to 0.18 (Particle−4) presents the same value of Re_c=130, further confirming that the particle shape has a significant influence on the cavitation inception but that changing the height of the irregular surface on a particle exhibits a negligible effect on this.

To assess the influence of the particle shape and surface roughness on the generation of cavitation, the numerical results for the predicted volume of the cavitation are compared for Particle−1 to Particle−4. Fig. 4.9c shows the volume ratio of vapor to particle V_v/V_p as a function of the Reynolds number Re. From this profile, the particle shape and surface roughness are clearly seen to have a significant influence on the production of the vapor. As

can be seen in the figure, the higher vapor volume is produced from Particle−4, Particle−3, and Particle−2 except for the lowest computed value from Particle−1. Moreover, the trend for the vapor volume to rise when the Reynolds number increases from 180 to 260 is clearly seen for all particle types. Fig. 4.9d presents the relationship between the volume ratio of vapor to particle V_v/V_p and the pressure loss coefficient K. The development of the vapor volume is seen to increase as the value of K decreases from 0.7 to 0.3. In particular, the smooth cylindrical particle (Particle−2) generates more vapor than the smooth spherical particle (Particle−1) and the particle with a higher roughness coefficient (Particle−4) produces more vapor than that with a lower roughness coefficient (Particle−3). This higher value of the vapor volume can be attributed to the expanding lower static pressure region around the particle surface as the particle shape and surface roughness change.

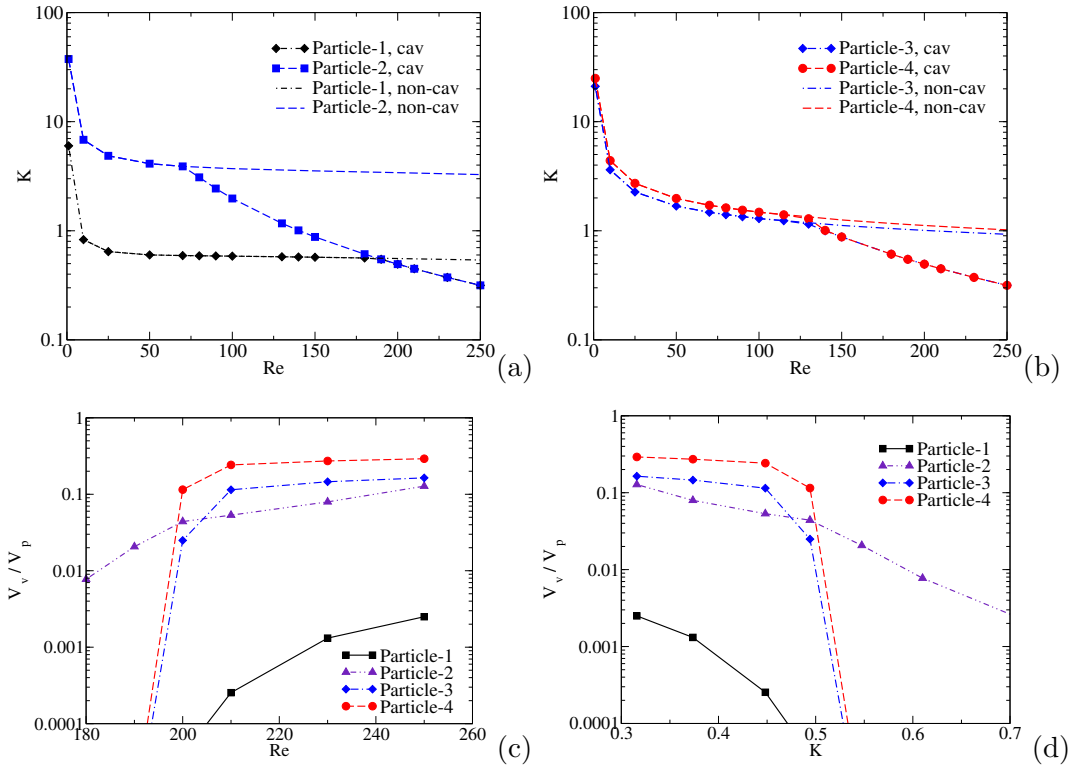

Figure 4.9: Integral characteristics predicted numerically for particle with D_p=10 μm: (a) - pressure loss coefficient as a function of Reynolds number for Particle−1 and Particle−2; (b) - pressure loss coefficient as a function of Reynolds number for Particle−3 and Particle−4; (c) - the ratio of volume-averaged vapor volume to particle volume as a function of the Reynolds number; (d) - the ratio of volume-averaged vapor volume to particle volume as a function of the pressure loss coefficient.

To analyze the cavitation behaviors, the distributions of the vapor volume fraction around Particle−1 to Particle−4 with D_p=10 μm obtained from various Reynolds number are plotted in Fig. 4.10 to 4.12. From the plots, different performance can be seen between different particles with variations in the Reynolds number. As shown in these figures, the cavity first appears on the top region of each particle surface, then grows further and attaches along the particle surface to the back of the particle as Re increases from the critical Reynolds number to 250. For Particle−1 and Particle−2, a clear cavity region can first be observed at Re=190 and 70, while an earlier appearance of cavitation can be seen at Re=130 for Particle−3 and Particle−4, respectively. This can be observed in Figs 4.10a2,c2, Fig 4.11a2, and 4.12a2, which presents the zoomed view of the vapor volume fraction distribution on the surface of each particle.

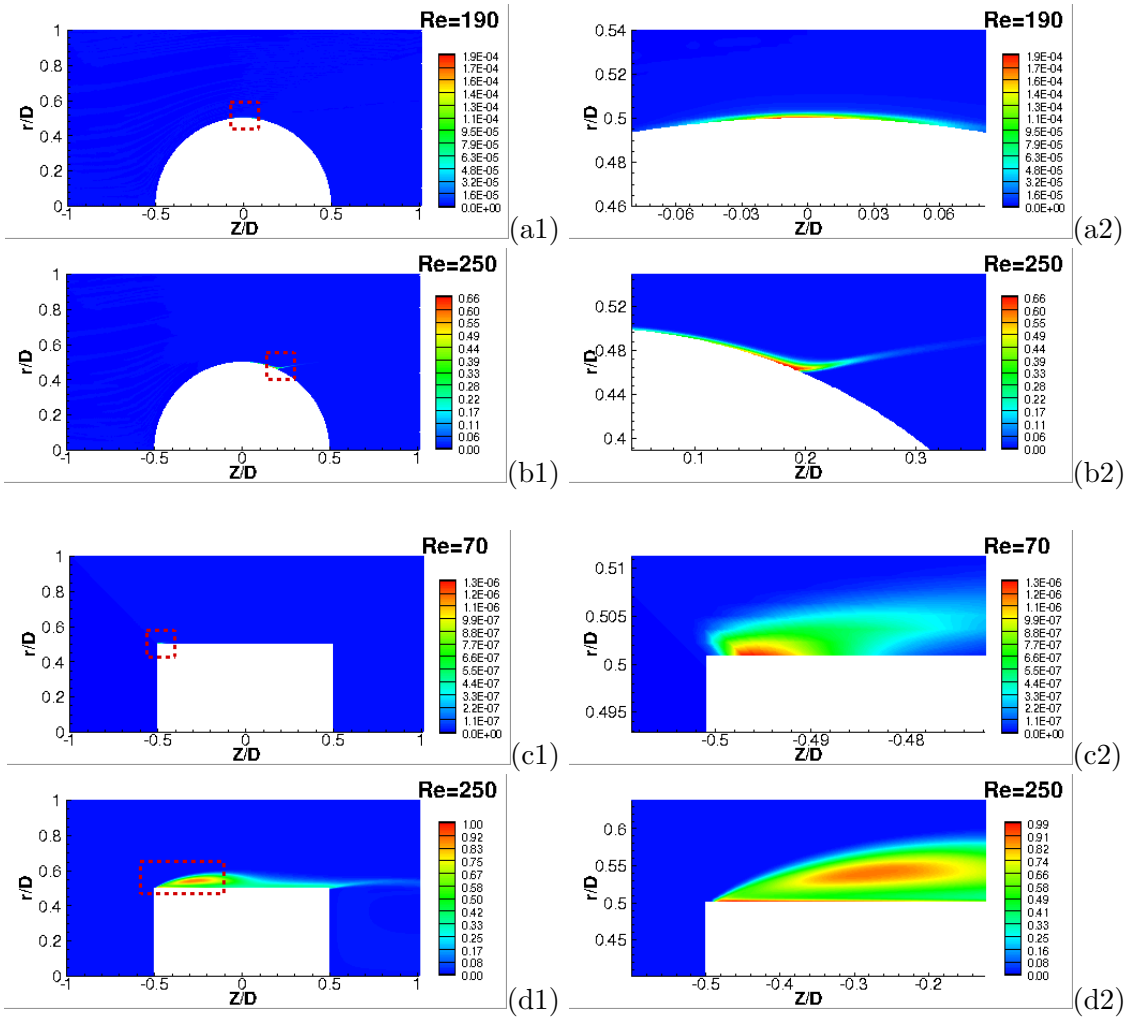

Figure 4.10: Full view - (1) and zoom view - (2) of vapor volume fraction for Particle−1 and Particle−2 with D_p=10 μm: (a) - Re=190; (b) - Re=250; (c) - Re=70; (d) - Re=250;

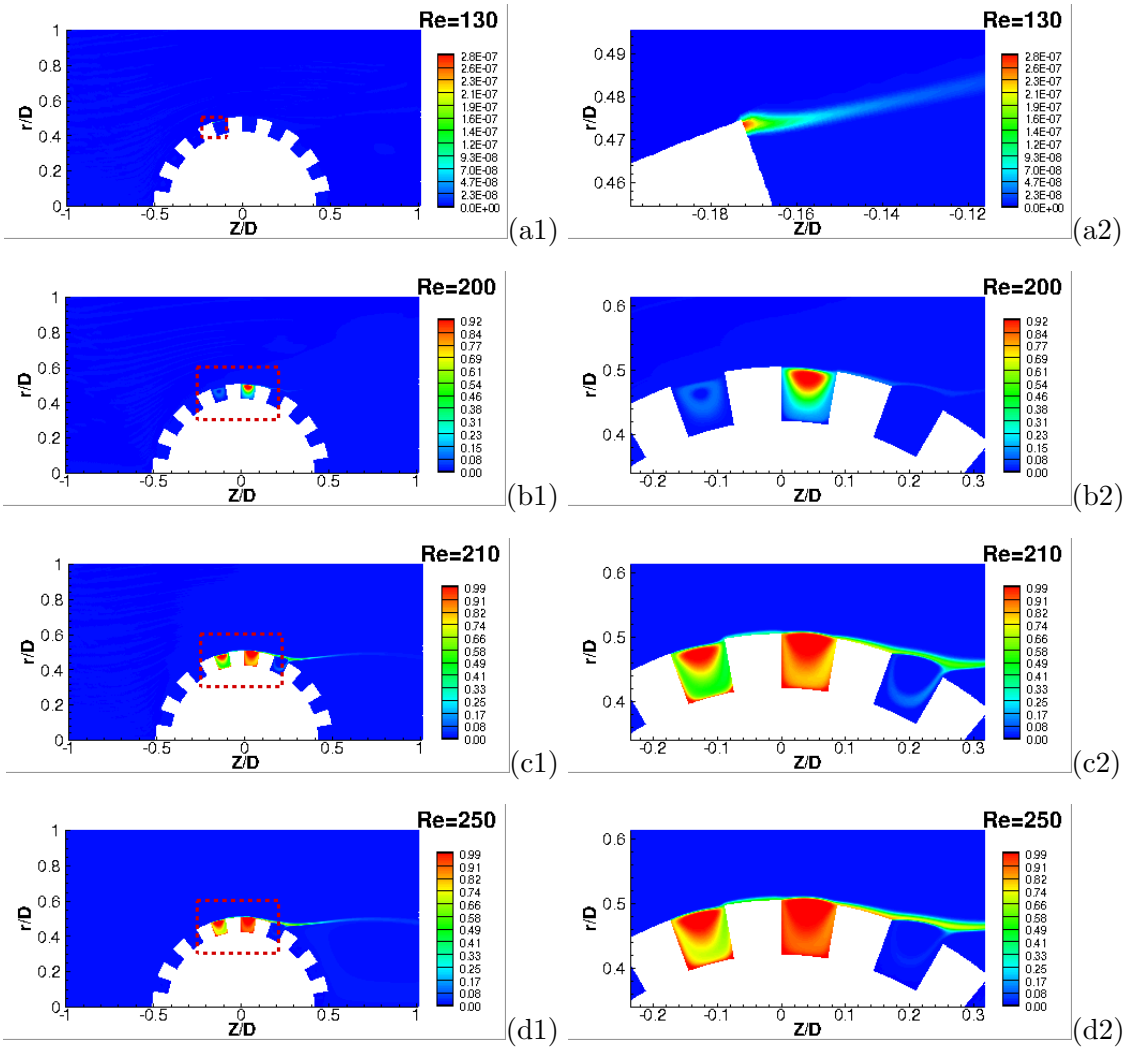

Figure 4.11: Full view - (1) and zoom view - (2) of vapor volume fraction for Particle−3 with D_p=10 μm: (a) - Re=130; (b) - Re=200; (c) - Re=210; (d) - Re=250;

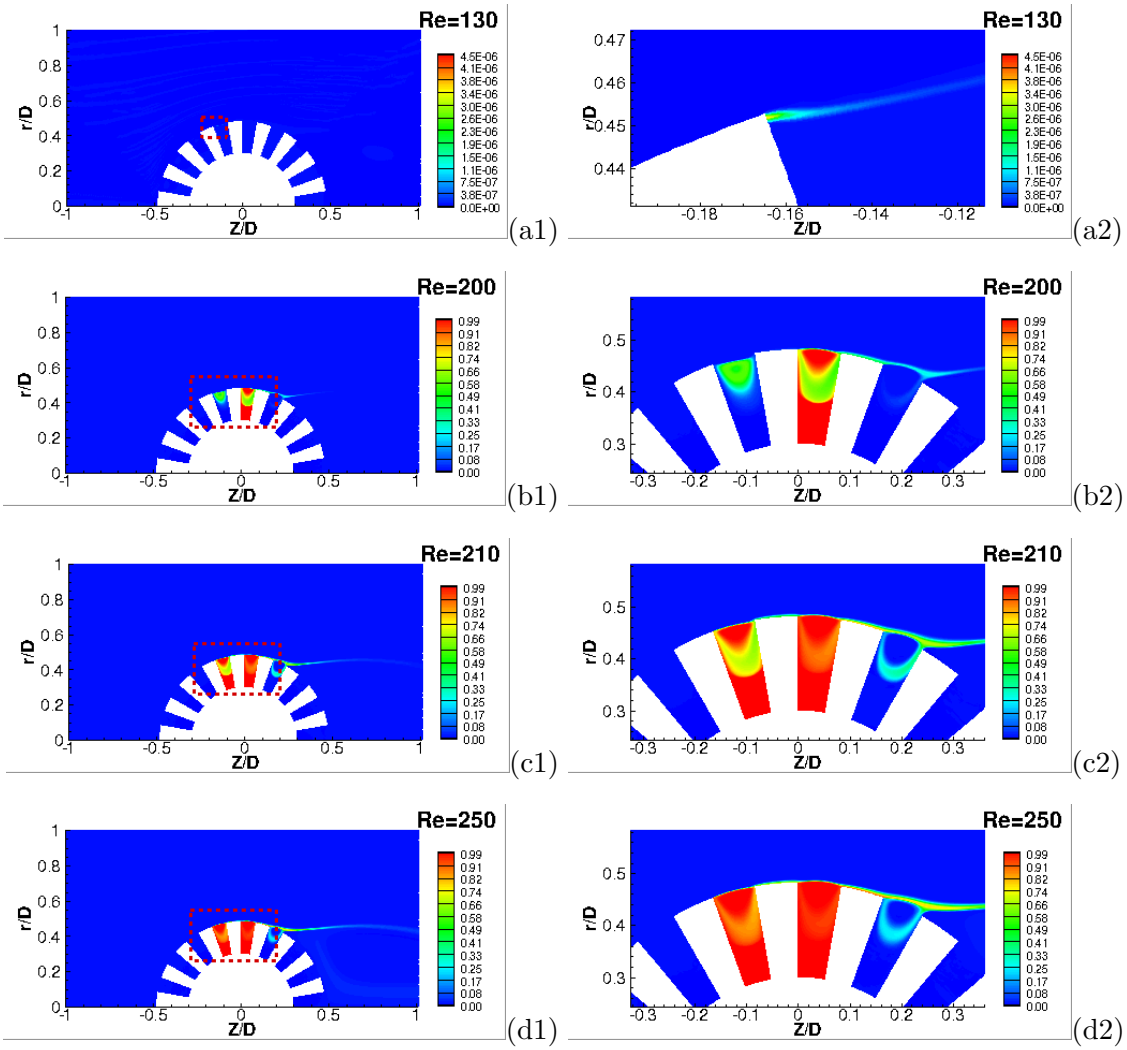

Figure 4.12: Full view - (1) and zoom view - (2) of vapor volume fraction for Particle−4 with D_p=10 μm: (a) - Re=130; (b) - Re=200; (c) - Re=210; (d) - Re=250;

4.5.3 Single−particle versus multiple−particles

To investigate the effect of the particle number on the flow characteristics and cavitation generation, single Particle−1 and multiple Particle−1, with a diameter of D_p=10 μm, are used, respectively (see Fig. 4.2a and e). It should be noted that the multiple-particle case consists of 10 particles in a horizontal line, and the distance between two particles is 10 μm. Fig. 4.13a compares the ratio of static pressure drop to vapor pressure $\Delta P/P_V$ of the single and multiple Particle−1 at different ratios of dynamic head to vapor pressure, P_d/P_V. As seen, the value of $\Delta P/P_V$ increases linearly with P_d/P_V for single and multiple-particle cases in the non-cavitating flows. In the case of a cavitating flow, the onset of cavitation

appears at $P_{d,c}/P_V = 77$ and 94 for single-particle and multiple-particle cases, respectively. The comparison reveals that as the particle number increases in a horizontal line, the onset of cavitation is delayed. This can be explained by the relatively high-pressure region established between the particles. Given the high pressure in this region, the local pressure over the particle surface is affected. Hence, the inception of cavitation is delayed with multiple−particles in a line.

Fig. 4.13b shows the relationship between K and Re with different numbers of particles under non-cavitational and cavitational conditions. It can be seen that a rapid decline in K occurs in the range of Re between 1 and 10 and a gradually decreasing trend can be found over the range between 10 and 250 in the non-cavitating flow conditions. On the other side, the value of K starts to decrease significantly when the onset of cavitation takes place in the cavitating flow, contributing to a critical Reynolds number of $Re_c = 190$ and 210 for the single-particle and multiple-particle cases, respectively. This further confirms that the multiple−particles arranged in a horizontal line delay the inception of cavitation as compared to the single−particle in a free-stream domain.

Figs. 4.13c and d present a comparison between the trends of a volume ratio of vapor to particle V_v/V_p as a function of the Reynolds number Re and the pressure loss coefficient K for the single-particle and multiple-particle cases. As can be observed from the figures, the trends for single- and multiple-particle cases are qualitatively similar. In particular, the value of V_v/V_p is reported to increases from 1×10^{-8} to 3×10^{-3} as Re increases from 180 to 250 and to decline in K from 0.55 to 0.32 for the single-particle case, while the value of V_v/V_p ascends from 1×10^{-8} to 9×10^{-4} as Re increases from 205 to 250 and K decreases from 0.46 to 0.32 for the multiple-particle case. At a fixed Re or K value, the single-particle case gives a higher value of V_v/V_p, while the multiple-particle case shows a minimum value of V_v/V_p. This suggests that the single−particle, in the absence of bubbles trapped on its surface, produces more cavitation bubbles than multiple−particles under laminar cavitating flow conditions.

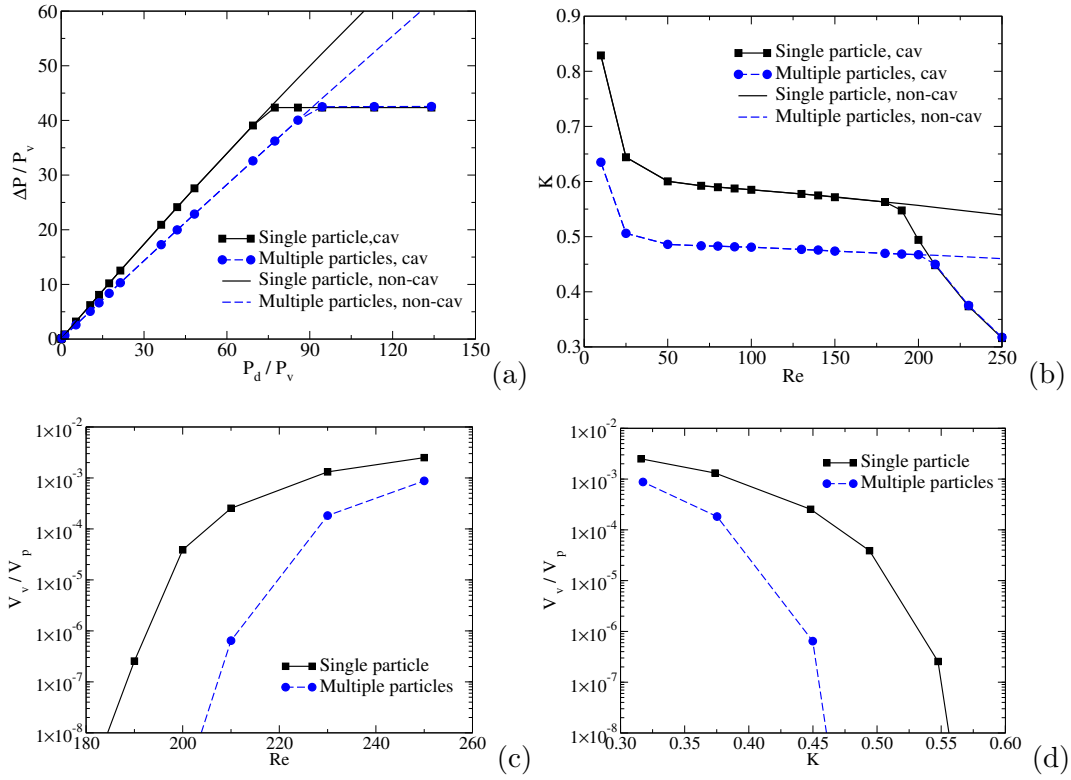

Figure 4.13: Integral characteristics predicted numerically for single−particle and multiple−particles with D_p=10 μm: (a) - the ratio of static pressure drop to vapor pressure $\Delta P/P_V$, as a function of the ratio of dynamic head to vapor pressure, P_d/P_V; (b) - pressure loss coefficient as a function of the Reynolds number; (c) - The ratio of volume-averaged vapor volume to particle volume as a function of the Reynolds number; (d) - The ratio of volume-averaged vapor volume to particle volume as a function of the pressure loss coefficient.

4.5.4 Effect of particle surface temperature

To study the effect of non-isothermal conditions on the flow characteristics in detail, calculations are performed on Particle−4 with surface temperatures of T_p=40°C, 60°C, 80°C and 99.9°C. Fig. 4.14a demonstrates the effect of the particle surface temperature on the pressure loss coefficient K for various Reynolds numbers Re. One can see that in all cases, the value of K declines significantly as Re rises from 1 to 250. The particle temperature in the range between T_p=40°C and 80°C leads to a slightly earlier inception of cavitation from Re_c=140 to 110. Going beyond this range, the effect of the particle surface temperature is significant. In particular, an increase in the particle surface temperature from 80 to 99.9°C shifts the inception of cavitation to a lower value of Re_c from 110 to 25, which indicates that the higher particle surface temperature is beneficial to the inception of cavitation.

The variation curve for a volume ratio of vapor to particle V_v/V_p with the Reynolds number Re is shown in Fig. 4.14b. As can be seen from the figure, the value of V_v/V_p increases as Re rises from 1 to 250, and the rate of increase declines gradually beyond the critical Reynolds number for each particle surface temperature. Raising the particle surface temperature from 20°C to 99.9°C leads to notable changes in the vapor production. In particular, a higher V_v/V_p can be found at a constant value of Re when the particle surface temperature increases from T_p=20 to 99.9°C. The averaged vapor production increases 200% as Re >200, which indicates that the higher particle surface temperature generates more cavitation bubbles. In fact, with a fixed inlet fluid temperature, the increase in the particle surface temperature means that more heat is transferred from the particle surface to the fluid flow, thus more molecules absorb sufficient energy to overcome the intermolecular forces of attraction and subsequently more cavities form in the liquid.

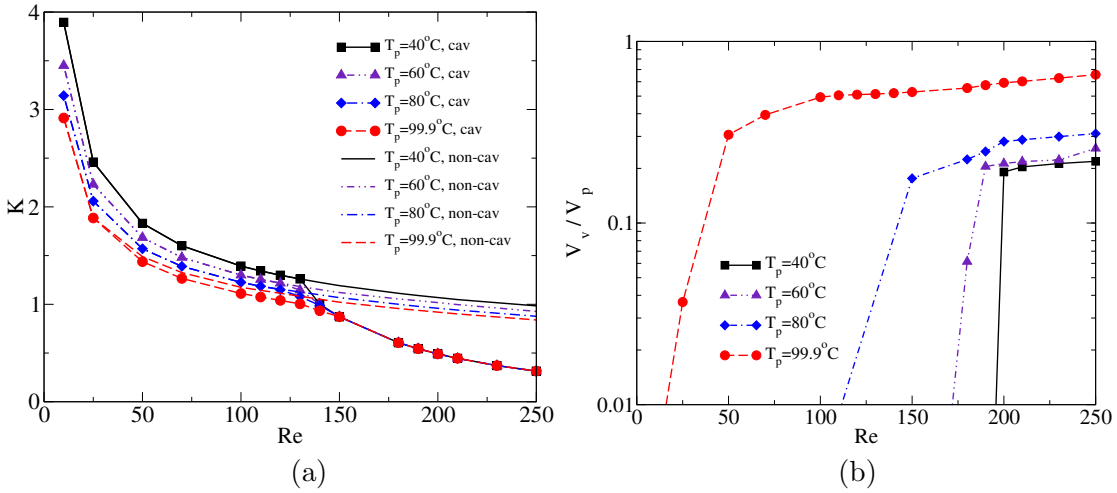

Figure 4.14: Integral characteristics predicted numerically for Particle−4 with D_p=10 μm: (a) - pressure loss coefficient as a function of the Reynolds number; (b) - The ratio of volume-averaged vapor volume to particle volume as a function of the Reynolds number.

Figs. 4.15a1-a4 show the temperature fields around Particle−4 with particle surface temperatures of T_p=40°C, 60°C, 80°C and 99.9°C. Here, the Reynolds number Re is set to 200 and the inlet fluid temperature T_{in}=20 °C. As can be observed from the figures, the use of different particle surface temperatures shows that there is the same extent of fluid temperature on the particle surface, while the magnitude of the fluid temperature increases as the particle surface temperature arises from 40°C to 99.9°C. Figs. 4.15b1-b4 show the vapor volume fraction contour plots for Particle−4 with corresponding particle surface temperatures. It is evident from the simulation results that the cavitation area near the surface of the particle expands rapidly as the particle surface temperature increases

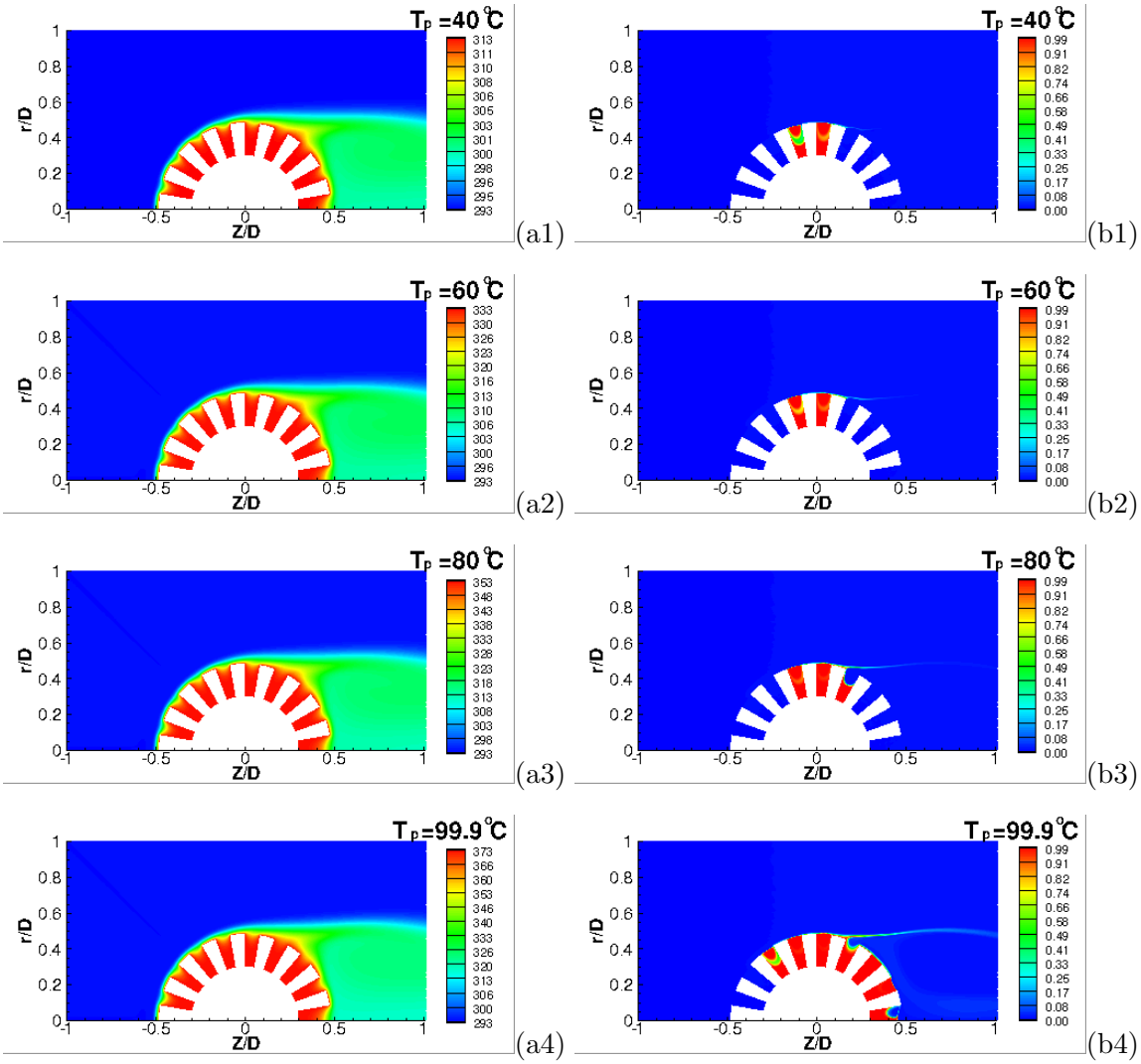

Figure 4.15: Contours of (a) - fluid temperature and (b) - vapor volume fraction for Particle−4 with D_p=10 μm at Re=200: (1) - T_p=40°C; (2) - T_p=60°C; (3) - T_p=80°C; (4) - T_p=99.9°C.

from 20 to 99.9°C. This means that a higher particle surface temperature promotes the development of cavitation.

Studying the relationship between various particle sizes and the inception of cavitation in the isothermal system, Fig. 4.16 depicts the comparison results between the approximation and the CFD model for the diameter of Particle−1 between 10 and 100 μm. The cavitation flow over the particle with a diameter of 10 μm was modelled in a 2D axis−symmetric free stream domain, while the cavitation flow around the particle with a diameter in the range between 20 and 100 μm was simulated in a 3D free stream domain.

As can be seen from the figure, the critical Reynolds number, Re_c, increases from 190 to 1800 as the value of the diameter of the particle, D_p, rises from 10 to 100 μm. To predict Re_c based on any given value of the particle diameter, a linear regression method is proposed to generate an empirical model using the statistical toolbox of MATLAB. The equation seen in the figure corresponds to the linear regression line fitted to the CFD data points using the least square method. A good agreement is obtained between the empirical and the modelled measured values, revealing that the empirical model developed here is a reliable and accurate means of predicting the cavitation inception for various particle sizes between D_p= 10 and 100 μm. Table 4.5 shows the critical Reynolds number, Re_c, and the corresponding volume ratio of vapor to particle, V_v/V_p, for various particle sizes. The predicted critical values of V_v/V_p are 3×10^{-5}%, 0.15%, 2.5%, and 1.63% for particles with diameters of 10, 20, 50 and 100 μm, respectively. It should be noted, that the critical value of V_v/V_p for the particle of 10 μm is significantly smaller than for particles of 20 μm, 50 μm and 100 μm. This is mainly due to the fact that the numerical result for the particle of 10 μm was obtained from the 2D model, while that for other particles was obtained from the 3D model.

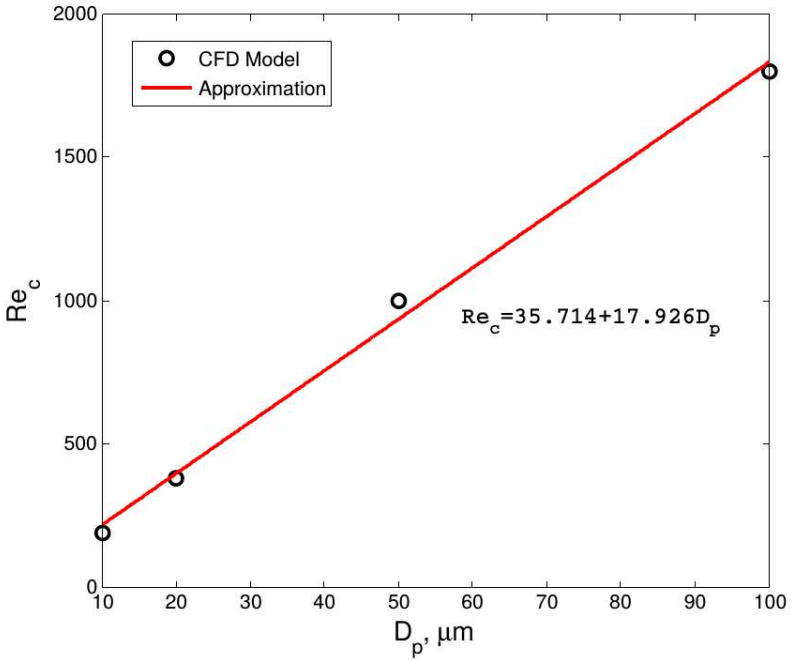

Figure 4.16: Global fit between the approximation and CFD results: critical Reynolds number as a function of the diameter of Particle−1 in the range between 10 and 100 μm.

D_p, μm	Re_c	V_v/V_p, %
10	190	3×10^{-5}
20	380	0.15
50	1000	2.50
100	1800	1.63

Table 4.5: The critical Reynolds number and the volume ratio of vapor to particle for various particle sizes.

Fig. 4.17 depicts the particle Reynolds number contours for three solid mass concentrations of 5 wt%, 15 wt%, and 30 wt% at the critical inlet velocity of 0.9 m/s, 0.6 m/s, and 0.4 m/s, respectively. The particle size of D_p=23 μm was used in the simulation. It can be observed that the large velocity difference between the liquid and solid phases is mainly distributed near the inlet and outlet of the throat section. The maximum value of Re_p decreases from 30 to 8 as the solid mass concentration increases from 5 wt% to 30 wt%. Based on the empirical model (see Fig. 4.16) developed in the micro-scale cavitating flow study, the Re_p can be calculated for a special particle diameter. For particle size of D_p=23 μm, the Re_p is calculated to be 488. In the macro-scale study, we considered that the entrapped air bubbles on the crevices of the solid particles is mainly responsible for the enhanced cavitation activities. In the micro-scale study, we found that the cavitation behavior is affected by each particle-flow interaction near the particle surface. However, the maximum value of Re_p obtained from the macro-scale cavitating flow study (Re_p=30) is significantly less than the value calculated from the micro-scale cavitating flow study (Re_p=488). This indicates that each particle-flow interaction has negligible effect on the macro-scale cavitation activities in comparison to the entrapped air bubbles on the crevices of the solid particles.

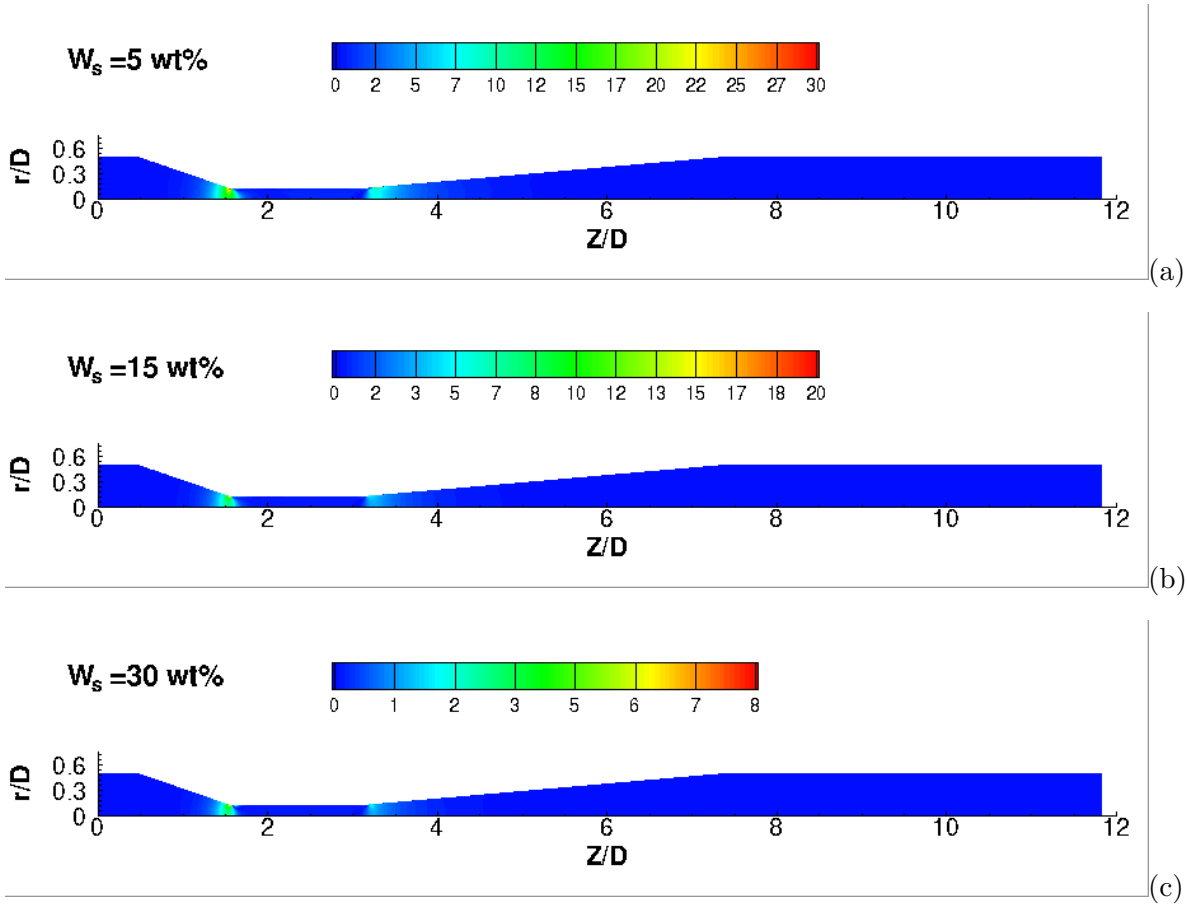

Figure 4.17: Particle Reynolds number, $Re_p = \frac{\rho_l D_p |U_l - U_s|}{\mu_l}$, at critical inlet velocity of $U_{in,c}$=0.9 m/s for W$_s$=5 wt% - (a); $U_{in,c}$=0.6 m/s for W$_s$=15 wt% - (b); and $U_{in,c}$=0.4 m/s for W$_s$=30 wt% - (c).

4.6 Conclusions

In the present study, the cavitation around a solid particle in a laminar and turbulent free-stream domain was analyzed numerically using a 2D and 3D mixture-based CFD-based model available in the commercial CFD software ANSYS FLUENT 16.2. The liquid-vapor phase-mixture-based model combined with the Schnerr-Sauer cavitation model was validated with the experimental data from the literature and good agreement was obtained. The influence of the particle shape, the surface roughness, the number of particles, and the surface temperature on flow characteristics and cavitation behaviors were studied. The following are the main conclusions that can be drawn from this study:

- The results of the CFD study clearly illustrate that the particle shape and sur-

face roughness strongly influence the cavitation behaviors. In particular, the critical Reynolds numbers (Re_c) for Particles−1, 2, 3 and 4 are 190, 70, 130, 130, respectively. This reveals that the cavitation might depend on the particulate Re number for different particle types.

- The studies of the isothermal process clearly showed that the particles with a cylindrical shape (Particle−2) and rough surface (Particle−3 and Particle−4) lead earlier cavitation inception and greater vapor production than the one with a smooth, spherical shape (Particle−1), while increasing the number of particles from one to ten in the horizontal direction leads to a corresponding delay in the cavitation inception from Re_c=190 to Re_c=210 and a reduction in the vapor production.

- The influence of the thermal conditions on cavitation behaviors was potentially very large. Increasing the particle surface temperature from 40°C to 99.9°C is beneficial to the development of cavitation. In particular, the cavitation inception starts to develop much earlier from Re_c=130 to Re_c=25 and the average vapor production increases 200% for Re >200.

- An increases in the particle size from 10 to 100 μm results in an increase in the Re_c from 190 to 1800. Meanwhile, a CFD-based empirical mathematical model for the particle size was proposed to link the particle diameter and critical Reynolds number. The empirical model provided good agreement with the numerically predicted data, which indicates that it can be used to accurately estimate the inception of cavitation for particles with various particle sizes ranging from 10 to 100μm.

4.7 Acknowledgments

Financial support from the Natural Science and Engineering Research Council of Canada (NSERC) is greatly appreciated.

Bibliography

[1] H Shi, M Li, P Nikrityuk, and Q Liu. Experimental and numerical studies of cavitation flows in venturi tubes: geometry and scale-up. *Chemical Engineering Science*, 207: 672–687, 2019.

[2] Hongbo Shi, Mingda Li, Qingxia Liu, and Petr Nikrityuk. Experimental and numerical study of cavitating particulate flows in a venturi tube. *Chemical Engineering Science*, page 115598, 2020.

[3] Robert T Knapp, James W Daily, and Frederick G Hammitt. *Cavitation*. McGraw-Hill, 1970.

[4] Christopher E Brennen. *Cavitation and bubble dynamics*. Cambridge University Press, 2014.

[5] Haipeng Li, Artin Afacan, Qingxia Liu, and Zhenghe Xu. Study interactions between fine particles and micron size bubbles generated by hydrodynamic cavitation. *Minerals Engineering*, 84:106–115, 2015.

[6] Muthupandian Ashokkumar, Raul Rink, and Sergey Shestakov. Hydrodynamic cavitation-an alternative to ultrasonic food processing. *Technical Acoustics/Tekhnicheskaya Akustika*, (9), 2011.

[7] P Senthil Kumar, M Siva Kumar, and AB Pandit. Experimental quantification of chemical effects of hydrodynamic cavitation. *Chemical Engineering Science*, 55(9): 1633–1639, 2000.

[8] Parag R Gogate. Hydrodynamic cavitation for food and water processing. *Food and Bioprocess Technology*, 4(6):996–1011, 2011.

[9] Joe Z Zhou, Haihong Li, Ross S Chow, Qingxia Liu, Zhenghe Xu, and Jacob Masliyah. Role of mineral flotation technology in improving bitumen extraction from mined athabasca oil sands ii. flotation hydrodynamics of water-based oil sand extraction. *The Canadian Journal of Chemical Engineering*, 2019.

[10] Anthony A Atchley and Andrea Prosperetti. The crevice model of bubble nucleation. *The Journal of the Acoustical Society of America*, 86(3):1065–1084, 1989.

[11] HB Marschall, Knud Aage Mørch, AP Keller, and M Kjeldsen. Cavitation inception by almost spherical solid particles in water. *Physics of fluids*, 15(2):545–553, 2003.

[12] JJ Kwan, S Graham, R Myers, R Carlisle, E Stride, and CC Coussios. Ultrasound-induced inertial cavitation from gas-stabilizing nanoparticles. *Physical Review E*, 92 (2):023019, 2015.

[13] Matevž Dular, Rudolf Bachert, Bernd Stoffel, and Brane Širok. Influence of the velocity distribution at the inlet boundary on the cfd prediction of local velocity and pressure fields around a hydrofoil. *Experimental Thermal and Fluid Science*, 32(3): 882–891, 2008.

[14] Narotam Jangir, Prateek Diwedi, and Sumana Ghosh. Design of a hydrodynamic cavitating reactor. *Chemical Engineering & Processing: Process Intensification*, 122: 128–142, 2017.

[15] Alister Simpson and Vivek V Ranade. Modelling of hydrodynamic cavitation with orifice: Influence of different orifice designs. *Chemical Engineering Research and Design*, 136:698–711, 2018.

[16] Boxiong Chen and Michael Oevermann. An eulerian stochastic field cavitation model coupled to a pressure based solver. *Computers and Fluids*, 162:1–10, 2018.

[17] H Yu, L Goldsworthy, PA Brandner, J Li, and V Garaniya. Modelling thermal effects in cavitating high-pressure diesel sprays using an improved compressible multiphase approach. *Fuel*, 222:125–145, 2018.

[18] Mohammad-Reza Pendar and Ehsan Roohi. Cavitation characteristics around a sphere: An les investigation. *International Journal of Multiphase Flow*, 98:1–23, 2018.

[19] Bostjan Gregorc, Matjaz Hribersek, and Andrej Predin. The analysis of the impact of particles on cavitation flow development. *Journal of Fluids Engineering*, 133(11): 111304, 2011.

[20] Buxuan Li, Youwei Gu, and Min Chen. Cavitation inception of water with solid nanoparticles: A molecular dynamics study. *Ultrasonics sonochemistry*, 51:120–128, 2019.

[21] AE Kabeel and Mohamed Abdelgaied. Study on the effect of alumina nano-fluid on sharp-edge orifice flow characteristics in both cavitations and non-cavitations turbulent flow regimes. *Alexandria Engineering Journal*, 55(2):1099–1106, 2016.

[22] Min-Rui Chen, Jin-Yuan Qian, Zan Wu, Chen Yang, Zhi-Jiang Jin, and Bengt Sunden. The hydraulic cavitation affected by nanoparticles in nanofluids. *Computation*, 6(3): 44, 2018.

[23] Xinsheng Cheng, Xueming Shao, and Lingxin Zhang. The characteristics of unsteady cavitation around a sphere. *Physics of Fluids*, 31(4):042103, 2019.

[24] Aswin Gnanaskandan and Krishnan Mahesh. Numerical investigation of near-wake characteristics of cavitating flow over a circular cylinder. *Journal of Fluid Mechanics*, 790:453–491, 2016.

[25] Inc Ansys. Ansys fluent theory guide. *Canonsburg, Pennsylvania*, page 794, 2011.

[26] Elmar Achenbach. Influence of surface roughness on the cross-flow around a circular cylinder. *Journal of fluid mechanics*, 46(2):321–335, 1971.

[27] F. Dierich and P.A. Nikrityuk. A numerical study of the impact of surface roughness on heat and fluid flow past a cylindrical particle. *Int. J. Thermal Sciences*, 65:92–103, 2013.

[28] Günter H Schnerr and Jürgen Sauer. Physical and numerical modeling of unsteady cavitation dynamics. In *Fourth international conference on multiphase flow, New Orleans, USA*, volume 1, 2001.

[29] George Wm Thomson. The antoine equation for vapor-pressure data. *Chemical reviews*, 38(1):1–39, 1946.

[30] Brian P Leonard. A stable and accurate convective modelling procedure based on quadratic upstream interpolation. *Computer methods in applied mechanics and engineering*, 19(1):59–98, 1979.

[31] Frank P Incropera, Adrienne S Lavine, Theodore L Bergman, and David P DeWitt. *Fundamentals of heat and mass transfer*. Wiley, 2007.

[32] PA Brandner, GJ Walker, PN Niekamp, and B Anderson. An experimental investigation of cloud cavitation about a sphere. *Journal of Fluid Mechanics*, 656:147–176, 2010.

Chapter 5

Numerical Study of Mixing of Cavitating Flows in a Venturi Tube[1]

5.1 Introduction

Hydrodynamic cavitation is the process of vapor bubbles forming and growing in a flowing liquid as a result of a decrease in the local pressure at a constant temperature [1, 2]. Hydrodynamic cavitation is one of the candidate technologies that have been successfully adopted in various industrial applications ranging from biodiesel synthesis, food production and water purification to mineral processing. In the mineral extraction process, cavitating Venturi tubes offer the prospect of significantly improving the efficiency of fine particle separation using flotation technology. The main features of Venturi tubes are a convergent section, throat section and divergent section. When the pressure falls to the value of the vapor pressure of the liquid medium as the fluid passes through the throat section of the Venturi tube, cavitation begins to occur at the throat section. A cavitating Venturi tube is a device commonly used in industry to generate micro- and nano-size vapor and air bubbles. Conventional flotation columns produced by injecting cavitation bubbles through Venturi tubes can significantly improve the performance of flotation processes by increasing the probability of bubble-particle collision and adhesion. In addition, Venturi tubes have been widely applied as a passive mixer to the fluid mixing area, such as when mixing gas−gas components [3, 4] and liquid−liquid components [5, 6]. The major advantages of using a Venturi mixer are the high level of mixing efficiency, low energy consumption and

[1]This chapter has been submitted as: Hongbo Shi, Qingxia Liu and Petr Nikrityuk. Numerical Study of Mixing of Cavitating Flows in a Venturi Tube. *The Canadian Journal of Chemical Engineering.*

short mixing length [6]. In this respect, the hydrodynamic cavitation process involving the mixing of two flows is of particular interests in the mining and chemical industries.

With the development of the computational fluid dynamics (CFD) technique, numerical simulation is becoming a common method to provide a detailed understanding of the flow of fluids and phenomena associated with the cavitation system. Since the flow fields in the cavitating Venturi tubes are usually highly turbulent, an accurate computation of the turbulent flow is required in order to evaluate how realistic the flow characteristics of the Venturi tube are. In CFD modeling, two different approaches are commonly used to simulate turbulent flows in cavitating Venturi tubes: Reynolds-averaged Navier-Stokes (RANS) (e.g. Refs.[7, 8, 9]) and Large-eddy Simulations (LES) (e.g. Refs.[10, 11]). Shi et al. [12] used a 2D $k-\omega$ model to develop an empirical model to predict cavitation in different Venturi tubes. Ashrafizadeh et al. [13] employed a 2D $k-\varepsilon$ realizable model to simulate cavitating flows in different Venturi tubes and observed that the cavitation activities can be promoted by a lower divergence angle, higher throat diameter and shorter throat length. Margot et al. [14] studied how the precision of numerical results gathered in a throttle channel was affect by seven different 3D RANS-based turbulence models (($k-\varepsilon$/ low Re/ hybrid, $k-\varepsilon$/ high Re/ standard, $k-\varepsilon$ Re-Normalisation Group (RNG)/ standard, $k-\omega$ shear stress transport (SST) and standard/ high and low Re/hybrid and standard). Nouri et al. [15] used a 3D LES turbulence model to predict the cavitating flow in two different Venturi tubes. They found that the LES model has some merits over the RANS models in capturing the inherent unsteady turbulent structure. Orley et al. [16] numerically investigated cavitating flows in a Venturi nozzle using the LES turbulence model, observing that the cavitation promotes the liquid jet break-up in a lateral direction. Dittakavi et al. [17] employed the 3D LES turbulence model to study turbulence-cavitation interactions within a Venturi tube. The numerical results indicate that the collapse of the vapor bubbles in the divergent section is the major source of vorticity production.

Alongside the numerical studies focused on single-liquid flows from many different aspects, there are almost no CFD studies considering a detailed numerical consideration of a mixing of two-liquid miscible flows in a cavitating Venturi tube. Therefore, the aim of present work is to conduct a computational analysis of two miscible turbulent water flows with a high viscosity difference ($\frac{\mu_2}{\mu_1}$=1 and 10) mixing in a cavitating Venturi tube. In this study, 2D axis−symmetric steady RANS and 3D LES turbulence models are used to predict the mixing behavior of two horizontal water flows for a static pressure drop of 297487 Pa (Case−1) and 297571 Pa (Case−2). Particular attention is paid to the turbulence-cavitation interactions. The numerical simulations are carried out using the commercial CFD software ANSYS FLUENT 16.2 [18]. The following sections describe the model formulation, and numerical results.

5.2 Model formulation

The numerical simulations of water-vapor-phase flows were carried out in a Venturi tube to study the cavitation and mixing characteristics. The schematic drawing of the Venturi tube and its specifications are shown in Fig. 5.1 and Table 5.1, respectively. This design was used by Shi et al. [12] to study the two-phase cavitating flows. The numerical models were validated in the study conducted by Shi et al. [12]. In the present research, liquid water was employed as the liquid phase and water−vapor was used as the vapor phase. The mixing process between two volumetric components without chemical reactions was only conducted within the liquid phase.

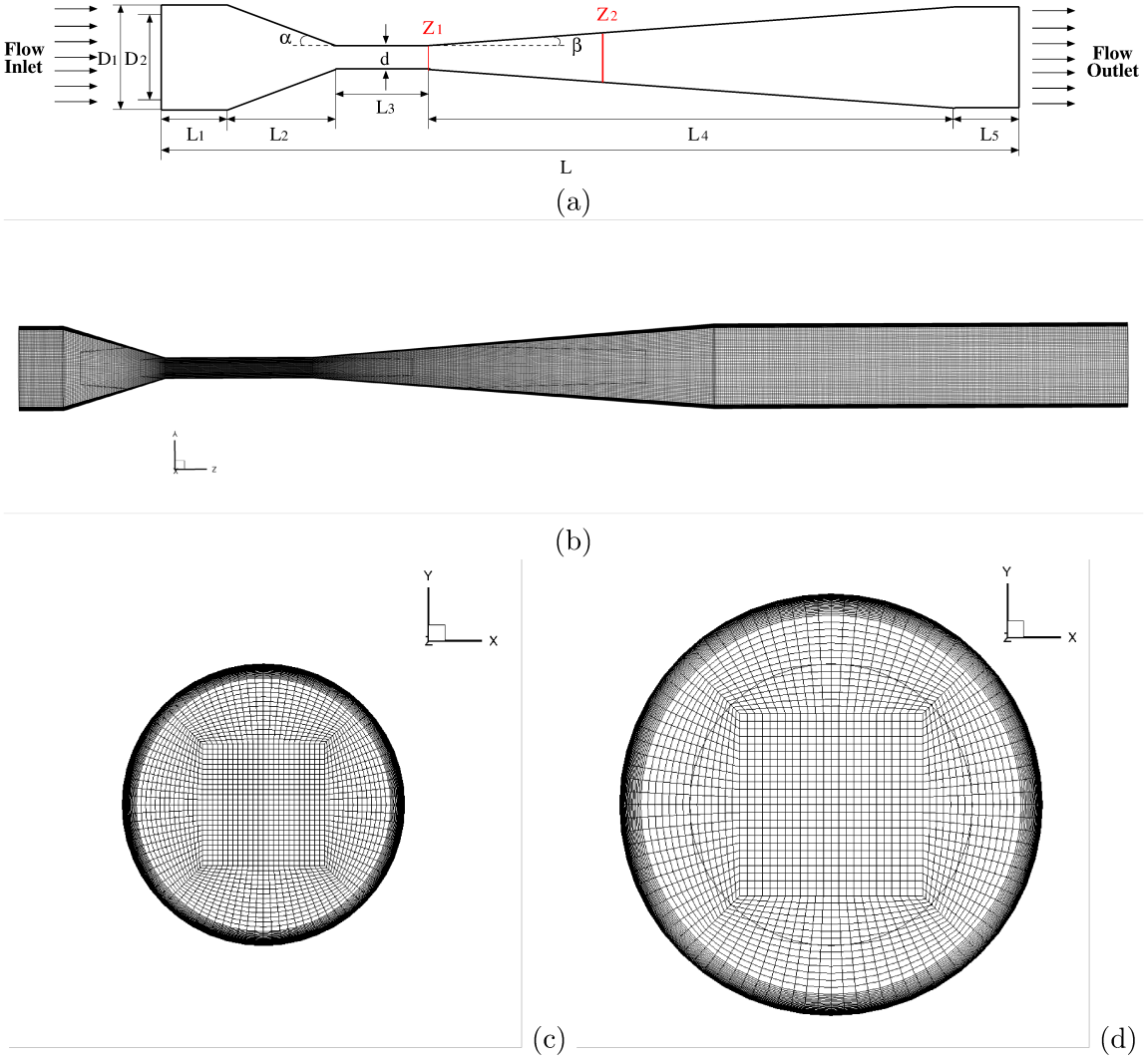

Figure 5.1: Schematic diagram of the Venturi tube - (a); 3D computational structured mesh in the middle plane - (b); Z_1 - (c); and Z_2 - (d).

D_1 *(mm)*	12.7
D_2 *(mm)*	11.43
d *(mm)*	3.18
L_1 *(mm)*	6
L_2 *(mm)*	14
L_3 *(mm)*	20
L_4 *(mm)*	54
L_5 *(mm)*	56
Z_1 *(mm)*	40
Z_2 *(mm)*	49
α *(°)*	19
β *(°)*	5

Table 5.1: Specifications of the cavitating Venturi tube.

The calculations reported in this study represent two sets of cases that differ in the properties of the flow entering into the inlet of the Venturi tube. In the first set of calculations, liquid water with a viscosity of μ_1=0.001 kg/m-s (component−1) was fed into the inner tube and the outer annulus. In the second set of calculations, liquid water with a viscosity of μ_1=0.001 kg/m-s (component−1) and μ_2=0.01 kg/m-s (component−2) was fed into the inner tube and the outer annulus, respectively. The mixture mass diffusivity of 10^{-9} m^2/s is used, corresponding to the Schmidt number of 10^3 (calculated based on the properties of component−1). The physical properties for each material are specified in Table 5.2.

Material	ρ (kg/m^3)	μ $(kg/m-s)$	$D_{i,m}$ (m^2/s)
water−1 (component−1)	998.16	0.001	–
water−2 (component−2)	998.16	0.01	–
vapor	0.0173	9.727×10^{-6}	–
mixture (water−1−water−2)	volume-weighted -mixing−law	mass-weight -mixing−law	1×10^{-9}

Table 5.2: Physical properties used for CFD computations in the mixing flows study.

In the present paper, the numerical simulations for the Venturi tube were executed in the commercial CFD software ANSYS FLUENT 16.2. The single-fluid mixture model is selected as a multiphase model to simulate the cavitating two-phase flows (water-vapor) in this study. The mixture model solves a single set of mass and momentum equations for the mixture and the volume fraction equation for the disperse phase [18]. In the simulation, the flow is assumed to be isothermal, incompressible, and with zero-slip velocity between the liquid phase and vapor phase.

5.2.1 RANS model

The steady-state RANS solver and transient LES solver are used to solve the two-phase flows with turbulence effect in a Venturi tube. The $k-\varepsilon$ and $k-\omega$ turbulent models are chosen to solve the 2D axis−symmetric, Reynolds-Averaged Navier-Stokes equations. Within the RANS approach, convection by eddies is considered as additional diffusion and involves transport equations for the turbulent kinetic energy, k, the turbulent dissipation rate, ε, or the specific dissipation rate, ω. The RANS-based turbulence models involve affordable computational costs and acceptable prediction accuracy. The main drawback of the RANS model is that the turbulence-cavitation interactions cannot be fully captured. In the RANS approach, the mass conservation equation and the momentum equation are defined as follows [18]:

$$\frac{\partial}{\partial t}\left(\rho_m\right) + \nabla \cdot \left(\rho_m \vec{v}_m\right) = 0 \tag{5.1}$$

$$\frac{\partial}{\partial t}(\rho_m \vec{v}_m) + \nabla \cdot (\rho_m \vec{v}_m \vec{v}_m) = -\nabla P + \nabla \cdot [(\mu_m + \mu_t)(\nabla \vec{v}_m + \nabla \vec{v}_m^T)] \tag{5.2}$$

where ρ_m, μ_m, and $\vec{v}_m$ are the density, viscosity, and velocity of the mixture phase, respectively. The turbulent viscosity, μ_t, in the k-ε RANS model is calculated as follows [18]:

$$\mu_t = \rho_m C_\mu \frac{k^2}{\varepsilon} \tag{5.3}$$

The transport equations for k and ε are then written as follows [18]:

$$\frac{\partial}{\partial t}(\rho k) + \frac{\partial}{\partial x_i}(\rho k v_i) = \frac{\partial}{\partial x_j}[(\mu + \frac{\mu_t}{\sigma_k})\frac{\partial k}{\partial x_j}] + G_k - \rho\varepsilon \tag{5.4}$$

$$\frac{\partial}{\partial t}(\rho \varepsilon) + \frac{\partial}{\partial x_i}(\rho \varepsilon v_i) = \frac{\partial}{\partial x_j}[(\mu + \frac{\mu_t}{\sigma_\varepsilon})\frac{\partial \varepsilon}{\partial x_j}] + C_{1\varepsilon}\frac{\varepsilon}{k}(G_k + C_{3\varepsilon}) - C_{2\varepsilon}\rho\frac{\varepsilon^2}{k} \tag{5.5}$$

where

$$G_k = \mu_t S^2, \quad S \equiv \sqrt{2 S_{ij} S_{ij}}, \quad S_{ij} = \frac{1}{2}\left(\frac{\partial v_j}{\partial x_i} + \frac{\partial v_i}{\partial x_j}\right) \tag{5.6}$$

In these equations, G_k is the production of kinetic energy due to the mean velocity gradients. S is the modulus of the mean rate-of-strain tensor and S_{ij} is the mean strain rate. The model constants have the following values [18]: $C_{1\varepsilon}$=1.44, $C_{2\varepsilon}$=1.92, C_μ=0.09, σ_k=1, σ_ε=1.3.

In the k-ω RANS model, the turbulent viscosity is calculated as follows [18]:

$$\mu_t = \frac{\rho_m k}{\omega} \tag{5.7}$$

The transport equations for k and ω are then written as follows [18]:

$$\frac{\partial}{\partial t}(\rho k) + \frac{\partial}{\partial x_i}(\rho k v_i) = \frac{\partial}{\partial x_j}[(\mu + \frac{\mu_t}{\sigma_k})\frac{\partial k}{\partial x_j}] + G_k - Y_k \tag{5.8}$$

$$\frac{\partial}{\partial t}(\rho \omega) + \frac{\partial}{\partial x_i}(\rho \omega v_i) = \frac{\partial}{\partial x_j}[(\mu + \frac{\mu_t}{\sigma_\omega})\frac{\partial \omega}{\partial x_j}] + G_\omega - Y_\omega \tag{5.9}$$

where

$$G_k = \mu_t S^2, \quad G_\omega = \frac{\omega}{k} G_k, \quad S \equiv \sqrt{2 S_{ij} S_{ij}}, \quad S_{ij} = \frac{1}{2}\left(\frac{\partial u_j}{\partial x_i} + \frac{\partial v_i}{\partial x_j}\right) \tag{5.10}$$

In these equations, G_k, S and S_{ij} are defined in the same ways as for the k-ε model. G_w is the generation of ω. Y_k and Y_ω is the dissipation of k and ω due to turbulence [18].

The conservation equation for component i (Y_i) takes the following form [18]:

$$\frac{\partial}{\partial t}(\rho_{m,l} Y_i) + \nabla \cdot (\rho \vec{v}_{m,l} Y_i) = -\nabla \cdot ((\rho_{m,l} D_m + \frac{\mu_t}{Sc_t})\nabla Y_i) \tag{5.11}$$

where Sc_t is the turbulent Schmidt number and $D_{i,m}$ is the mass diffusion coefficient for component i. In this study, the Sc_t and $D_{i,m}$ are assumed to be 0.7 and 10^{-9} m^2/s, respectively. In the liquid phase, the mixture density $\rho_{m,l}$ and mixture viscosity $\mu_{m,l}$ of two components (Y_1 and Y_2) are determined using the volume-weighted mixing law and the mass-weighted mixing law, respectively.

5.2.2 LES model

The LES turbulence model is selected to solve the 3D spatially filtered Navier-Stokes equations. In this approach, the large eddies that can be captured by meshing are resolved directly and the small eddies that cannot be captured by meshing are modeled with a Subgrid-Scale (SGS) turbulence model. In the present study, the WALE model [19], which has been successfully applied in many contexts [20, 21], was used as the SGS turbulence model. The characteristic length of the unresolved small components is smaller than the size of the control volume of the mesh. Thus, a finer mesh and a smaller time step than those for the RANS model are required to resolve more total kinetic energy in the LES model. Because the LES turbulence model calculates directly for large eddies and relies less on the modeling, it can provide a more accurate and more reliable prediction of the flow motion than simulations based on the RANS model. The basic equations of LES simulations take the following form [18]:

$$\frac{\partial}{\partial t}(\rho_m) + \nabla \cdot (\rho_m \vec{u}_m) = 0 \tag{5.12}$$

$$\frac{\partial}{\partial t}(\rho_m \vec{u}_m) + \nabla \cdot (\rho_m \vec{u}_m \vec{u}_m) = -\nabla P + \nabla \cdot [(\mu_m + \mu_t)(\nabla \vec{u}_m + \nabla \vec{u}_m^T)] \tag{5.13}$$

$$\frac{\partial}{\partial t}(\rho_{m,l} Y_i) + \nabla \cdot (\rho \vec{u}_{m,l} Y_i) = -\nabla \cdot ((\rho_{m,l} D_m + \frac{\mu_t}{Sc_t}) \nabla Y_i) \tag{5.14}$$

In the WALE model, the eddy viscosity is modeled using the following equation [18]:

$$\mu_t = \rho L_s^2 \frac{(S_{ij}^d S_{ij}^d)^{3/2}}{(\bar{S}_{ij}\bar{S}_{ij})^{5/2} + (S_{ij}^d S_{ij}^d)^{5/4}} \tag{5.15}$$

where $\bar{S}_{ij}$ is the rate-of-strain tensor for the resolved scales, S_{ij}^d is the velocity gradient traceless quadratic symmetry tensor, and L_s is the mixing length for subgrid scales. Detailed information on the LES model can be found in the ANSYS FLUENT Theory Guide [18]. The volume-weighted mixing law and the mass-weighted mixing law are used to calculate the mixture density $\rho_{m,l}$ and mixture viscosity $\mu_{m,l}$ of two components (Y_1 and Y_2) in the liquid phase.

5.2.3 Cavitation model

The Schnerr-Sauer cavitation model [22], based on the simplified Rayleigh-Plesset equation, is applied to describe the mass transfer between liquid-vapor phases. It should be mentioned that the dissolved gas effect and collision and coalescence phenomena are not taken into account in this study. In this model, the vapor volume fraction is computed from a transport equation for the vapor phase [18]:

$$\frac{\partial}{\partial t}(\alpha_v \rho_v) + \nabla \cdot (\alpha_v \rho_v \vec{v}_m) = R_e - R_c \tag{5.16}$$

where α_v is the volume fraction of the vapor phase, ρ_v is the vapor density, and ρ_l is the liquid density. The phase change due to cavitation is governed by the mass transfer source terms, R_e and R_c, connected to the growth (evaporation) and collapse (condensation) of bubbles in the cavitating flows. The form of the equation describing the process of evaporation R_e and condensation R_c can be obtained thus [22]:

When $P_v \geq P_\infty$,

$$R_e = \frac{\rho_v \rho_l}{\rho_m} \alpha_v (1 - \alpha_v) \frac{3}{R_b} \sqrt{\frac{2}{3} \frac{P_v - P_l}{\rho_l}} \tag{5.17}$$

When $P_v \leq P_\infty$,

$$R_c = \frac{\rho_v \rho_l}{\rho_m} \alpha_v (1 - \alpha_v) \frac{3}{R_b} \sqrt{\frac{2}{3} \frac{P_l - P_v}{\rho_l}} \tag{5.18}$$

where P_∞ is the fully recovered downstream pressure.

The volume fraction of the vapor phase can be represented as [22]:

$$\alpha_v = \frac{V_v}{V_m} = \frac{n_b \frac{4}{3}\pi R_b^3}{1 + n_b \frac{4}{3}\pi R_b^3} \tag{5.19}$$

The radius of bubbles can be computed by:

$$R_b = (\frac{\alpha_v}{1-\alpha_v}\frac{3}{4\pi n_b})^{\frac{1}{3}} \tag{5.20}$$

In this study, the bubble number density n_b is assumed to be 10^{13} since this value has been validated against a wide range of flow cases (see the works in Refs. [23, 24, 25]). The saturation vapor pressure of water, P_v is calculated to be 2338 Pa at 20°C using the Antoine equation [26]:

$$LogP_v = A - \frac{B}{T + C} \tag{5.21}$$

where A, B, and C are substance-specific constants with a value of 8.07131, 1730.63, and 233.426, respectively.

5.2.4 Boundary conditions and numerics

For boundary conditions, a constant total pressure inlet is used for the water with a value of 400000 Pa. The atmospheric pressure boundary condition is used at the outlet of the Venturi tube. The no-slip boundary condition was imposed for the liquid and vapor phases on all walls. In the RANS approach, the turbulence intensity and turbulent viscosity ratio are set as 10% and 10, respectively. The Wall-Adapting Local Eddy−viscosity (WALE) subgrid scale model is employed to model the turbulent viscosity in the LES approach. The calculated inlet Reynolds number, Re_{in}=$\frac{\rho_l U_{in} D}{\mu_l}$, for Cases 1 and 2 are 19738 and 19286, respectively.

The coupled algorithm is used for pressure-velocity coupling, with the PRESTO! discretization scheme applied for the pressure. The Quadratic Upwind Interpolation for Convection Kinematics (QUICK) scheme is used to discretize the transport equation for the volume fraction of vapor. The third-order Monotone Upstream-Centered Scheme for Conservation Laws (MUSCL) is used to discretize the components conservation equation. The second−order upwind scheme is utilized to discretize the convection terms in the RANS model. The second−order upwind scheme and the bounded central differencing scheme are used for momentum conservation equations in the RANS model and LES model, respectively. The first−order implicit and bounded second order implicit transient formulations

are used in the RANS model and LES model, respectively. The details of the models and schemes used in the two-phase cavitating system are given in Table 5.3.

Dimension	*Name*	*Model/ Scheme Name*
2D	Multiphase Flow	Mixture [18]
	Viscous Model	RANS$-k-\varepsilon$ & $k-\omega$ model[18]
	Cavitation Model	Schnerr-Sauer model [22]
	Pressure-Velocity Coupling	Coupled Scheme [18]
	Spatial Discretization-Gradient	Least Squares Cell Based [18]
	Spatial Discretization-Pressure	PRESTO! [18]
	Spatial Discretization-Momentum	Second$-$Order Upwind [18]
	Spatial Discretization-Volume Fraction	QUICK [27]
	Spatial Discretization-Turbulence	$k-\omega$ 2nd$-$Order Upwind [18]
	Spatial Discretization-Species	Third$-$Order MUSCL [28]
3D	Multiphase Flow	Mixture [18]
	Viscous Model	LES model[18]
	Cavitation Model	Schnerr-Sauer model [22]
	Subgrid-Scale Model	WALE [19]
	Pressure-Velocity Coupling	Coupled Scheme [18]
	Spatial Discretization-Gradient	Least Squares Cell Based [18]
	Spatial Discretization-Pressure	PRESTO! [18]
	Spatial Discretization-Momentum	Bounded Central Differencing [18]
	Spatial Discretization-Volume Fraction	QUICK [27]
	Spatial Discretization-Species	Third$-$Order MUSCL [28]
	Transient Formulation	Bounded Second$-$Order Implicit [18]

Table 5.3: List of different models and schemes used in 2D RANS and 3D LES models for modeling the two-phase flows.

The 2D axis$-$symmetric and 3D computational geometries are discretized with block-structured (hexahedral) meshes using a finite-volume method with 310000 (2D) and 3041280 (3D) computational cells. The mesh independence study was conducted by Shi et al. [12]. The 2D RANS simulations are calculated using a steady condition, while the 3D LES simulations are calculated using a transient condition. The total flow time of 0.03 s was completed for each simulation. The time-averaged values were obtained from the last 0.025 s after a stable transient converge solution was reached within 0.005 s after the process initiation. To avoid instability, small constant time steps of Δt= 1$\times$ 10^{-4} s and 4$\times$ 10^{-6} s were used in the RANS model and LES model, respectively. The maximum number of iterations at each time step was set to 30 for each simulation. The maximum value of residuals for each time step is about 10^{-8} and 10^{-3} in the RANS model and LES model, respectively. In the 3D LES calculations, the maximum value of the non-dimensional wall distance y^+ near the walls is about 3.86 and the Courant-Friedrich-Levy number (CFL=UΔt/Δx) is

about 3.15.

5.3 Results

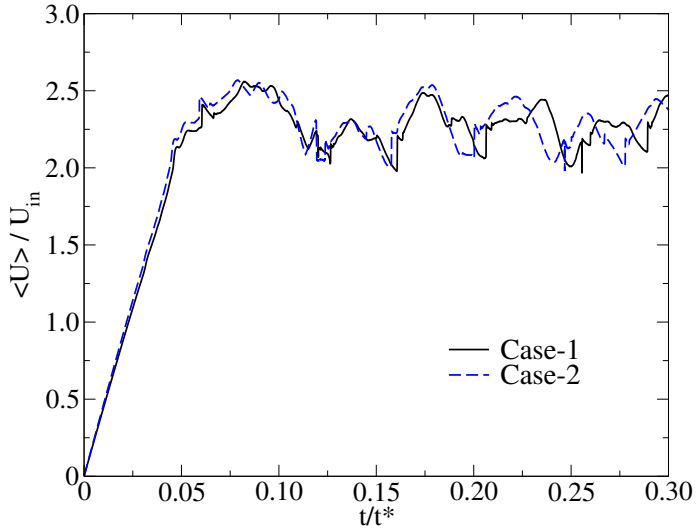

Figure 5.2: Scaled velocity over time for 3D LES simulations. $<U>=\frac{1}{V}\int_V \left(\sqrt{u_x^2+u_y^2+u_z^2}\right) dV$; $t^*=L/U_{in}$; t^*=0.0965 s (Case−1), t^*=0.0988 s (Case−2); U_{in}=1.557 m/s (Case−1), U_{in}=1.521 m/s (Case−2); L=0.15 m.

To study the transient dynamics of the mixing flows in a Venturi tube, we use the dimensionless velocity, $\frac{<U>}{U_{in}}$, of the mixture phase in the entire Venturi. The value of the volume-averaged flow velocity, $<U>$, and the inlet flow velocity, U_{in}, can be calculated from the following equation [29]:

$$U_{in} = \frac{\dot{m}}{\rho_m \pi (\frac{D_1}{2})^2} \tag{5.22}$$

$$< U >= \frac{1}{V}\int_V \left(\sqrt{u_x^2+u_y^2+u_z^2}\right) dV \tag{5.23}$$

where $\dot{m}$ is the mass flow rate, V is the volume of the Venturi tube and u is the velocity of the mixture phase. This dimensionless velocity is used to calculate a spin−up or start up time for volume-force−driven flows [29]. Time histories of $\frac{<U>}{U_{in}}$ calculated using different values of viscosity for 3D LES approaches are depicted in Fig. 5.2. The flow time, t, has been non-dimensionalized by the length, L, of the Venturi tube and the inlet flow velocity, U_{in}. A noticeable narrow peak in the dimensionless velocity profile within $\frac{t}{t^*}$=0.08 is captured in all cases. This peak corresponds to the start-up time. Therefore, the mixing

flows reach a stable transient state within $\frac{t}{t^*}$=0.08 of the process initiation. After the start-up period, steady fluctuations in the vapor volume fraction are observed in the Venturi tube that might be explained by the continuous evaporation and condensation of vapor bubbles. The analysis of $\frac{<U>}{U_{in}}$ time history shown in Fig. 5.2 reveals that Case−1 and Case−2 exhibit a similar trend regarding the flow velocity in a 3D model. This suggests that the flow velocity is not sensitive to the change in the component viscosity in the range between μ=0.001 to 0.01 $kg/m-s$.

To characterize the flow characteristics predicted using the LES approach, Fig. 5.3 and Fig. 5.4 show time-averaged results gained by means of the 3D LES turbulence model for Case−1 and Case−2, respectively. The iso-surface contour plots of the volume-averaged volume fraction of vapor, ϕ_v=0.25, and volume-averaged component−2, Y_2=0.25, are used to visualize the distribution of the vapor bubbles and component−2 in the Venturi tube. As can be seen from Fig. 5.3a-b and Fig. 5.4a-b, the cavitation bubbles are mostly formed at the beginning of the throat section, and develop further along the divergent section of the Venturi tube. On the other hand, the component−2 injected from the inlet of the Venturi tube travels a significant distance further downstream to the divergent section. The similarity of the cavitation region and component−2 region found in Case−1 and Case−2 confirms that the change in the component viscosity in the range between μ=0.001 to 0.01 $kg/m-s$ has a negligible effect on the cavitation and mixing behaviors. Fig. 5.3c and Fig. 5.4c show the iso-surface contour plots of the subgrid turbulent viscosity ratio, $\frac{\mu_t}{\mu_o}$=1.8 and $\frac{\mu_t}{\mu_o}$=1.6 $\times$ 10^{-3}, for Case−1 and Case−2, respectively. The subgrid turbulent viscosity ratio−defined as the ratio between the subgrid scale turbulent μ_t and the molecular μ_o dynamic viscosities−is necessary to estimate the subgrid turbulence levels within the 3D simulation domain. It is observed that the maximum magnitude of $\frac{\mu_t}{\mu_o}$ decreases significantly from 7 to 6 $\times$ 10^{-3} as the the component viscosity increases from 0.001 to 0.01 $kg/m-s$. The subgrid turbulent viscosity ratio is shown to significantly influence the development of cavitation. A higher subgrid turbulent viscosity, which is mainly concentrated in the divergent section for Case−1 and Case−2, leads more cavitation bubbles collapse and thus restricts the cavitation development. To visualize the vortices in the mixing flow, Fig. 5.3d and Fig. 5.4d show the instantaneous iso-surfaces of Q−criterion, equaling 5 $\times$ 10^7 s^{-2} for Case−1 and Case−2 at t/t^*=0.3, respectively. Similar vortex structures are displayed in both the low- and high- component viscosity cases. A higher Q−criterion value is located in the throat and divergent sections, where the local pressure is lower than the atmospheric pressure. This reveals the strong vortical nature of the flow. The vortex which is generated by the Venturi tube increases the turbulence intensity in the divergent section.

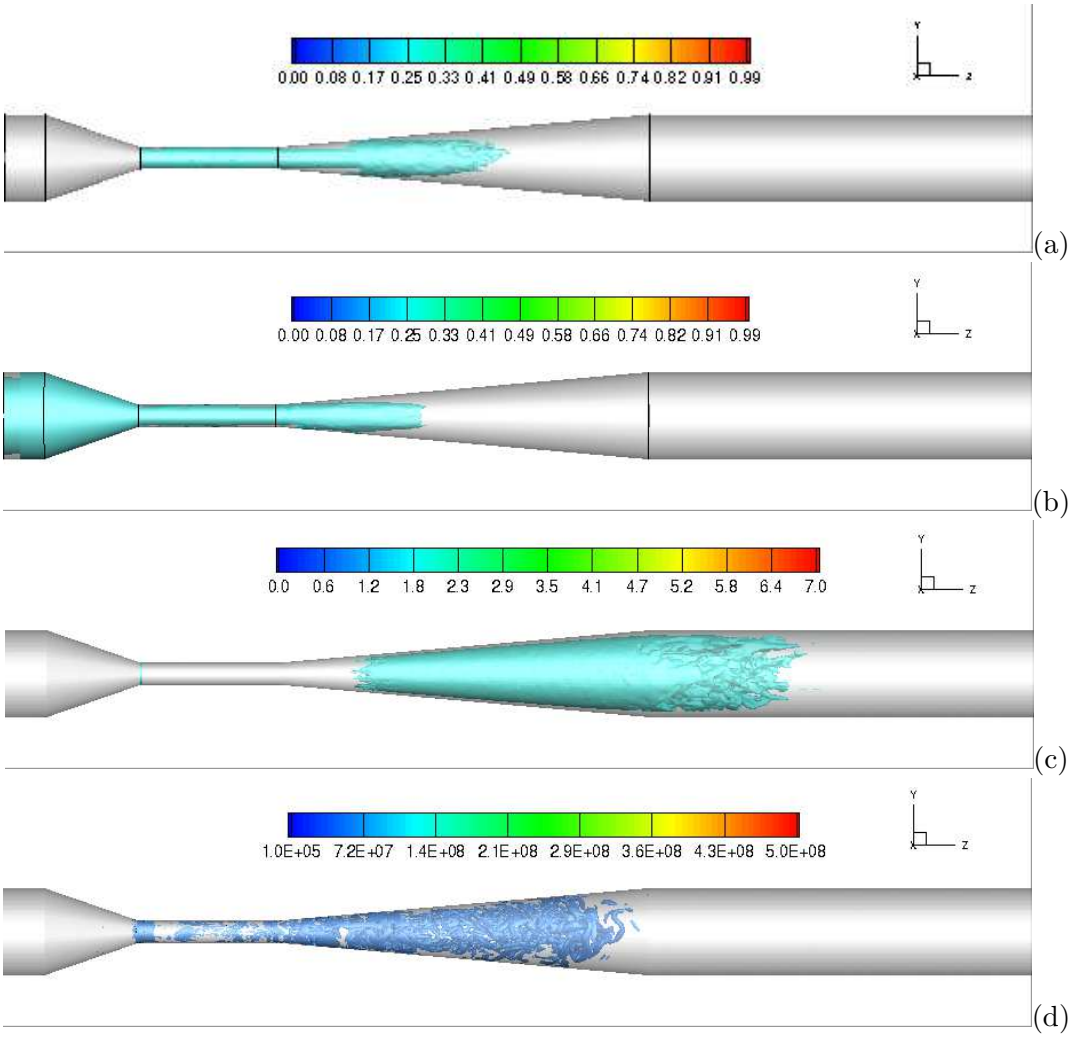

Figure 5.3: Iso-surface contours of 3D LES simulations for Case−1: (a) - time- and volume-averaged volume fraction of vapor; (b) - time- and volume-averaged Y_2; (c) - time- and volume-averaged subgrid turbulent viscosity ratio; (d) - instantaneous Q criterion $(1/s^2)$ at t/t^*=0.3.

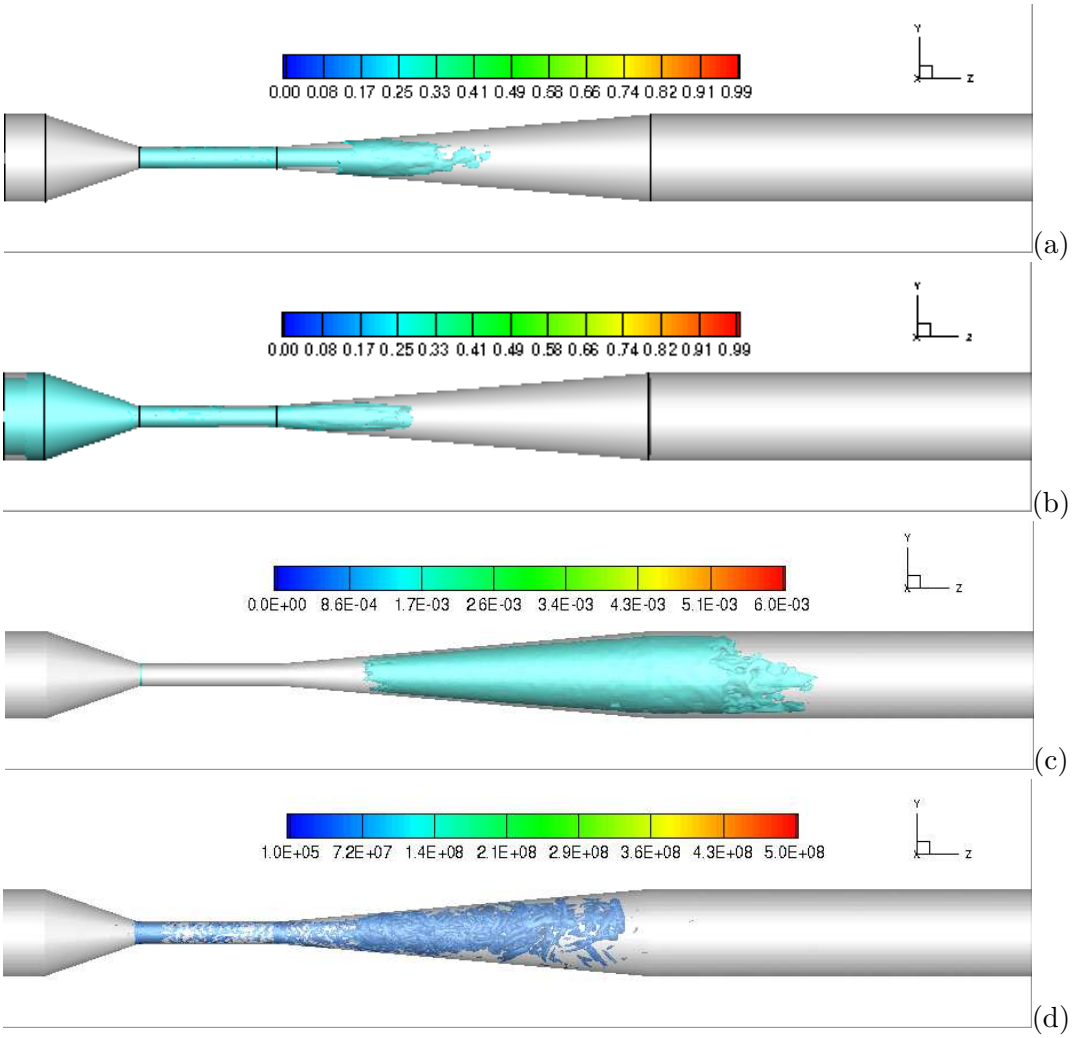

Figure 5.4: Iso-surface contours of 3D LES simulations for Case−2: (a) - time- and volume-averaged volume fraction of vapor; (b) - time- and volume- averaged Y_2; (c) - time- and volume-averaged subgrid turbulent viscosity ratio; (d) - instantaneous Q criterion ($1/s^2$) at t/t^*=0.3.

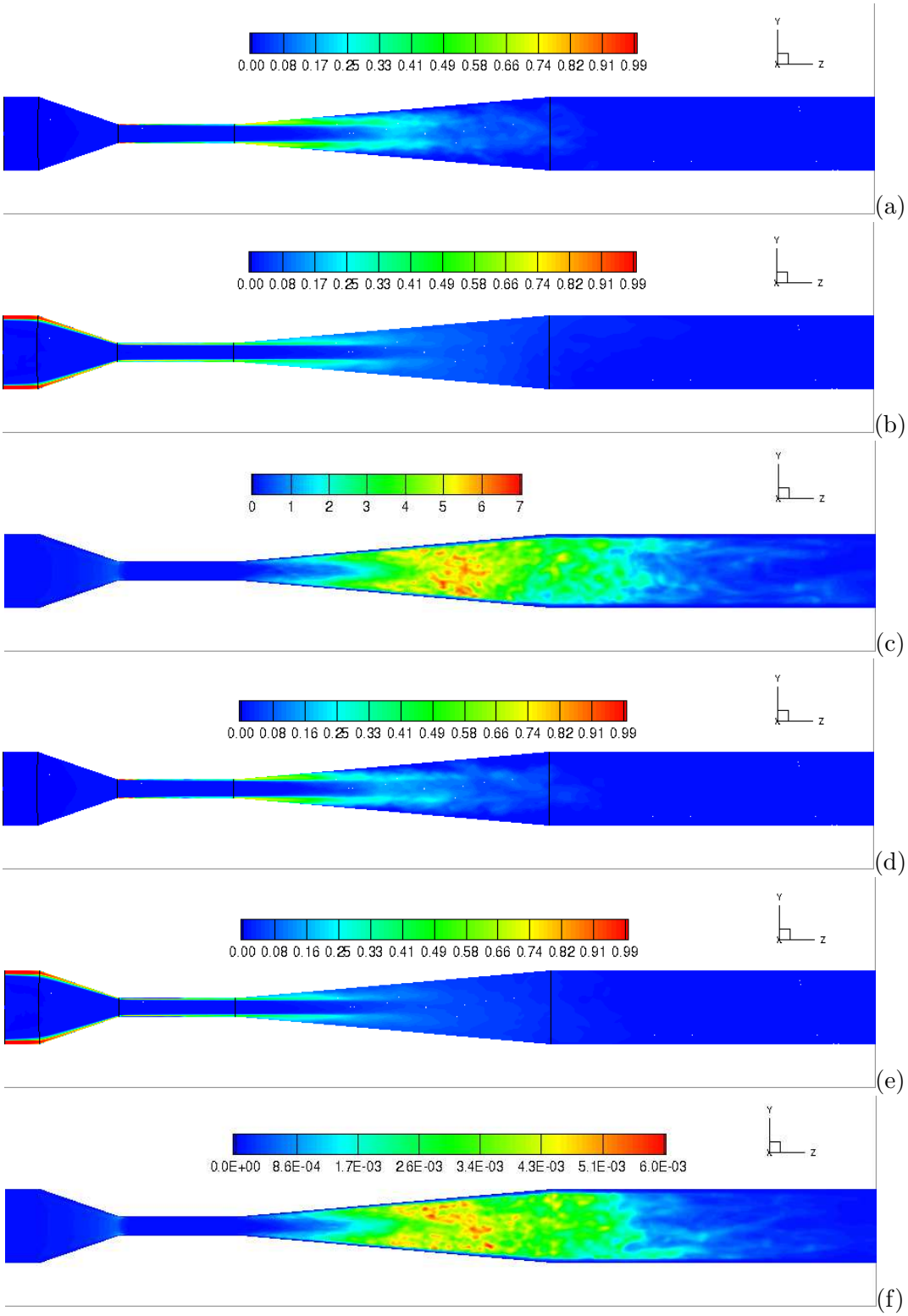

Figure 5.5: Contours of 3D time-averaged LES simulations in the middle plane: (a) - Case−1, volume-averaged volume fraction of vapor; (b) - Case−1, volume-averaged Y_2; (c) - Case−1, volume-averaged subgrid turbulent viscosity ratio; (d) - Case−2, volume-averaged volume fraction of vapor; (e) - Case−2, volume-averaged Y_2; (f) - Case−2, volume-averaged subgrid turbulent viscosity ratio.

To illustrate more clearly the overall flow structures predicted by the 3D LES turbulence model, contour plots of the time-averaged vapor volume fraction (ϕ_v), component-2 (Y_2), and the subgrid turbulent viscosity ratio ($\frac{\mu_t}{\mu_o}$) in the middle plane are shown in Fig. 5.5. As can be seen from Figs. 5.5a and d, a wide range of vapor volume fractions ($0-0.99$) is distributed along the wall of the throat section and then extends into the end of the divergent section for both cases. Figs. 5.5b and e depict the distribution of Y_2 with different viscosities. The mixing of two components in the divergent section is apparent, as is the decay of Y_2 along the centerline. Figs. 5.5c and f compare the $\frac{\mu_t}{\mu_o}$ obtained from Case-1 and Case-2. The higher component viscosity case exhibits a similar distribution of $\frac{\mu_t}{\mu_o}$ to the lower component viscosity case. However, the magnitude of $\frac{\mu_t}{\mu_o}$ decreases significantly as the component-2 viscosity increases from 0.001 to 0.01 $kg/m-s$.

To compare LES results with RANS, Fig. 5.6 presents the predicted vapor volume fraction (ϕ_v), component-2 (Y_2), and turbulent viscosity ratio ($\frac{\mu_t}{\mu_o}$) contours from the 2D $k-\omega$ model for different cases. As can be seen from Figs. 5.6a and 5.6d, similar stable cavitation flow behaviors are displayed in both Case-1 and Case-2. In contrast to the results of the 3D LES simulations, in the RANS simulations, the mass transfer from water-1 (Y_1) to vapor starts from the end of the throat section and then extends to the beginning of the divergent section. The cavitation zone predicted by the RANS model is significantly smaller than that predicted by the LES model. A comparison of Figs. 5.6b and e shows that the distribution and magnitude of Y_2 is similar in both cases. However, the mixing behavior obtained with the RANS model is clearly different from that of the LES simulations. We note that the mixing zone predicted by the RANS model occupies nearly the entire downstream area of the Venturi tube. A reasonable explanation for the cavitation zone and mixing pattern predicted by the RANS model can be suggested by considering the results in Figs. 5.6c and 5.6f. Figs. 5.6c and 5.6f show the contour plots of turbulent viscosity ratio calculated using the RANS model for Case-1 and Case-2. Similarly to the results of the LES simulations, in the RANS simulations, there is higher turbulence in the divergent section for all simulation cases. However, the maximum value of $\frac{\mu_t}{\mu_o}$ predicted by the RANS model is 250 orders (Case-1) and 100000 (Case-2) orders of magnitude larger than that predicted by the LES model. Similar findings were reported by Sepehr et al. [30] who used the LES and RANS models to simulate the mixing of two different miscible oils in a 3D channel. They observed that the turbulent viscosity predicted by RANS is higher than the comparable LES. This is caused by the fact that RANS model, based on the Boussinesq approximation, overpredicts the eddy viscosity and causes excessive damping of unsteady-flow motion. As a result, the overestimated turbulent viscosity in the cavitation zones prevents the development of cavitation. On the other hand, the higher turbulence viscosity leads to enhanced mixing through turbulent dispersion.

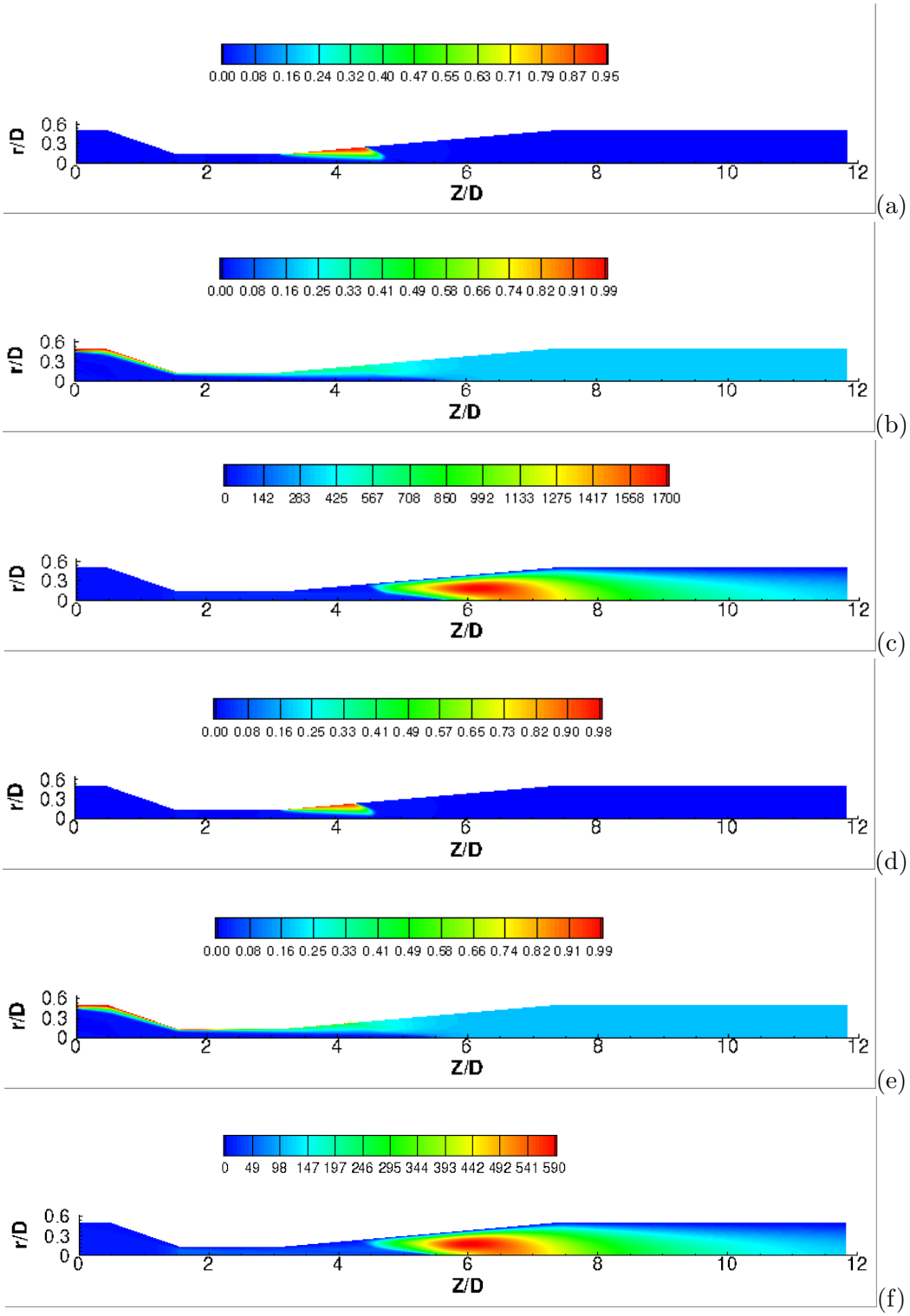

Figure 5.6: Contours of 2D $k-\omega$ simulations: (a) - Case−1, volume-averaged volume fraction of vapor; (b) - Case−1, volume-averaged Y_2; (c) - Case−1, turbulent viscosity ratio; (d) - Case−2, volume-averaged volume fraction of vapor; (e) - Case−2, volume-averaged Y_2; (f) - Case−2, turbulent viscosity ratio.

The qualitative difference between the predictions of the RANS and LES models is shown in Fig.5.7. A cross-section and volume-averaged evolution of the main variables such as the volume-averaged vapor volume fraction (ϕ_v), volume-averaged component-2 (Y_2), and turbulent viscosity ratio ($\frac{\mu_t}{\mu_o}$) as a function of the r/D have been collected at different locations. Two different locations have been identified, namely, (a) - end of the throat section (Z_1=3.15D), and (b) - front of the divergent section (Z_2=3.86D). These locations are shown on the Venturi tube geometry in Fig. 5.1.

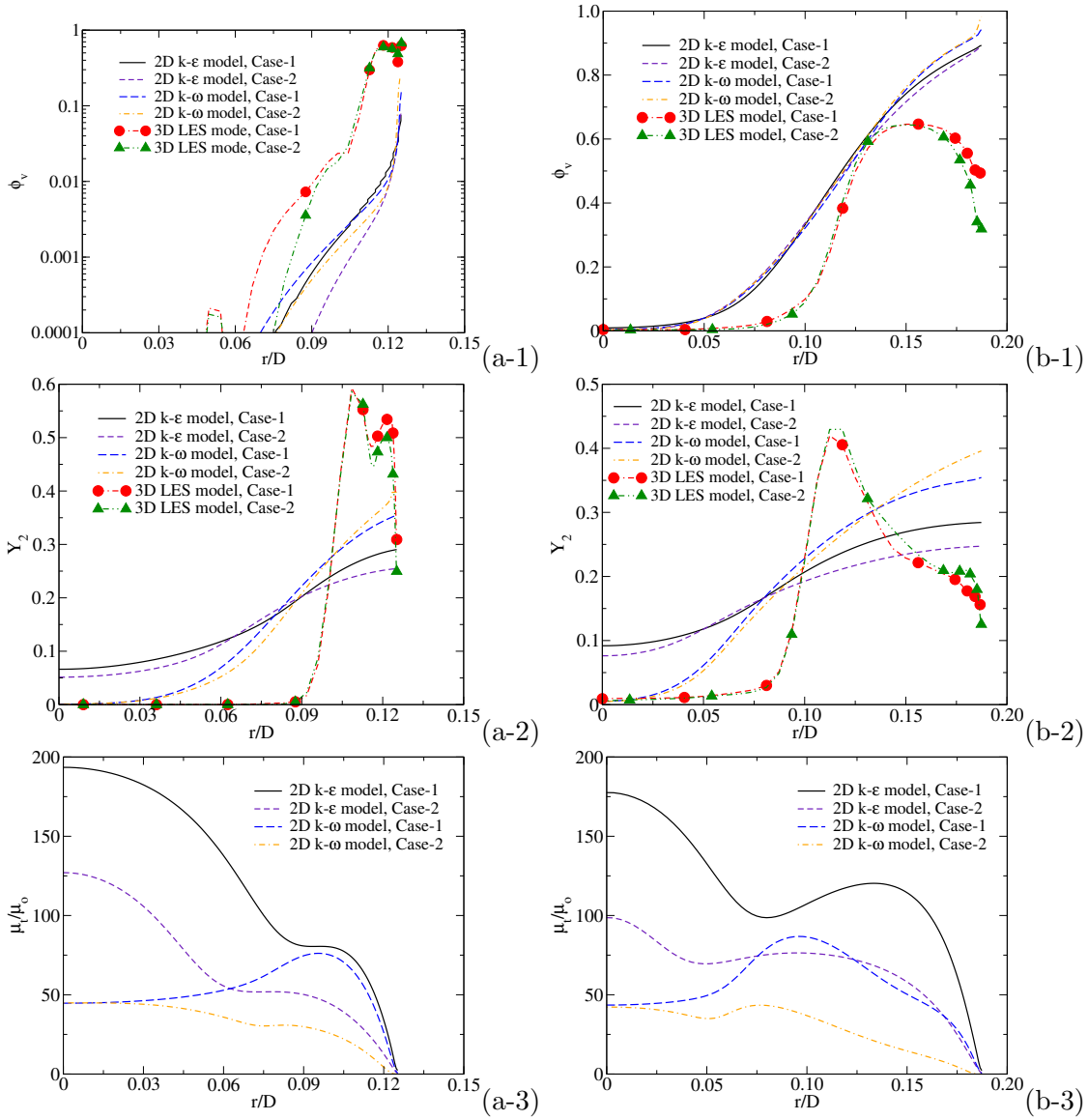

Figure 5.7: Axial distribution of (1) - volume-averaged volume fraction of vapor; (2) - volume-averaged Y_2; and (3) - turbulent viscosity ratio along r/D at (a) - $Z_1 = 3.15D$ and (b) - $Z_2 = 3.86D$.

Comparing Figs. 5.7a-1 and 5.7b-1, it is easy to observe the differences in ϕ_v generated by the simulated Venturi tube, using two turbulence models. The increasing vapor volume fraction can be observed from both turbulence models. However, the vapor volume fraction predicted by the LES model is higher than that by the RANS model at the location of Z_1. A different effect of the turbulence model is observed at the location of Z_2. The vapor volume fraction predicted by the LES simulations is slightly lower than the comparable RANS simulations. Figs. 5.7a-2 and b-2 show the radial Y_2 profile distribution at Z_1 and Z_2, respectively. The results from the RANS model show the steadily increasing trend along the radial direction. The results from the LES model indicate a rapid increase in Y_2 over r/D=0.09 to 0.11 and a dramatic decline near the wall at both locations. Figs. 5.7a-3 and b-3 display the distribution of the turbulent viscosity ratio at two different locations. It can be observed that the turbulent viscosity ratio is large in the central region and less in the near−wall region. Note that the distributions of ϕ_v and Y_2 are similar in Case−1 and Case−2, while $\frac{\mu_t}{\mu_o}$ predicted in Case−1 is higher in comparison with the value obtained from Case−2. For Figs. 5.7a-3 and b-3, the subgrid turbulence viscosity ratio profiles for the LES model are not shown here since their value is significantly small ($\frac{\mu_t}{\mu_o}$=0 to 7) in comparison with the value obtained by the RANS model ($\frac{\mu_t}{\mu_o}$=0 to 200).

LES and RANS predictions for the volume-averaged vapor volume fraction, volume-averaged component−2, and turbulent viscosity ratio profiles along the midplane line (r/D=0) of the Venturi tube are shown in Figs. 5.8a, b, and c, respectively. Compared with the LES vapor volume fraction profiles, in the RANS profiles, the length of the vapor volume fraction appears to be much shortened (see Fig. 5.8a). A higher vapor volume fraction (ϕ_v=0.0001 to 0.1) predicted from RANS simulations is present in the region beween z/D=3 and z/D=4.5, while that from the LES model is located in the region between z/D=3 and z/D=8. This indicates that the RANS solutions underpredict the rate of vapor production along the axial direction in comparison with the LES solutions. Fig. 5.8b shows the axial component−2 distribution along the centerline (r/D=0). Accordingly, the curves present two different trends in different turbulence models. The Y_2 profile is generally higher in the case of the RANS simulations. The Y_2 predicted using RANS shows a considerable increase in the throat section, and remains constant near the outlet. However, the Y_2 predicted using LES tends to rise first but then decreases sharply close to the outlet. In particular, the RANS models overpredict by 113% (Case−1) and 140% (Case−2) Y_2 in the divergent region (z/D=6) and by 192400% (Case−1) and 180000% (Case−2) near the outlet region (z/D=11). This highlights the enhanced mixing in the RANS cases relative to the LES predictions. Additionally, the results from the LES model indicate that the Y_2 predicted under non-cavitation condition is relatively higher than the value obtained under cavitation condition. For Fig. 5.8c, the $\frac{\mu_t}{\mu_o}$ predicted in Case−1 is higher than the value

obtained from Case−2. The peak of $\frac{\mu_t}{\mu_o}$ in Fig. 5.8c is consistent with that of Y_2 in Fig. 5.8d. It confirms that the turbulent viscosity promotes the mixing intensity.

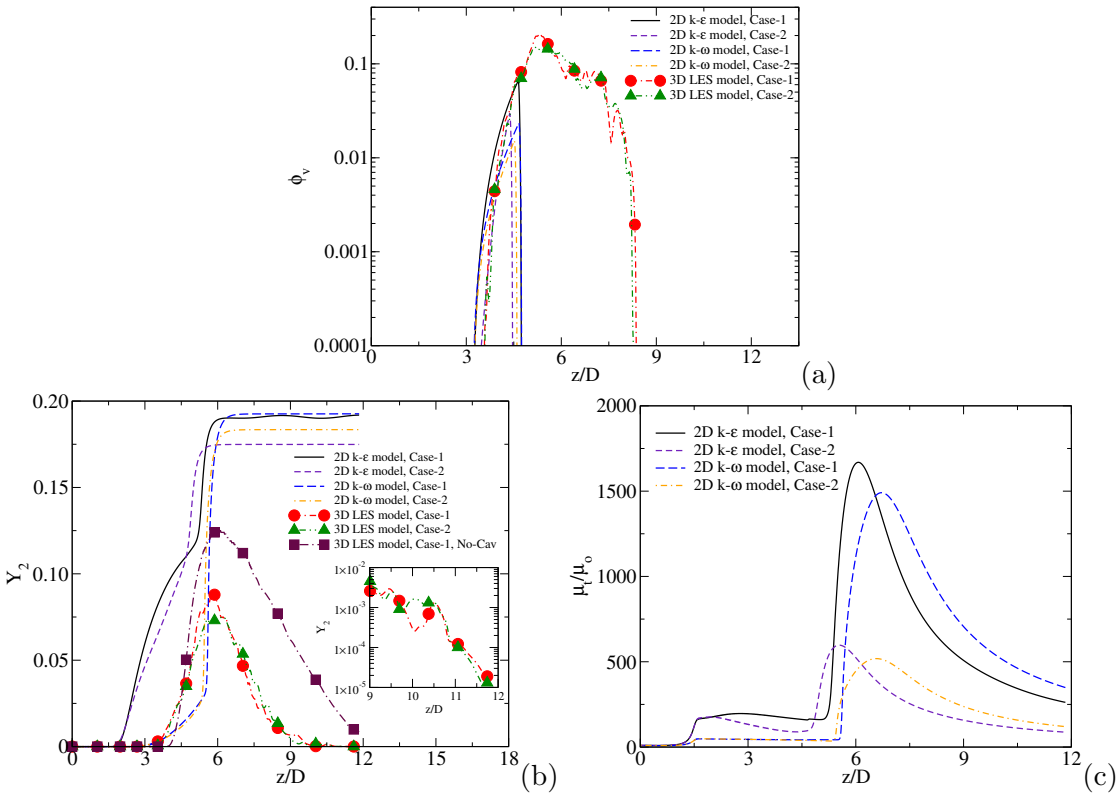

Figure 5.8: Axial distribution of (a) - volume-averaged volume fraction of vapor; (b) - volume-averaged Y_2; and (c) - turbulent viscosity ratio along z/D in the midplane line (r/D=0) of the Venturi tube.

Case	*Dimension*	*Turbulence model*	ΔP *(Pa)*	ϕ_v
Case−1 (μ_2/μ_1=1)	2D	$k-\varepsilon$	297488	1.58×10^{-2}
	2D	$k-\omega$	297426	1.55×10^{-2}
	3D	LES	297487	2.77×10^{-2}
Case−2 (μ_2/μ_1=10)	2D	$k-\varepsilon$	297733	1.17×10^{-2}
	2D	$k-\omega$	297593	1.26×10^{-2}
	3D	LES	297571	2.55×10^{-2}

Table 5.4: The calculated static pressure drops and volume-averaged volume fraction of vapor for Case−1 and Case−2.

The quantitative difference between the predictions of the RANS and LES models are presented in Table 5.4. As can be seen from the table, the static pressure drop calculated by the LES model and RANS model are basically the same, with a devitation of 0.01%

for Case−1 and 0.03% for Case−2. However, the value of ϕ_v in the LES model is about two orders of magnitude larger than that in the other two RANS models. It indicates that the cavitation intensity is sensitive to the turbulence model. Therefore, CFD modeling of multiphase flows in cavitating Venturi tubes could not be sufficiently validated by performing a direct comparison of the relationship between the pressure difference and flow rate. Further comparison of the numerically and experimentally measured cavitation region (location and size) should be considered to guarantee the reliability and accuracy of the CFD solvers.

5.4 Conclusions

In the present study, numerical simulations of mixing in a Venturi tube were performed using the 2D axis−symmetric and 3D CFD-based models available in the commercial CFD software ANSYS FLUENT 16.2. A model based on a water-vapor−mixture was used to study the cavitating and mixing behaviors of two miscible turbulent water flows with high viscosity differences. Simulations were carried out for inlet Reynolds numbers of 19738 (Case−1) and 19286 (Case−2) and a Schmidt number of $Sc = 10^3$.

Numerical results indicate that the turbulence restricts the development of cavitation but promotes mixing behaviors. To ensure the reliability of numerical results, it is key to select a suitable turbulence model based on the flow characteristics. The comparisons of LES and RANS results reveal a small differences (0.01%−0.03%) in the pressure. However, the vapor volume fraction predicted in the LES model is two orders of magnitude higher than those in the RANS model. The mixing characteristics in RANS are overpredicted than that in LES. In particular, the RANS model resulted in a higher (113%−140% in the divergent section and 180000%−1924000% near the outlet) volume-averaged component−2 along the centerline of the Venturi tube than that in the LES model. The comparisons of the CFD simulation and experimental data based on the pressure difference and flow rate provide little information about the cavitation activities, and thus are not sufficient to validate the accuracy of a CFD solver. Therefore, a validation methodology that quantifies the performance of a CFD solver by evaluating the cavitation region (location and size) is required to ensure the reliability of numerical results.

5.5 Acknowledgments

Financial support from the Natural Science and Engineering Research Council of Canada (NSERC) is greatly appreciated.

Bibliography

[1] Robert T Knapp, James W Daily, and Frederick G Hammitt. *Cavitation*. McGraw-Hill, 1970.

[2] Christopher E Brennen. *Cavitation and bubble dynamics*. Cambridge University Press, 2014.

[3] Dominicus Danardono, Ki-Seong Kim, Sun-Youp Lee, and Jang-Hee Lee. Optimization the design of venturi gas mixer for syngas engine using three-dimensional cfd modeling. *Journal of mechanical science and technology*, 25(9):2285, 2011.

[4] Mathias Romańczyk. Influence of gas inlet angle on the mixing process in a venturi mixer. In *ITM Web of conferences*, volume 15, page 07005. EDP Sciences, 2017.

[5] S Sundararaj and V Selladurai. An analysis on proportional mixing of liquids using venturi jet mixer. *International Journal of Applied Engineering Research*, 7:891–902, 2008.

[6] S Sundararaj and V Selladurai. Numerical and experimental study on jet trajectories and mixing behavior of venturi-jet mixer. *Journal of fluids engineering*, 132(10), 2010.

[7] Gaurav G Dastane, Harsh Thakkar, Rushabh Shah, Sivaramakrishna Perala, Janhavi Raut, and AB Pandit. Single and multiphase cfd simulations for designing cavitating venturi. *Chemical Engineering Research and Design*, 149:1–12, 2019.

[8] Alister Simpson and Vivek V Ranade. Modelling of hydrodynamic cavitation with orifice: Influence of different orifice designs. *Chemical Engineering Research and Design*, 136:698–711, 2018.

[9] Hongbo Shi, Qingxia Liu, and Petr Nikrityuk. Modeling of cavitating flows past a micro-sized particle. *International Journal of Multiphase Flow*, page 103276, 2020.

[10] LuYan Wang, Bin Ji, HuaiYu Cheng, Jiong Wang, and XinPing Long. One-dimensional/three-dimensional analysis of transient cavitating flow in a venturi tube with special emphasis on cavitation excited pressure fluctuation prediction. *Science China Technological Sciences*, pages 1–11, 2019.

[11] Christian P Egerer, Stefan Hickel, Steffen J Schmidt, and Nikolaus A Adams. Large-eddy simulation of turbulent cavitating flow in a micro channel. *Physics of Fluids*, 26 (8):085102, 2014.

[12] Hongbo Shi, Mingda Li, Petr Nikrityuk, and Qingxia Liu. Experimental and numerical study of cavitation flows in venturi tubes: From cfd to an empirical model. *Chemical Engineering Science*, 207:672–687, 2019.

[13] Seyed Mehdi Ashrafizadeh and Hojat Ghassemi. Experimental and numerical investigation on the performance of small-sized cavitating venturis. *Flow Measurement and Instrumentation*, 42:6–15, 2015.

[14] Xandra Margot, S Hoyas, A Gil, and STAVROULA Patouna. Numerical modelling of cavitation: validation and parametric studies. *Engineering Applications of Computational Fluid Mechanics*, 6(1):15–24, 2012.

[15] NM Nouri, SMH Mirsaeedi, and M Moghimi. Large eddy simulation of natural cavitating flows in venturi-type sections. *Proceedings of the Institution of Mechanical Engineers, Part C: Journal of Mechanical Engineering Science*, 225(2):369–381, 2011.

[16] F Örley, T Trummler, S Hickel, MS Mihatsch, SJ Schmidt, and NA Adams. Large-eddy simulation of cavitating nozzle flow and primary jet break-up. *Physics of Fluids*, 27(8):086101, 2015.

[17] Nagendra Dittakavi, Aditya Chunekar, and Steven Frankel. Large eddy simulation of turbulent-cavitation interactions in a venturi nozzle. *Journal of Fluids Engineering*, 132(12):121301, 2010.

[18] Inc. Ansys. ANSYS FLUENT theory guide. *Canonsburg, Pennsylvania*, page 794, 2011.

[19] Franck Nicoud and Frédéric Ducros. Subgrid-scale stress modelling based on the square of the velocity gradient tensor. *Flow, turbulence and Combustion*, 62(3):183–200, 1999.

[20] B Ji, XW Luo, Roger EA Arndt, Xiaoxing Peng, and Yulin Wu. Large eddy simulation and theoretical investigations of the transient cavitating vortical flow structure around a naca66 hydrofoil. *International Journal of Multiphase Flow*, 68:121–134, 2015.

[21] M Sedlar, B Ji, T Kratky, T Rebok, and R Huzlik. Numerical and experimental investigation of three-dimensional cavitating flow around the straight naca2412 hydrofoil. *Ocean Engineering*, 123:357–382, 2016.

[22] Günter H Schnerr and Jürgen Sauer. Physical and numerical modeling of unsteady cavitation dynamics. In *Fourth international conference on multiphase flow, New Orleans, USA*, volume 1, 2001.

[23] Huiying Li, Frank J Kelecy, Aleksandra Egelja-Maruszewski, and Sergio A Vasquez. Advanced computational modeling of steady and unsteady cavitating flows. In *ASME 2008 International Mechanical Engineering Congress and Exposition*, pages 413–423. American Society of Mechanical Engineers, 2008.

[24] Da-Qing Li, M Grekula, and P Lindell. A modified sst k-omega turbulence model to predict the steady and unsteady sheet cavitation on 2d and 3d hydrofoils. In *Proccedings of the 7th International Symposium on Cavitation, CAV2009*, 2009.

[25] Hou-lin Liu, Dong-xi Liu, Yong Wang, Xian-fang Wu, and Jian Wang. Application of modified κ-ω model to predicting cavitating flow in centrifugal pump. *Water Science and Engineering*, 6(3):331–339, 2013.

[26] George Wm Thomson. The antoine equation for vapor-pressure data. *Chemical Reviews*, 38(1):1–39, 1946.

[27] Brian P Leonard. A stable and accurate convective modelling procedure based on quadratic upstream interpolation. *Computer Methods in Applied Mechanics and Engineering*, 19(1):59–98, 1979.

[28] Bram Van Leer. Towards the ultimate conservative difference scheme. v. a second-order sequel to godunov's method. *Journal of Computational Physics*, 32(1):101–136, 1979.

[29] Hongbo Shi, Alexandra Komrakova, and Petr Nikrityuk. Fluidized beds modeling: Validation of 2d and 3d simulations against experiments. *Powder Technology*, 343: 479–494, 2019.

[30] H Sepehr, P Nikrityuk, D Breakey, and RS Sanders. Numerical study of crude oil batch mixing in a long channel. *Petroleum science*, 16(1):187–198, 2019.

Chapter 6

Conclusions and Future Work

6.1 Conclusions

Cavitating Venturi tubes play a significant role in mineral processing and their performance depends to a great extent on the geometrical parameters, operation conditions, and presence of solid particles. The main purpose of the current study was to experimentally and numerical studies of hydrodynamic cavitation phenomenon in the Venturi tubes, in order to validate and further develop numerical multi-phase flow models with the obtained data. The CFD simulations were preformed in the commercial CFD software ANSYS FLUENT 16.2. Laboratory-scale experiments was designed in order to validate the simulations.

In the study of two-phase (water-vapor) flows, the numerical simulations of cavitaitng Venturi tubes were performed using a 2D axis−symmetric CFD-based model. A mixture model based on a water-vapor-phase mixture is used to reproduce the experiments. The numerical results generally agree well with the experimental data, with a deviation in the pressure drop within [2.23−15.32]%. Both the numerical and experimental studies reveal that the averaged vapor volume fraction in the divergent section increases rapidly with decreasing divergent angle from 90° to 2.5°. The average vapor volume fraction in the throat section increases with increasing convergent angle from 15° to 90° but higher power consumption are required. In this view, a required cavitational intensity can be controlled by the convergent and divergent angles of the cavitating Venturi tube taking into account the effect of energy consumption. The effect of scale-ratio on cavitational activities was investigated numerically. It was shown that the scaled-up Venturi tubes produce more vapor as lab-scale Venturi tubes, which is favorable to achieve commercialization capacity and greatly benefit industrial operations in mineral processing. Additionally, a simplified empirical model enabling of cavitation to be predicted in different Venturi tubes was established employing regression analysis based on CFD results. The developed

empirical model serves as a valuable tool for industrial engineers to accurately estimate the significant dimensionless parameters (the inlet Reynolds number Re_{in}, the pressure loss coefficient K, the cavitation number σ, and the vapor volume fraction ϕ_v) and involves in the design of cavitating Venturi tubes with different geometrical parameters and scales.

In the study of four-phase (water-solid-vapor-air) flows, the numerical simulation of a Venturi tube was studied using a 2D axis−symmetric CFD-based model. A new global model of four-phase (liquid-solid-vapor-air) cavitating flows was developed based on the simple engineering approach, and validated against the experimental measurements. The experimental data obtained provided good agreement with numerical results, with a deviation in the pressure drop within [4.49−8.07]%. To the best of our knowledge, this appears to be first time that a four-phase cavitating flows through a Venturi tube has been successfully simulated using the CFD model. In particular, the results of the experimental and CFD studies clearly illustrate that the presence of solid particles (W_s=5∼30 wt%) has a significant influence on the cavitation behaviors. In general, the higher the solid mass concentration, the earlier the cavitation inception and the greater the vapor and air production, but accompanied by a higher energy consumption. Accordingly, the required cavitation yield can be controlled by adding solid particles to the cavitating Venturi tube, taking into account the effect of the energy consumption. In addition to this, it was shown numerically that the distribution of the solid volume fraction in the four-phase flows is increased significantly in the throat section and the divergent cone center of the cavitating Venturi tube.

In the study of particle-flow interaction, the cavitation around a solid particle in a laminar and turbulent free-stream domain was analyzed numerically using a 2D axis−symmetric and 3D CFD-based model. The liquid-vapor phase-mixture-based model was validated with the experimental data from the literature and good agreement was obtained. The results of the CFD study clearly illustrate that the particle shape and surface roughness strongly influence the cavitation behaviors. In particular, the critical Reynolds numbers (Re_c) for Particles−1, 2, 3 and 4 are 190, 70, 130, 130, respectively. This reveals that the cavitation might depend on the particulate Re number for different particle types. The studies of the isothermal process clearly showed that the particles with a cylindrical shape (Particle−2) and rough surface (Particle−3 and Particle−4) lead earlier cavitation inception and greater vapor production than the one with a smooth, spherical shape (Particle−1), while increasing the number of particles from one to ten in the horizontal direction leads to a corresponding delay in the cavitation inception from Re_c=190 to Re_c=210 and a reduction in the vapor production. The influence of the thermal conditions on cavitation behaviors was potentially very large. Increasing the particle surface temperature from 40°C to 99.9°C is beneficial to the development of cavitation. In particular, the cavitation inception starts to

develop much earlier from Re_c=130 to Re_c=25 and the average vapor production increases 200% for Re >200. An increases in the particle size from 10 to 100 μm results in an increase in the Re_c from 190 to 1800. Meanwhile, a CFD-based empirical mathematical model for the particle size was proposed to link the particle diameter and critical Reynolds number. The empirical model provided good agreement with the numerically predicted data, which indicates that it can be used to accurately estimate the inception of cavitation for particles with various particle sizes ranging from 10 to 100 μm. In the macro-scale study, we found each particle-flow interaction has negligible effect on the cavitation activities in comparison with the entrapped air bubbles on the crevices of the solid particles.

Finally, a model based on a water-vapor-mixture was used to study the cavitating and mixing behaviors of two miscible turbulent water flows with high viscosity difference. Simulations were carried out for inlet Reynolds numbers of 19738 (Case−1) and 19286 (Case−2) and a Schmidt number of $Sc = 10^3$. Numerical results indicate that the turbulence restricts the development of cavitation but promotes mixing behaviors. To ensure the reliability of numerical results, it is key to select a suitable turbulence model based on the flow characteristics. The comparisons of LES and RANS results reveal a small differences (0.01%−0.03%) in the pressure. However, the vapor volume fraction predicted in the LES model is two orders of magnitude higher than those in the RANS model. The mixing characteristics in RANS are overpredicted than that in LES. In particular, the RANS model resulted in a higher (113%−140% in the divergent section and 180000%−1924000% near the outlet) volume-averaged component−2 along the centerline of the Venturi tube than that in the LES model. The comparisons of the CFD simulation and experimental data based on the pressure difference and flow rate provide little information about the cavitation activities, and thus are not sufficient to validate the accuracy of a CFD solver. Therefore, a validation methodology that quantifies the performance of a CFD solver by evaluating the cavitation region (location and size) is required to ensure the reliability of numerical results.

6.2 Recommendations for Future work

Following recommendations for future work can be made based on the findings of this thesis:

- The presence and expansion of non-condensable gas in the liquid phase was not considered in the study of two-phase cavitaitng flows. In reality, a small quantity of micro-bubbles of non-condensable gases (nuclei) are always present in the liquid. It remain unknown how much impact it will have on the cavitation inception and the development of cavitation in a Venturi tube. Therefore, this work can be extended to

include the non-condensable gas to account for actual cavitation activities observed in numerical studies.

- The four-phase (liquid-solid-vapor-air) global model was developed and validated considering problems of cavitating particulate flows with hydrophilic particles (e.g. bare silica). For applications to cavitating flow problems in that the four-phase flows with hydrophobic particles (e.g. coal, treated silica), further improving the global models would be desirable, for example, by considering the change of contact angle between liquid and the particle surface.

- Based on the micro- and macro-scale studies, we found each particle-flow interaction has negligible effect on the cavitation activities in a Venturi tube. For further quantification of the cavitation, modeling the particle-flow interaction would be desirable in other geometries (e.g. sharp edged orifices, valves) including various influential parameters (e.g. sizes, shape, particle surface roughness and surface temperature).

- Studies should be undertaken for obtaining high quality reliable experimental data. Though simulations presented in this thesis show quantitative agreement with experiments based on the pressure drop and flow rate. Light sources and high-speed camera can be used to provide visual observation to predict the inception and development of cavitation in a Venturi tube. The further comparison of numerical and experimental measured cavitation region (location and size) should be considered to guarantee the reliability and accuracy of the CFD solvers.

General Bibliography

Inc Ansys. Ansys fluent theory guide. *Canonsburg, Pennsylvania*, page 794, 2011.

Frank P Incropera, Adrienne S Lavine, Theodore L Bergman, and David P DeWitt. *Fundamentals of heat and mass transfer*. Wiley, 2007.

Timothy J Mason and J Phillip Lorimer. Applied sonochemistry: the uses of power ultrasound in chemistry and processing. 2002.

Fabiana A Perrechil and RL Cunha. Oil-in-water emulsions stabilized by sodium caseinate: Influence of ph, high-pressure homogenization and locust bean gum addition. *Journal of Food Engineering*, 97(4):441–448, 2010.

Jitendra Carpenter, Mandar Badve, Sunil Rajoriya, Suja George, Virendra Kumar Saharan, and Aniruddha B Pandit. Hydrodynamic cavitation: an emerging technology for the intensification of various chemical and physical processes in a chemical process industry. *Reviews in Chemical Engineering*, 33(5):433–468, 2017.

Seyed Shaham Aldin Hosseininejad. CFD *Modeling of Cavitation for Fine Particle Flotation*. PhD thesis, University of Alberta, 2016.

Hongbo Shi, Mingda Li, Petr Nikrityuk, and Qingxia Liu. Experimental and nu- merical study of cavitation flows in venturi tubes: from cfd to an empirical model. *Chemical Engineering Science*, 207:672–687, 2019.

Robert T Knapp, James W Daily, and Frederick G Hammitt. *Cavitation*. McGraw-Hill, 1970.

Christopher E Brennen. *Cavitation and bubble dynamics*. Cambridge University Press,

2013.

P Senthil Kumar, M Siva Kumar, and AB Pandit. Experimental quantification of chemical effects of hydrodynamic cavitation. *Chemical Engineering Science*, 55(9): 1633–1639, 2000.

Parag R Gogate and Aniruddha B Pandit. A review and assessment of hydrodynamic cavitation as a technology for the future. *Ultrasonics sonochemistry*, 12(1-2):21–27, 2005.

S Arrojo and Y Benito. A theoretical study of hydrodynamic cavitation. *Ultrasonics Sonochemistry*, 15(3):203–211, 2008.

Jitendra Carpenter, Suja George, and Virendra Kumar Saharan. Low pressure hydrodynamic cavitating device for producing highly stable oil in water emulsion: Effect of geometry and cavitation number. *Chemical Engineering and Processing: Process Intensification*, 116:97–104, 2017.

ZA Zhou, Zhenghe Xu, JA Finch, H Hu, and SR Rao. Role of hydrodynamic cavitation in fine particle flotation.*International Journal of Mineral Processing*, 51(1-4): 139–149, 1997.

Parag R Gogate. Application of hydrodynamic cavitation for food and bioprocessing. *Ultrasound Technologies for Food and Bioprocessing*, pages 141–173. Springer, 2011.

Francesca Patrignani and Rosalba Lanciotti. Applications of high and ultra high pressure homogenization for food safety. *Frontiers in microbiology*, 7, 2016.

Muthupandian Ashokkumar et al. Theoretical and experimental sonochemistry involving inorganic systems. *Springer Science & Business Media*, 2010.

Manickam Sivakumar and Aniruddha B Pandit. Wastewater treatment: a novel energy efficient hydrodynamic cavitational technique. *Ultrasonics sonochemistry*, 9 (3):123–131, 2002.

M. Gagola, A. Przyjaznyb, and G. Boczkaja. Wastewater treatment by means of advanced oxidation processes based on cavitation - A review. *Chemical Engineering Journal*, 338:599–627, 2018.

Mark Duerkop, Eva Berger, Astrid Durauer, and Alois Jungbauer. Impact of cavitation,

high shear stress and air/liquid interfaces on protein aggregation. *Biotechnology journal*, 13(7):1800062, 2018.

V Ross, A Singh, and K Pillay. Improved flotation of pgm tailings with a high-shear hydrodynamic cavitation device. *Minerals Engineering*, 137:133–139, 2019.

Mohan M Gore, Virendra Kumar Saharan, Dipak V Pinjari, Prakash V Chavan, and Aniruddha B Pandit. Degradation of reactive orange 4 dye using hydrodynamic cavitation based hybrid techniques. *Ultrasonics sonochemistry*, 21(3):1075–1082, 2014.

Ashok K Singhal, Mahesh M Athavale, Huiying Li, and Yu Jiang. Mathematical basis and validation of the full cavitation model. *Transactions-American Society of Mechanical Engineers Journal of Fluids Engineering*, 124(3):617–624, 2002.

Stephane Barre, Julien Rolland, Guillaume Boitel, E Goncalves, and R Fortes Patella. Experiments and modeling of cavitating flows in venturi: attached sheet cavitation. *European Journal of Mechanics-B/Fluids*, 28(3):444–464, 2009.

Eric Goncalves and Regiane Fortes Patella. Numerical simulation of cavitating flows with homogeneous models.*Computers & Fluids*, 38(9):1682–1696, 2009.

Boris Charriere, Jean Decaix, and Eric Goncalves. A comparative study of cavitation models in a venturi flow. *European Journal of Mechanics-B/Fluids*, 49:287–297, 2015.

JX Zhang. Analysis on the effect of venturi tube structural parameters on fluid flow. *AIP Advances*, 7(6):065315, 2017.

Liang Zhao, Licheng Sun, Zhengyu Mo, Min Du, Jiang Huang, and Jingjing Bao. Effects of the divergent angle on bubble transportation in a rectangular venturi channel and its performance in producing fine bubbles. *International Journal of Multiphase Flow*, 2019.

Tausif A Bashir, Advait G Soni, Amit V Mahulkar, and Aniruddha B Pandit. The cfd driven optimisation of a modified venturi for cavitational activity. *The Canadian Journal of Chemical Engineering*, 89(6):1366–1375, 2011.

Alister Simpson and Vivek V Ranade. Modeling hydrodynamic cavitation in venturi: influence of venturi configuration on inception and extent of cavitation. *AIChE Journal*,

65(1):421–433, 2019.

K. Sampath Kumar and Vijayanand S. Moholka. Conceptual design of a novel hydrodynamic cavitation reactor. *Chemical Engineering Science*, 62:2698–2711, 2007.

Mei-Shan Jin, Cong-Tu Ha, and Warn-Gyu Park. Numerical study on heat transfer effects of cavitating and flashing flows based on homogeneous mixture model. *International Journal of Heat and Mass Transfer*, 109:1068–1083, 2017.

X Margot, S Hoyas, A Gil, and S Patouna. Numerical modelling of cavitation: validation and parametric studies. *Engineering Applications of Computational Fluid Mechanics*, 6(1):15–24, 2012.

Youwei Gu, Buxuan Li, and Min Chen. An experimental study on the cavitation of water with effects of sio2 nanoparticles. *Experimental Thermal and Fluid Science*, 79:195–201, 2016.

M Medrano, PJ Zermatten, Christian Pellone, Jean-Pierre Franc, and Fred eric Ayela. Hydrodynamic cavitation in microsystems. i. experiments with deionized water and nanofluids. *Physics of Fluids*, 23(12):127103, 2011.

Patrick F Dunn, Flint O Thomas, Michael P Davis, and Irina E Dorofeeva. Experimental characterization of aviation-fuel cavitation. *Physics of Fluids*, 22(11):117102, 2010.

Mingda Li. Influence of venturi tube geometry and particle properties on the hydrodynamic cavitation for fine particle flotation. *Master thesis*, 2017.

Bostjan Gregorc, Matjaz Hribersek, and Andrej Predin. The analysis of the impact of particles on cavitation flow development. *Journal of Fluids Engineering*, 133(11):111304, 2011.

AE Kabeel and Mohamed Abdelgaied. Study on the effect of alumina nano-fluid on sharp-edge orifice flow characteristics in both cavitations and non-cavitations turbulent flow regimes. *Alexandria Engineering Journal*, 55(2):1099–1106, 2016.

Min-Rui Chen, Jin-Yuan Qian, Zan Wu, Chen Yang, Zhi-Jiang Jin, and Bengt Sun den. The hydraulic cavitation affected by nanoparticles in nanofluids. *Computation*, 6(3):44, 2018.

Buxuan Li, Youwei Gu, and Min Chen. Cavitation inception of water with solid nanoparticles: A molecular dynamics study. *Ultrasonics sonochemistry*, 51:120–128, 2019.

Mohammad-Reza Pendar and Ehsan Roohi. Cavitation characteristics around a sphere: An les investigation. *International Journal of Multiphase Flow*, 98:1–23, 2018.

Matevz Dular, Rudolf Bachert, Bernd Stoffel, and Brane Sirok. Influence of the velocity distribution at the inlet boundary on the cfd prediction of local velocity and pressure fields around a hydrofoil. *Experimental thermal and fluid science*, 32(3): 882–891, 2008.

Narotam Jangir, Prateek Diwedi, and Sumana Ghosh. Design of a hydrodynamic cavitating reactor. Chemical Engineering & Processing: *Process Intensification*, 122:128–142, 2017.

Eduardo Gomez Santos, Junmei Shi, Manolis Gavaises, Celia Soteriou, Mark Winterbourn, and Wolfgang Bauer. Investigation of cavitation and air entrainment during pilot injection in real-size multi-hole diesel nozzles. *Fuel*, 263:116746, 2020.

Anne Boorsma and Stewart Whitworth. Understanding the details of cavitation. In *Second International Symposium on Marine Propulsors*, pages 319–327, 2011.

Stefano Gaggero and Diego Villa. Steady cavitating propeller performance by using openfoam, starccm+ and a boundary element method. Proceedings of the Institution of Mechanical Engineers, Part M: *Journal of Engineering for the Maritime Environment*, 231(2): 411–440, 2017.

S Brinkhorst, E von Lavante, and G Wendt. Experimental and numerical investigation of the cavitation-induced choked flow in a herschel venturi-tube. *Flow Measurement and Instrumentation*, 54:56–67, 2017.

Boxiong Chen and Michael Oevermann. An eulerian stochastic field cavitation model coupled to a pressure based solver. *Computers and Fluids*, 162:1–10, 2018.

Abolfazl Asnaghi, Urban Svennberg, and Rickard E Bensow. Large eddy simulations of cavitating tip vortex flows. *Ocean Engineering*, 195:106703, 2020.

Kazem Hejranfar, Eslam Ezzatneshan, and Kasra Fattah-Hesari. A comparative study of two cavitation modeling strategies for simulation of inviscid cavitating flows. *Ocean Engineering*, 108:257–275, 2015.

Gunter H Schnerr and Jurgen Sauer. Physical and numerical modeling of unsteady cavitation dynamics. In *Fourth international conference on multiphase flow*, New Orleans, USA, volume 1, 2001.

Philip J Zwart, Andrew G Gerber, Thabet Belamri, et al. A two-phase flow model for predicting cavitation dynamics. In *Fifth international conference on multiphase flow*, Yokohama, Japan, volume 152, 2004.

Z. Zhou, Z. Xu, J.A. Finch, H. Hu, and S.R. Rao. Role of hydrodynamic cavitation in fine particle flotation. *Int. J. Miner. Process.*, 51:139–149, 1997.

RH Yoon and GH Luttrell. The effect of bubble size on fine coal flotation. *Coal Preparation*, 2(3):179–192, 1986.

Roe-Hoan Yoon, Darrin H Flinn, and Yakov I Rabinovich. Hydrophobic interactions between dissimilar surfaces. *Journal of colloid and interface science*, 185(2):363–370, 1997.

Daniel Tao. Role of bubble size in flotation of coarse and fine particles—a review. *Separation Science and Technology*, 39(4):741–760, 2005.

H. Oliveira, A. Azevedo, and J. Rubio. Nanobubbles generation in a high-rate hydrodynamic cavitation tube. *Minerals Engineering*, 116:32–34, 2018.

Rahman Ahmadi, Darban Ahmad Khodadadi, Mahmoud Abdollahy, and Maoming Fan. Nano-microbubble flotation of fine and ultrafine chalcopyrite particles. *International Journal of Mining Science and Technology*, 24(4):559–566, 2014.

Haipeng Li. Role of hydrodynamic cavitation in fine particle flotation. *Master's thesis*, University of Alberta, 2014.

W. Zhou, H. Chen, L. Ou, and Q. Shi. Aggregation of ultra-fine scheelite particles induced by hydrodynamic cavitation. *International Journal of Mineral Processing*, 157:236–240, 2016.

Seyed Mehdi Ashrafizadeh and Hojat Ghassemi. Experimental and numerical investigation on the performance of small-sized cavitating venturis. *Flow measurement and Instrumentation*, 42:6–15, 2015.

Donghua Li, Shenghua Liu, Yanju Wei, Tongtong Ren, and Yonghong Tang. A turbulent two-phase model for predicting cavitating flow based on homogenous nucleation theory. *International Communications in Heat and Mass Transfer*, 97:17–19, 2018.

Vedanth Srinivasan, Abraham J. Salazar, and Kozo Saito. Modeling the disintegration of cavitating turbulent liquid jets using a novel vof-cimd approach. *Chemical Engineering Science*, 65:2782–2796, 2010.

D Li, Mikael Grekula, and Per Lindell. A modified sst k-ω turbulence model to predict the steady and unsteady sheet cavitation on 2d and 3d hydrofoils. *7th International Symposium on Cavitation*, 2009.

Hou-lin Liu, Dong-xi Liu, Yong Wang, Xian-fang Wu, and Jian Wang. Application of modified k-ω model to predicting cavitating flow in centrifugal pump. *Water Science and Engineering*, 6(3):331–339, 2013.

Huiying Li, Frank J Kelecy, Aleksandra Egelja-Maruszewski, and Sergio A Vasquez. Advanced computational modeling of steady and unsteady cavitating flows. In ASME 2008 International Mechanical Engineering Congress and Exposition, pages 413–423. *American Society of Mechanical Engineers*, 2008.

George Wm Thomson. The antoine equation for vapor-pressure data. *Chemical reviews*, 38(1):1–39, 1946.

Brian P Leonard. A stable and accurate convective modelling procedure based on quadratic upstream interpolation. *Computer methods in applied mechanics and engineering*, 19(1): 59–98, 1979.

Henry Scheffe. The relation of control charts to analysis of variance and chi-square tests. *Journal of the American Statistical Association*, 42(239):425–431, 1947.

Hongbo Shi, Alexandra Komrakova, and Petr Nikrityuk. Fluidized beds modeling: Val-

idation of 2d and 3d simulations against experiments. *Powder Technology*, 343:479–494, 2019.

MATLAB User's Guide. The mathworks. *Inc., Natick, MA*, 5:333, 1998.

William Mendenhall, Terry Sincich, and Nancy S Boudreau. A *second course in statistics: regression analysis*, volume 5. Prentice Hall Upper Saddle River, NJ, 1996.

Christopher E Brennen. *Cavitation and bubble dynamics*. Cambridge University Press, 2014.

Matevz Dular, Tjasa Griessler-Bulc, Ion Gutierrez-Aguirre, Ester Heath, Tina Kosjek, Aleksandra Krivograd Klemencic, Martina Oder, Martin Petkovsek, Nejc Racki, Maja Ravnikar, et al. Use of hydrodynamic cavitation in (waste) water treatment. *Ultrasonics sonochemistry*, 29:577–588, 2016.

SK Kawatra and TC Eisele. Froth flotation-fundamental principles. *Research, Michigan Technical University*, pages 1–30, 2002.

HJ Schulze, B Radoev, Th Geidel, H Stechemesser, and E Topfer. Investigations of the collision process between particles and gas bubbles in flotation—a theoretical analysis. *International Journal of Mineral Processing*, 27(3-4):263–278, 1989.

Daniel Chipfunhu, M Zanin, and S Grano. Flotation behaviour of fine particles with respect to contact angle. *Chemical engineering research and design*, 90(1):26–32, 2012.

FAN Maoming, TAO Daniel, Rick HONAKER, and LUO Zhenfu. Nanobubble generation and its application in froth flotation (part i): nanobubble generation and its effects on properties of microbubble and millimeter scale bubble solutions. *Mining Science and Technology (China)*, 20(1):1–19, 2010.

Mingda Li, Adrien Bussonni‘ere, Matthew Bronson, Zhenghe Xu, and Qingxia Liu. Study of venturi tube geometry on the hydrodynamic cavitation for the generation of microbubbles. *Minerals Engineering*, 132:268–274, 2019.

Jiakai Zhu, Huangjun Xie, Kesong Feng, Xiaobin Zhang, and Minqiang Si. Unsteady cavitation characteristics of liquid nitrogen flows through venturi tube. *International Journal*

of Heat and Mass Transfer, 112:544–552, 2017.

Jiong Wang, Luyan Wang, Shuangjie Xu, Bin Ji, and Xinping Long. Experimental investigation on the cavitation performance in a venturi reactor with special emphasis on the choking flow. *Experimental Thermal and Fluid Science*, 2019.

Anthony A Atchley and Andrea Prosperetti. The crevice model of bubble nucleation. *The Journal of the Acoustical Society of America*, 86(3):1065–1084, 1989.

HB Marschall, Knud Aage Mørch, AP Keller, and M Kjeldsen. Cavitation inception by almost spherical solid particles in water. *Physics of fluids*, 15(2):545–553, 2003.

JJ Kwan, S Graham, R Myers, R Carlisle, E Stride, and CC Coussios. Ultrasound-induced inertial cavitation from gas-stabilizing nanoparticles. *Physical Review E*, 92(2):023019, 2015.

Robert E Apfel. The role of impurities in cavitation-threshold determination. *The Journal of the Acoustical Society of America*, 48(5B):1179–1186, 1970.

XiaoBin Zhang, JiaKai Zhu, LiMin Qiu, and XueJun Zhang. Calculation and verification of dynamical cavitation model for quasi-steady cavitating flow. *International Journal of Heat and Mass Transfer*, 86:294–301, 2015.

Guo-Dong Li, Song-Sheng Deng, Jin-Fa Guan, and Su Yao. Numerical analysis on cavitation effects in submerged water jet added with turbulent drag-reducing additives of ctac. *Chemical Engineering Science*, 196:391–401, 2019.

Houcun Zhou, Min Xiang, Shiwei Zhao, and Weihua Zhang. Development of a multiphase cavitation solver and its application for ventilated cavitating flows with natural cavitation. *International Journal of Multiphase Flow*, 115:62–74, 2019.

S Brinkhorst, E von Lavante, and G Wendt. Numerical investigation of cavitating herschel venturi-tubes applied to liquid flow metering. *Flow Measurement and Instrumentation*, 43:23–33, 2015.

DR Kaushal, Kimihiko Sato, Takeshi Toyota, Katsuya Funatsu, and Yuji Tomita. Effect of particle size distribution on pressure drop and concentration profile in pipeline flow of

highly concentrated slurry. *International Journal of Multiphase Flow*, 31(7):809–823, 2005.

C Simonin and PL Viollet. Predictions of an oxygen droplet pulverization in a compressible subsonic coflowing hydrogen flow. *Numerical Methods for Multiphase Flows*, FED91, pages 65–82, 1990.

Z Naumann and L Schiller. A drag coefficient correlation. *Z. Ver Deutsch. Ing*, 77:318–323, 1935.

Madhava Syamlal and Thomas J O'Brien. Computer simulation of bubbles in a fluidized bed. In *AIChE Symp. Ser*, volume 85, pages 22–31, 1989.

CKK Lun, S Br Savage, DJ Jeffrey, and N Chepurniy. Kinetic theories for granular flow: inelastic particles in couette flow and slightly inelastic particles in a general flow field. *Journal of fluid mechanics*, 140:223–256, 1984.

Paul C Johnson and Roy Jackson. Frictional–collisional constitutive relations for granular materials, with application to plane shearing. *Journal of fluid Mechanics*, 176:67–93, 1987.

Jianmin Ding and Dimitri Gidaspow. A bubbling fluidization model using kinetic theory of granular flow. *AIChE journal*, 36(4):523–538, 1990.

Hongbo Shi, Mingda Li, Petr Nikrityuk, and Qingxia Liu. Experimental and numerical studies of cavitation flows in venturi tubes: geometry and scale-up. *Chemical Engineering Science*, 207:672–687, 2019.

Hongbo Shi, Mingda Li, Qingxia Liu, and Petr Nikrityuk. Experimental and numerical study of cavitating particulate flows in a venturi tube. *Chemical Engineering Science*, page 115598, 2020.

Haipeng Li, Artin Afacan, Qingxia Liu, and Zhenghe Xu. Study interactions between fine particles and micron size bubbles generated by hydrodynamic cavitation. *Minerals Engineering*, 84:106–115, 2015.

Muthupandian Ashokkumar, Raul Rink, and Sergey Shestakov.Hydrodynamic cavitation-an alternative to ultrasonic food processing. *Technical Acoustics/Tekhnicheskaya Akustika*, (9), 2011.

Parag R Gogate. Hydrodynamic cavitation for food and water processing. *Food and Bioprocess Technology*, 4(6):996–1011, 2011.

Joe Z Zhou, Haihong Li, Ross S Chow, Qingxia Liu, Zhenghe Xu, and Jacob Masliyah. Role of mineral flotation technology in improving bitumen extraction from mined athabasca oil sands ii. flotation hydrodynamics of water-based oil sand extraction. *The Canadian Journal of Chemical Engineering*, 2019.

Alister Simpson and Vivek V Ranade. Modelling of hydrodynamic cavitation with orifice: Influence of different orifice designs. *Chemical Engineering Research and Design*, 136:698–711, 2018.

H Yu, L Goldsworthy, PA Brandner, J Li, and V Garaniya. Modelling thermal effects in cavitating high-pressure diesel sprays using an improved compressible multiphase approach. *Fuel*, 222:125–145, 2018.

Xinsheng Cheng, Xueming Shao, and Lingxin Zhang. The characteristics of unsteady cavitation around a sphere. *Physics of Fluids*, 31(4):042103, 2019.

Aswin Gnanaskandan and Krishnan Mahesh. Numerical investigation of near-wake characteristics of cavitating flow over a circular cylinder. *Journal of Fluid Mechanics*, 790:453–491, 2016.

Elmar Achenbach. Influence of surface roughness on the cross-flow around a circular cylinder. *Journal of fluid mechanics*, 46(2):321–335, 1971.

F. Dierich and P.A. Nikrityuk. A numerical study of the impact of surface roughness on heat and fluid flow past a cylindrical particle. *Int. J. Thermal Sciences*, 65:92–103, 2013.

PA Brandner, GJ Walker, PN Niekamp, and B Anderson. An experimental investigation of cloud cavitation about a sphere. *Journal of Fluid Mechanics*, 656:147–176, 2010.

Dominicus Danardono, Ki-Seong Kim, Sun-Youp Lee, and Jang-Hee Lee. Optimization the design of venturi gas mixer for syngas engine using three-dimensional cfd modeling. *Journal of mechanical science and technology*, 25(9):2285, 2011.

Mathias Romanczyk. Influence of gas inlet angle on the mixing process in a venturi mixer. In *ITM Web of conferences*, volume 15, page 07005. EDP Sciences, 2017.

S Sundararaj and V Selladurai. An analysis on proportional mixing of liquids using venturi jet mixer. *International Journal of Applied Engineering Research*, 7:891–902, 2008.

S Sundararaj and V Selladurai. Numerical and experimental study on jet trajectories and mixing behavior of venturi-jet mixer. *Journal of fluids engineering*, 132(10), 2010.

Gaurav G Dastane, Harsh Thakkar, Rushabh Shah, Sivaramakrishna Perala, Janhavi Raut, and AB Pandit. Single and multiphase cfd simulations for designing cavitating venturi. *Chemical Engineering Research and Design*, 149:1–12, 2019.

Hongbo Shi, Qingxia Liu, and Petr Nikrityuk. Modeling of cavitating flows past a micro-sized particle. *International Journal of Multiphase Flow*, page 103276, 2020.

LuYan Wang, Bin Ji, HuaiYu Cheng, Jiong Wang, and XinPing Long. One-dimensional/three-dimensional analysis of transient cavitating flow in a venturi tube with special emphasis on cavitation excited pressure fluctuation prediction. *Science China Technological Sciences*, pages 1–11, 2019.

Christian P Egerer, Stefan Hickel, Steffen J Schmidt, and Nikolaus A Adams. Large-eddy simulation of turbulent cavitating flow in a micro channel. *Physics of Fluids*, 26(8):085102, 2014.

NM Nouri, SMH Mirsaeedi, and M Moghimi. Large eddy simulation of natural cavitating flows in venturi-type sections. Proceedings of the Institution of Mechanical Engineers, Part C: *Journal of Mechanical Engineering Science*, 225(2):369–381, 2011.[120] F Orley,

T Trummler, S Hickel, MS Mihatsch, SJ Schmidt, and NA Adams. Large-eddy simulation of cavitating nozzle flow and primary jet break-up. *Physics of Fluids*, 27(8):086101, 2015.

Nagendra Dittakavi, Aditya Chunekar, and Steven Frankel. Large eddy simulation of turbulent-cavitation interactions in a venturi nozzle. *Journal of Fluids Engineering*, 132(12): 121301, 2010.

Franck Nicoud and Frederic Ducros. Subgrid-scale stress modelling based on the square of

the velocity gradient tensor. *Flow, turbulence and Combustion*, 62(3):183–200, 1999.

B Ji, XW Luo, Roger EA Arndt, Xiaoxing Peng, and Yulin Wu. Large eddy simulation and theoretical investigations of the transient cavitating vortical flow structure around a naca66 hydrofoil. *International Journal of Multiphase Flow*, 68:121–134, 2015.

M Sedlar, B Ji, T Kratky, T Rebok, and R Huzlik. Numerical and experimental investigation of three-dimensional cavitating flow around the straight naca2412 hydrofoil.*Ocean Engineering*, 123:357–382, 2016.

Bram Van Leer. Towards the ultimate conservative difference scheme. v. a second-order sequel to godunov's method. *Journal of Computational Physics*, 32(1):101–136, 1979.

H Sepehr, P Nikrityuk, D Breakey, and RS Sanders. Numerical study of crude oil batch mixing in a long channel. *Petroleum science*, 16(1):187–198, 2019.